NEUTRON SCATTERING STUDIES OF FLUORITE OXIDES AT HIGH TEMPERATURES

John Emyr Macdonald

A thesis submitted for the degree of
Doctor of Philosophy in the University of Oxford

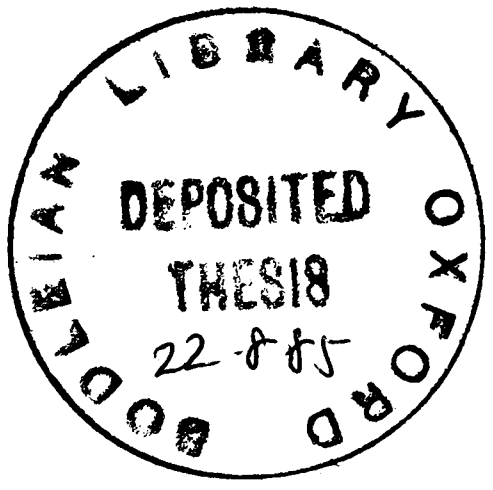

St. John's College
Oxford

Hilary Term
1985

ABSTRACT

J. Emyr Macdonald

D. Phil.

St. John's College, Oxford

Hilary Term 1985

NEUTRON SCATTERING STUDIES OF FLUORITE OXIDES AT HIGH TEMPERATURES

The high temperature behaviour of the fluorite oxides UO_2, ThO_2 and Y_2O_3-stabilised ZrO_2 have been investigated using a variety of neutron scattering techniques. Interest has centred on the cause of the anomalously large enthalpy of UO_2 at temperatures above 1500K, an understanding of which is important in view of its use as a fission reactor fuel. High temperature techniques have been developed which enable the performance of neutron scattering at temperatures up to 3000K. Bragg diffraction measurements have shown that a growing fraction of anions vacate their regular sites above 2100K in UO_2 and above 2300K in ThO_2, attaining vacancy concentrations of $\sim$20% at 2900K in both materials. Quasielastic scattering investigations have confirmed the occurrence of anion Frenkel disorder in UO_2 at high temperatures and have shown that the disorder is of a dynamic nature. Both sets of results may be interpreted in terms of fluctuating, dynamic clusters of vacancies and interstitials, having lifetimes of a few phonon periods. The elastic constants of UO_2, which have been determined up to 2930K from measurements of the long wavelength acoustic phonons, show an increased rate of softening above 2400K. The zone-centre optic phonons broaden rapidly above 2000K in UO_2. The full phonon dispersion relation of ThO_2, measured at 293K, resembles closely that of UO_2. The results provide the first direct, unambiguous evidence of thermally-induced Frenkel disorder in UO_2, which is analágous to the disorder observed in the fast-ion phase of the fluorite halides, such as CaF_2.

Quasielastic scattering techniques have also been used to study the defect structure of Y_2O_3-stabilised ZrO_2 between 293K and 2000K. Many general features of the scattering observed at room temperature may be explained in terms of nearest neighbour relaxations around oxygen vacancies. The diffuse scattering broadens in energy above 1000K, signifying that these clusters of relaxed ions have a finite lifetime of $\sim$5ps at 1500K. The results have been interpreted in terms of a vacancy hopping model which is consistent with the enhanced conductivity observed in this temperature range.

ACKNOWLEDGEMENTS

This work was carried out with the support of a CASE studentship funded by the Science and Engineering Research Council and AERE Harwell. Use of the neutron scattering facilities at AERE Harwell, ILL Grenoble and Risø National Laboratory, Denmark is gratefully acknowledged. Particular thanks are due to W. Hayes, M. T. Hutchings, K. Clausen, R. Osborn and P. Schnabel for their generous advice and encouragement during the study. The technical support of P. Bowen, W. Futcher and many other colleagues at Harwell, without whose aid this work could not have been performed, cannot be underestimated. Thanks are also due to V. Champaneria for the excellent preparation of the manuscript.

CONTENTS

CONTENTS (Continued)

CONTENTS (Continued)

CONTENTS (Continued)

Note: In order to facilitate cross-reference, diagrams are located at the end of each chapter. Tables are incorporated in the text.

CHAPTER 1

INTRODUCTION

1.1 GENERAL INTRODUCTION

The high temperature properties of compounds possessing the fluorite structure have been the subject of considerable interest in recent years. Whereas extensive experimental work has been performed on the fluorite halides (Chadwick 1983), investigations of the fluorite oxides have been limited as a result of their high melting temperatures (~3000K). This thesis describes an experimental investigation of the fluorite oxides UO_2, ThO_2 and Y_2O_3 - doped ZrO_2 at high temperatures using a variety of neutron scattering techniques.

The fluorite structure, shown in Fig. 1.1, has a face-centred cubic lattice with a basis comprising a cation at the origin and anions at $\pm(\frac{1}{4},\frac{1}{4},\frac{1}{4})$. The unit cell is a cube of side a_o, which is twice the anion nearest-neighbour separation. The structure may be viewed as an array of simple cubic cells of anions, with alternate cube-centres occupied by cations.

Most fluorite halides, such as CaF_2, PbF_2 and $SrCl_2$, exhibit a broad Schottky-type anomaly in their heat capacity at a temperature T_c, a few hundred degrees below their melting temperature T_m. This anomaly is accompanied by substantial enhancement of their electrical conductivity, in the crystalline state, to a value comparable with that of the ionic melt (Fig. 1.2). A high degree of dynamic anion disorder occurs in the high temperature phase, as a result of which these materials are classed as fast-ion conductors. In fact, the fluorite halides provide one of the simplest systems for the study of the

phenomenon of fast-ion conduction.

Anomalous behaviour has also been observed in the enthalpy and electrical conductivity of UO_2 between 1500K and its melting temperature 3120K. This has attracted considerable attention because of the use of UO_2 as a fuel for some designs of nuclear reactors. An understanding of its thermal properties and the cause of its excess heat capacity is especially important in the safety analysis of fast reactors, in view of their high operating temperatures. Unfortunately, all experimental measurements to date have been of macroscopic quantities, such as enthalpy and electrical and thermal conductivity. This work is an attempt to provide information on the cause of the excess enthalpy of UO_2 on a microscopic scale, using neutron scattering techniques.

In this chapter we outline the relevant experimental data on UO_2 and ThO_2 that have been collected above 1500K, and the theoretical work that has ensued. Then we review the use of neutron scattering techniques for the study of the nature of the high-temperature disordered regime of the fluorite halides. Lastly we discuss their proposed use in the investigation of the high temperature behaviour of the fluorite oxides UO_2, ThO_2 and Y_2O_3-doped ZrO_2.

1.2 PHYSICAL PROPERTIES OF UO_2 AND ThO_2 AT HIGH TEMPERATURES

1.2.1 ENTHALPY AND HEAT CAPACITY

Practical difficulties such as thermal isolation and accurate measurement of temperature changes discourage the direct evaluation of heat capacities above 2000K. Consequently, high temperature values of

heat capacities are normally extracted from the temperature derivative of the enthalpy H(T).

$$C_p(T) = \left(\frac{\partial H(T)}{\partial T} \right)_{P,T} \qquad (1.1)$$

where C_p is the heat capacity at constant pressure.

Five independent sets of data have been reported for the enthalpy of UO_2 within the temperature range 298 - 3120K. These are by Moore and Kelley (1947), Ogard and Leary (1968), Hein et. al. (1968), Leibowitz et. al. (1969) and Frederickson and Chasanov (1970). The measurements were made mainly using drop-calorimetry techniques, in which the samples were encapsulated in tungsten, heated to the required temperature, dropped into a calorimeter and the resulting temperature rise of the liquid monitored. The agreement between the sets of data, shown in Fig. 1.3, is about 1 - 2%.

In order to derive the heat capacity from the enthalpy measurements, an analytical function must first be fitted to the data, thus introducing some model-dependence. Szwarc (1969) and Kerrisk and Clifton (1972) found that the heat capacity curves for UO_2, obtained by fitting the customary polynomial or spline functions to the enthalpy data, behave as for a traditional solid up to 1400K. However, above this temperature there seemed to be an additional exponential contribution. They assumed that this contribution was due to Frenkel defects, which had been shown to exist in fluorite halides at elevated temperatures. This gave an additional term in the enthalpy function which, for Szwarc's analysis, became

$$H(T) = A + BT + CT^2 + D \exp(-E_d/2RT) \qquad (1.2)$$

where the parameters A, B, C and D and the defect formation energy E_d were fitted to the data. Both resulting heat capacity curves were similar, showing an exponential rise above 1500K (Fig. 1.4). The values of E_d obtained were 3.10 eV (Szwarc 1969) and 3.28 eV (Kerrisk and Clifton 1972). It should be noted here that E_d is twice the activation energy E_a, obtained from a $\exp(-E_a/RT)$ temperature dependence. This follows from the fact that each Frenkel defect involves the formation of an interstitial and a vacancy.

However, Bredig (1972) noted that the enthalpy analysis of Szwarc showed a linear temperature dependence, signifying a constant C_p value, above about 2700K and that there was a systematic trend in the deviations from the fitted curve around this temperature. The six points in the temperature range 2340 - 2580K all showed negative deviations whereas seven out of the eight points in the range 2610 - 2880K had positive deviations. He interpreted this, somewhat speculatively , as evidence for a cooperative lambda-type transition at 2670K, and claimed it to be similar to that observed in the fluorite halides (Fig. 1.2). Rand et. al. (1978) agreed with Bredig's claim that the enthalpy is linear with temperature above 2700K and they also observed similar non-random deviations in Kerrisk and Clifton's analysis. Further support was given by a report by Ackermann et. al. (1956) of a textural change in UO_2 at 2700K, which they, in fact, interpreted as melting. Consequently, Fink et. al. (1981) re-analysed the UO_2 enthalpy data with the function

$$H_T - H_{298} = C_1\theta_E \left\{ \left[\exp(\theta_E/T)-1 \right]^{-1} - \left[\exp(\theta_E/298)-1 \right] \right\}^{-1}$$

$$+ C_2 \left[T^2 - (298)^2 \right]$$

$$+ C_3 k_B \left[T \exp(-E_a/k_BT) - 298 \exp(-E_a/k_BT) \right] \qquad (1.3a)$$

for $T < 267$OK, and

$$H_T - H_{298} = C_4T - C_5 \qquad (1.3b)$$

for 267OK $< T <$ 312OK. The fitted parameters were the variables C_i, the Einstein temperature θ_E and the activation energy E_a, k_B being Boltzmann's constant. The resulting values of θ_E and E_a were 516K and 1.88eV respectively. The three terms in equation (1.3a) represent the respective contributions from phonons, thermal expansion and the additional thermally-activated term. The derived heat capacity curve is compared with that of Kerrisk and Clifton (1972) in Fig. 1.4.

Further light is shed on the behaviour of the enthalpy of UO_2 by comparison with the corresponding data for the isostructural oxide ThO_2 (Fischer et. al. 1981), also shown in Fig. 1.3. These indicate a change in gradient at about 295OK and a linear dependence above this temperature. The ThO_2 data were also fitted with the function given in equation (1.3), excluding the exponential activated term since its inclusion did not improve the fit significantly. The heat capacity curve deduced from the fit is shown, together with those obtained for UO_2, in Fig. 1.4.

The picture which emerges from these analyses, involving the fitting of an analytical function to the enthalpy data, is the following. The enthalpies of both UO_2 and ThO_2 behave normally up to about 150OK. Above this temperature, there is an additional

exponential thermally-activated contribution in UO_2, which does not exist in ThO_2. Both materials show evidence of a transition at higher temperatures: T_c = 2670K in UO_2 and 2950K in ThO_2. The ratio T_c/T_m is 0.86 for UO_2 and 0.81 for ThO_2 (T_m = 3640K), indicating a possible similarity between the transitions in each material. In direct contrast with the above analyses, Browning et. al. (1983) calculated the separate contributions to the enthalpy of UO_2 from phonons, lattice dilation, anharmonic vibrations of the oxygen ions and the population of crystal field levels, using existing thermophysical data. They claimed that these contributions alone account well for the enthalpy data up to 2500K, above which the enthalpy is anomalously large.

These contradicting conclusions, drawn from the enthalpy data, and the large variation in the behaviour of the extrapolated heat capacity (Fig. 1.4) emphasise the need for an experimental investigation on a microscopic scale.

1.2.2 ELECTRICAL CONDUCTIVITY

The most comprehensive investigation of the temperature dependence of the electrical conductivity of UO_2 is that performed by Bates et. al. (1967). They investigated its temperature variation in polycrystalline and single crystal samples, at frequencies up to 5kHz, from ambient temperature up to 3000K. No significant frequency variation of the conductivity was observed, but the results varied between samples at low temperatures. A rapid increase in the conductivity σ was observed at around 1400K (Fig. 1.5), above which it was best described as

$$\sigma = \sigma_o \exp(-E_a/k_B T) \qquad (1.4)$$

with $\sigma_o = 3.57 \times 10^3 \ \Omega^{-1}cm^{-1}$ and with an activation energy $E_a = 1.15eV$.

Other investigations of the variation of the electrical conductivity of UO_2 over more limited temperature ranges, are in substantial agreement with those of Bates et. al. (Killeen 1980, Munir 1981). However a two-fold increase in conductivity at frequencies between 0.5MHz and 5MHz at room temperature has recently been observed (G. A. Saunders and N. Hampton, private communication).

1.3 THEORETICAL ASPECTS OF THE PHYSICAL PROPERTIES OF UO_2 AND ThO_2

When the enthalpy of UO_2 was first shown to increase anomalously above 1500K, its cause was attributed to the creation of Frenkel defects (Szwarc 1969, Kerrisk and Clifton 1972). Consideration of the fluorite structure shows that the unoccupied cube centres provide suitable sites for the formation of Frenkel interstitial ions, as have been shown to occur in fluorite halides at low temperatures (Lidiard 1974).

Diffraction studies up to 1400K indicate that the anions vibrate anisotropically towards the empty cube centres (Willis 1963). Further support for such a model is given by analogy with the fluorite halides, in which the presence of Frenkel disorder at high temperatures has been established (e.g. Chadwick 1983).

The Frenkel defect model for the anomalous excess enthalpy of UO_2 above 1500K was first challenged by MacInnes (1978, 1979). He noted firstly that the anomaly occurs in UO_2 at a much lower fraction of T_m than in the fluorite halides, for which $T_c/T_m \sim 0.8$. Secondly, there is little evidence for an analogous anomaly in ThO_2 (Fig. 1.3), which would be expected to have similar lattice properties on account of their comparable cation masses (m_U = 238 a.m.u., m_{Th} = 232 a.m.u.). In view of the uranium ion's multiplicity of possible oxidation states, contrasting with the electronically stable Th^{4+} ion, MacInnes concluded that the disorder giving rise to the anomalous excess enthalpy of UO_2 above 1500K is electronic in nature.

Further support for an electronic model is given by calculations of the activation energies E_a for Frenkel defects and for electronic disorder (Catlow 1977). Using a static model of a cube-centre anion Frenkel interstitial and an isolated vacancy, involving inter-atomic potentials deduced from experimental measurements of elastic constants and other parameters, a value of $E_a = \frac{1}{2}E_d = 2.7$eV was obtained. The activation energy for electronic excitations of the uranium ion, giving rise to small polarons, of the type

$$2U^{4+} \longrightarrow U^{3+} + U^{5+} \qquad (1.5)$$

was found to be about 2eV. Similar results were obtained by Harding et. al. (1980). A summary of experimental and theoretical values of E_a is given in Table 1.1, from which it may be seen that the calculated values for electronic disorder are smaller than the calculated values for Frenkel defects, and are in better agreement with the experimental values. Caution is needed regarding these calculated values because of the approximations involved, such as the neglect of the effects of temperature and thermal expansion on the

TABLE 1.1

COMPARISON OF EXPERIMENTALLY-DETERMINED ACTIVATION ENERGIES FOR UO_2 WITH VALUES CALCULATED FROM MODELS OF FRENKEL DEFECT FORMATION AND OF SMALL POLARON EXCITATION

EXPERIMENTAL

Reference	Measured Quantity	E_a (eV)
Szwarc 1969	Enthalpy	1.55
Kerrisk and Clifton 1972	Enthalpy	1.64
Fink et.al. 1981	Enthalpy	1.88
Bates et.al. 1967	Electrical Conductivity	1.15
Matzke 1976	Oxygen Diffusion	1.15

CALCULATION

Reference	Model	E_a (eV)
Catlow 1977	Frenkel Defect	2.7 †
Harding et.al. 1980	Frenkel Defect	2.6 †
Catlow 1977	Small Polaron	~2
Harding et.al. 1980	Small Polaron	1.7

† $E_d = 2E_a$ for Frenkel defect formation

inter-atomic potentials. Nevertheless, these calculations do suggest that electronic disorder may play an important role in the behaviour of UO_2 above 1500K. However, the calculations of Browning et. al. (1983) indicate that the magnitude of the small polaron enthalpy contribution is less than the experimental uncertainty of the enthalpy data in the temperature range 1500 - 2500K.

1.4 NEUTRON SCATTERING INVESTIGATIONS OF FLUORITE HALIDES

The work described in this thesis forms part of a collaborative programme of research between the Clarendon Laboratory, A.E.R.E. Harwell and Risø National Laboratory, Denmark, aimed at the investigation of the high-temperature properties of fluorites using neutron scattering techniques. An outline of the results obtained for the fluorite halides is given here; the details of the measurements are discussed and compared with those of the present work on the fluorite oxides in subsequent chapters. A review of the work is given by Hutchings (1982), and the details by Smith (1980) and Schnabel (1983). The various neutron scattering techniques employed will be discussed more fully in chapter 3; a description of the results will suffice at this stage.

The time-averaged distribution of nuclei for CaF_2, $SrCl_2$, PbF_2 and BaF_2, obtained from diffraction studies, all show similar properties. The normal fluorite structure accounts well for the data up to about 200^{o} below T_c. As the temperature is increased further, a growing fraction of anions vacate their regular sites. Saturation is reached before melting at vacancy levels of about 10 - 20%, probably due to repulsive interactions between defects. This behaviour is consistent with the decrease in heat capacity

observed above the transition, and is inconsistent with total melting of the anion sub-lattice. There is no evidence of cation migration. A more surprising fact which emerges from the analysis is that the empty cube-centre site is not occupied to any significant degree at high temperatures. This result is in agreement with molecular dynamics (Gillan and Richardson 1979), static energy calculations (Catlow and Hayes 1982) and X-ray diffraction data (Koto et. al. 1980). The data may be interpreted in terms of a cluster model of vacancies, interstitial and relaxed ions, the nature of which is discussed in § 1.4.1.

Inelastic phonon scattering experiments on PbF_2 show that the optic and large wave-vector acoustic phonon modes broaden rapidly in the region of T_c. The full-width at half-maximum (FWHM) linewidths, 2Γ, of the transverse acoustic phonons increase with the square of their wave-vector q around T_c, indicating a hydrodynamic, collision-dominated regime. To a good approximation, $2\Gamma = \gamma q^2$ for all three symmetry directions, where the constant of proportionality γ increases rapidly around T_c. The elastic constants, obtained from low-q phonon measurements, all decrease steadily from ambient temperature to T_c as predicted by the thermal expansion of the lattice. In the region of T_c the rate of decrease of C_{12} and C_{44} is accelerated slightly, but not as markedly as that of C_{11}. No soft mode behaviour was observed.

Coherent diffuse quasi-elastic scattering (QES) gives the most information on the defect structures. Whereas in a perfect crystal all the scattering occurs at the reciprocal lattice points, the presence of defects gives rise to scattering elsewhere in reciprocal space. The measurements on the halides are characterised by the

build-up of such QES around (0, 0, 2.3) in the fast-ion phase. The degree of structure observed in the QES intensity indicates strong correlations in the positions of the defective ions. The energy broadening of this scattering signifies a defect life-time of about 10^{-12} s, i.e. a few phonon periods.

The behaviour of incoherent QES, observed in $SrCl_2$, can be fitted quite well by a model of instantaneous, uncorrelated anion hops mainly in [100] directions between nearest neighbour sites, and also in [110] directions between next nearest neighbour anion sites.

1.4.1 THE CLUSTER MODEL

All the neutron scattering experiments indicate a fairly high level of anion disorder in the high temperature fast-ion phase of the fluorite halides. The defective anion distribution is highly correlated, indicating some dynamic clustering of defects, having a life-time of a few phonon periods. The simplest model which accounts for the diffraction and coherent QES data is that of a cluster comprising an anion Frenkel interstitial located on the mid-point between regular anion sites, causing its nearest neighbour anions to relax away in the [111] directions towards empty cube-centres. The position of the vacancy associated with the Frenkel interstitial cannot be ascertained from neutron scattering, but static energy calculations suggest that it is situated at (0, 0, 1.25) with respect to the interstial site (Catlow and Hayes 1982). Agreement with the diffraction and QES data is slightly improved if the interstitial is displaced from the mid-anion site in a [110] direction towards an unoccupied cube-centre. Such a cluster, named the 3:1:2 cluster, is

illustrated in Fig. 1.6. We use the notation v:i:r where v is the number of vacancies (due to interstitials or relaxed ions), i the number of true interstitials and r the number of relaxed ions. We also refer to interstitial and relaxed ion sites as I and R sites respectively.

It should be emphasised that the cluster model described here is certainly not unique in the fast-ion region, in view of the complex and highly dynamic environment. Static energy calculations have shown that such clusters can be stable in the fast-ion state, provided that the Frenkel vacancy is correctly located (Catlow and Hayes 1982). Static clusters, similar to the dynamic cluster described here, have been observed at room temperature in fluorites having an excess of anions, such as hyperstoichiometric UO_{2+x} (Willis 1978) and halides doped with rare-earth ions (Cheetham 1973, Kjems et. al. 1983). Molecular dynamics calculations have confirmed many features of the QES results, such as the peak beyond the (002) reciprocal lattice point in the coherent QES intensity (Gillan and Dixon 1981) and the incoherent QES from $SrCl_2$ (Jacucci and Rahman 1978). However these calculations do not give direct support for a cluster model, possibly as the result of the very small sample size used (8 unit cells).

1.5 PROPOSED INVESTIGATION OF FLUORITE OXIDES

This thesis describes an extension of the investigations of the fluorite halides, described in the previous section, to the fluorite oxides UO_2 and ThO_2. Because of the higher temperatures involved, furnace techniques for neutron scattering up to 3000K had to be developed. These are described in the next chapter, and

in chapter 3 a more detailed description of neutron scattering techniques and instrumentation is given.

The most obvious first step for the neutron measurements is the determination of the time-averaged distribution of ions using diffraction. Such measurements on UO_2 and ThO_2 are reported in chapter 4. Following the comparison of lattice disorder in the two oxides, a comparison of their lattice dynamics in undertaken in order to establish the degree of similarity between the interionic potentials in the compounds. Measurements of the phonon dispersion curves of ThO_2 are described in chapter 5, which may be compared with those obtained for UO_2 by Dolling et. al. (1965). Investigations of the high temperature behaviour of phonons in UO_2 are described in chapter 6, and an account of coherent QES measurements on UO_2 is given in chapter 7. In chapter 8, an investigation of the behaviour of Y_2O_3 - doped ZrO_2 from room temperature up to 2100K is described. This material is of great technological interest and may also be useful as a model of possible small polaron behaviour in UO_2, as a result of the introduction of Y^{3+} ions into a host cation sub-lattice of Zr^{4+} ions. Results and conclusions are summarised in the last chapter.

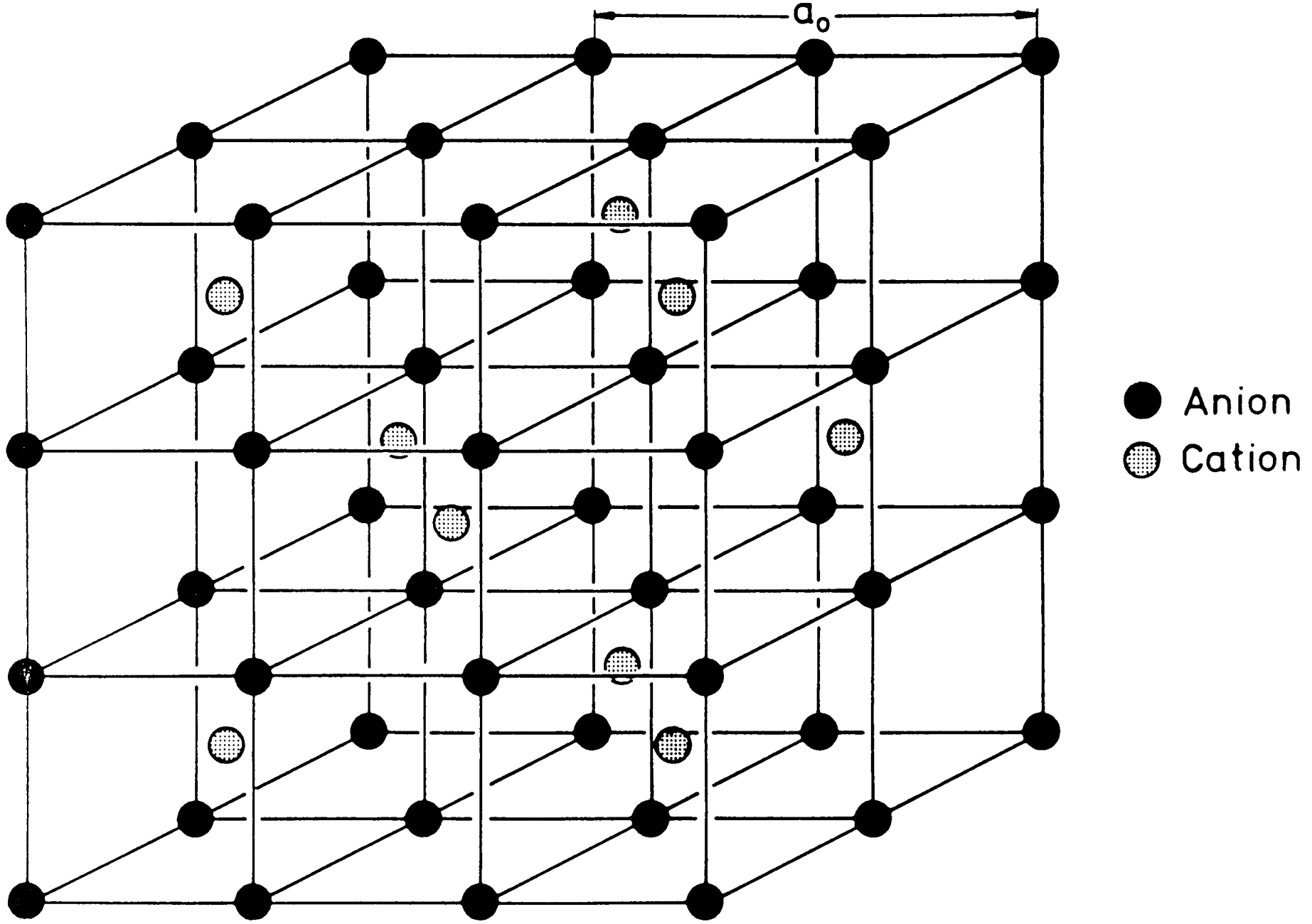

Fig 1.1 The Fluorite Structure

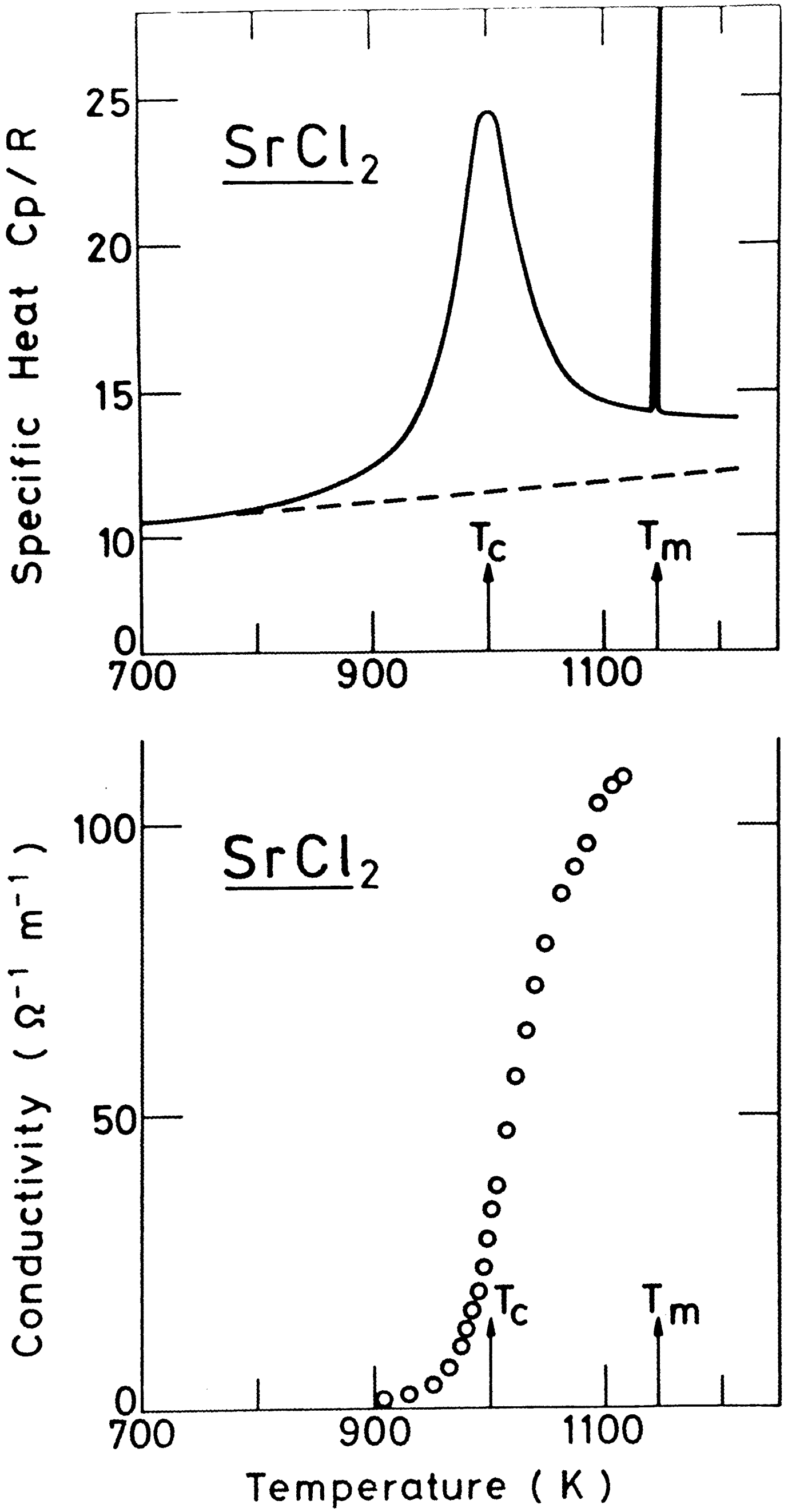

Fig. 1.2 Temperature variation of the specific heat (Schröter and Nölting 1980) and electrical conductivity (Carr et.al. 1978) of the fast-ion conductor $SrCl_2$

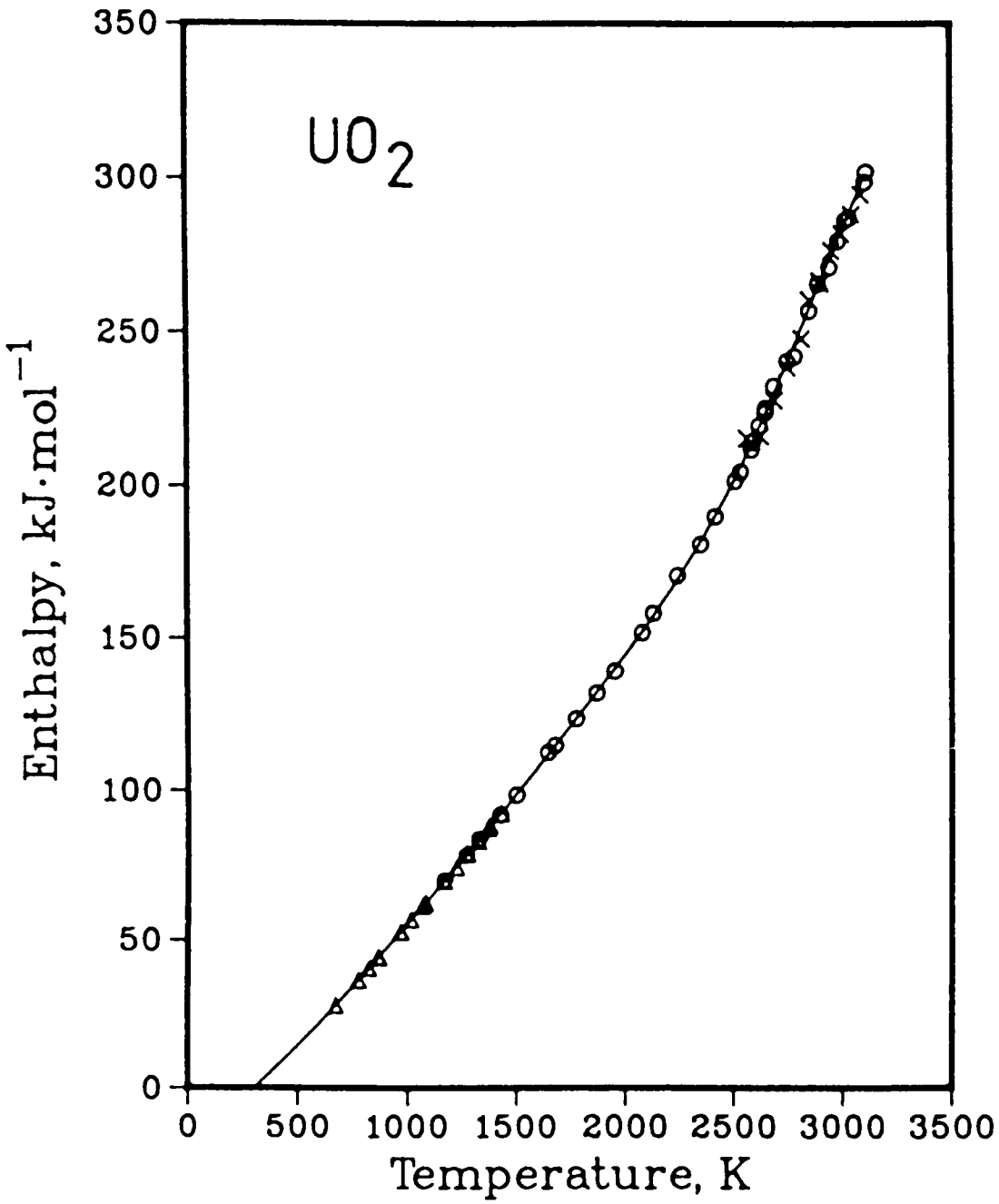

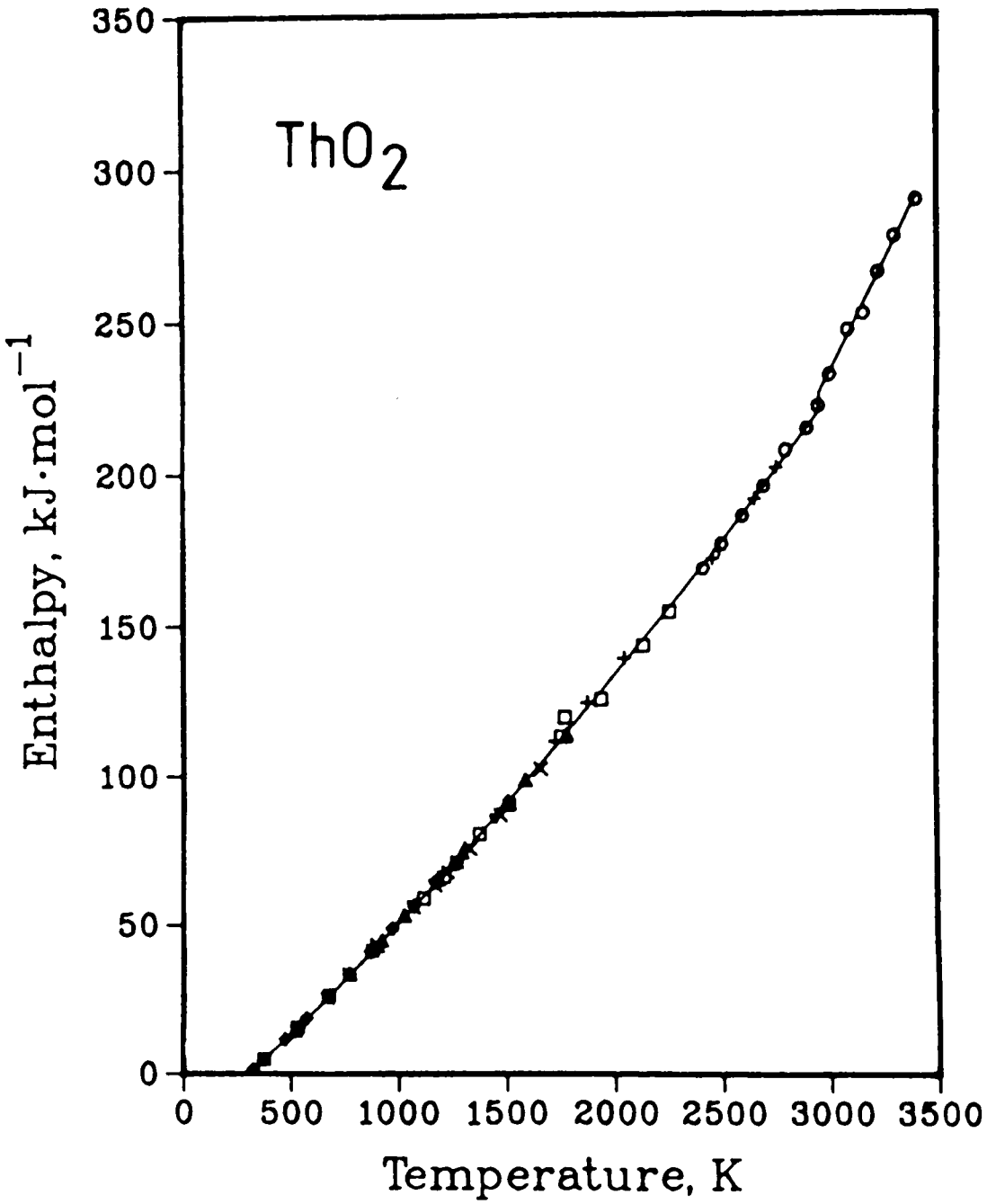

Fig. 1.3 Temperature variation of the enthalpy of UO_2 and ThO_2 (after Fink 1983).

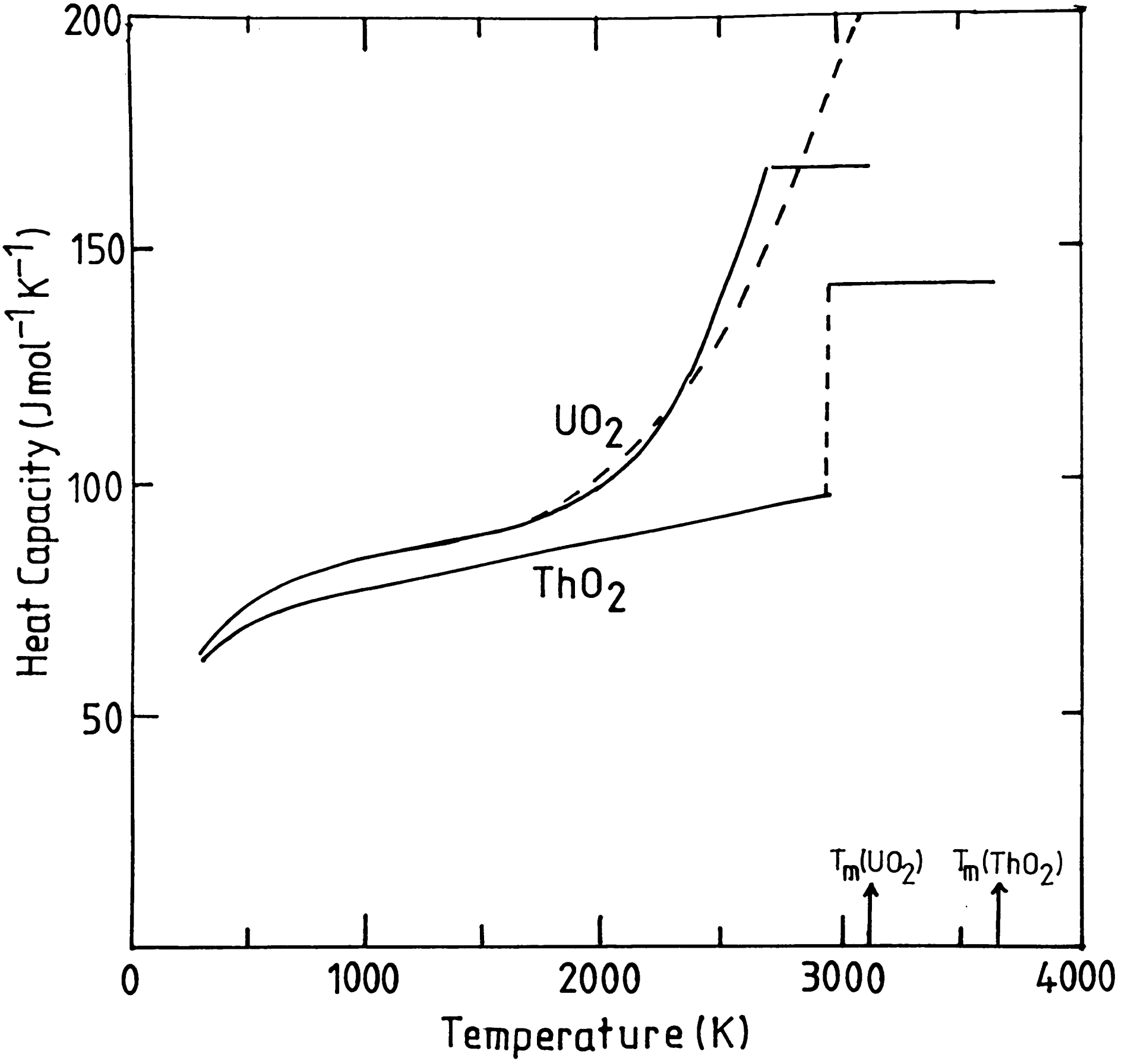

Fig. 1.4 Temperature variation of the heat capacity C_p of UO_2 and ThO_2 as deduced from analysis of enthalpy data. The full curves represent the analyses of Fink et.al.(1981) and Fischer et.al.(1981), and the broken line that of Kerrisk and Clifton(1972).

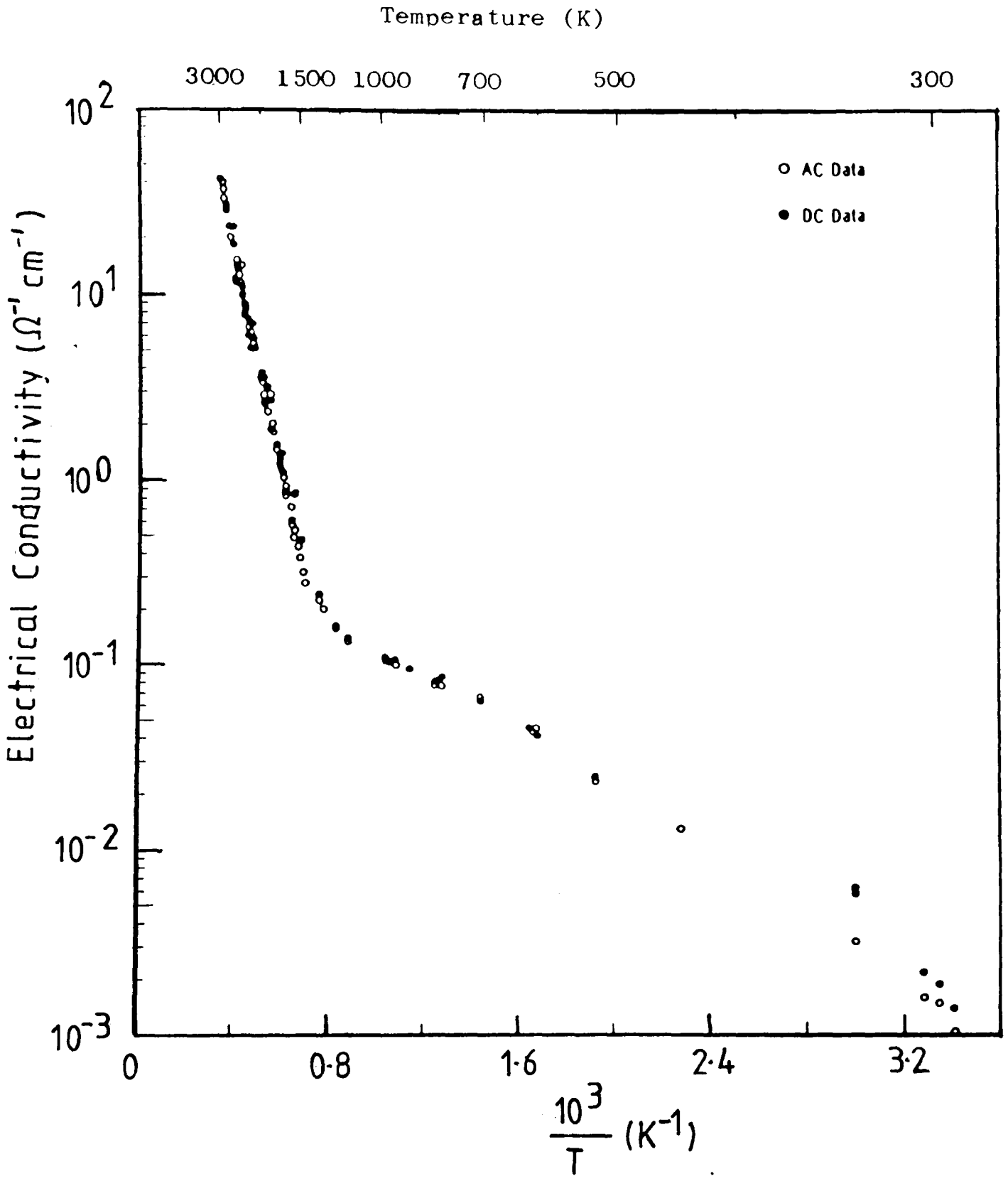

Fig. 1.5 Temperature variation of the electrical conductivity of UO_2 (after Bates et.al. 1967).

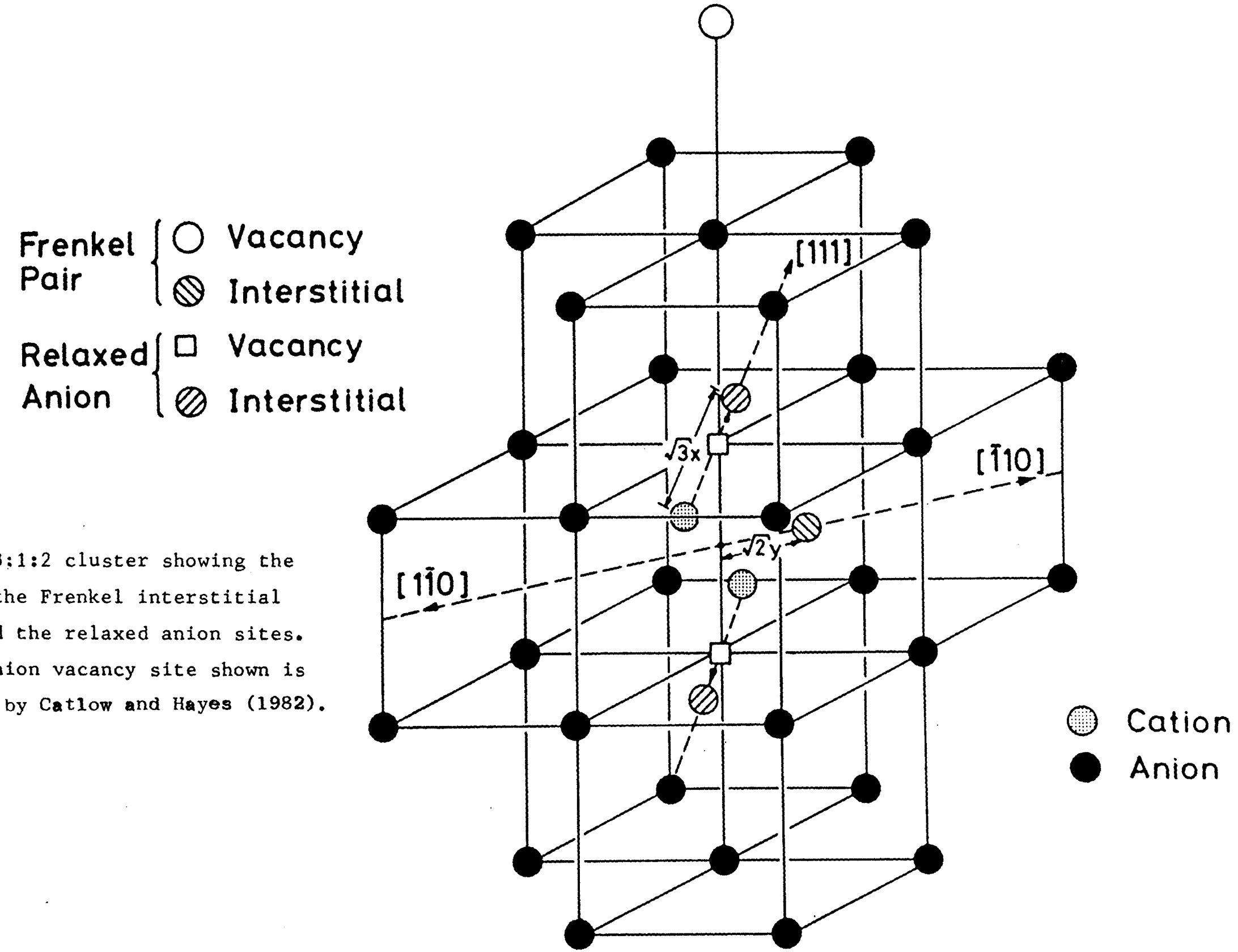

Fig. 1.6 The 3:1:2 cluster showing the positions of the Frenkel interstitial anion site and the relaxed anion sites. The Frenkel anion vacancy site shown is that proposed by Catlow and Hayes (1982).

CHAPTER 2

FURNACE TECHNOLOGY

2.1 INTRODUCTION

As was indicated in the previous chapter, the proposed investigation of the properties of UO_2 and ThO_2 at the temperatures of interest requires the development of furnace techniques for neutron scattering. Although many measurements of a macroscopic nature have been performed at higher temperatures, there has been a paucity of microscopic observations of any kind because of the experimental difficulties involved. The only neutron scattering measurements performed above 2200K are those of Aldebert and co-workers using powdered samples (e.g. Aldebert and Traverse 1981), but no neutron experiments on single crystals have been reported at temperatures above 2000K. Although diffraction studies may be performed on either powdered or crystalline samples, the measurement of phonons or QES necessitates the use of single crystals. This work constitutes an attempt to develop single crystal techniques above 2000K.

In the next section, various aspects of furnace design for high temperature neutron scattering experimentation are discussed. A detailed description of the Harwell High Temperature Furnace, developed and used for most of these measurements, is then given, and a comparison is made with Aldebert's furnace used at ILL for some UO_2 measurements. Finally, the practicalities of sample preparation and mounting are discussed.

2.2 ASPECTS OF FURNACE DESIGN

2.2.1 MATERIALS

The number of materials which are suitable for the manufacture of components situated in the hot region of the furnace is limited by their melting temperatures. The only candidates for the construction of heater elements, sample mounts and heat shields at the temperatures under consideration are iridium (T_m = 2683K), niobium (2743K), molybdenum (2890K), tantalum (3269K), osmium (3318K), rhenium (3450K), tungsten (3680K) and graphite (which sublimes at 3820K). Their relative merits must be judged further according to other properties which are now discussed, and later summarised in Table 2.1.

a) Neutron Absorption

For most high temperature applications, there is no constraint on the size and thickness of furnace components. However, in neutron scattering experiments the attenuation of the beam through absorption by the furnace is a very important consideration. The transmission of an object is given by

$$t = I/I_o = e^{-\mu D} \qquad (2.1)$$

where D is its thickness and μ its linear absorption coefficient. All the materials mentioned above have appreciable absorption coefficients, so care must be taken in the design of heater elements and heat-shields. Moreover, the section of the furnace which is in the beam must be cylindrically symmetrical to avoid any angular dependence of the absorption. In practice this is achieved by aligning all seams, joints and water pipes in a 'dead sector' of about 30^o in the furnace, which must be kept away from both the incident and scattered neutron beams. Since the absorption coefficient is generally proportional to the neutron wavelength, these effects are particularly important for QES measurements

where low-energy neutrons are employed and the signal:noise ratio is low.

b) Neutron Scattering Cross-sections

Another factor which must be considered in choosing materials is the scattering from furnace components, which appears as spurious contributions to the data. Coherent scattering gives rise to sharp Bragg peaks, whereas incoherent scattering results in an approximately isotropic contribution to the background level. Hence it is important to mask down the incident beam as far as possible in order to reduce the amount of spurious scattering from the furnace. The sample mount, heater element and inner shields should, if possible, be made from the same material so that only one set of spurious Bragg peaks is produced.

c) Mechanical Properties

One of the most important requirements of neutron scattering experiments on single crystals, as opposed to powders, is that the sample must be mounted rigidly since sample rotations of greater than 0.05^{o} cannot be tolerated. Whilst this never constitutes a problem at temperatures below 2000K, it is nevertheless an important factor in choosing a material for the sample mount at higher temperatures. The main cause of the problem is recrystallisation and grain growth within the material. For instance, during a diffraction experiment at 2200K, for which the sample was encapsulated in a machined tantalum tube, the crystal was observed to rotate through several degrees and disintegrate within twelve hours as a result of severe distortion of the tube! Tantalum is particularly bad in this respect - heater elements which had been maintained at about 2200K for a few days were observed to have individual grains of surface area $\sim 20mm^{2}$.

There are two ways of reducing the rate of grain growth in a material. The first technique, which is useful for machined metals, is that of doping with impurities which congregate at the grain boundaries and hence oppose the recrystallisation. For instance, tungsten is often doped with small amounts of ThO_2. The alternative method is to 'grow' the sample tube in a highly crystalline form by condensed vapour deposition (CVD). In this technique, a mandrel is made to the shape of the article required from an easily-machined metal such as stainless steel or copper. It is then mounted in an atmosphere of tungsten chloride vapour which decomposes on heating, resulting in the deposition of a uniform layer of tungsten onto the mandrel. The mandrel may then be dissolved leaving the required product. This technique is useful for fabricating tungsten articles of uniform thickness up to about 1mm which are stress-free and highly crystalline, thus reducing the extent of grain growth. Tungsten is also a notoriously difficult material to machine since it is one of the hardest available and is very brittle below 500°C.

d) Reactivity

The chemical reactivity of materials increases with increasing temperature, so that those which are normally inert may become extremely reactive at the temperatures under consideration here. The most important possible reaction, which must be avoided, is that between the sample and its container. Despite its favourable neutron properties, graphite was rejected as a material because of its incompatibility with UO_2, ThO_2 and tungsten, with which it readily forms carbides. A slow reaction has been reported between tungsten and UO_2 at 2800K. Tungsten sample tubes may be coated with TaN which is compatible with UO_2 up to its melting point (Burnett 1964).

e) Evaporation

The ultimate limitation on the life-time of furnace components is their rate of evaporation. Tungsten is preferable to the other elements in that it is far less volatile than the other elements. The rate of evaporation may be substantially reduced by operation under a pressurised inert atmosphere such as helium or argon. Sample evaporation will be discussed later.

f) Summary

The various physical properties of elements having melting points above 2600K are summarised in Table 2.1. It can be seen that tungsten and graphite are the best candidates for the manufacture of furnace components. Graphite must be ruled out for the present work because of its chemical incompatibility with the oxides under study, but it should be recommended for use with suitable samples. Tungsten's large absorption coefficient is offset by its strength and low volatility which enables the use of thinner cross-sections. Molybdenum has been used satisfactorily up to 2300K. Tantalum may be used for heat-shields and heaters but not for sample containment and mounting because of recrystallisation problems. It is advisable to make use of only one material in the vicinity of the sample in order to minimise the number of spurious peaks.

2.2.2 LIFETIMES OF FURNACE COMPONENTS

An important decision of general policy must be made concerning the permanence of components situated in the hottest region of a furnace. The element and heat-shields must either be made from very thin foil and disposed of after each experimental run or else be made

TABLE 2.1

SUMMARY OF THE PHYSICAL PROPERTIES OF REFRACTORY ELEMENTS

HAVING MELTING POINTS ABOVE 2600K

ELEMENT	MELTING POINT (K)	VAPOUR PRESSURE AT 2000°C (TORR)	TOTAL CROSS-SECTION σ (10^{-28} m^2) FOR ABSORPTION[a]	COHERENT SCATTERING	INCOHERENT SCATTERING
Iridium	2683	2.5×10^{-5}	440.0	14.1	-
Niobium	2743	2.5×10^{-6}	1.2	6.2	0.006
Molybdenum	2890	2×10^{-5}	2.7	6.1	< 0.6
Tantalum	3269	2.2×10^{-8}	21.	6.0	0.02
Osmium	3318	$2. \times 10^{-6}$	15.3	15.0	0.5
Rhenium	3450	2.3×10^{-8}	86.	10.6	-
Tungsten	3680	1.2×10^{-9}	19.2	2.9	1.9
Graphite	3820[b]	2.3×10^{-7} [c]	5.6	< 0.02	0.003

[a] for neutron wavelength $\lambda = 1.8\text{Å}$ [b] sublimation [c] at 2300°C

to last, which is expensive because of the difficulty of machining metals such as tungsten and tantalum. In order to minimise attenuation, it is clear that as little material as possible should be positioned in the neutron beam. On the other hand, if the measurements are to extend over several days or weeks at high temperatures, the element and heat-shields must be of sufficient thickness and strength to withstand evaporation and mechanical stress. Similarly it must be decided how large a temperature gradient can be tolerated, which will influence the number of heat shields required. However the most important factor to be considered is the type of experiment to be performed. For work on powders, the duration of measurements is limited by inherent sintering of the sample, so that little is gained by using long-lasting components. On the contrary, single crystal experiments require much longer measuring times, especially for inelastic work, and therefore thicker, more permanent components should be used. The relative merits of powdered and crystalline samples are discussed further in §2.2.6.

2.2.3 MODE OF HEATING

At low temperatures the heat losses are mainly due to conduction (and convection if the furnace is not evacuated), but above about 2000K radiation is the dominant factor. Since the radiated heat loss varies as T^4, the power input required increases dramatically at higher temperatures. For instance, the radiation losses increase five-fold between 2000K and 3000K. This must be borne in mind when designing a power supply.

There are three modes of heating the sample which should be considered, namely resistive, electron beam and radio-frequency induction heating. Conventional resistive heating requires more power, and hence

more heat-shields, because of the need to heat the element as well as the sample. The electron beam technique could create local heating, and hence temperature gradients, along the sample. Constraints on the size of a neutron scattering furnace and the need for cylindrical symmetry in the sample environment would also make the siting of an electron gun rather difficult. The main concern regarding radio-frequency induction heating is its possible effect on the neutron detector and monitor, especially the latter in view of its proximity to the sample table on most spectrometers. In the design of the Harwell furnace, resistive heating was chosen because objections to the other techniques were considered to be more serious, and also on account of its simplicity.

2.2.4 TEMPERATURE MEASUREMENT

The two kinds of monitors available for high temperatures are thermocouples and pyrometers. The best thermocouples in the temperature range under consideration are tungsten - tungsten/$\sim$25% rhenium which are reliable up to about 2400K. At higher temperatures, gradual changes of composition may occur at the junction, brought about by the diffusion of rhenium atoms. The simplest form of pyrometer is one in which the current through a thin filament is varied until it achieves the same brightness as the light from the sample. It has an accuracy of about $\pm$ 50K, which is inadequate for this work. The second type of pyrometer is a photocell in which an emf is generated as a function of the intensity of radiation emitted by the sample. This design, which was chosen for the Harwell furnace, enables the detection of temperature changes of less than 5^{o}. A third more advanced pyrometer compares the radiated intensity at two wavelengths, giving a temperature reading which is independent of emissivity and window transmission.

Thermocouples are more sensitive than pyrometers at lower temperatures and are less prone to systematic errors, but they do have a limiting maximum operating temperature. On the other hand, the sensitivity of pyrometers improves with increasing temperature and they do not suffer from an upper limit on their operating temperature. However they do require a clear optical path to the sample, and corrections might have to be made for the sample emissivity. Another source of systematic error in the present work is the fact that the reading is taken from the upper surface of the sample container, which may be up to 20mm away from the centre of the crystal for large samples. The magnitude of systematic errors in temperature readings is discussed in §2.3.3, where the performance of the Harwell furnace is described.

2.2.5 TEMPERATURE REGULATION

In order to maintain the sample environment at a constant temperature, a signal must be fed back to the temperature controller to regulate the power input into the furnace. The most obvious parameter to use for regulation is the observed sample temperature. However this is unsatisfactory above 2500K because of the difficulty involved in continuous monitoring of the temperature. Clouding of the pyrometer window due to tungsten evaporation and thermocouple degradation would both cause the power input to increase slowly. A second option is to regulate on the temperature of a cooler part of the furnace, and to monitor the sample temperature intermittently. The control parameter which was chosen for the Harwell furnace is the power input, which should be kept constant. This is achieved using a $(V + I)^2$ mode which accounts for changes in the element's resistance due to evaporation. Since the heat losses are approximately proportional to T^4 at high temperatures,

the effect of power input variations is reduced with increasing temperature. Stability of $\pm 10^{o}$ or better may thus be achieved at all temperatures.

2.2.6 POWDERS OR SINGLE CRYSTALS ?

Whereas phonon dispersion curves can only be investigated using single crystals, diffraction and phonon density of states measurements may be performed on either powdered or single crystal samples. Powder techniques rely on a uniform distribution of crystallite orientations, a condition well-satisfied in practice at normal temperatures. Powder diffraction experiments thus avoid systematic errors such as extinction and multiple reflections. Powder measurements are also much faster because many reflections can be measured simultaneously, since there are always crystallites orientated in a diffracting setting. On the other hand, single crystal reflections must be measured individually since the diffraction condition is only satisfied for one reflection at a time. This advantage of powder diffraction is particularly attractive at very high temperatures because of the limited lifetimes of furnace components. A further merit of the powder technique is its insensitivity to sample movement, whereas shifts of greater than 0.05^{o} cannot be tolerated for single crystal measurements. This is again a particular problem at very high temperatures, since movement can be caused by annealing of the sample mount, as previously noted. Consequently, single crystal samples must be left to anneal for several hours before measurements can commence. One further drawback of crystalline samples is possible disintegration at high temperatures due to internal stresses.

There are however several disadvantages associated with powder diffraction at very high temperatures. Firstly, large samples are

required, which may result in large temperature variations within the sample. This problem may be avoided by using well-designed heat-shields. Another difficulty is that of distinguishing spurious Bragg peaks from furnace materials, which are also of a polycrystalline nature. This is much easier in single crystal work since the Bragg peaks are sharp δ-functions in reciprocal space, as opposed to isotropic shells of scattering for powders. A far more serious objection to powder diffraction at very high temperatures is that caused by sintering of the sample, resulting in preferred orientations. Changes in Bragg intensities of a factor of 2 within one hour at 2300K in polycrystalline La_2O_3 have been reported (Aldebert and Traverse 1981). Similar effects have also been observed in ThO_2 at 2500K (B. T. M. Willis, private communication), which made accurate measurements impossible. Another consequence of limited sample lifetimes, caused by sintering, is the need for a high neutron flux and multidetectors to complete measurements quickly. Temperature dependences are also difficult to explore since a new sample is required for each temperature. Further, the furnace must be heated quickly to prevent excessive sintering before attainment of the required temperature, and the subsequent repeated, rapid thermal cycling may damage furnace components.

In contrast with the above problems, several experiments on single crystals are reported in this work which involved continuous measurements at temperatures above 2000K over extended periods of a fortnight or longer. We therefore conclude that, despite problems such as sample movement and long measuring times, single crystal techniques have greater potential than powder diffraction at very high temperatures. Powder techniques may however be preferable at lower temperatures where sintering is not severe.

2.3 THE HARWELL HIGH TEMPERATURE FURNACE

2.3.1 CONSTRUCTION

The furnace, used for most of the experiments reported here, was designed and built to our specifications by D. Hukin of Crystalox Ltd., Wantage. Its main features are illustrated in Fig. 2.1. The power is taken across two phases of a three-phase supply, and is controlled by a thyristor unit operating in the phase-angle mode. The thyristor output is stepped down to about 10V, 1000A (at $\sim$2900K) in the transformer secondary circuit. The current is carried to the furnace through thick water-cooled copper leads, and then via water-cooled connectors to the heater element. The element consists of two concentric tungsten cylinders, joined at the base by a tungsten annular ring and central disc, such that the current passes down one cylinder and up the other. (Some early elements had tantalum base rings which disintegrated on heating above 2500K, probably as the result of recrystallisation.) This heater design has greater strength than a single slit cylinder, and the outer cylinder also acts as an additional heat-shield. The inner and outer cylinders have diameters of 25mm and 35mm and thicknesses of 0.4mm and 0.25mm respectively. The upper ends of the tungsten element are welded onto thicker tantalum cylindrical electrodes, which are clamped by phosphor bronze collars providing good electrical and thermal contact and accurate alignment.

The heat-shield assembly detaches as one unit and consists of two replaceable inner tungsten shields and three outer molybdenum shields. The innermost and outermost shields are 0.25mm thick and the others 0.12mm thick. A further molybdenum shield is positioned just inside the aluminium water-cooled vacuum chamber. A second heat shield assembly

has been tried, in which zirconium is substituted for molybdenum by virtue of its preferable absorption coefficient. However, it was found that the zirconium becomes embrittled and deformed after several weeks at high temperatures, and it also reacts with the stainless steel top and base plates of the shield assembly.

The sample, sealed in a CVD tungsten tube, is attached to the base of a CVD tungsten sighting tube which provides an unobstructed view of the sample for the Land silicon-sensor infra-red pyrometer. The upper end of the sighting tube is clamped to a cool part of the furnace using grub screws. On heating, the tungsten has been found to fracture at the point of clamping, and therefore a thin molybdenum sleeve is welded around this region, onto which the grub screws can grip. The base of the pyrometer sighting tube approximates well to a black body, so no emissivity correction is required. Clouding of the pyrometer window is prevented by a shutter which is only opened for intermittent temperature readings. Boron nitride spacers are inserted between the inner and outer tantalum heater electrodes and between the inner electrode and the sighting tube, in order to keep them concentric and to reduce heat loss upwards. On operation of the furnace above 2700K, a vigorous reaction has been observed between the boron nitride and the tantalum electrodes. Consequently, the spacers have been shortened or omitted altogether for some experiments. For experiments not exceeding $\sim$2450K, two tungsten/tungsten 26% rhenium thermocouples are used to measure the temperature. The pyrometer and sighting tube are replaced by a thermocouple assembly, for which the sample tube is mounted on a tungsten rod. Details of sample preparation and the welding techniques developed are described in §2.4 and Appendix A.1.

2.3.2 OPERATION

During initial test experiments, the furnace and power leads were cooled using water taken from a reactor secondary cooling circuit. However, it was found that electrolysis resulted from the solutes which the water contained. Consequently, a F & R RCU6 water chiller unit was obtained, having a tank capacity of 350 litres. Demineralised water at $\sim 10^{\circ}C$ is pumped around a closed circuit at a rate of ~ 17 l/min., shared between the power leads and the outer furnace casing. A reactor water supply is used to cool the chiller secondary circuit. Flow trips, which switch off the furnace power when triggered, have been inserted in both branches of the circuit. A temperature trip, set to an upper limit of $35^{\circ}C$, has also been fitted in the return pipe. In addition to these trips, a relay has been fitted which ramps down the furnace power steadily if the chiller refrigerant pressure decreases due to a refrigerant leak, or increases as a result of a failure of the secondary circuit cooling water flow. This avoids thermal shocks to the furnace caused by instantaneous tripping of the power. A third flow trip, installed on the return to the chiller, cuts out the water pump in the event of a water leak, thus preventing flooding of the reactor floor. A schematic diagram of the cooling water circuit and the safety trips is shown in Fig. 2.2.

The furnace may be operated either under dynamic vacuum or under a closed argon atmosphere. The latter procedure was always adopted for these measurements in order to minimise tungsten evaporation. Since it is a closed system, it also avoids any danger of releasing UO_2 dust into the atmosphere. When operation under argon is intended, the furnace must be first baked out by heating to 1500 - 2000K under dynamic vacuum for a few hours, in order to remove any adsorbed gases or solvents. After cooling the furnace, high purity argon is introduced via a BOC rare gas

purifier which removes any traces of oxygen or water vapour. This is extremely important because slight oxidation reduces a heater's lifetime dramatically. Similarly, a very good vacuum ($\sim 10^{-5}$ torr) is required for operation under dynamic vacuum. When heating the furnace, the argon pressure must be released periodically. It is normally operated at a pressure of $\sim$10 p.s.i. above ambient - a safety valve is incorporated which releases at $\sim$15 p.s.i. . The alignment of the pyrometer must be checked regularly during experiments.

2.3.3 PERFORMANCE

Apart from a few teething problems, the furnace's performance has been very satisfactory. It has a maximum temperature of 2930K, operates continuously for over three weeks above 2500K and for over a week at 2800K.

The power input as a function of temperature, for operation under vacuum and under argon, is shown in Fig. 2.3. At lower temperatures, more power is consumed when operating under argon because of the additional convection and conduction losses, whereas at high temperatures the values merge because of the predominance of radiation losses. There is no systematic discrepancy between power values for which the temperature was determined with thermocouples and with the pyrometer, and sample size has little effect. It should be noted that the quoted power values are for the primary circuit and that the low temperature values shown are too large because the thyristor phase-angle output was measured using meters designed for sinusoidal wave-forms. The furnace's absorption is about 35% for a neutron wavelength of 2Å: the contributions from each component are listed in Table 2.2. The temperature variation in the hot zone of the furnace is small - about $\pm$ 5K over 3cm at 1900K.

TABLE 2.2

TRANSMISSION FACTORS OF COMPONENTS OF THE HARWELL HIGH TEMPERATURE FURNACE, MEASURED WITH NEUTRONS OF WAVELENGTH 2.28Å

COMPONENT	TRANSMISSION (%)
Outer Casing	93.3
Outer Mo Shield	97.8
Heat-Shield Assembly (3Mo, 2W)	77.4 †
Heater Element	88.6
Complete Furnace	62.6

† The transmission of the substitute heat-shield assembly (2Zr, 1Mo, 2W) is 86.3%.

The stability of the sample temperature is ± 10K or better at all temperatures, and relative temperatures within the same experimental run also have accuracies of about ± 10K. Comparison of the measured temperature variations of the furnace power input and of the lattice constant of UO_2 (Figs. 2.3 and 4.1) indicates that temperatures measured during different experiments agree to within ± 30K. Systematic effects, such as the transmission of the pyrometer window and the distance between the centre of the sample and the upper end of the sample tube from which the pyrometer reading is taken, make estimation of the absolute temperature value difficult. However, the small temperature gradient in the sample environment and the agreement between pyrometer and thermocouple readings noted above suggest an overall error of ± 50K or less. A better test of the absolute temperature would be given by calibration against the melting point of alumina (T_m = 2324 ± 6K). No errors will be quoted on temperature values throughout this work. The values given above for stability and errors of relative and absolute temperatures should be assumed unless otherwise stated.

It was found that the power input needed to maintain a given temperature was consistently larger than that quoted in test data supplied by Crystallox Ltd. . Consequently, the manufacturer's tests were repeated under identical conditions. All the operating parameters were recorded at 1930K and 2795K, and compared with those quoted by Crystallox Ltd. (Table 2.3). The power input to the transformer primary circuit was found to be 19% higher than the quoted value at 1930K and 64% higher than the quoted value at 2795K. The large discrepancy at 2795K indicates that the radiated heat loss is much larger than during the manufacturer's tests. One possible cause of the additional heat loss at high temperatures is damage to internal shields of the heat-shield

TABLE 2.3

COMPARISON OF FURNACE OPERATING PARAMETERS MEASURED IN JULY 1983 WITH THOSE MEASURED BY CRYSTALLOX LTD. ON MANUFACTURE IN OCTOBER 1981.

	Crystallox Ltd October 1981	Our Data July 1983	Crystallox Ltd October 1981	Our Data July 1983
Temperature (K)	1923	1946	2793	2795
Furnace Atmosphere	Dynamic Vacuum	Dynamic Vacuum	Argon (10 p.s.i.)	Argon (10 p.s.i.)
Primary Circuit Voltage (V)	134	146	264	363
Primary Circuit Current (A)	13.8	15	19.6	23
Primary Circuit Power (kW)	1.84	2.19	5.16	8.5
Secondary Circuit Voltage (total)	3.05	3.3	-	8.7
(heater)	1.87	2.2	-	6.4
(power leads)	1.18	1.1	-	2.3
Secondary Circuit Current (A)	-	520	-	975
Secondary Circuit Power (kW) (dissipated in heater element)	-	1.1	-	6.2

assembly, which cannot be examined easily. Further work is required to establish the origin of this heat loss, and subsequently to increase the furnace's maximum operating temperature.

2.3.4 COMPARISON WITH OTHER FURNACES

Two other high temperature furnaces were used - one at Risø National Laboratory, Denmark and the other at Institut Lave-Langevin (ILL), Grenoble. The Risø furnace is of a similar, but simpler, design to the Harwell furnace. Its heater element consists of a thin tantalum split cylinder of larger resistance, so that water cooling of the power leads is not required. It was designed to operate up to 1900K, but it may be 'pushed' to 2300K by coupling three transformers in parallel. The ILL furnace is based on Aldebert's design (Aldebert and Traverse 1981), and it can attain temperatures of 2500K for a few days. It has a 10mm diameter, thin ($\sim$0.05mm) tungsten heater element with a spiralled tungsten heat-shield around it. The element is 10cm long and is clamped at both ends, which introduces an additional heat loss. Together with the thin heat-shield, this gives rise to a larger temperature gradient along the sample than necessary. Both furnaces are operated under dynamic vacuum.

2.4 SAMPLE PREPARATION

Crystalline boules of UO_2 of varying quality and size, grown from a melt, were obtained from Degussa Ltd. and Nukem Ltd. (W. Germany), Norton Research Corporation (Canada) and T. Griffiths (Leeds University). Similar boules of ThO_2 were also obtained from T. Griffiths and Norton Research Corporation. Smaller, good quality ThO_2 crystals were grown using a flux method by B. Garrard and B. Wanklyn (Clarendon Laboratory). Large Y_2O_3-doped ZrO_2 crystals were supplied by J. Wenckus of Ceres

Corporation. The crystals were aligned using a diffractometer and cut into cylinders of varying dimensions, mostly having a $\langle 1\bar{1}0 \rangle$ axis, by S. Hughes (Harwell). Diffraction samples were of diameter 1.6mm and length ~4mm; those of inelastic measurements had diameters between 7 and 12mm and length ~20mm. After cutting, UO_2 crystals were heated in a hydrogen atmosphere at 1730K for several hours by M. Mignanelli (Harwell) in order to attain stoichiometry. Tests of the oxygen:metal ratio of typical samples gave a value of 2.0001 ± 0.0003 (I. G. Jones, private communication).

Vapour-deposited tungsten sample tubes and end caps of thickness 0.3mm were fabricated by Archer Technicoat Ltd.. Because of the aforementioned reaction between tungsten and UO_2 above 2800K, the sample tubes were electrolytically coated with TaN by P. Coad (Harwell). The crystals were held tightly in place in the sample tubes with compressed tungsten foil and the caps were sealed using electron beam welding by K. Habgood and M. Paul (Harwell). The sealed sample tubes were welded onto machined tungsten collars, which in turn were welded onto a pyrometer sighting tube or onto a tungsten rod for use with thermocouples. Considerable difficulty was experienced in electron beam welding tungsten of 0.3mm thickness, as might be expected. In order to avoid burning a hole through the thin tungsten, the electron beam must be focussed onto the thicker tungsten collar and the molten metal allowed to flow onto the thinner metal of the sample tube. The techniques developed for sealing and mounting the sample tubes are described in Appendix A.1. Details of all UO_2 and ThO_2 samples used in this work are summarised in Table 2.4, together with the labels by which they are referred to in the remainder of the thesis.

TABLE 2.4

DETAILS OF UO_2 AND ThO_2 CRYSTALLINE SAMPLES USED FOR EXPERIMENTS

Sample	Supplier	∅ (mm)	Length (mm)	Mass (g)	Encapsulation Material	Vertical Axis
UO_2						
US1	Degussa A. G.	1.6	3.5	0.07	W (CVD)	$1\bar{1}0$
US2	"	1.6	5.0	0.10	Ta (machined)	$1\bar{1}0$
US3	"	1.6	4.5	0.09	W (CVD)	$1\bar{1}0$
US4	"	1.6	6.0	0.11	W (CVD)	$1\bar{1}0$
US5	"	1.6	7.5	0.15	W (CVD)	110
UL1	"	11.3	30	30.5	Mo (machined)	$1\bar{1}0$
UL2	"	7.6	25	12.3	W (CVD)	$1\bar{1}0$
UL3	Nukem Ltd.	7.6	18	9.0	W (CVD)	001
UL4	Norton Research Corp.	11.4	20	19.0	W (CVD)	$1\bar{1}0$
UL5	Degussa A. G.	10.0	15	13.5	W (CVD)	001
ThO_2						
TS1	Clarendon Lab.	1.6	5	0.08	W (CVD)	110
TL1	T. Griffiths	Irregular		9.0	None	-

Notation U: UO_2 S: Small sample (for diffraction experiments)

T: ThO_2 L: Large sample (for inelastic scattering experiments)

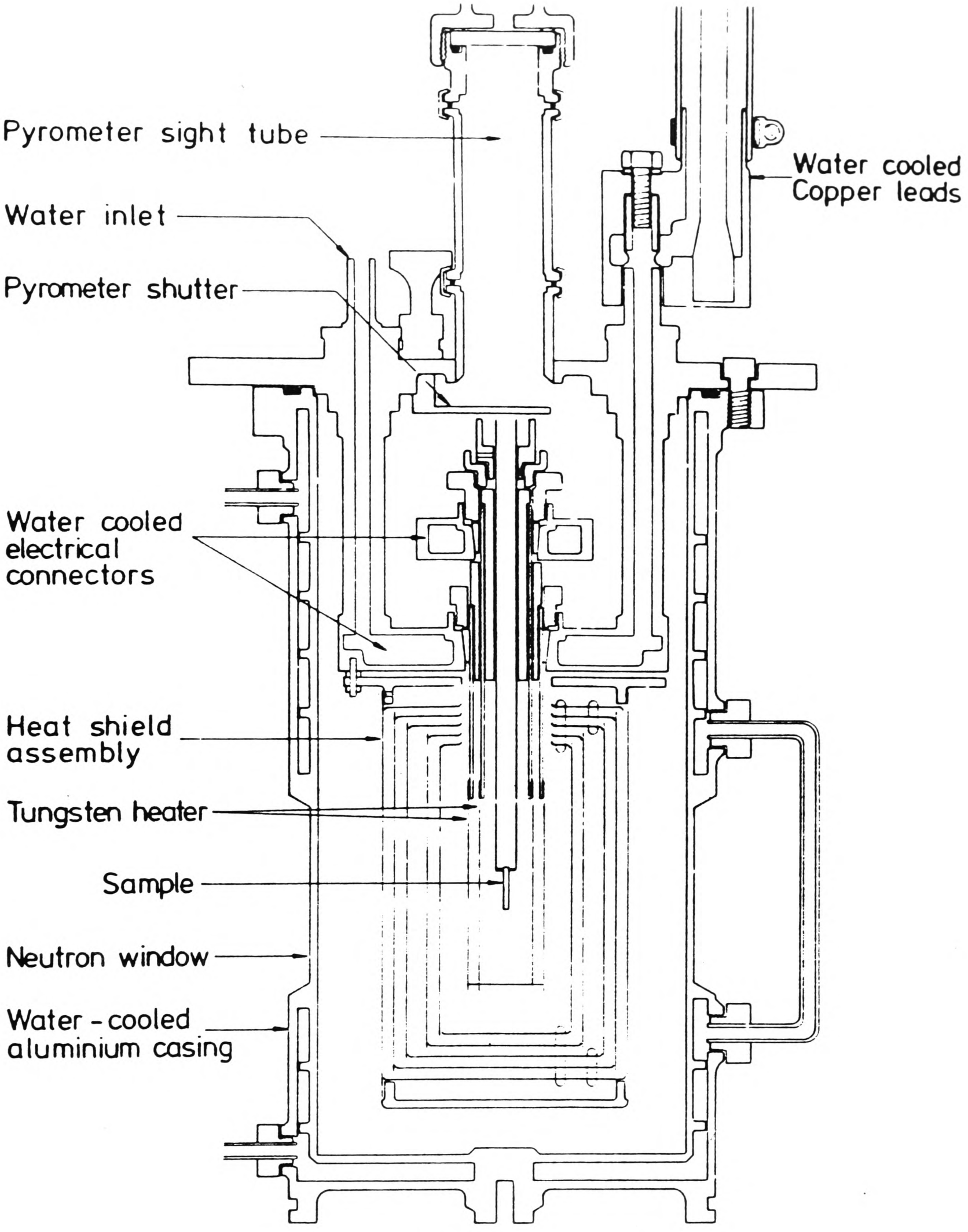

Fig. 2.1 The Harwell high temperature furnace, designed and constructed by D.Hukin, Crystallox Ltd.

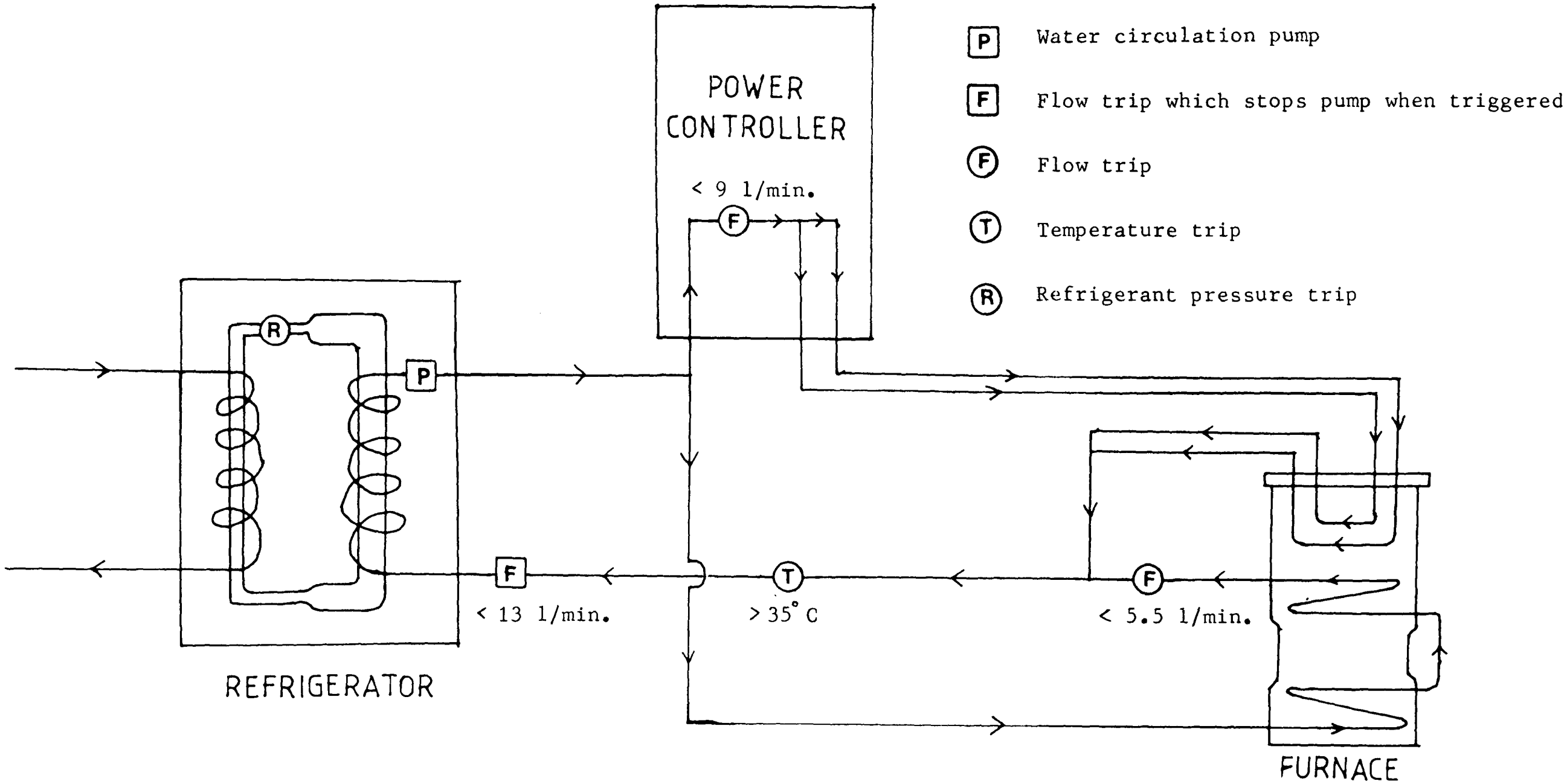

Fig. 2.2 The furnace cooling water circuit. Also shown are the control trips and the values at which they are triggered. The refrigerant pressure trip ramps down the furnace input power when triggered, whereas the other trips denoted by circular symbols cut out the power instantaneously.

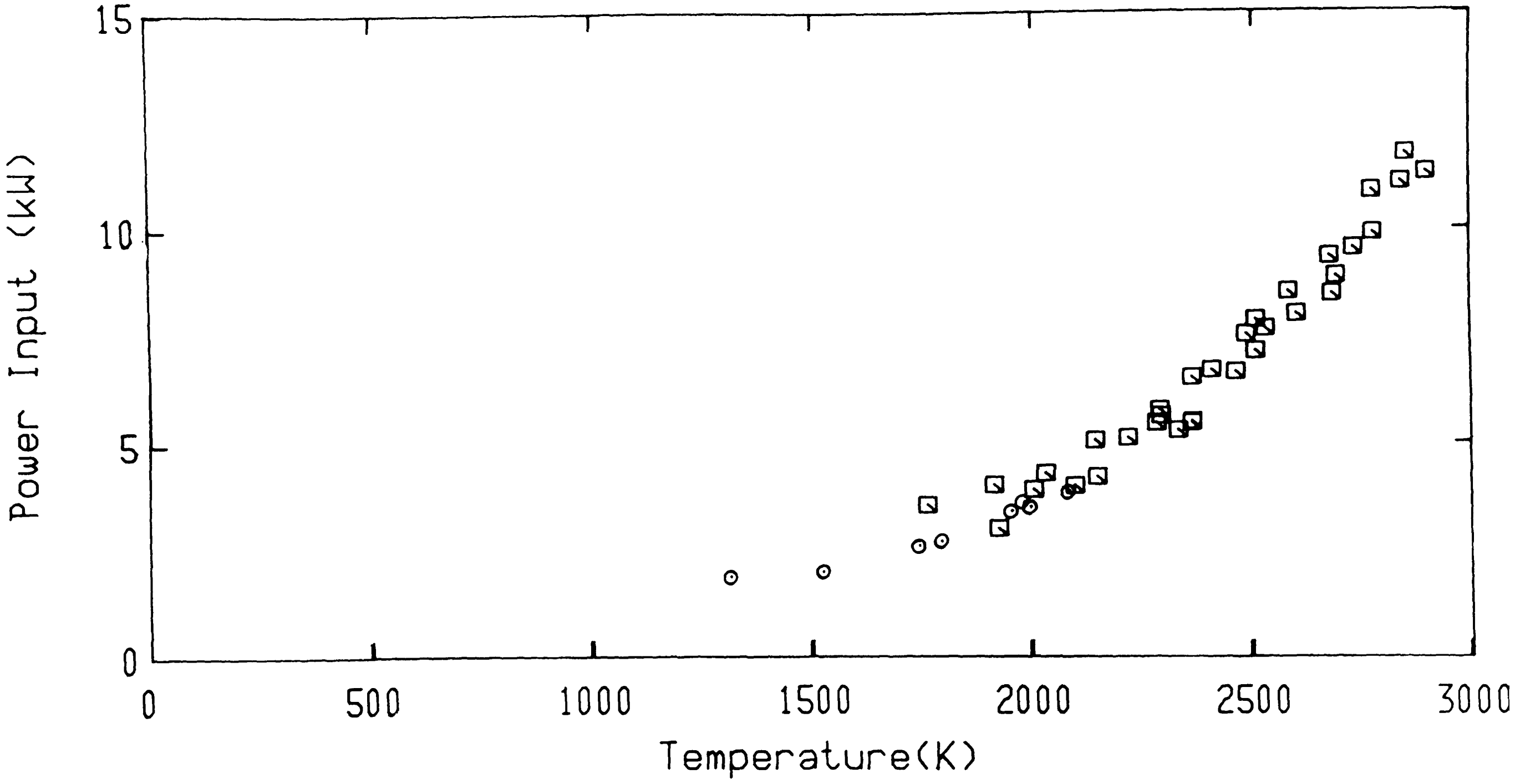

Fig. 2.3 Temperature variation of the power input for the Harwell furnace. Squares denote values for operation under a 10 p.s.i. argon atmosphere and circles denote values for the evacuated furnace. Values at low temperatures are unreliable because of the use of meters designed for sinusoidal waveforms to monitor thyristor-pulsed signals.

CHAPTER 3

NEUTRON SCATTERING TECHNIQUES

3.1 BASIC PROPERTIES OF THE NEUTRON

A propagating neutron can be described as a particle wave for which the relation between its wavelength and velocity is determined by its mass, through the de Broglie relation $\lambda = h/m_n v$. The neutron energy is given by

$$E = \tfrac{1}{2} m_n v^2 = \frac{h^2}{2m_n \lambda^2} \qquad (3.1)$$

where m_n, v and λ are the mass, velocity and wavelength of the neutron respectively, and h is Planck's constant. For neutrons corresponding to a temperature of 293K, $E = k_B T = 25.3$ meV and $\lambda = 1.8\mathring{A}$.

It can be seen from this simple calculation that the wavelength of thermal neutrons is of the same order of magnitude as interatomic distances in solids. Therefore a neutron beam can be used for diffraction studies of crystalline structures in the same way as X-rays are used. Consideration of the calculated neutron energy shows that it also has a value of the same order of magnitude as those of typical lattice vibrations, so that it can be used to investigate phonon frequencies in the same way as Raman scattering or infra-red absorption. The power of neutron scattering as a technique for studying condensed matter lies in its combination of these two properties. The scattering of a neutron in a crystal can be considered as the result of an interaction between the neutron wave and a density wave in the crystal. If the density wave is a plane wave representing the vibration of the lattice, then the exchange of both energy and momentum between the two waves may be observed in the same scattering process. The relation

between these two quantities, namely the dispersion relation, can hence be determined. Although X-rays may be used for diffraction measurements, their energy is far too large to observe phonon excitations. For instance, X-rays of wavelength 1.8Å have an energy of 6.9 keV, which is five orders of magnitude greater than that of thermal neutrons having the same wavelength. Conversely, infra-red radiation may be used for studying excitations, but its wavelength is so long that observation of momentum transfer is almost impossible. This is illustrated in Fig. 3.1.

Whereas X-rays are scattered by the electrons of the atom, neutrons are scattered mainly by the nucleus. Hence the X-ray scattering cross-section is propertional to the atomic number, thus making lighter atoms difficult to detect, whereas there is no such systematic variation in the corresponding cross-section for neutrons. This is an obvious advantage for neutrons is a search for anion disorder in compounds such as UO_2 because of the disparity in atomic numbers. The absorption cross-section is much smaller for neutrons than for X-rays in most materials, thus enabling the use of furnaces containing absorbing metals. The disadvantage of neutrons, when compared with X-rays, is that the scattering cross-section is smaller.

3.2 NEUTRON SCATTERING THEORY

3.2.1 GENERAL EXPRESSIONS

Consider an incident beam of neutrons having a wavevector k_i and energy E_i, scattered with wavevector k_f and energy E_f, where the magnitude of a wavevector k is

$$k = {}^{2\pi}/_{\lambda} \qquad (3.2)$$

The energy transferred to the sample is

$$\hbar\omega = E_i - E_f = \frac{\hbar^2}{2m} (k_i^2 - k_f^2) \qquad (3.3)$$

where $\hbar = h/2\pi$, and ω is a frequency, the significance of which will be seen later. Similarly the scattering vector is

$$\underset{\sim}{Q} = \underset{\sim}{k}_i - \underset{\sim}{k}_f \qquad (3.4)$$

and the quantity $\hbar\underset{\sim}{Q}$ is the momentum transfer, by virtue of de Broglie's relation (Fig. 3.2(a)).

We now define the scattering cross-sections and consider the resulting expressions for the experiments described in this work. The details of the calculations are given by Squires (1978). The partial differential cross-section is defined as

$$\frac{d^2\sigma}{d\Omega dE} = (\text{number of neutrons scattered per second into solid angle } d\Omega \text{ with energies between E and dE}) / \Phi\, d\Omega dE \qquad (3.5)$$

where Φ is the inc dent neutron flux. If this is integrated over scattered neutron energies then the differential cross-section is obtained.

$$\frac{d\sigma}{d\Omega} = (\text{number of neutrons scattered per second into } d\Omega)/\Phi d\Omega \qquad (3.6)$$

The total scattering cross-section is

$$\sigma = (\text{total number of neutrons scattered per second}) / \Phi \qquad (3.7)$$

The general expression for the partial differential cross-section may be derived by applying Fermi's golden rule using a pseudo-potential

consisting of delta functions located at the positions of the nuclei. The resulting equation is

$$\frac{d^2\sigma}{d\Omega dE} = \frac{k_f}{k_i} \frac{1}{2\pi\hbar} \sum_{mm'} b_m b_{m'} \int_{-\infty}^{\infty} \left\langle \exp\left\{-i\underset{\sim}{Q}.\underset{\sim}{R}_{m'}(t=0)\right\} . \exp\left\{i\underset{\sim}{Q}.\underset{\sim}{R}_{m}(t)\right\} \right\rangle \times \exp(-i\omega t)\, dt \qquad (3.8)$$

where $\underset{\sim}{R}_m(t)$ is the time-dependent Heisenberg operator for the position of the m'th nucleus. The scattering length b is related to the total scattering cross-section for a single atom by $\sigma = 4\pi b^2$, and the brackets $\langle\ \rangle$ denote a thermally-averaged expectation value.

3.2.2 COHERENT AND INCOHERENT SCATTERING

For a single element in which the scattering length b varies randomly from one nucleus to the next due to isotopic differences or nuclear spins, equation (3.8) may be expressed as

$$\frac{d^2\sigma}{d\Omega dE} = \frac{k_f}{k_i} \frac{1}{2\pi\hbar} \sum_{mm'} \overline{b_m b_{m'}} \int \langle m', m \rangle \exp(-i\omega t)\, dt \qquad (3.9)$$

where $\langle m', m \rangle = \left\langle \exp\left\{-i\underset{\sim}{Q}.\underset{\sim}{R}_m(0)\right\} \exp\left\{i\underset{\sim}{Q}.\underset{\sim}{R}_m(t)\right\} \right\rangle$

On the basis of the random distribution of the b values,

$$\overline{b_m b_{m'}} = (\bar{b})^2 , \quad m' \neq m$$

$$\overline{b_m b_{m'}} = \overline{b^2} , \quad m' = m \ .$$

So

$$\frac{d^2\sigma}{d\Omega dE} = \frac{k_f}{k_i}\frac{1}{2\pi\hbar}\Big[(\bar{b})^2 \sum_{\substack{m,m' \\ m\neq m'}} \int \langle m',m\rangle \exp(-i\omega t)\,dt + \overline{b^2} \sum_{m} \int \langle m,m\rangle \exp(-i\omega t)\,dt\Big] \quad (3.10)$$

$$= \frac{k_f}{k_i}\frac{1}{2\pi\hbar}\Big[(\bar{b})^2 \sum_{m,m'} \int \langle m',m\rangle \exp(-i\omega t)\,dt + \Big\{\overline{b^2} - (\bar{b})^2\Big\}\sum_{m} \int \langle m,m\rangle \exp(-i\omega t)\,dt\Big] \quad (3.11)$$

In going from (3.10) to (3.11), the self-term in the summation has been added onto the first term and subtracted from the second term. It can be seen that the first term in equation (3.11), which is the coherent scattering cross-section $\left(\frac{d^2\sigma}{d\Omega dE}\right)_{coh}$, stems from the correlations between the positions of the same nucleus at different times and between the positions of different nuclei at different times, thus causing interference effects. The second term in equation (3.11) represents the incoherent scattering, which depends only on the correlation between the positions of the same nucleus at different times. Physically, it arises from the random distribution of deviations of the scattering lengths from their mean value. This randomness produces an incoherent partial cross-section $\left(\frac{d\sigma}{d\Omega}\right)_{inc}$ which has no $\underset{\sim}{Q}$ - variation, except that caused by thermal vibrations.

The coherent and incoherent scattering cross-sections are

$$\sigma_{coh} = 4\pi(\bar{b})^2$$

$$\sigma_{inc} = 4\pi\left[(\overline{b^2}) - (\bar{b})^2\right] . \qquad (3.12)$$

Henceforth all scattering should be assumed to be coherent unless otherwise stated.

3.2.3 VAN HOVE CORRELATION FUNCTIONS

The neutron scattering cross-sections may be related to correlation functions, primarily due to Van Hove (1954), which are determined solely by the properties of the scattering system.

$$\left(\frac{d^2\sigma}{d\Omega dE}\right)_{coh} = \frac{\sigma_{coh}}{4\pi}\,\frac{k_f}{k_i}\,S(\underset{\sim}{Q},\omega) \qquad (3.13)$$

where the Van Hove Scattering Function $S(\underset{\sim}{Q},\omega)$ is the double Fourier transform in space and time of the time-dependent Pair Correlation Function $G(\underset{\sim}{r},t)$. The Intermediate Function $I(\underset{\sim}{Q},t)$, a space-coordinate Fourier transform of $G(\underset{\sim}{r},t)$, may also be defined.

$$S(\underset{\sim}{Q},\omega) = \frac{1}{2\pi\hbar}\iint G(\underset{\sim}{r},t)\,\exp\left\{i(\underset{\sim}{Q}.\underset{\sim}{r} - \omega t)\right\}\,d\underset{\sim}{r}\,dt \qquad (3.14a)$$

$$G(\underset{\sim}{r},t) = \frac{1}{(2\pi)^3}\int I(\underset{\sim}{Q},t)\,\exp\left\{-i\,\underset{\sim}{Q}.\underset{\sim}{r}\right\}\,d\underset{\sim}{Q} \qquad (3.14b)$$

$$I(\underset{\sim}{Q},t) = \frac{1}{N}\sum_{jj'}\left\langle \exp\left[-i\underset{\sim}{Q}.\underset{\sim}{R}j(0)\right] . \exp\left[i\underset{\sim}{Q}.\underset{\sim}{R}j(t)\right]\right\rangle \qquad (3.14c)$$

Analogous self-correlation functions $S_s(\underset{\sim}{Q},\omega)$, $G_s(\underset{\sim}{r},t)$ and $I_s(\underset{\sim}{Q},t)$ may also be defined from the incoherent partial cross-section $\left(\frac{d^2\sigma}{d\Omega dE}\right)_{inc}$.

3.3 SCATTERING CROSS-SECTIONS FOR CRYSTALS

In order to evaluate equation (3.8) for scattering by crystals, $\underset{\sim}{R}_m(t)$ may be replaced by

$$\underset{\sim}{R}_{l\kappa}(t) = \underset{\sim}{r}(l) + \underset{\sim}{r}(\kappa) + \underset{\sim}{u}_{l\kappa}(t) \tag{3.15}$$

where $\underset{\sim}{r}(l)$ is the lattice vector of the l'th unit cell, $\underset{\sim}{r}(\kappa)$ is the equilibrium position of the κ'th atom in the unit cell and $\underset{\sim}{u}_{l\kappa}(t)$ is its instantaneous displacement from its equilibrium position (fig. 3.2(c)). Equation (3.8) then becomes

$$\frac{d^2\sigma}{d\Omega dE} = \frac{k_f}{k_i}\frac{1}{2\pi\hbar}\sum_{l\kappa l'\kappa'} \bar{b}_\kappa \bar{b}_{\kappa'} \Big\langle \exp\left\{ i \underset{\sim}{Q}.(\underset{\sim}{r}(l\kappa) - \underset{\sim}{r}(l'\kappa')) \right. \quad x$$

$$\left. \exp\left\{ - i\underset{\sim}{Q}.\underset{\sim}{u}_{l'\kappa'}(0) \right\} \exp\left\{ i \underset{\sim}{Q}.\underset{\sim}{U}_{l\kappa}(t) \right\} \Big\rangle \exp(-i\omega t)\, dt \tag{3.16}$$

where $\underset{\sim}{r}(l\kappa) = \underset{\sim}{r}(l) + \underset{\sim}{r}(\kappa)$.

Assuming harmonic interatomic forces, the atomic displacements $\underset{\sim}{u}_{l\kappa}$ may be expressed as a sum of displacements due to a set of normal vibration modes. This enables the expansion of the thermal averaged term in equation (3.16) as a series, of which the first two terms correspond to the elastic scattering (diffraction) and one-phonon scattering respectively.

3.3.1 DIFFRACTION

The resulting cross-section for Bragg diffraction is

$$\frac{d\sigma}{d\Omega} = N\frac{(2\pi)^3}{v_o}\sum_{\underset{\sim}{\tau}} |F(Q)|^2 \, \delta(\underset{\sim}{Q} - \underset{\sim}{\tau}) \tag{3.17}$$

where the elastic structure factor

$$F(\underset{\sim}{Q}) = \sum_{\kappa} \bar{b}_{\kappa} \exp\,(i\underset{\sim}{Q}.\underset{\sim}{r}(\kappa)) \exp\,(-W_{\kappa}), \tag{3.18}$$

$$W_{\kappa} = \frac{1}{(4\pi)2} \cdot B_{\kappa} Q^2 = B_{\kappa}\left(\frac{\sin\theta}{\lambda}\right)^2 \tag{3.19}$$

and N : number of atoms in the crystal

V_o: unit cell volume

$\exp\,(-W_{\kappa})$: Debye-Waller factor

B_{κ}: isotropic thermal vibration parameter

$\underset{\sim}{\tau} = h\underset{\sim}{a}^* + k\underset{\sim}{b}^* + l\underset{\sim}{c}^*$: reciprocal lattice vector.

For cubic crystals, the mean square atomic displacement $\langle U_{\kappa}^2 \rangle$ may be extracted from the Debye-Waller factor since

$$B_{\kappa} = \frac{8\pi^2}{3} \langle U_{\kappa}^2 \rangle \quad . \tag{3.20}$$

The delta function in equation (3.17) gives rise immediately to the familiar Bragg's law (Fig. 3.2 (b)),

$$\tau = 2k \sin\theta \tag{3.21}$$

where 2θ is the angle between $\underset{\sim}{k}_i$ and $\underset{\sim}{k}_f$. The measured intensity $\mathcal{I}$, obtained by integrating (3.17) over the scan, is

$$\mathcal{I} = S \frac{F(\tau)^2}{\sin 2\theta} \tag{3.22}$$

where $S = \frac{N}{V_o} \Phi \lambda^3$.

3.3.2 ONE-PHONON SCATTERING

The scattering cross-section for one-phonon creation is

$$\frac{d^2\sigma}{d\Omega dE} = \frac{k_f}{k_i} \frac{(2\pi)^3}{V_o} \sum_{j,q,\tau} \frac{1}{\omega_j(\underset{\sim}{q})} |G(\underset{\sim}{Q})|^2 \langle n_j(\underset{\sim}{q}) + 1 \rangle$$

$$\times \quad \delta(\omega - \omega_j(q)) . \delta(\underset{\sim}{Q} - \underset{\sim}{q} - \underset{\sim}{\tau}) \tag{3.23}$$

where $G(\underset{\sim}{Q}) = \sum_{\kappa} \frac{b_\kappa}{\sqrt{M_\kappa}} \exp(-W_\kappa) \exp(i \underset{\sim}{Q}.\underset{\sim}{r}(\kappa)) \underset{\sim}{Q}.\underset{\sim}{\xi}_{\kappa j}(\underset{\sim}{q})$ (3.24)

and $\langle n_j(q) + 1 \rangle = \frac{\exp(\hbar\omega/k_B T)}{\exp(\hbar\omega/k_B T) - 1}$ (3.25)

$G(\underset{\sim}{Q})$ is the inelastic structure factor, which is analogous to $F(\underset{\sim}{Q})$ in (3.18), and M_κ is the mass of the κ'th atom. A phonon of wave-vector $\underset{\sim}{q}$ and polarisation index $j(= 1, 2, 3)$ has frequency $\omega_j(\underset{\sim}{q})$, population $n_j(\underset{\sim}{q})$ and a polarisation vector for atom κ of $\underset{\sim}{\xi}_{\kappa j}(\underset{\sim}{q})$. The corresponding cross-section for one-phonon annihilation is

$$\frac{d^2\sigma}{d\Omega dE} = \frac{k_f}{k_i} \frac{(2\pi)^3}{v_o} \sum_{j\underset{\sim}{q}\underset{\sim}{\tau}} \frac{1}{\omega_j(\underset{\sim}{q})} |G(\underset{\sim}{Q})|^2 \langle n_j(\underset{\sim}{q}) \rangle \times \delta(\omega + \omega_j(q)) \quad (\underset{\sim}{Q} + \underset{\sim}{q} - \underset{\sim}{\tau}) \qquad (3.26)$$

where $\langle n_j(q) \rangle = [\exp(\hbar\omega/k_B T) - 1]^{-1}$ (3.27)

The two delta functions give the following conditions for phonon scattering

$$\omega = \pm \omega_j(q)$$
$$\underset{\sim}{Q} = \underset{\sim}{\tau} \pm \underset{\sim}{q} \qquad (3.28)$$

which define the energy and momentum transfers. The positive sign refers to phonon creation (neutron energy loss) and the negative sign to phonon annihilation (neutron energy gain). Multi-phonon processes do not give discrete peaks, but result in a continuous spectrum which, in practice, may be included in the background scattering.

3.3.3. COHERENT DIFFUSE QUASIELASTIC SCATTERING

Coherent diffuse scattering is the scattering observed away from reciprocal lattice points for disordered systems. Static disorder gives

rise to purely elastic diffuse scattering. However if the disorder is of a dynamic nature, having a finite life-time τ , then the diffuse scattering acquires an energy width $\Delta\omega \sim \hbar/\pi\tau$ and is called Quasielastic Scattering (QES). In the quasistatic approximation, $\Delta\omega << \omega$ (Squires 1978, p. 78), the cross-section is

$$\left(\frac{d\sigma}{d\Omega}\right)^{qs}_{coh} = \frac{\sigma_{coh}}{4\pi} N\hbar \int_{-\infty}^{\infty} S(\underset{\sim}{Q},\omega)\, d\omega = \frac{\sigma_{coh}}{4\pi} N\, S(\underset{\sim}{Q}) \qquad (3.29)$$

where the structure factor

$$S(\underset{\sim}{Q}) = \hbar \int S(\underset{\sim}{Q},\omega)\, d\omega = \iint I(\underset{\sim}{Q},t)\, \exp(-i\omega t)\, d\omega\, dt$$

$$= \int I(\underset{\sim}{Q},t)\ \delta(t)\, dt = I(\underset{\sim}{Q},o) \qquad (3.30)$$

From (3.14c) it can be seen that $I(\underset{\sim}{Q},o)$ describes the instantaneous correlations between the nuclei, and hence $S(Q)$ gives a 'snapshot' picture of their arrangement. In contrast, the purely elastic coherent cross-section, giving the scattering at $\omega = o$, is related to $I(\underset{\sim}{Q},\infty)$ which gives a time-averaged picture of the nuclear distribution.

$$\left(\frac{d\sigma}{d\Omega}\right)^{el}_{coh} = \frac{\sigma_{coh}}{4\pi} N\ I(\underset{\sim}{Q},\infty) \qquad (3.31)$$

We now define a quantity $S^D(\underset{\sim}{Q})$ which is related to an integral over only the quasielastic part of $S(\underset{\sim}{Q},\omega)$, thus omitting the contribution from phonon scattering. Furthermore, we shall consider only the diffuse contribution, that is excluding the Bragg peak contribution $I^B(\underset{\sim}{Q},\infty)$. Thus

$$S^D(\underset{\sim}{Q}) = \hbar \int_{QES} S(\underset{\sim}{Q},\omega)d\omega - I^B(\underset{\sim}{Q},\infty)\ . \qquad (3.32)$$

Detailed expressions for $S^D(\underset{\sim}{Q})$ will be considered in chapter 7.

3.3.4 INCOHERENT DIFFUSE QUASIELASTIC SCATTERING

As was seen in equation (3.11) and the subsequent discussion, incoherent scattering gives information on the behaviour of individual atoms. The incoherent scattering function $S_s(\underset{\sim}{Q},\omega)$ for random instantaneous hopping of ions between Bravais lattice sites has a Lorentzian line-shape.

$$S_s(\underset{\sim}{Q},\omega) = \frac{1}{\pi\hbar} \frac{\Gamma(\underset{\sim}{Q})}{\Gamma(\underset{\sim}{Q})^2 + \omega^2} \tag{3.33}$$

where $\Gamma(Q)$ is the half-width-at-half-maximum (HWHM), given by

$$\Gamma(\underset{\sim}{Q}) = \frac{1}{n\tau} \sum_{\underset{\sim}{l}} [1 - e^{-i\underset{\sim}{Q}\cdot\underset{\sim}{l}}] \tag{3.34}$$

where τ is the residence time, n is the number of possible jump sites and $\underset{\sim}{l}$ is the jump vector (Chudley and Elliott 1961).

This model gives a good account of data on $SrCl_2$ at high temperature (Schnabel 1983). The incoherent scattering originates from the differing scattering lengths of ^{35}Cl and ^{37}Cl isotopes. Such measurements are impractical on the oxides because of the lack of available isotopes having a scattering length which differs appreciably from that of ^{16}O.

3.4 NEUTRON SCATTERING INSTRUMENTATION

3.4.1 SINGLE CRYSTAL DIFFRACTOMETER

The geometry of neutron diffractometers is very similar to that of standard X-ray instruments, the main difference being their larger size. A single wavelength is selected from the reactor spectrum by Bragg reflection from a monochromator crystal. A wavelength of about 1Å is normally chosen so that a reasonable number of Bragg peaks may be measured

without losing neutron flux in the tail of the spectrum. Although the higher order wavelengths $\lambda/2$, $\lambda/3$, ... are also diffracted by the monochromator, their contribution to the main beam is usually less than 1% because they originate from the high-energy tail of the Maxwellian neutron distribution.

The sample is mounted on goniometer arcs, so that the crystal may be aligned accurately in the diffractometer plane, and can be rotated through an angle $\omega = \pm 180^{\circ}$. On a 4 - circle diffractometer the goniometer is then mounted on a cradle which enables any crystal orientation to be chosen. This is ruled out for work involving a furnace, therefore a two-circle instrument must be used, which restricts the number of reflections which can be measured.

For most two-circle diffractometers, the detector may be rotated to an angle γ in the base plane and raised through an angle ν, the resulting Bragg angle θ being given by

$$\cos 2\theta = \cos\gamma \cos\nu \,, \tag{3.35}$$

as shown in Fig. 3.3. This enables the measurement of reflections in the first layer as well as in the base plane. For operation out of the plane, equation (3.22) must be changed to

$$\int = S \frac{|F(\tau)|^2}{\sin\gamma \cos\nu} \,. \tag{3.36}$$

Counting times are controlled by a neutron monitor installed in the monochromatised incident beam in order to overcome fluctuations in the reactor flux.

3.4.2 TRIPLE-AXIS SPECTROMETER

Diffractometers are used to measure the differential cross-section

$d\sigma/d\Omega$, where neutrons of all energies scattered into a solid angle $d\Omega$ are counted. In order to perform inelastic measurements, where the partial differential cross-section $d^2\sigma/d\Omega dE$ is required, the scattered neutron energy must be analysed. A time of flight spectrometer is often used, in which the scattered beam is chopped and its velocity distribution determined by measuring the time of flight over a known path length. The main alternative is the triple-axis spectrometer (TAS), in which the scattered beam impinges on an analyser crystal set to diffract a particular wavelength. The TAS is less efficient in its use of neutrons, but it has better $\underset{\sim}{Q}$ - resolution and is more versatile in the types of scans available. The PLUTO TAS at Harwell, on which most of these measurements were performed, is illustrated in Fig. 3.4.

Because of the need for energy resolution, the angular divergence of the neutrons in each arm of the spectrometer is limited by collimators, which consist of evenly spaced slats of an absorbing material such as cadmium. The monochromator crystal must be chosen in view of the requirements of intensity and resolution. The energy spread of the neutron beam is approximately given by

$$\Delta E_i = 2 E_i \alpha \cot\theta \qquad (3.37)$$

where α is the angular divergence of the collimators, so that, by Bragg's law, monochromator crystals having small inter-atomic spacings should be chosen to attain short wavelength neutrons. Filters, such as pyrolytic graphite or cooled beryllium powder, may be used to suppress troublesome higher order wavelengths. Any value of $\underset{\sim}{Q}$ may be chosen by varying the angles ϕ and ψ , which are the angles of the sample - analyser arm and sample rotation respectively. The values of E_i and E_f, and hence the energy transfer, are determined by the monochromator and analyser settings.

Thus any type of scan in reciprocal space may be performed, the most common being constant - $\underset{\sim}{Q}$ and constant - energy scans. Energy transfer may be varied by changing either the incident or scattered energy. The former has the advantage that the analyser-detector efficiencies are kept constant, while variations of the incoming flux are recorded by the neutron monitor, whose efficiency may be assumed to have a linear wavelength dependence. The latter method suffers from the possibility of an irregular energy-dependence of the analyser reflectivity. On some spectrometers the monochromator-sample angle, $2\theta_M$, is fixed thus necessitating the scanning of the scattered energy.

3.4.3 RESOLUTION FUNCTION OF A TRIPLE AXIS SPECTROMETER

Although the cross-sections defined in § 3.3 contain delta functions of $\underset{\sim}{Q}$ and ω, the observed peaks are broadened by resolution effects. These are due to the finite values of collimations and mosaic spreads of the crystals.

The observed intensity at a nominal point $(\underset{\sim}{Q}_o, \omega_o)$, determined by the spectrometer setting, is given by

$$\mathcal{J}(\underset{\sim}{Q}_o, \omega_o) = \frac{\sigma_{coh}}{4\pi} NA \iint S(\underset{\sim}{Q}, \omega) \; R(\underset{\sim}{Q} - \underset{\sim}{Q}_o, \omega - \omega_o; \underset{\sim}{Q}_o, \omega_o) \; d\underset{\sim}{Q} \; d\omega \qquad (3.38)$$

(Dorner 1972). $S(Q,\omega)$ is the scattering function , A is a constant incorporating the incident neutron flux and R is the spectrometer resolution function which may be represented as a four-dimensional ellipsoid in reciprocal space.

$$R(\underset{\sim}{Q} - \underset{\sim}{Q}_o, \omega - \omega_o; \underset{\sim}{Q}_o, \omega_o) = R_o(\underset{\sim}{Q}_o, \omega_o) \times \exp\left\{ - \tfrac{1}{2} \sum_{k=1}^{4} \sum_{l=1}^{4} M_{kl}(\underset{\sim}{Q}_o, \omega_o) X_k X_l \right\} \qquad (3.39)$$

where M_{kl} is a matrix describing the ellipsoid and the four coordinates X_k represent the three Cartesian components of $\underset{\sim}{Q} - \underset{\sim}{Q}_o$ and $\omega - \omega_o$. The efficiency factor is

$$R_o\ (\underset{\sim}{Q}_o, \omega_o) = \frac{V_I\ V_F}{\pi^2 \prod_{k=1}^{4} W_k\ (Q_o, \omega_o)} \qquad (3.40)$$

where W_k are the ellipsoid widths along its four principal axes. $V_I \propto k_i^3 \cot \theta_M$ and $V_F \propto k_f 3 \cot \theta_A$ are the resolution volumes of the monochromator and analyser components respectively, and θ_M and θ_A are the respective Bragg angles.

If $S(\underset{\sim}{Q},\omega)$ varies slowly with $\underset{\sim}{Q}$ over the resolution volume, then equations (3.38) and (3.39) may be simplified to

$$J\ (Q_o, \omega_o) = \frac{\sigma_{sh} N A}{4\pi} \int S(\underset{\sim}{Q},\omega)\ R'(\omega - \omega_o ; \underset{\sim}{Q}_o, \omega_o)\, d\omega \qquad (3.41)$$

$$\text{where } R'(\omega-\omega_o;\ Q_o,\omega_o) = R'_o\ \exp\left\{ - a^2 (\omega-\omega_o)^2 \right\}$$

$$\text{and} \quad a = \frac{2\sqrt{\ln 2}}{W} \qquad (3.42)$$

Here W is the full-width at half-maximum (FWHM) of the overall energy resolution as determined by an energy scan at constant $\underset{\sim}{Q}$ of an incoherent elastic scatterer such as vanadium. The modified efficiency factor is

$$R'_o = \frac{V_I\ V_F}{\exp\left\{ - a^2 (\omega-\omega_o)^2 \right\} d\omega} \qquad (3.43)$$

There are two important consequences of the finite non-spherical volume of the resolution ellipsoid. Firstly, peak distortion may be observed, expecially for rapidly varying scattering functions. Significant shifts of the peak position often occur during measurement

of low $\underset{\sim}{q}$ acoustic phonons, as a result of the tight curvature of the scattering surface and of the ω^{-1} dependence of the scattering cross-section (equation (3.23)). Secondly, the peak line-shape depends on the relative orientation of the resolution ellipse with respect to the scattering surface. If the major axis of the ellipse is parallel to the scattering surface then contributions to the intensity occur over a small range of ω values and a sharp, focussed, well-defined peak results. However if the resolution ellipse is badly aligned with respect to the scattering surface then contributions to the peak intensity will occur over a large range of ω values, giving a broad de-focussed peak. Pronounced focussing effects are usually observed when measuring transverse phonons, whereas such effects are less marked for longitudinal phonons since the major axis of the ellipse is roughly parallel to the

axis in the $\omega - Q_{//}$ plane.

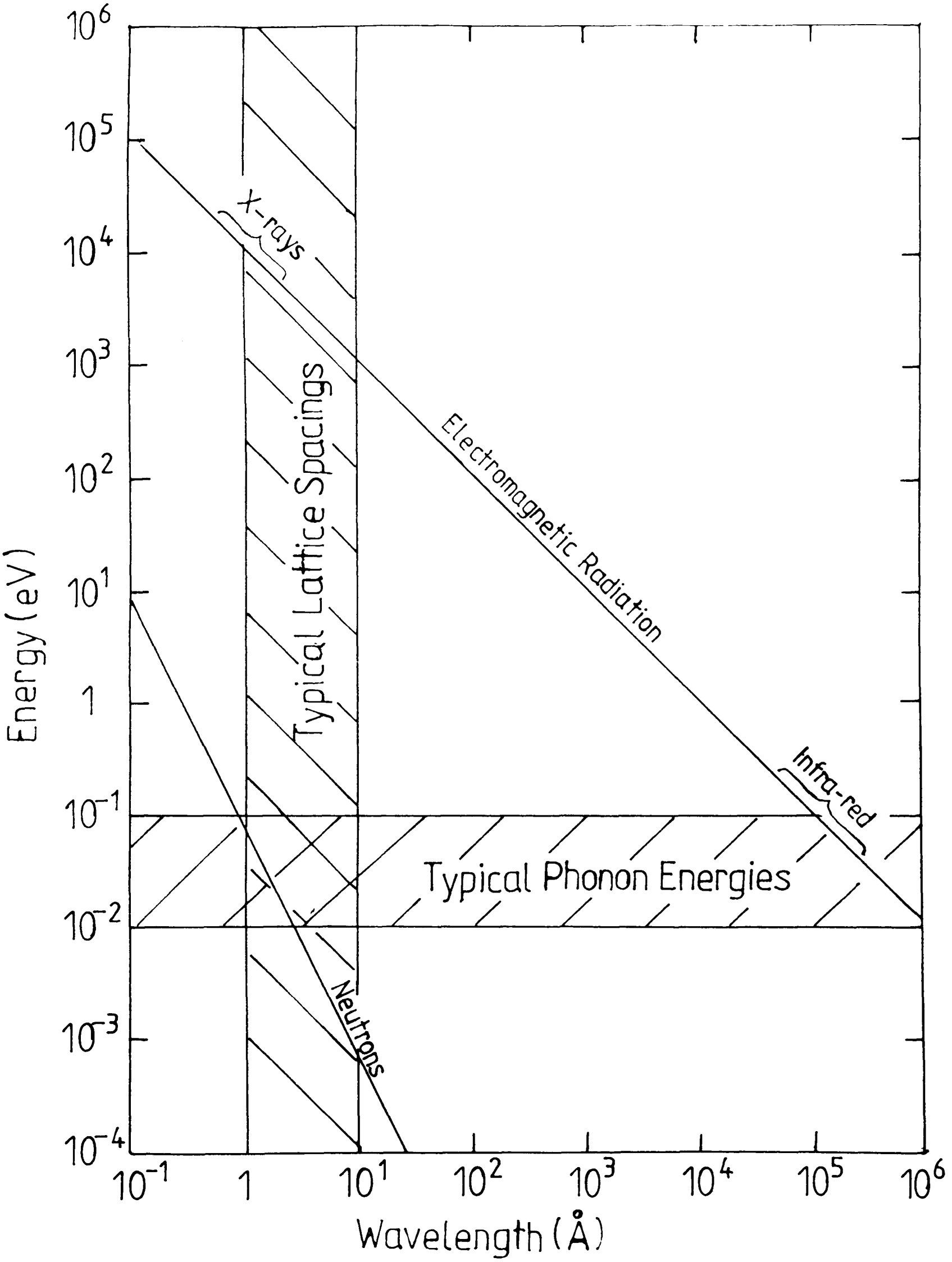

Fig. 3.1 The energy-wavelength relation for neutrons and photons.

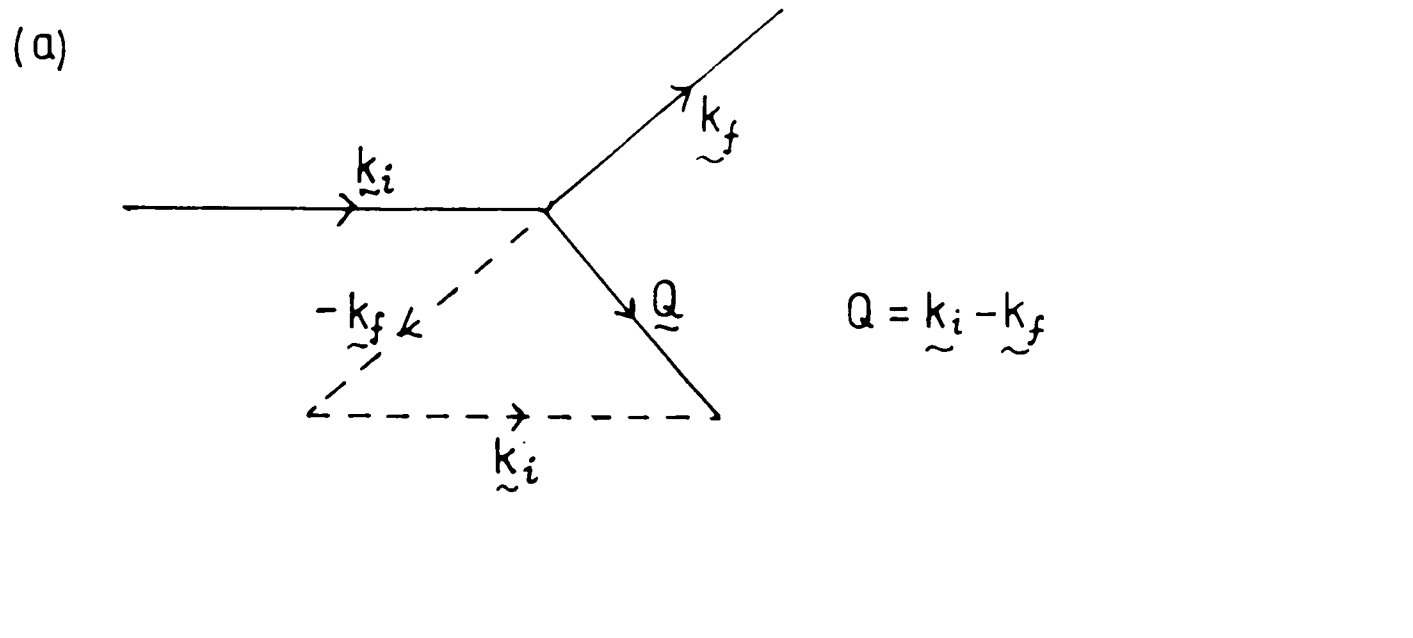

Fig. 3.2 Diagrams illustrating some basic relations of neutron scattering

(a) Scattering vector $\underset{\sim}{Q} = \underset{\sim}{k}_i - \underset{\sim}{k}_f$

(b) Bragg's law

(c) Coordinate system for describing the displacement u_{lK} of ion K in unit cell l.

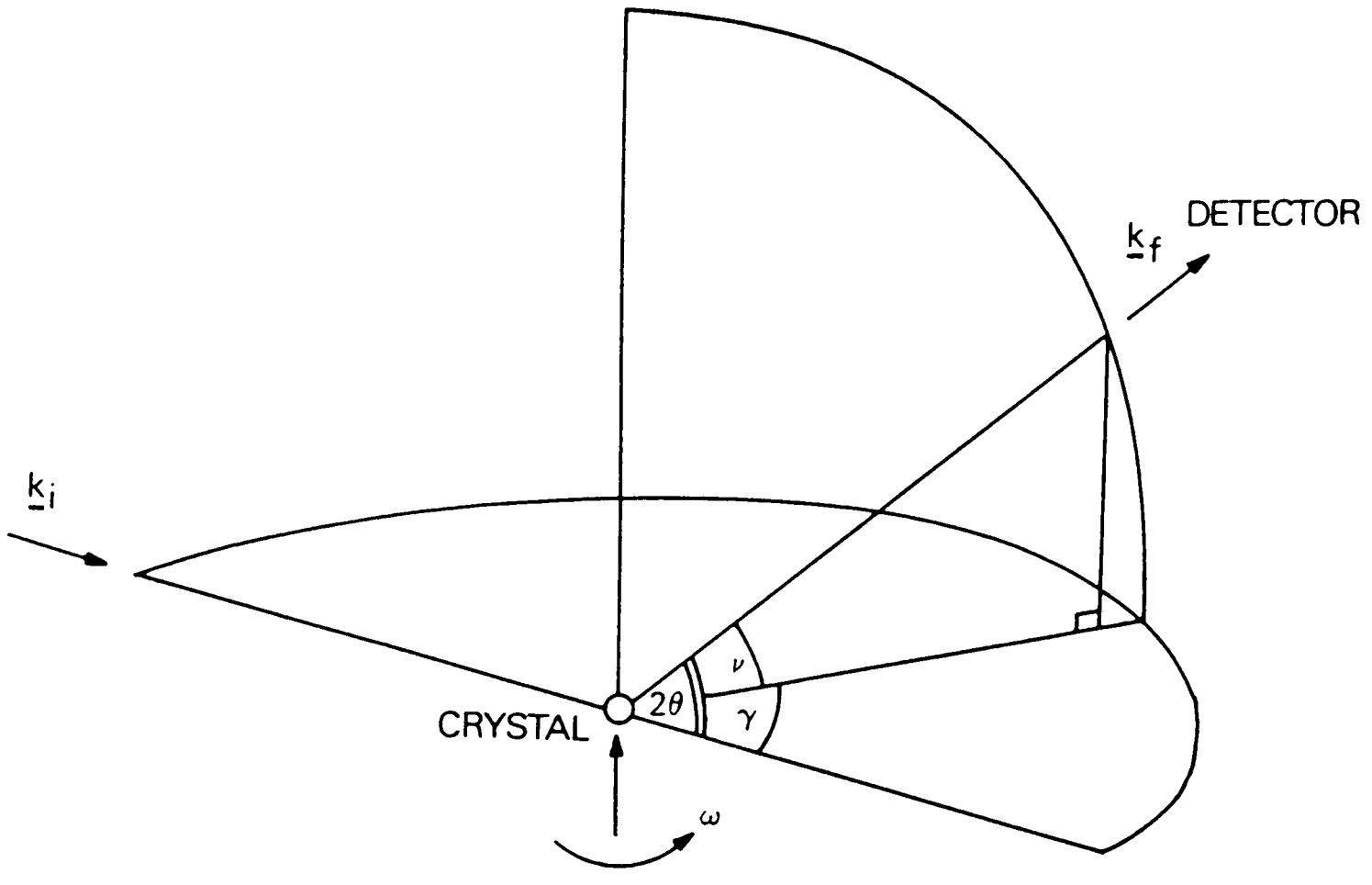

$$\text{Cos } 2\theta = \text{Cos } \gamma \text{ Cos } \nu$$

Fig. 3.3 Scattering geometry of a 2-circle diffractometer.

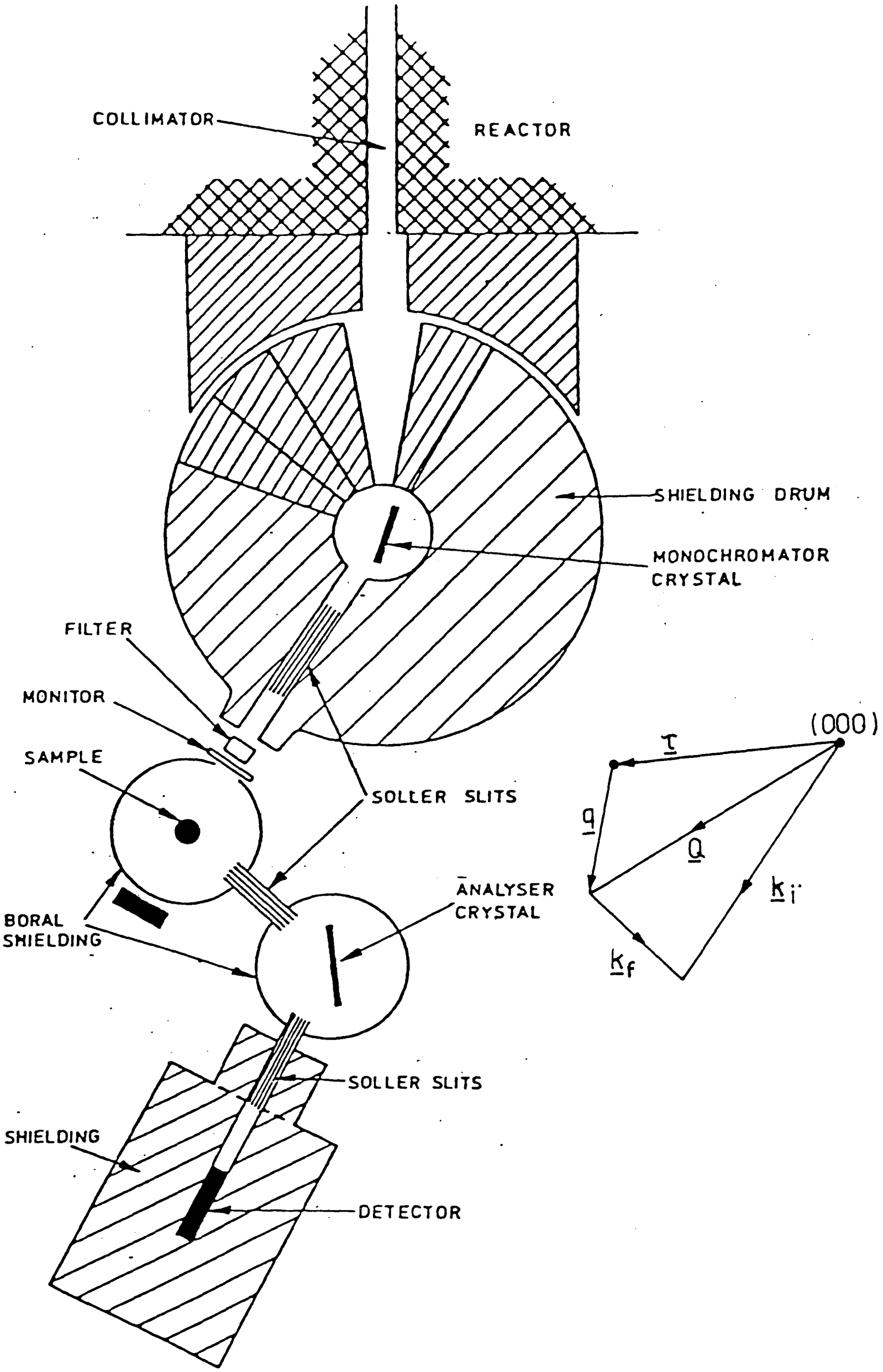

Fig. 3.4 Schematic diagram of the PLUTO Triple Axis Spectrometer.

CHAPTER 4

DIFFRACTION STUDIES OF UO_2 AND ThO_2

4.1 INTRODUCTION

The first step in the investigation of the high temperature regime of UO_2 and ThO_2 is the determination of their structural properties. Diffraction measurements give information concerning the time-averaged distribution of ions within the unit cell, and hence afford a sensitive probe of lattice disorder. In this chapter we describe such measurements on UO_2 and ThO_2, and compare the results obtained for both materials.

4.2 EXPERIMENTAL PROCEDURE

Four experiments on UO_2 and two experiments on ThO_2 were performed mainly using the Mk6 2-circle diffractometer at Harwell, the sample being heated by the Harwell High Temperature Furnace. One set of data on UO_2 was taken with the D15 diffractometer (in 2-circle mode) at ILL Grenoble, using the ILL High Temperature Furnace. The D15 diffractometer is preferable for high temperature experiments because of its high incident neutron flux, enabling the use of shorter counting times, and its good resolution at large scattering angles, which is important in view of the large Debye-Waller factors and thermal diffuse scattering contributions experienced at large values of 2θ. However, the difficulties involved in transporting the Harwell furnace and its associated equipment constrained us to perform the experiments at Harwell. The single crystal samples, cut in cylinders of diameter $\sim$1.6mm and length $\sim$4mm with a $\langle 1\bar{1}0 \rangle$ axis, were sealed in vapour-deposited tungsten tubes as described in chapter 2. Data were taken at a series of increasing temperatures, with room temperature runs performed at the beginning and end of each experiment when possible.

These served to fix the values of scale factors and to check the quality of the crystals after cooling from high temperatures. A summary of experimental details is given in Table 4.1.

The following procedure was performed at each temperature. Having allowed the temperature to stabilise for several hours, the sample was carefully centred on the rotation axis of the sample table. This was done by iteratively moving the furnace on orthogonal slides until equal scattering angles were obtained for Friedel pairs of low angle reflections, such as (111), $(\bar{1}\bar{1}\bar{1})$ and $(11\bar{3})$, $(\bar{1}\bar{1}3)$reflections. The detector tilt zero angle ν_o was also determined at each temperature from the optimised ν angles of Friedel pairs. This was done in order to account for vertical sample movements caused by expansion of the pyrometer sighting tube, on which the sample was mounted. The detector angle γ, tilt angle ν and sample rotation angle ω (Fig. 3.3) were optimised iteratively, using suitable cadmium slits over the detector aperture, for four or more reflections. The optimised angles were input into the RAFIN routine (Written by M. Lehmann and adapted for use on the Harwell diffractometers), which refines the lattice constant and the UB matrix, a matrix which defines the crystal orientation with respect to the diffractometer axes.

The integrated intensities of about 25 independent reflections, each the average intensity of between two and four equivalent reflections, were determined at each temperature. The intensity of each reflection was obtained by integrating over $\theta/2\theta$ scans, in which the detector and sample rotations are in the ratio 2:1, corresponding to a radial scan along $\underset{\sim}{Q}$ in reciprocal space. The background contribution was determined by repeating the scan with the ω shaft offset by 4^{o}. This has the advantage that Bragg scattering from polycrystalline furnace components

TABLE 4.1

SUMMARY OF EXPERIMENTAL DETAILS FOR DIFFRACTION STUDIES OF UO_2 AND ThO_2

	DATE	DIFFRACTOMETER	WAVELENGTH (Å)	SAMPLE	TEMPERATURES (K)	FURNACE DETAILS
UO_2						
1	October 1981	D15, ILL (2-circle mode)	1.175	US1	293	No furnace. Crystal in tungsten tube.
				US2	293 1873	ILL High Temperature Furnace. Crystal sealed in machined tantalum tube. Temperature monitored by W/5% Re - W/25% Re thermocouples.
2	March 1982	Harwell Mk6, 2-circle	1.0928	US3	293 2098 2403	Harwell High Temperature Furnace. Crystal sealed in CVD tungsten tube. Temperature monitored by W-W/26% Re thermocouples.
3	October 1982	Harwell Mk6, 2-circle	1.0928	US4	2218 2690 2778 2905 293	Harwell High Temperature Furnace. Crystal sealed in CVD Tungsten tube. Temperature monitored by infra-red pyrometer.
4	November 1982	Harwell Mk6, 2-circle	1.0924	US5	293 2527 2843 293	
ThO_2						
5	December 1982	Harwell Mk6, 2-circle	1.0924	TS1	293 2803	Harwell High Temperature furnace. Crystal sealed in CVD tungsten tube. Temperature monitored by infra-red pyrometer.
6	June 1983	Harwell Mk6, 2-circle	1.0924	TS1	293 2291 2555 2738 2903 293	

should contribute equally to the peak and background scans, thus minimising its effect on the resulting intensities. Each set of scans, of reflections in the $(1\bar{1}0)$ base plane and the first layer in reciprocal space, took about 48 hours to complete.

One standard reflection was scanned repeatedly after every 10 or 15 reflections in order to check the sample condition and alignment. A strong reflection, occuring at a large 2θ angle, such as (440) or (444), was chosen for the standard reflection in order to avoid changing extinction levels caused by sample annealing. No change in the standard reflection intensity with time was observed in ThO_2 at any temperature, nor in UO_2 up to 2600K. However, a steady decrease in the intensity of the standard reflection, and of equivalent reflections measured at different times, was observed in UO_2 at 2690K and 2778K. Consequently, the integrated intensities at these temperatures were corrected using the smoothed time-variation of the standard reflection, after which no systematic variations could be detected. Above 2800K, significant reductions (~20%) in the standard reflection intensity were observed after attaining a given temperature, but the intensity reached a stable value after several hours. In practice, the sample was left to stabilise overnight before commencing sample alignment and data collection. The most probable explanation for this behaviour is evaporation of the UO_2 crystal, the equilibration resulting from attainment of the saturation vapour pressure of UO_2 inside the sample tube.

The intensities of the strong, low-angle reflections, such as (220) and (111), showed a further steady decrease with time at temperatures above 2500K in UO_2 and above 2800K in ThO_2, whereas the high angle reflections showed no such variation. This may be explained by increasing

extinction levels due to annealing of the sample, since the extinction correction does have such a strong angular dependence (equation 4.6). Consequently, equivalent reflections were measured at equal times before and after the middle scan of the set of reflections at each temperature. The averaged integrated intensities of equivalent reflections, with an assigned error equal to their root-mean-square deviations, are tabulated in Appendix A.3 for all the UO_2 and ThO_2 experiments.

4.3 SYSTEMATIC ERRORS IN DIFFRACTION MEASUREMENTS

There are several effects for which the data must be corrected before the analysis can proceed. These are absorption, extinction, thermal diffuse scattering (TDS) and multiple reflections. Of these, extinction and TDS are of particular importance at high temperatures.

In order to account for these corrections, the expression for the calculated intensity of a Bragg peak (equation 3.36) must be modified to

$$I = A(\rho + \alpha)\, S \frac{|F(\underline{\tau})|^2}{\sin\gamma \cos\nu} \qquad (4.1)$$

where

A is the transmission factor (for absorption)

ρ is the secondary extinction factor

α is the TDS correction factor

These correction factors will be defined in the coming sections.

4.3.1. ABSORPTION

In passing through a crystal a neutron or X-ray beam is attenuated by normal absorption processes, resulting in a reduction of the observed

Bragg intensity. The transmission factor is given by

$$A = \frac{1}{V} \int \exp \{ -\mu(p + q) \} \, dV \qquad (4.2)$$

where μ is the linear absorption coefficient, p and q are the path lengths of the incident and reflected beams in the crystal for radiation reflected in a volume dV, and V is the crystal volume. This correction has been evaluated for cylindrical and spherical samples by Rouse et.al. (1970).

In general, the absorption coefficients are much smaller for neutrons than for X-rays, and consequently the correction is often ignored for neutron diffraction. It becomes even less significant for single crystal work because of the smaller samples employed. However, the correction should not be blandly ignored for UO_2 because of the very large absorption cross-section of ^{235}U nuclei: hence it is clearly dependent on the degree of enrichment. For the natural UO_2 samples used, the linear absorption coefficient is 0.18 cm^{-1}, resulting in a correction of about 2%. This gives the transmission factor an angular variation of about 0.2%, which is insignificant compared to the magnitude of the other corrections. The correction for absorption may therefore be safely omitted.

4.3.2 EXTINCTION

A far more serious form of attenuation, occuring when the crystal is in a reflecting position, is that caused by diffraction of neutrons out of the primary beam. It may be shown that the penetration distance of a neutron beam in a perfect crystal, which is in a diffracting setting, is typically of the order of 10^{-4} cm (e.g. Bacon 1975). Any further increase in thickness will contribute little to the measured intensity. Such attenuation caused by diffraction in a perfect crystal

is called primary extinction. Diffraction occurs in a perfect crystal only over a very narrow angular range of a few seconds of arc. However, most real crystals are permeated by dislocations which have the effect of dividing the crystal into much smaller regions having linear dimensions of the order of 5000Å. These mosaic blocks are usually misorientated by a few minutes of arc, so few blocks are in a diffracting position at the same time. Consequently, the penetration of the incedent beam is greatly increased. Extinction caused by diffraction from successive mosaic blocks is called secondary extinction, and this is the dominant type in most crystals (except highly perfect crystals such as germanium).

Formulae have been derived by Zachariasen (1967) for the secondary extinction caused by mosaic blocks of mean radius r, having a Gaussian distribution. His formulation agrees well with experimental data for small extinction levels, but it cannot cope with extinction greater than 40%. Cooper and Rouse have extended his theory to cope with severe extinction, and tests have shown that their expressions can account for observed extinction levels of greater than 80% in spherical and cylindrical crystals (Cooper and Rouse 1970). Their expressions, which were obtained analytically in the main, but some by trial of various functions, are

$$\rho = 1 - \frac{1 - \rho'}{f(\theta)} \tag{4.3}$$

where $f(\theta) = 1 + {}^{1}/_{3} \sin^{2.5}\theta$ (4.4)

$$\rho' = \left[\frac{\sqrt{\pi}}{2} \frac{\mathrm{erf}\ (\sqrt{3 \times f_o})}{\sqrt{3 \times f_o}} \right]^{5/4} \quad \text{(for cylindrical crystals)}, \tag{4.5}$$

$$x = \frac{\lambda^2}{V} \frac{F(hkl)}{\sin 2\theta}^2 \left[{}^{3}/_{2}\, r(r + r^*) + r^* \bar{T} \right] \tag{4.6}$$

$$r^* = r \left[1 + \left(\frac{r}{\lambda g} \right)^2 \right]^{-\frac{1}{2}} \tag{4.7}$$

(Cooper and Rouse 1970, Rouse and Cooper 1980). The parameters r and g are the domain radius and mosaic spread parameter as defined by Zacharaisen (1967), and $\bar{T}$ is the mean path length through the crystal. In the current data analysis, to avoid having two extinction parameters r and g, they have been combined to give one parameter e given by

$$e = \frac{1}{V} \left[{}^{3}/_{2}\, r(r + r^*) + r^* \bar{T} \right] , \qquad (4.8)$$

which may be substituted into equation (4.6). An alternative treatment of secondary extinction is described by Becker and Coppens (1974).

4.3.3 THERMAL DIFFUSE SCATTERING (TDS)

So far we have assumed that no extra scattering is observed when scanning a Bragg peak, except spurious Bragg scattering from the furnace. But since the resolution aperture is finite, some scattering from phonons at small q values may be detected along with the Bragg scattering. Equation (3.23) shows that the cross-section for phonons contains a factor kT/ω^2 for small ω, which demands consideration for acoustic phonons at high temperatures.

Rouse and Cooper (1969) have evaluated the TDS factor α for cubic crystals by integrating the one phonon scattering cross-sections (equations 3.23 and 3.26) over ω, making the following assumptions.

1. TDS arising from optic modes and multiphonon processes may be accounted for by the normal background correction i.e. we only consider first order acoustic phonon scattering. Further, only low wavevector modes are important, so that dispersion effects may be ignored.

2. The elastic properties are approximately isotropic i.e. $(C_{11}-C_{12}) \approx 2C_{44}$.

3. Resolution effects, due to divergence of the incident beam and crystal mosaic spread, may be ignored.

4. The classical high temperature approximation is applicable, in which each mode is given an energy of $k_B T$.

The resulting expression for the TDS factor is

$$\alpha = \frac{4\, k_B T}{3\lambda^3} \sin 2\theta \,.\, \sin^2\theta \,.\, \kappa\sigma \qquad (4.9)$$

where

$$\kappa = \frac{1/5\; b_1 (C_{11} + C_{12}) + C_{44}(2C_{11} + C_{44})}{\frac{1}{105} b_1^2 b_2 + 1/5 b_1 (C_{11} + C_{12})\, C_{44} + C_{11} C_{44}^2} \,, \qquad (4.10)$$

with $b_1 = C_{11} - C_{12} - 2C_{44}$

$b_2 = C_{11} + 2C_{12} + C_{44}$

and $$\sigma = \frac{1}{\pi k \sin 2\theta} \int \frac{dx\, dy\, dz}{|q|^2} \qquad (4.11)$$

C_{11}, C_{12} and C_{44} are the elastic constants for a cubic crystal, their values for UO_2 being taken from the measurements described in chapter 6. The elastic constants for ThO_2 were calculated from the room temperature values determined in chapter 5, assuming that their temperature dependence involves the same parameter T/T_m as for UO_2.

$$C_{ThO_2}(T) = C_{ThO_2}(293) \times \frac{C_{UO_2}(T')}{C_{UO_2}(293)} \qquad (4.12)$$

with $$T' = \frac{T_m(UO_2)}{T_m(ThO_2)} \times T$$

The above derivation is valid for X-rays and for neutrons where the neutron velocity v_n is greater than the phonon velocity $v_j(q)$. For slower-than-sound neutrons ($v_n < v_j(q)$), on the other hand, the scattering surface is an ellipsoid with the reciprocal lattice point at one focus.

The scattering corresponds to phonon absorption only when the crystal setting is on one side of the Bragg position, and to phonon emission only when on the other side. As the crystal setting approaches the Bragg position from either side, the scattering surface contracts and collapses at the reciprocal lattice point. This contraction has an approximate q^2 dependence, which when coupled to the q^{-2} term in equation (4.11) gives an essentially constant contribution near the Bragg reflection, so that the normal background correction is adequate.

For the experiments described here the neutron velocity is 3.6 kms^{-1}, the phonon velocity for the transverse acoustic (TA) mode varies between 2.5 and 1.4 kms^{-1} and between 5.0 and 3.7 kms^{-1} for the longitudinal acoustic (LA) mode in the temperature range 300 - 2900K. In order to correct for the fact that it is only the TA modes which contribute to the TDS, the value of K in (4.10) was multiplied by the factor $\frac{2/v_{TA}^2}{1/v_{LA}^2 + 2/v_{TA}^2} = \frac{2/C_{44}}{1/C_{11} + 2/C_{44}}$ (Willis 1969). This amounts to a $\sim$10% decrease in the value of K. The importance of the TDS correction for this work is demonstrated by the fact that $K \gtrsim 0.7$ for some high-angle reflections in UO_2 at the highest temperatures. However, small inaccuracies in α will be compensated by small changes in the fitted thermal parameters.

4.3.4 MULTIPLE REFLECTIONS

The measured intensity can be increased or decreased by successive reflections from different Bragg planes, especially for weak reflections. Their occurence may be tested by rotating the sample around the $\underline{\tau}$-vector. This can easily be done on a 4-circle diffractometer, but it is impractical when using a furnace on a 2-circle machine. The magnitude of the correction for multiple reflections should be much smaller than those for extinction and TDS and its effect has therefore been neglected in this work.

4.4 DATA ANALYSIS

4.4.1 GENERAL CONSIDERATIONS

In principle it is possible to obtain a time averaged probability density of nuclei over the unit cell from neutron diffraction data by performing a Fourier transform of the complete set of structure factors. The resulting map of the scattering density may then be used to provide information on the time-averaged positions of the ions and the potentials in which they vibrate. However, in practice difficulties arise from termination errors, since all reflections are not measured, and also from extinction corrections which are difficult to calculate ab initio. In view of the size and temperature dependence of the extinction correction for this work, an alternative method of analysis has been adopted. This involves the comparison of the measured intensities of the Bragg reflections, after correction for systematic errors, with calculated intensities derived from a model of the time-averaged positions of the ions together with associated harmonic and anharmonic temperature factors to describe the effects of thermal vibrations. The extinction parameter e (equation 4.8) is included in the model as a fitted parameter. In the case of highly defective structures, this form of analysis becomes difficult as it necessitates the development and testing of a large number of possible models of the averaged ionic positions which may not have an unique solution. The models postulated for the analysis of the present data are discussed in the next sub-section. A third method of analysis of diffraction data on fast-ion conductors has recently been suggested, which involves the direct fitting of appropriate atomic potential functions to the measured intensitites (Schulz and Zucker 1981 , Walker et.al. 1981).

For the data analysis reported here the Bragg peak intensities

were calculated from the expression given in equation (4.1), omitting the absorption correction. The structure factor $F_c(hkl)$ of the (hkl) reflection is calculated for a particular model of the ionic positions. S is a scale factor, the determination of which will be discussed later.

4.4.2 MODELS OF THE DISORDERED STRUCTURE

The simplest model which can be applied to the data is the defect-free regular fluorite structure. Each ion has its isotropic harmonic vibration parameter B_i (equation 3.19): B_M for the metal ions and B_o for the oxygen ions. This model has been shown to be inadequate for UO_2 and other fluorites at temperatures well below T_c (e.g. Willis 1963), where different intensities were reported for reflections having the same structure factor and Bragg angle, such as (117) and (551). Dawson et.al. (1967) showed that this could be accounted for by the lack of inversion symmetry at the oxygen site. (The cube centre on one side is occupied by a metal ion whereas the cube-centre on the opposite side is unoccupied.) The anisotropic vibrations thus caused may be expressed as a third cumulant coefficient C^o_{123} of the oxygen ion (Willis and Hazell 1980), which is related to the oxygen single-particle potential V by

$$V = V_o + \tfrac{1}{2}\,\alpha_o(x^2 + y^2 + z^2) + \beta_o xyz \qquad (4.13)$$

$$\text{where} \quad C^o_{123} = -\,8\pi^3\,\frac{(k_B T)^2}{a_o^3\,\alpha_o^3}\,\beta_o \qquad (4.14)$$

$$\text{and} \quad B_o = 8\pi^2\,\frac{k_B T}{\alpha_o} \qquad (4.15)$$

The structure factor for the fluorite structure, with anisotropic vibrations, is given by

$$
F_c(hkl) = \begin{cases} 4b_M e^{-W_M} + 8b_o e^{-W_o}, & (h+k+l) = 4n \\ 4b_M e^{-W_M} - 8b_o e^{-W_o}, & (h+k+l) = 4n \pm 2 \\ 4b_M e^{-W_M} + 8b_o e^{-W_o} C^o_{123} hkl, & (h+k+l) = 4n + 1 \\ 4b_M e^{-W_M} - 8b_o e^{-W_o} C^o_{123} hkl, & (h+k+l) = 4n - 1 \end{cases} \quad (4.16)
$$

(Dawson et.al. 1967). The anisotropy can be seen to explain the different intensities at the same 2θ values reported for $(4n \pm 1)$ reflections. These two models involving the regular defect-free fluorite structure, without and with an anisotropic vibration parameter, are denoted I and IA respectively. (All the models and parameters are denoted consistently with Dickens et.al. (1982)).

The simplest way to introduce defects into the model is to allow a fraction n_d of anions to vacate their regular sites, and for these interstitials to be distributed uniformally throughout the unit cell, thus only contributing to the scattering at $\underset{\sim}{Q} = 0$ (model II). (This has the same effect on the structure factor as a reduction in the oxygen scattering length b_o.) The next step is to allocate specific sites to the interstitial ions. The most obvious site, also suggested by work on the low temperature Frenkel defects (Lidiard 1974), is the empty cube centre, represented by model III. The interstitial thermal vibration parameter B^I_o is introduced into the fit.

Now we introduce a set of models based on the cluster model deduced from work on the fluorite halides, as outlined in §1.4 and illustrated in Fig. 1.6. It may be described in terms of anion vacancies and displaced anions occupying two types of site, referred to as R and I sites. There are eight R sites with positional parameter x, situated at $\pm(\frac{1}{2} - x)$, $\pm(\frac{1}{2} - x)$, $\pm(\frac{1}{2} - x)$ relative to the empty cube-centre, and twelve

I sites with positional parameter y at positions $\pm$ ($^1/_4$ - y), $\pm$ ($^1/_4$ - y),0 etc. relative to the empty cube-centre. The R sites are at positions $\pm$ (x,x,x) relative to the cations and the I sites are displaced by $\pm$ (y,y,0) towards the empty cube-centres from the mid-point between adjacent anions. In the simplest form of the cluster model (model IV), the interstitials are located on a cube-edge mid-way between adjacent regular anion sites i.e. at the I sites with y = 0, each site having an average occupancy $^n d/3$. In model V,R sites only are considered, each of occupancy $^n d/4$.

Models VI, VII and VIII represent cluster models consisting of both I and R sites, having two positional parameters x and y. The relative occupancy of each kind of site is expressed as a fraction d (of all displaced ions) which occupy I sites. In models VI and VII the value of d is fixed at $^1/_3$ or $^1/_2$ respectively, and in model VIII d is treated as a variable parameter. The thermal parameter B^I_o is constrained to be equal for I and R sites. In the cluster notation of § 1.4.1, model VI represents a 3:1:2 cluster and model VII represents a 4:2:2 cluster. On the grounds of their molecular dynamics simulation of PbF_2, Walker et.al. (1982) have suggested that the apparent existence of I sites might be the consequence of anion hopping along [100] directions. Therefore model IX, which is an adaptation of model VI, has been tried, in which the I sites have been replaced by anions 'smeared' uniformally in [100] directions between regular anion sites. The various models and their fitted parameters are summarised in Table 4.2 and the occupancy of the sites for each model in Table 4.3. Expressions for the structure factors of each model are listed in Appendix A.2.

4.4.3 LEAST SQUARES FITTING

Each of the different models of the time-averaged structure

TABLE 4.2

SUMMARY OF MODELS OF THE TIME-AVERAGED STRUCTURE AND THEIR FITTED PARAMETERS

Model	Description	Fitted Parameters
I	Regular Fluorite (Isotropic Vibrations only)	S, e, B_M, B_o
IA	Regular Fluorite (including Anisotropic Vibrations)	$S, e, B_M, B_o, C^o_{123}$
II	Vacancies only (Uniform distribution of Defective Anions)	$S, e, B_M, B_o, C^o_{123}, n_d$
III	Cube-centre interstitial	$S, e, B_M, B_o, C^o_{123}, B^I_o, n_d$
IV	Cube-edge interstitial (I site with y = 0)	$S, e, B_M, B_o, C^o_{123}, B^I_o, n_d$
V	R site only	$S, e, B_M, B_o, C^o_{123}, B^I_o, n_d, x$
VI	R and I sites as cluster (3:1:2)	$S, e, B_M, B_o, C^o_{123}, B^I_o, n_d, x, y$
VII	R and I sites as cluster (4:2:2)	$S, e, B_M, B_o, C^o_{123}, B^I_o, n_d, x, y$
VIII	R and I sites as cluster (vary d)	$S, e, B_M, B_o, C^o_{123}, B^I_o, n_d, x, y, d$
IX	R sites with interstitials 'smeared' along [100] directions	$S, e, B_M, B_o, C^o_{123}, B^I_o, n_d, x$

TABLE 4.3

SUMMARY OF OCCUPANCIES AND POSITIONAL PARAMETERS FOR THE DIFFRACTION MODELS

Model	n_d	d	n_R	n_I	x	y
I	0	-	-	-	-	-
IA	0	-	-	-	-	-
II	$0 < n_d < 1$	-	-	-	-	-
III	$0 < n_d < 1$	0	$2n_{d/3}$	-	0.5	-
IV	$0 < n_d < 1$	1	0	$n_{d/3}$	-	0
V	$0 < n_d < 1$	0	$n_{d/4}$	0	$0.25 < x < 0.5$	-
VI	$0 < n_d < 1$	$1/3$	$n_{d/6}$	$n_{d/18}$	$0.25 < x < 0.5$	$0 \leqslant y < 0.25$
VII	$0 < n_d < 1$	$1/2$	$n_{d/8}$	$n_{d/12}$	$0.25 < x < 0.5$	$0 \leqslant y < 0.25$
VIII	$0 < n_d < 1$	$0 < d < 1$	$(1-d)n_{d/4}$	$dn_{d/6}$	$0.25 < x < 0.5$	$0 \leqslant y < 0.25$
IX	$0 < n_d < 1$	$1/3$	$n_{d/6}$	"$n_{d/18}$"	$0.25 < x < 0.5$	-

n_R and n_I denote the fractional occupancy of each R and I site .

described above was fitted in turn to the data at each temperature using the least squares refinement method. Two computer routines were used for this purpose: the Harwell program TAILS (Rouse and Cooper 1980) which was also used to calculate the TDS corrections α , and the program POWLS written by W C Hamilton, which was adapted to fit the different models. Identical results were obtained with both programs; the results presented here were all obtained using the latter program. The quality of the fit of a given model was judged by the weighted R-factor, R_W, given by

$$R_W^2 = \frac{\sum_i \left[(I_o^2 - I_c^i)/\sigma_o^i \right]^2}{\sum_i (I_o^2/\sigma_o^i)^2} \qquad (4.17)$$

where I_o^i and I_c^i are the observed and calculated values of the i'th integrated peak intensity, and σ_o^i is the error in the observed intensity. The minimum R-factor R_W^{min}, the value of R_W for a fit in which $(I_o^i - I_c^i) = \sigma_o^i$ for all reflections, was also calculated for each set of data.

As the models become more sophisticated, additional parameters become involved, so care must be exercised in evaluating the resulting R_W. Use was therefore made of significance tests (Hamilton 1965) and also of the physical reasonableness of the resulting parameters, when judging whether a genuine improvement in fit was attained by using a model with more parameters.

The published values of the scattering lengths, b_o = 5.805fm, b_{Th} = 9.842fm (Koester and Rauch 1981) and b_u = 8.417fm (Boeuf et.al. 1982), were used in the analysis. These values are in good agreement with fits to room temperature data, taken before and after heating to high temperatures, summarised in Table 4.4. Also given for these fits are the values of n_d for model II, deduced from the fitted scattering lengths. Although these fitted values of n_d do not deviate significantly

TABLE 4.4

RESULTS OF FITS TO ROOM TEMPERATURE DATA FOR UO_2 AND ThO_2

(Error in last digit(s) shown in parentheses)

UO_2

Exprt.	S	B_u ($Å^2$)	B_o ($Å^2$)	$ex10^3$	b_u (fm)	R_W (%)	n_d
1	422(3)	0.250(8)	0.466(9)	3.92(6)	8.42(2)	0.73	0.000(2)
1(a)	529(15)	0.32(3)	0.52(3)	8.4(5)	8.46(5)	1.79	0.005(6)
2(a)	6.65(10)	0.23(2)	0.50(6)	3.1(3)	8.49(27)	1.54	0.009(32)
3(b)	5.38(11)	0.28(3)	0.53(3)	5.0(3)	8.36(4)	3.16	-0.011(6)
4(a)	12.0 (9)	0.20(8)	0.56(8)	2.6(5)	8.07(30)	7.04	-0.041(36)
4(b)	3.19(11)	0.32(5)	0.39(5)	7.0(5)	8.28(7)	3.94	-0.017(9)

ThO_2

Exprt.	S	B_u ($Å^2$)	B_o ($Å^2$)	$ex10^3$	b_{Th} (fm)	R_W (%)	n_d
5(a)	3.61(32)	0.33(9)	0.46(11)	7.8(12)	9.82(32)	4.95	-0.002(33)
6(a)	3.63(08)	0.18(3)	0.48(3)	8.2(3)	9.77(9)	1.81	-0.007(9)
6(b)	4.48(19)†	0.14(4)	0.47(6)	10.3(7)	9.56(15)	2.67	-0.028(15)

(a) before heating

(b) after heating

† Changed neutron monitor rate.

Values of n_d are those obtained on assumption that b_u = 8.417fm, b_{Th} = 9.84fm.

from zero, it should be noted that this does not imply that the UO_2 samples are stoichiometric after cooling from high temperatures since UO_{2+x} and UO_{2-x} both dissociate to UO_2 at room temperature (M.H.Rand, private communication)

$$UO_{2+x} \longrightarrow (1 - 4x)\ UO_2 + x\ U_4O_9$$

$$UO_{2-x} \longrightarrow (1 - \tfrac{1}{2}x)\ UO_2 + \tfrac{1}{2}x\ U$$

The scale factor S at elevated temperatures was fixed, where possible, from its value S(amb) for the fits to room temperature data, using the expressing

$$S(T) = S(amb) \left(\frac{a_o(amb)}{a_o(T)} \right)^3 \qquad (4.18)$$

which arises from the v_o^{-1} term in equation (3.17). S was fixed in this way for ThO_2 at all temperatures, but it could not be done for UO_2 data at the higher temperatures because of the loss of crystal due to evaporation. It was sometimes necessary to constrain the thermal parameter for displaced ions, B_o^I, to a reasonable value. The positional parameter x was found to be highly correlated with several other parameters. For some temperatures, it was optimised by performing a succession of fits with x fixed at different values and choosing the fit which gave the lowest R_W. The various models gave consistent and sensible fits despite the relatively low number of peaks measured.

4.5 RESULTS OF DATA ANALYSIS

4.5.1 UO_2

The R_W values attained for each model and the best models at each temperature are summarised in Table 4.5 and the parameters for the best model at each temperature in Table 4.6. The observed and calculated

TABLE 4.5

VALUES OF THE WEIGHTED R-FACTOR R_W(%) FOR ALL FITS TO DATA ON UO_2 AND ThO_2

UO_2		R_W(%) FOR MODEL										
T(K)	R_W^{min}(%)	I	IA	II	III	IV	V	VI	VII	VIII	IX	BEST MODEL
293	0.79	0.73	0.70	0.70	-	-	-	-	-	-	-	I
1873	6.94	11.66	8.68	8.04	7.06	8.62	6.54	7.83	8.21	-	7.03	V
2098	6.87	12.15	4.88	4.81	4.89	4.84	4.77	4.76	4.88	-	4.87	IA,VI
2218	3.58	13.32	5.25	4.02	4.20	4.02	4.06	4.59	4.53	-	-	II,IV
2403	2.01	6.38	5.79	5.07	5.79	5.01	3.00	2.88	3.85	2.74	5.79	VI,VIII
2527	3.73	16.23	11.50	9.03	9.12	7.27	7.00	5.94	6.16	5.94	8.84	VI
2690	5.94	23.81	17.80	7.87	9.01	6.83	6.29	6.01	6.06	6.02	7.22	VI
2778	7.33	31.37	26.57	8.55	8.97	6.15	5.70	5.23	5.41	5.22	19.16	VI
2843	12.53	21.03	17.10	14.60	14.77	13.60	13.83	13.48	13.41	-	16.85	VI,VII
2905	14.81	26.20	23.35	13.97	13.68	7.72	-	6.43	6.73	6.53	7.07	VI

ThO_2		R_W(%) FOR MODEL										
T(K)	R_W^{min}(%)	I	IA	II	III	IV	V	VI	VII	VIII	IX	BEST MODEL
293	1.21	1.83	1.82	1.81	-	-	-	-	-	-	-	I
2291	2.51	7.58	4.08	3.70	4.20	2.85	3.61	3.06	2.87	2.80	-	IV,VII
2555	2.08	8.05	3.70	3.63	3.68	3.30	2.99	2.89	2.93	2.89	3.04	VI,VII
2738	2.86	12.10	6.18	5.80	5.38	4.06	3.70	2.78	2.93	2.78	4.90	VI
2803	5.70	22.17	17.11	13.32	12.21	7.74	12.60	7.73	6.68	6.64	12.54	VII
2909	4.56	17.82	11.31	6.22	8.79	6.58	5.30	4.74	4.72	4.69	8.33	VI,VII

TABLE 4.6

PARAMETERS OF BEST-FITTING MODELS OF DISORDERED STRUCTURE AT EACH TEMPERATURE

UO_2 Error in last digit(s) shown in parentheses

T(K)	S	B_u ($Å^2$)	B_o ($Å^2$)	$C^o_{123} \times 10^3$	n_d	B^I_o ($Å^2$)	x	y	$e \times 10^3$	MODEL
293	422(3)	0.25(1)	0.47(1)	-	-	-	-	-	3.9(1)	I
1873	437(22)	1.94(6)	3.23(7)	2.4(5)	0.03(1)	4.0†	0.33†	-	4.7(12)	V
2098	6.24†	2.49(6)	4.35(13)	5.8(9)	0.02(3)	4.5†	0.35(8)	0.0†	3.8(3)	VI
2218	9.50(4)	2.60(5)	4.78(6)	5.9(4)	0.03(1)	-	-	-	15.1(14)	II
2403	6.17†	2.92(7)	5.24(24)	4.7(20)	0.07(3)	0.9(13)	0.35(1)	0.03(2)	3.6(3)	VI
2527	10.0 (8)	3.66(13)	6.17(28)	5.7(20)	0.14(4)	5.3(16)	0.32(1)	0.01(3)	19.7(31)	VI
2690	7.4 (4)	4.08(10)	6.97(26)	9.0(15)	0.17(3)	7.6(14)	0.34(1)	0.0†	21.1(33)	VI
2778	6.3 (5)	4.51(15)	7.38(31)	13.6(18)	0.23(4)	10.7(18)	0.34(2)	0.04(3)	43.6(75)	VI
2843	3.7 (1)	4.50(61)	9.40(69)	15.5(63)	0.17(6)	12.0†	0.34†	0.06(8)	91. (59)	VI
2905	4.71†	5.35(7)	8.92(49)	11.1(36)	0.22(6)	11.3(31)	0.35(2)	0.02(6)	186. (17)	VI

† Fixed parameter

Contd...

TABLE 4.6 (Continued)

ThO_2

T(K)	S	$B_{Th}(\AA^2)$	$B_o(\AA^2)$	$C^o_{123} \times 10^3$	n_d	$B^I_o(\AA^2)$	x	y	$ex10^3$	MODEL
293	3.63(8)	0.18(3)	0.48(3)	-	-	-	-	-	8.2(3)	I
2291	3.36†	2.34(2)	4.17(6)	4.9(5)	0.06(1)	6.0†	. -	0.0†	7.8(2)	IV
2555‡	4.05†	2.81(3)	4.95(11)	5.9(7)	0.08(2)	6.4(27)	0.34†	0.02(5)	7.4(2)	VI
2738‡	4.00†	3.27(2)	5.47(12)	8.6(8)	0.16(2)	9.0(21)	0.35(2)	0.06(3)	7.2(3)	VI
2803	2.99†	3.19(9)	5.06(27)	6.9(17)	0.25(3)	4.8(17)	0.35(1)	0.04(1)	3.5(6)	VII
2909‡	3.96†	3.88(3)	6.45(18)	12.3(14)	0.17(2)	7.8(18)	0.37(2)	0.07(1)	8.8(7)	VII

† Fixed parameter

‡ Changed neutron monitor rate

intensities and the TDS factor α for each reflection at all temperatures are tabulated in Appendix A.3, together with details of all the fits. The agreement between fits to data taken at different temperatures is good considering that they were taken from five different samples over four separate experiments. In general, the parameters do not vary greatly with the model fitted, except for the value of B_o^I which is somewhat model-dependent. The model dependence of n_d is discussed in the next section.

Model I clearly cannot account for data at temperatures above ambient, whereas the introduction of anisotropic vibrations in model IA gives good agreement up to about 2400K. Above 2400K a significant improvement is obtained by the inclusion of anion vacancies in model II. The cube-centre interstitial site of model III is unsatisfactory, as it is for PbF_2 at high temperatures (Dickens et.al. 1982). This calls into question calculations based on cube-centre interstitial sites, such as calculated values of Frenkel defect formation energies (e.g. Catlow 1977). Models IV and V, representing I and R sites respectively, both reduce the R_W values significantly above 2500K. A note of caution should be sounded about model V, in that the existence of R sites does correlate strongly with C_{123}^o as may be expected, and consequently a degree of scepticism is needed concerning the values of C_{123}^o, B_o^I, x and n_d obtained from the fits. However, if the value of C_{123}^o is fixed at its value for model II, a substantial improvement in the fit is still obtained for model V, thus confirming the validity of R site interstitials. Models VI and VII, in which both I and R sites are occupied, have slightly lower R_W values than model V, but involve one extra parameter. Model VI ($d = {}^1/3$) is slightly better than model VII ($d = \frac{1}{2}$) at most temperatures. Model VI is also preferred to model V for the following reasons.

1. Model IV (I sites only) fits the data well at all temperatures.

2. When d is varied (model VIII), a value of 0.5 - 0.7 is obtained fairly consistently.

3. Better agreement between parameters for different temperatures is obtained for model VI than for model V.

4. The fit for model VI is insensitive to the value of the additional parameter y, which may be set to the same value at all temperatures.

The optimum values of $x = 0.34 \pm 0.02$ and $y = 0.04 \pm 0.03$ are almost independent of temperature for models VI and VII. Poor agreement with the data is given by model IX, which represents anion density 'smeared' in [100] directions between regular anion sites.

The measured values of the lattice constant at different temperatures are listed in Table 4.7, together with those measured with TAS spectrometers as described in chapter 6. The complete set of lattice constants is shown in Fig. 4.1, together with existing data (Hoch and Momin 1969 , Albinati et.al. 1980), measured using X-ray and neutron diffraction respectively, which are in good agreement with our data. The variation of the fraction of defective ions n_d for the best model at each temperature is shown in Fig. 4.3(a). It can be seen that n_d increases rapidly above 2000K to a defect concentration of ~20% at 2800K. There is some evidence of saturation of n_d above 2800K, which is probably caused by interactions between defects. The temperature variation of the isotropic thermal parameters B_u and B_o is shown in Fig. 4.4(a), together with Willis' reanalysed data up to 1400K (Willis 1963, Willis and Hazell 1980). Both parameters show a more rapid rate of increase with temperature above 2000K. Illustrated in Fig 4.5(a) is the variation of C^o_{123} which increases rapidly with increasing temperature. The data at high temperatures show large error bars because the value of

TABLE 4.7

TEMPERATURE VARIATION OF THE LATTICE CONSTANT OF UO_2

(Values of a_o have typical errors of ± 0.005Å)

T(K)	a_o (Å)	Instrument	Temperature Monitor
293	5.470	TAS	-
1211	5.524	TAS	tc
1873	5.568	Dif	tc
1963	5.575	TAS	tc
2081	5.593	TAS	pm
2098	5.591	Dif	tc
2098	5.595	TAS	tc
2198	5.594	TAS	tc
2218	5.604	Dif	pm
2271	5.628	TAS	pm
2390	5.625	TAS	pm
2403	5.611	Dif	tc
2478	5.634	TAS	pm
2528	5.635	Dif	pm
2589	5.649	TAS	pm
2683	5.659	TAS	pm
2690	5.660	Dif	pm
2771	5.672	TAS	pm
2778	5.674	Dif	pm
2843	5.678	Dif	pm
2905	5.689	Dif	pm
2929	5.690	TAS	pm

TAS: Triple Axis Spectrometer
Dif: Neutron Diffractometer
tc : thermocouple
pm : pyrometer

TABLE 4.8

TEMPERATURE VARIATION OF THE LATTICE CONSTANT OF ThO_2

(Values of a_o have typical errors of ± 0.005Å)

T(K)	a_o (Å)
293	5.598
293	5.604[a]
1073	5.655[a]
1473	5.685[a]
1653	5.695[a]
1873	5.699[a]
2123	5.712[a]
2273	5.721[a]
2291	5.728
2373[†]	5.718[a]
2473[†]	5.721[a]
2555	5.746
2573[†]	5.725[a]
2738	5.769
2803	5.763
2909	5.789

[†] Nominal temperature (Schnabel 1983, p.146)

[a] Schnabel 1983

TABLE 4.9

TEMPERATURE VARIATION OF THE ONE-PARTICLE POTENTIAL PARAMETERS FOR UO_2 AND ThO_2

(Error in last digit(s) shown in parentheses)

UO_2

T(K)	α_u (Jm^{-2})	α_o (Jm^{-2})	$-\beta_o$ ($10^{"}Jm^{-3}$)
293	129.9(42)	69.7(15)	-
1873	105.2(38)	63.2(14)	6.3(13)
2098	91.8(22)	52.6(16)	7.1(5)
2218	93.0(19)	50.6(6)	5.8(4)
2403	87.6(26)	54.1(36)	5.7(24)
2527	75.3(27)	44.6(22)	3.0(12)
2690	71.9(18)	42.1(16)	3.6(7)
2778	67.1(22)	41.0(17)	3.9(7)
2843	68.9(92)	33.0(25)	2.7(13)
2905	59.2(8)	35.5(20)	2.3(8)

ThO_2

T(K)	α_{Th} (Jm^{-2})	α_o (Jm^{-2})	$-\beta_o$ ($10^{"}Jm^{-3}$)
293	168.1(187)	69.4(30)	-
2291	106.7(9)	59.9(9)	8.1(9)
2555	99.1(11)	56.3(12)	6.5(9)
2738	91.3(6)	54.6(12)	7.6(9)
2803	95.8(27)	60.4(33)	7.8(23)
2909	81.7(6)	49.2(14)	7.1(10)

C^{o}_{123} is determined mainly by the intensities of the high-angle reflections, for which the resolution of the Mk6 Diffractometer is poor. Knowledge of these thermal parameters enables us to determine the one particle potential parameters α_i and β_i as a function of temperature through equations (4.13 - 4.15). These are listed in Table 4.9 and illustrated in Figs. 4.6(a) and 4.7(a) which show that α_u, α_o and β_o all decrease with increasing temperature above 1500K.

4.5.2 ThO_2

The R_W values for each fit are given in Table 4.5, and the parameters for the best model at each temperature in Table 4.6. The results are very similar to those for UO_2, indicating the development of anion Frenkel disorder at temperatures above 2200K in ThO_2. As for UO_2, the best fits to the data are given by models VI and VII. The R_W values are generally lower than for UO_2 and the standard deviations of the fitted parameters are also smaller as a consequence of being able to fix the scale factor. The temperature variation of a_o, n_d, B_{Th}, B_o, C^{o}_{123}, α_{Th}, α_o and β_o in ThO_2, for this investigation and for experiments performed by P. G. Schnabel, are shown in Figs. 4.2 - 4.7, together with the corresponding results for UO_2. In contrast with the data for UO_2, the agreement between values of a_o obtained from different experiments is poor. There is some uncertainty concerning the true sample temperature for Schnabel's data at nominal temperatures between 2273K and 2573K: the measured a_o is fairly constant in this temperature range whereas the thermal parameters increase monotonically with increasing temperature. (See Schnabel 1983, p. 147 and 169f for a discussion of these problems.) The temperature variation of n_d and of the thermal parameters in ThO_2 are similar to those observed in UO_2, but the disorder sets in at a higher temperature in ThO_2. The one-

particle potential parameters α_M and α_o are larger in ThO_2 than in UO_2 as may be expected on account of its higher melting temperature. There is some indication that the anharmonic parameter β_o is fairly constant with temperature in ThO_2, whereas it decreases with increasing temperature in UO_2 (Fig. 4.7).

4.6 DISCUSSION AND CONCLUSIONS

The most important result to emerge from the diffraction measurements is the unambiguous observation of anion Frenkel disorder in both UO_2 and ThO_2 at temperatures above 2000K. The temperature variation of the fraction n_d of oxygen ions which vacate their regular sites has also been established for both materials. The value of n_d is fairly model-independent and increases with increasing temperature, showing some evidence of saturation at a concentration of $\sim$20-25% at temperatures above 2700K in UO_2 and above 2800K in ThO_2. This saturation is probably caused by interactions between defects. The results for both materials show that the cube-centre site is not appreciably occupied at high temperatures. Good agreement with the data is obtained for a cluster model of anions occupying I sites, displaced in [110] directions from the mid-point between nearest-neighbour regular anion sites, and R sites which are displaced in [111] directions from regular anion sites. This cluster model, the simplest form of which is the 3:1:2 cluster, is very similar to that deduced for the high temperature region of the fluorite halides PbF_2, CaF_2 and $SrCl_2$ from diffraction measurements (Smith 1980, Dickens et.al. 1982) and from coherent QES measurements (Schnabel 1983, Hutchings et.al. 1984).

In relating the values of n_d obtained from this work to values which might be deduced from thermophysical measurements, it is important

to realise that not all the defective anions are true Frenkel interstitials. Anions occupying R sites may be viewed as being merely relaxed off their regular sites, whereas anions occupying I sites have associated vacancies, from which they are well separated in a cluster model, and should therefore be viewed as true Frenkel interstitials. In order to determine the concentration $n_f = dn_d$ of such true Frenkel interstitials one needs the parameter d, which is difficult to determine directly from the diffraction data. The best overall agreement with the data for both oxides is given by models VI (3:1:2 cluster) and VII (4:2:2 cluster), for which $d = {}^1/_3$ and $^1/_2$ respectively. Hence the values of $n_d \sim 20\%$, observed at the highest temperatures in UO_2 and ThO_2, correspond to true Frenkel interstitial concentrations $n_f \sim 7\text{-}10\%$.

The Frenkel pair formation energy, E_d, for UO_2 has been obtained from the data by fitting the values of n_d for the four temperatures between 2098K and 2527K with the function

$$n_d = \frac{n_f}{d} = n_o \exp(-E_d/2k_BT). \qquad (4.19)$$

The higher temperature data were omitted from the fit because of possible interactions between defects. The resulting values of the fitted parameters are $n_o = 5400 \pm 4000$ and $E_d = 4.6 \pm 0.5$ eV, which is in reasonable agreement with the calculated values $E_d = 5.3$ eV (Catlow 1977) and $E_d = 5.1$ eV (Harding et.al. 1980). The fitted curve is shown as a chain line in Fig. 4.3(a). The data for ThO_2 are not sufficiently accurate to fit E_d: the chain line shown in Fig. 4.3(b) was obtained by scaling the value of E_d for UO_2 using the ratio of the melting temperatures of the two compounds, giving $E_d = 5.3$ eV and $n_o = 12800 \pm 5600$ for ThO_2.

The onset of anion disorder is accompanied by a greater rate

of increase of the lattice constant and of the isotropic thermal vibration parameters with increasing temperature. The harmonic vibration root-mean-square displacement $\langle U_o^2 \rangle^{\frac{1}{2}}$ of the oxygen ions, which may be deduced from B_o through equation (3.20), rises to 0.58Å for the regular sites and to ~ 0.7Å for the interstitial sites in UO_2 at 2900K. These values represent a considerable fraction of the separation between regular oxygen sites of ~ 2.9Å. It is interesting to note that if the B_i data for UO_2 and ThO_2 are plotted as a function of (T/T_m) it is found that they fall quite close to common curves for the oxygen ions and for the cations (Fig. 4.8). This indicates that both materials have similar ionic potentials and hence similar lattice dynamics. This similarity will be investigated more thoroughly in the next chapter.

Knowledge of the properties of UO_2 on a microscopic scale, as afforded by neutron scattering data, enables us to calculate macroscopic physical quantities. Browning et.al.(1983) have calculated individual contributions to the enthalpy of UO_2 using existing data, in order to quantify its anomalous enthalpy at high temperatures. The present diffraction data enable us to recalculate the enthalpy contribution from anharmonic oxygen vibrations, which Hyland and Stoneham (1981) and Browning et.al.(1983) calculated from diffraction data up to 1400K (Willis 1963). The enthalpy H = U + D, where U is the total internal energy and D is the contribution from crystal dilation. The contribution to U from anharmonic oxygen vibrations is

$$U_{anh} = \frac{\beta_o^2}{\alpha_o^3} k_B R \left[T^2 - (298)^2 \right] \qquad (4.20)$$

$$= 66.4 \times \frac{a_o^6 C_{123}^2}{B_o^3} \frac{\left[T^2 - (298)^2 \right]}{T} \; J_{mol}^{-1}$$

where R is the molar gas constant and the units of a_o and B_o are Å and

A_o^2 respectively (Hyland and Stoneham 1981). U_{anh} has been calculated from the smoothed variation of a_o, B_o and C_{123}^o data for UO_2, the results of which are given in Table 4.10 together with the extrapolated values of Browning et.al.(1983). The results are in reasonable agreement up to 1200K, but at higher temperatures the experimental values are much smaller than the extrapolated values. This discrepancy is mainly due to the assumption of Browning et.al. that α_o and β_o do not vary with temperature, which does not hold at high temperatures as may be seen from Figs. 4.6 and 4.7. Nevertheless, this does not affect the analysis of Browning et.al. seriously since U_{anh} is the smallest contribution to the enthalpy, and is an order of magnitude less than the contributions from harmonic phonons and dilation effects.

We conclude therefore that analogous anion Frenkel disorder occurs in UO_2 and ThO_2 above 2000K. The time-averaged ionic distribution may be modelled satisfactorily by a 3:1:2 defect cluster comprising one interstitial ion and two relaxed ions, similar to those observed in the fast-ion region of the fluorite halides PbF_2, CaF_2 and $SrCl_2$. The temperature variations of n_d, a_o and the thermal parameters B_i and C_{123}^o are also very similar to those observed in the fluorite halides. The overall similarity between the results for the fluorite oxides, UO_2 and ThO_2, and for the fluorite halides indicates that the high temperature disorder is of an analogous nature in both sets of compounds, despite the large difference in melting temperatures. Further investigations of the disordered state of UO_2, through measurements of its lattice dynamical properties and coherent QES, are reported in chapters 6 and 7 respectively.

TABLE 4.10

CONTRIBUTION TO THE TOTAL INTERNAL ENERGY OF UO_2

FROM ANHARMONIC VIBRATIONS OF THE OXYGEN IONS

T(K)	a_o (Å)	B_o (Å^2)	$C^o_{123} \times 10^3$	U_{anh} (kJmol^{-1})	
				This Work	Browning et.al.
600	5.487	0.85	0.39	203	140
800	5.498	1.09	0.59	340	284
1000	5.510	1.45	0.92	450	469
1200	5.521	1.81	1.26	568	696
1400	5.534	2.19	1.86	881	964
1600	5.548	2.64	2.45	1011	1273
1800	5.561	3.19	3.23	1137	1623
2000	5.578	3.80	4.25	1318	2060
2200	5.599	4.56	5.59	1484	2493
2400	5.623	5.35	7.16	1687	2967
2600	5.647	6.36	9.41	1928	3482
2800	5.675	8.00	12.72	1964	4038

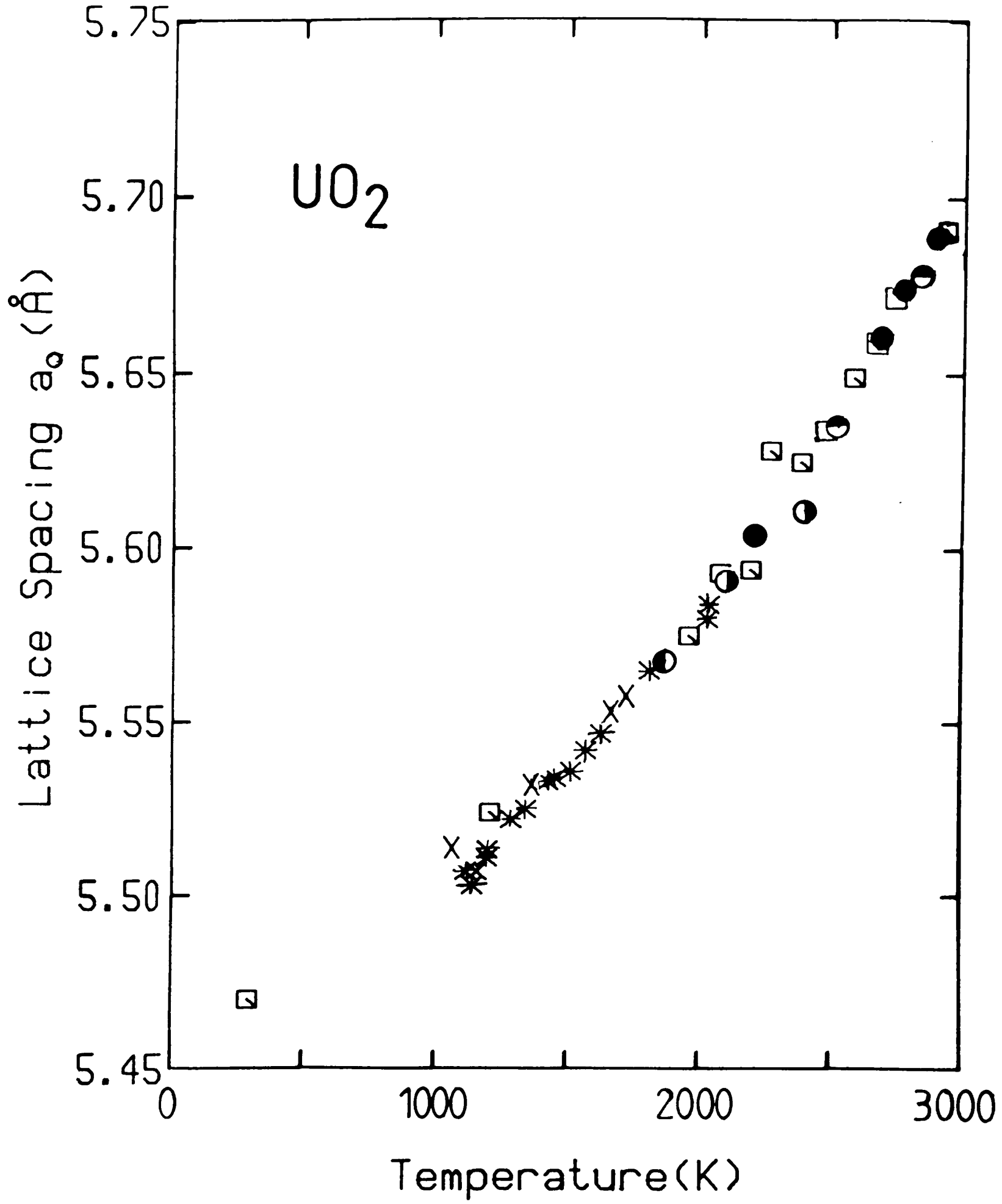

Fig. 4.1 Temperature variation of the lattice spacing of UO_2 .

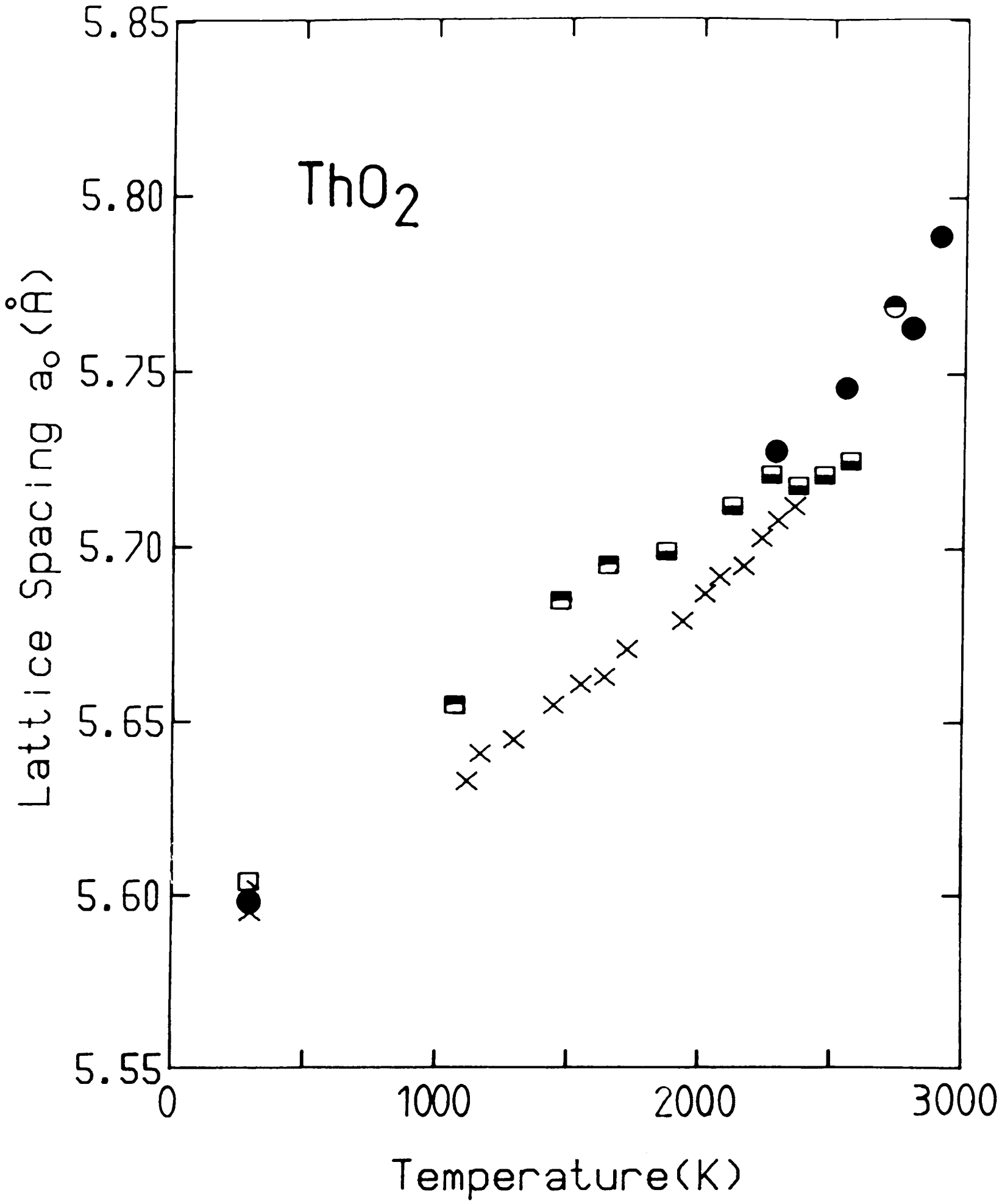

Fig. 4.2 Temperature variation of the lattice spacing of ThO_2 .

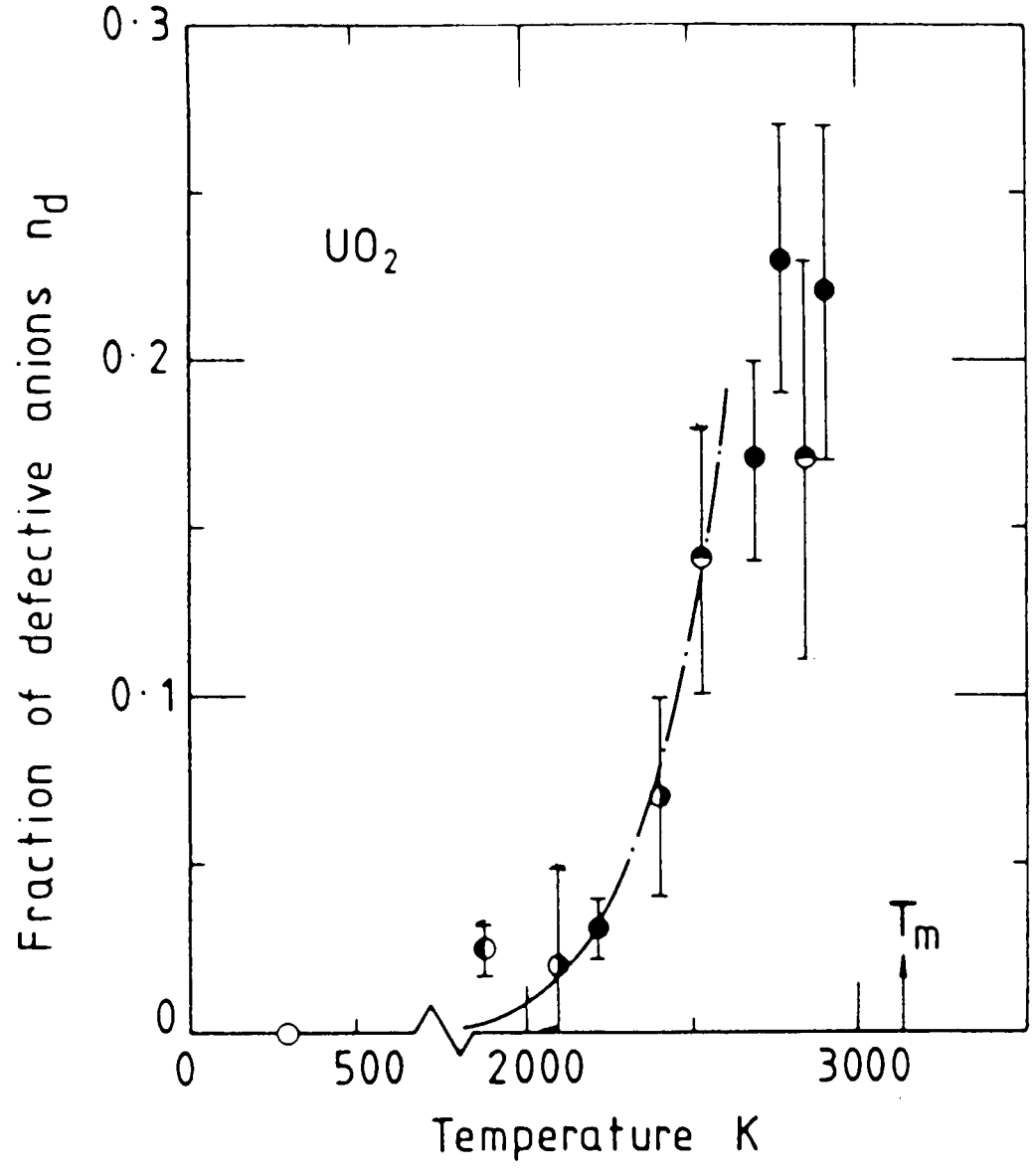

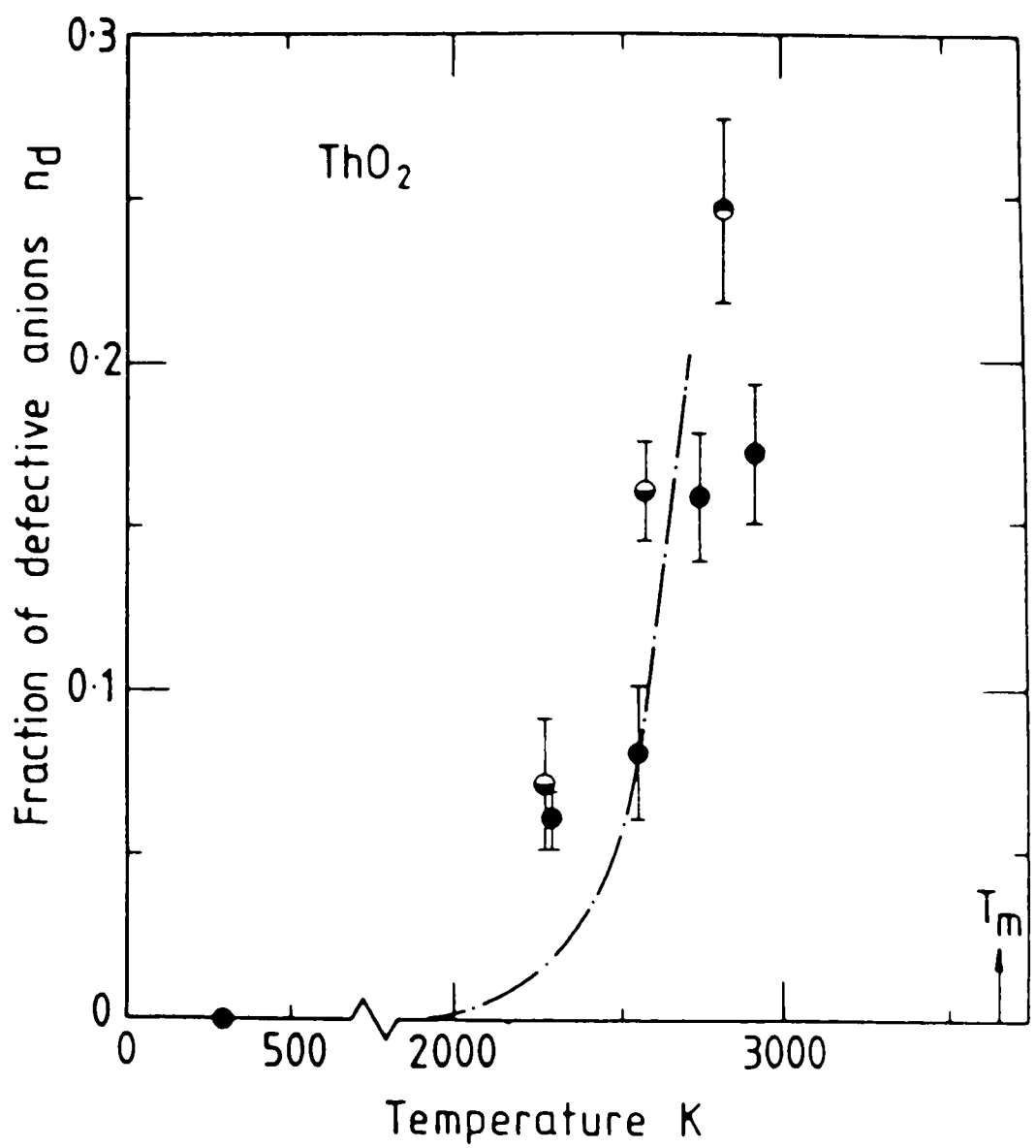

Fig. 4.3 Temperature variation of the total fraction of defective anions n_d in UO_2 and ThO_2. Chain line represents a fitted function of the form $n_d = n_0 \exp(-E_F/2k_BT)$. (Symbols are as listed in Figs. 4.1 and 4.2)

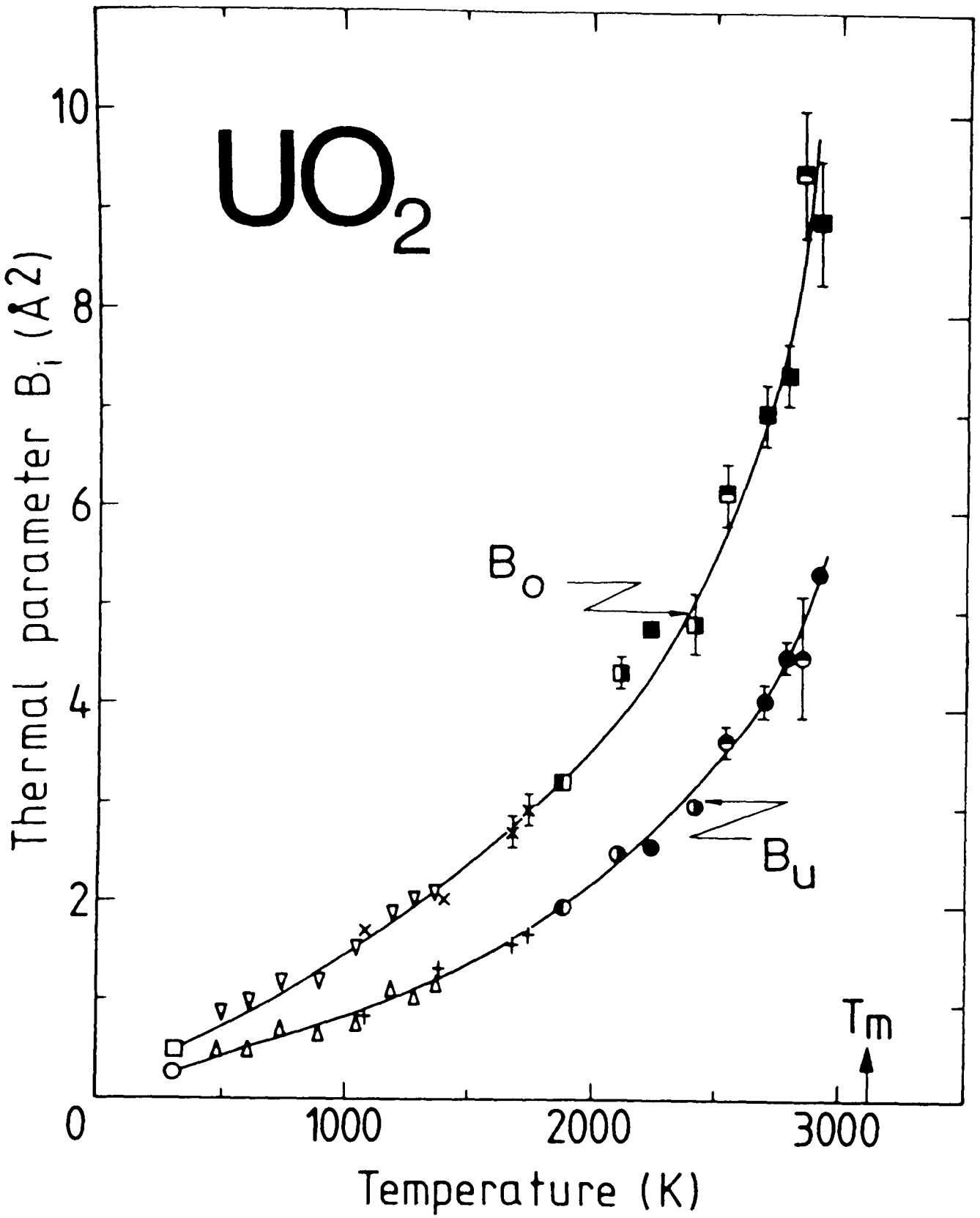

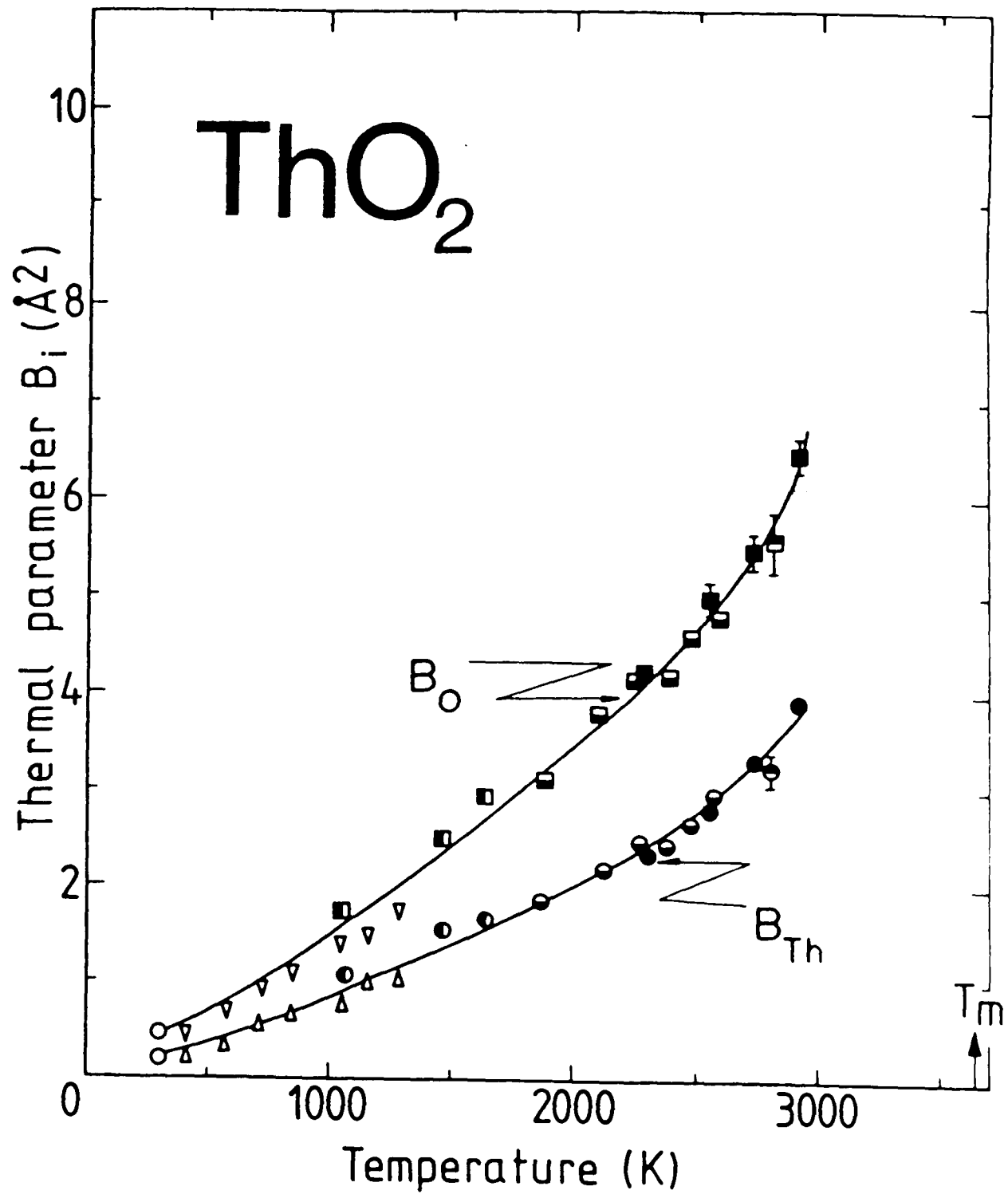

Fig. 4.4 Temperature variation of the isotropic thermal parameters B_i for UO_2 and ThO_2. (Symbols as in Figs. 4.1 and 4.2)

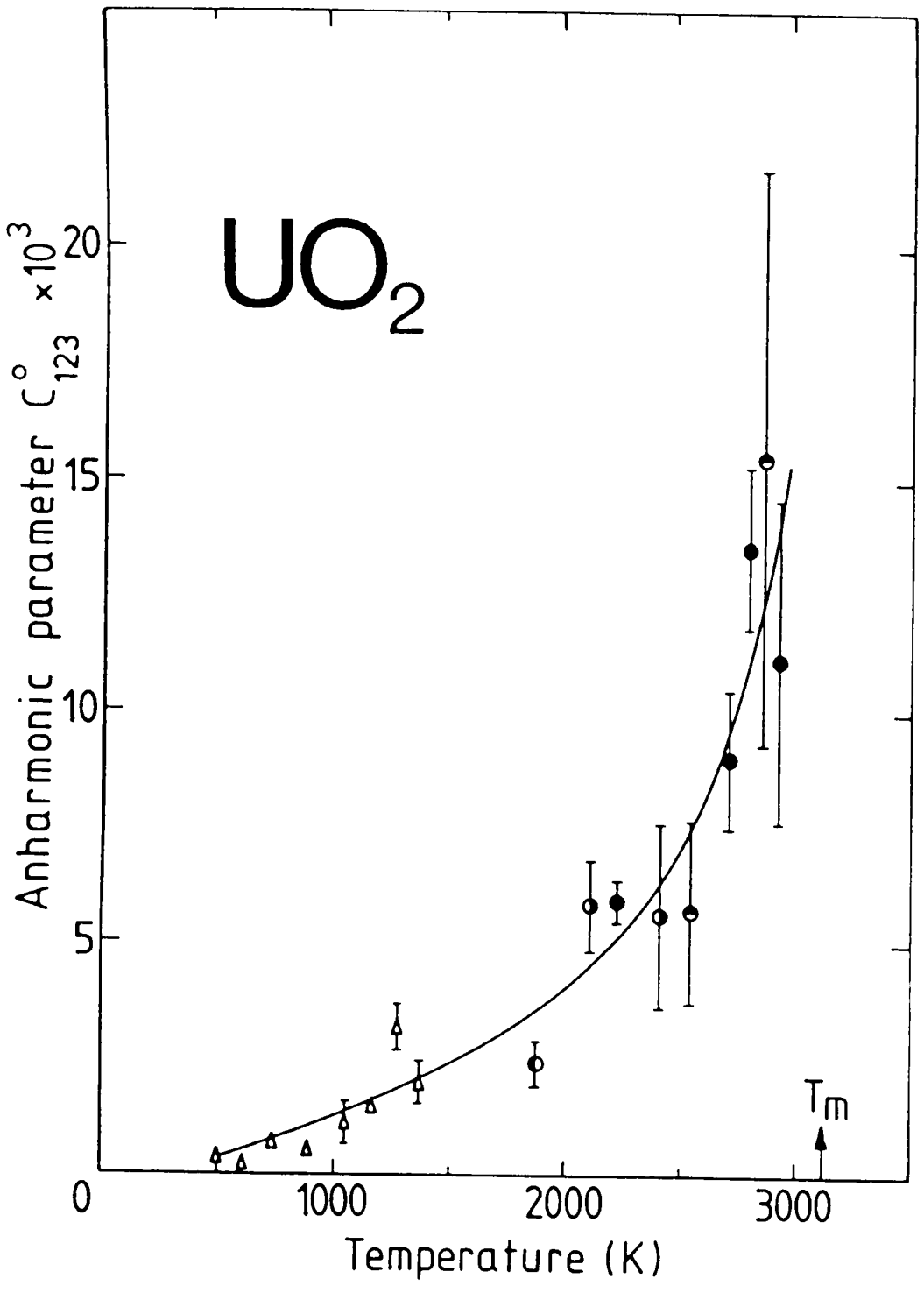

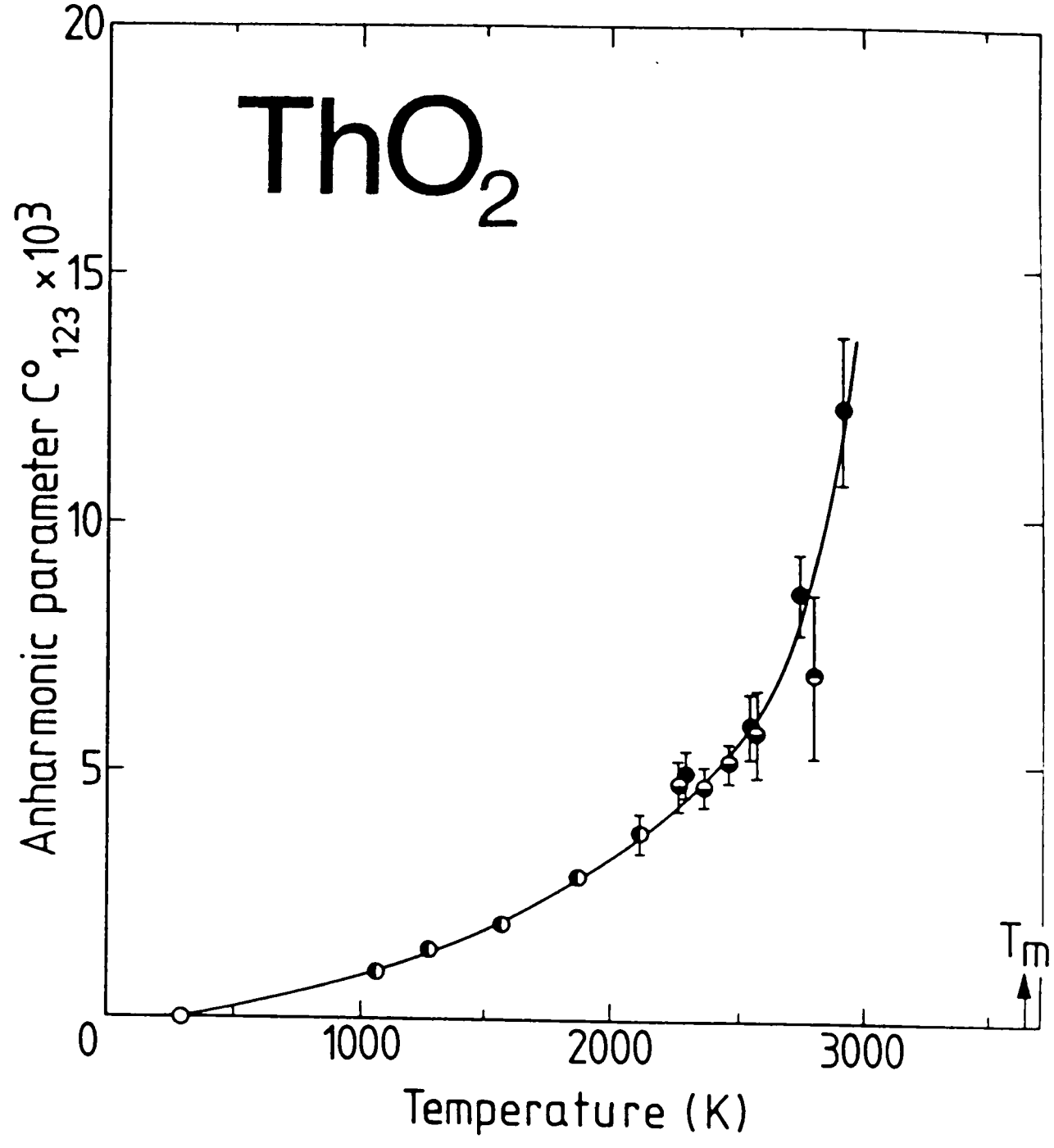

Fig. 4.5 Temperature variation of the anisotropic thermal parameter C^{O}_{123} for UO_2 and ThO_2. (Symbols as in Figs. 4.1 and 4.2)

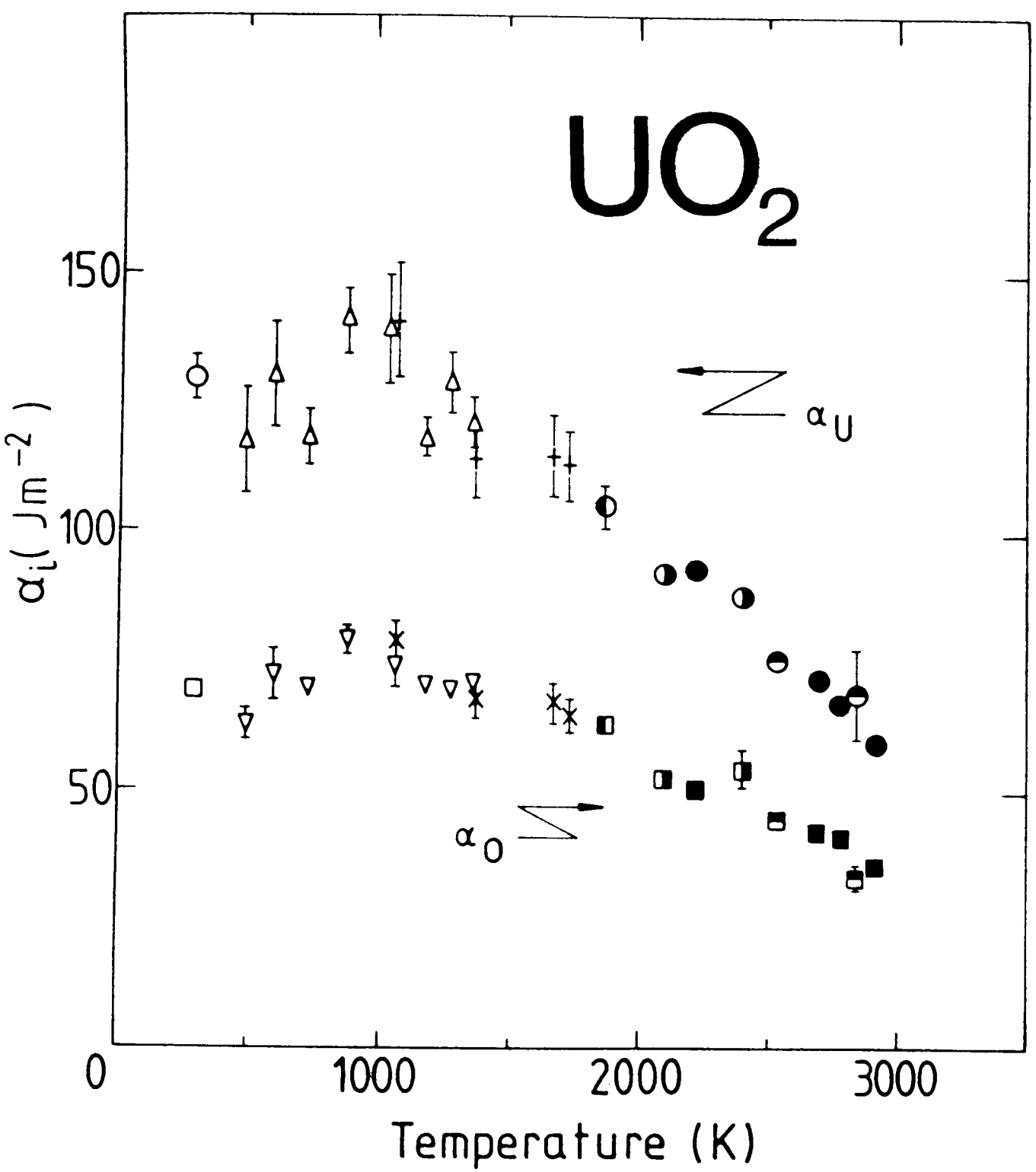

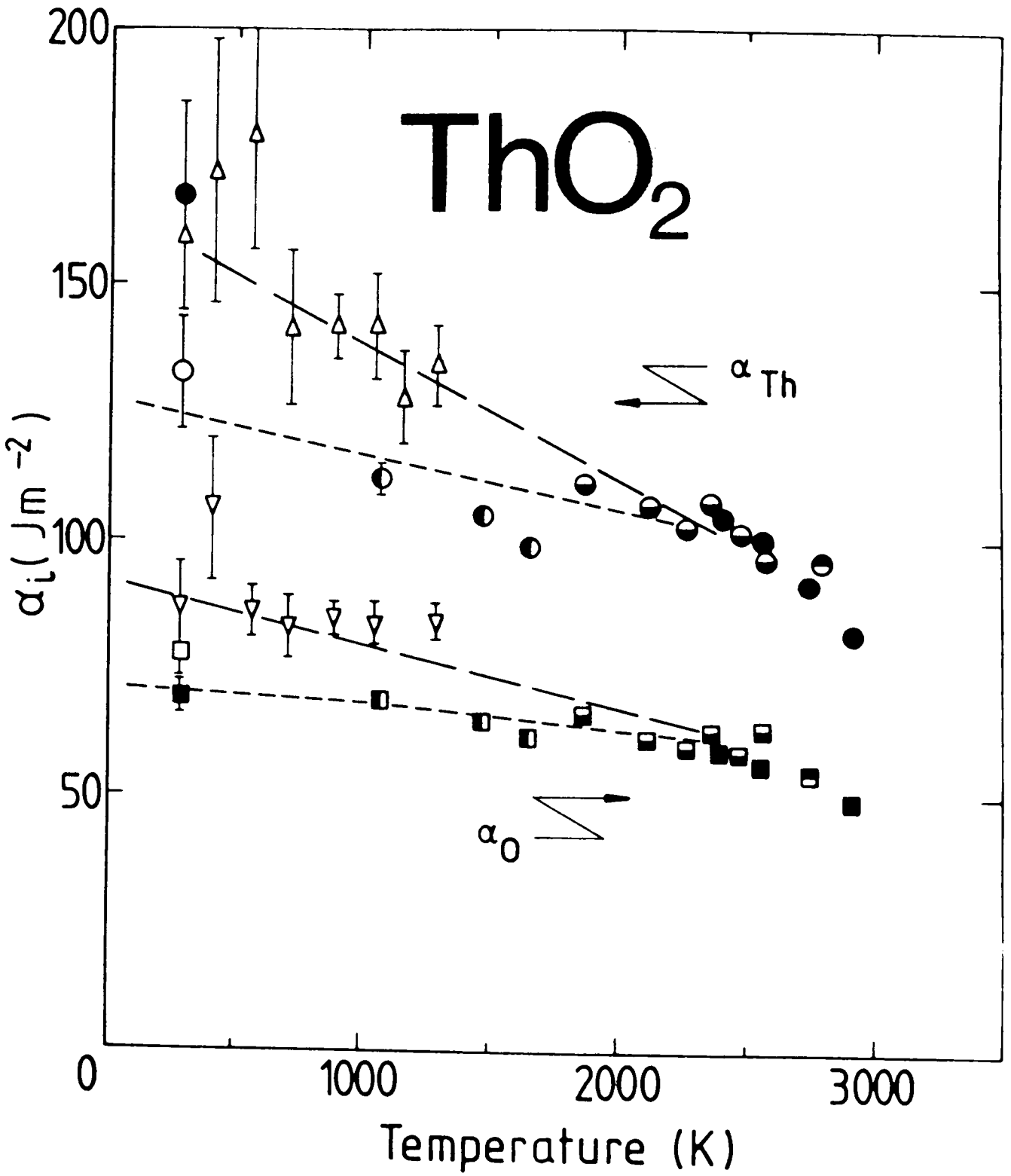

Fig. 4.6 Temperature variation of the one particle potential parameters α_i for UO_2 and ThO_2. (Symbols as in Figs. 4.1 and 4.2)

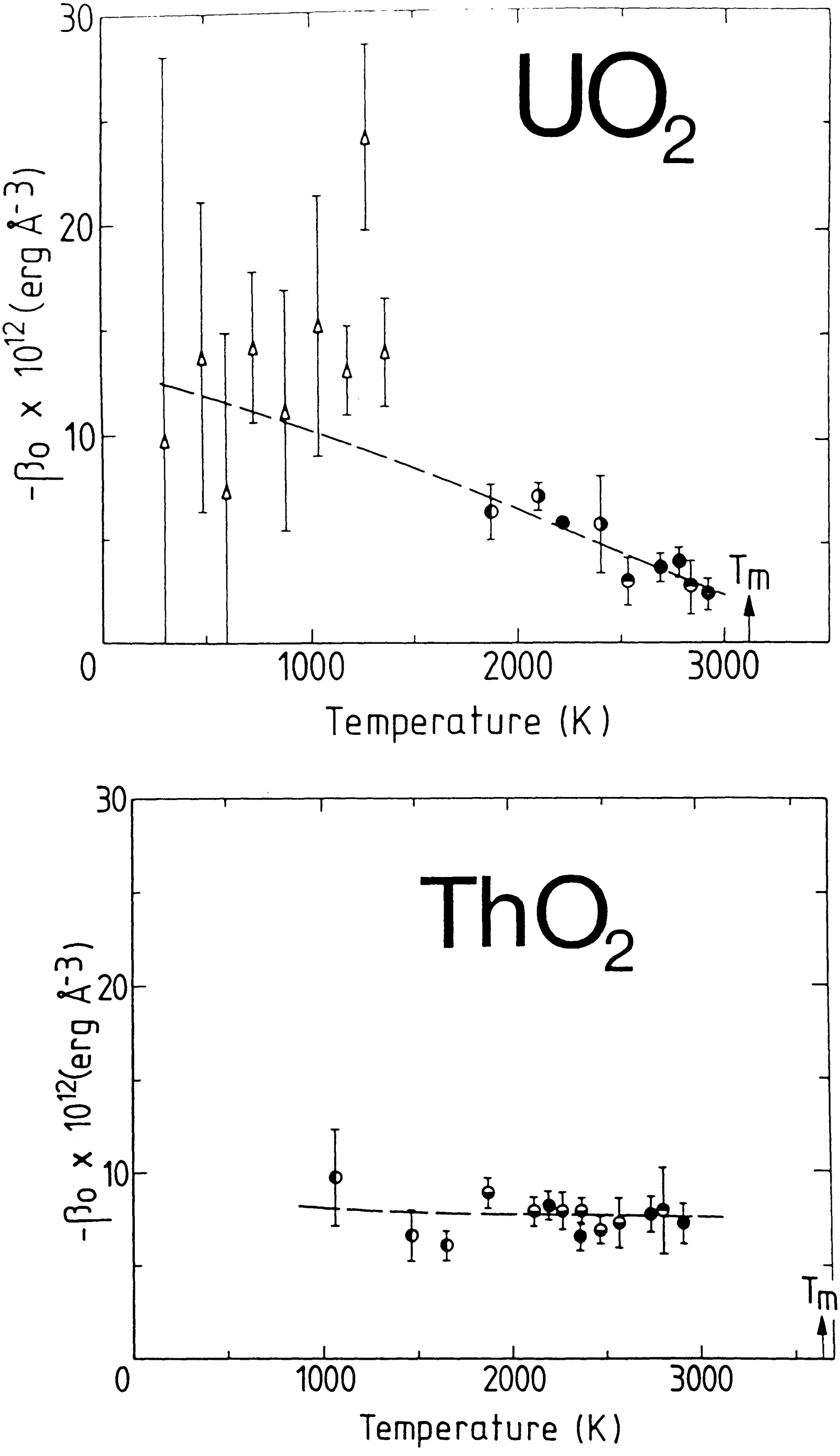

Fig. 4.7 Temperature variation of one particle potential parameter β_i.

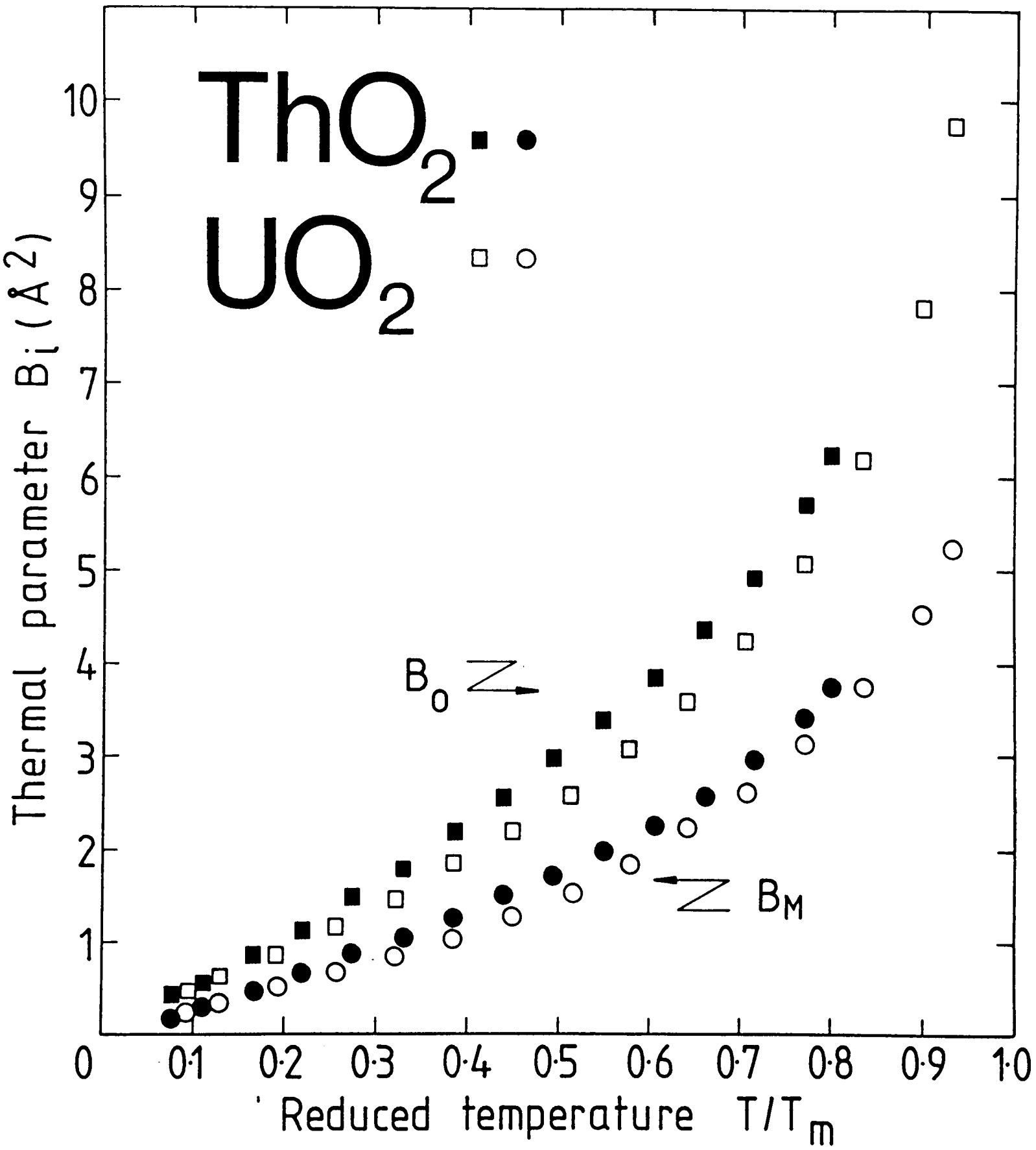

Fig. 4.8 A comparison of the isotropic thermal parameters for UO_2 and ThO_2 as a function of reduced temperature T/T_m

CHAPTER 5

THE LATTICE DYNAMICS OF ThO_2

5.1 INTRODUCTION

In the previous chapter we reported an investigation of the high temperature structure of UO_2 and ThO_2. We concluded that similar anion lattice disorder develops in both compounds, which also resembles that observed in the fluorite halides. Indeed, such a correspondence between the two oxides should be expected because of the similarity between their cation masses and charges, giving rise to comparable interatomic potentials. The most exacting comparison between these microscopic potentials is that afforded by the phonon dispersion relations. Techniques such as ultrasonics, infra-red absorption and Raman scattering give information on the long wavelength $\underset{\sim}{q} \approx 0$ phonons, but inelastic neutron scattering enables the measurement of the dispersion relation throughout the Brillouin zone. In this chapter, we describe the measurement of the complete phonon dispersion curves for ThO_2 at room temperature and compare the results with those for UO_2 (Dolling et.al 1965) and the fluorite halides.

5.2 EXPERIMENTAL PROCEDURE

All the measurements were performed at room temperature on a $\sim 1 cm^3$ single crystal of ThO_2 (sample TL1) using the PLUTO TAS at Harwell. The crystal was oriented with its $\langle 1\bar{1}0 \rangle$ axis vertical, except for the investigation of some branches which could only be observed in the (001) plane. Incident neutron energies ranging between 10 and 130 meV were obtained using pyrolytic graphite (002) and aluminium (111), (002) and (220) monochromator crystal planes. In order to strike a balance between intensity and resolution, the

graphite (002) plane was used typically up to 35 meV, Al (111) up to 60 meV and the Al (220) plane above 70 meV. The graphite (002) plane was used as the analyser for all the measurements. The scans were made in energy loss, keeping $\underset{\sim}{k}_i$ fixed. Collimation angles of 40' and 30' were normally used before and after the sample and 60' in the other two spectrometer arms. Whenever appropriate, a tuned graphite filter was inserted in the incident beam in order to minimise higher order wavelength contamination. If the value of E_i was unsuitable for use of the filter, care was taken to avoid spurious peaks from higher order contamination, which may be serious for $\hbar\omega > {}^5/_9\, E_i$.

The phonon energies were determined in the three principal symmetry directions, mainly using constant $\underset{\sim}{Q}$ scans. However, constant energy scans were used for steeply sloping branches, such as the longitudinal acoustic modes. Counting times varied from two minutes per point for low energy acoustic modes to about 40 minutes per point for high energy optic modes. Typical scans at low and high energies are shown in Fig 5.1, which illustrate the broadening resolution for larger incident energies (equation 3.37) and the ω^{-1} - dependence of the phonon scattering cross-section (equation 3.23).

The phonons were measured at a reciprocal lattice vector $\underset{\sim}{\tau}$, for which the dynamical structure factor $G(\underset{\sim}{Q})$ (equation 3.24) is a maximum. As a result of the $\underset{\sim}{Q}.\underset{\sim}{\xi}_{Kj}(q)$ term, longitudinal modes were measured with $\underset{\sim}{q} \parallel \underset{\sim}{Q}$, and transverse modes with $\underset{\sim}{q} \perp \underset{\sim}{Q}$. For phonons with small wavevectors, $G(\underset{\sim}{Q})$ tends to the elastic structure factor $F(\underset{\sim}{Q})$, evaluated for the fluorites in equation (4.16). Consequently, acoustic modes, in which the ions vibrate in phase, were measured around reciprocal lattice points for which (h+k+l) = 4n, where n is an integer. Optic modes, for which the cations and anions vibrate in

antiphase, were measured around (4n ± 2) lattice points, and the Raman mode, where the cation is stationary and the anions vibrate in anti-phase, were measured around (4n ± 1) lattice points. It should also be noted that the cross-section is approximately proportional to $Q^2\exp(-2W_K)$, and consequently, at low temperatures, phonons should be measured at the largest suitable scattering vector.

The low wavevector acoustic modes were corrected for resolution effects using two Harwell programs. RESCAL (written by M T Hutchings and M W Stringfellow) was used to calculate the resolution function from the spectrometer parameters, such as collimations and crystal mosaic spreads. Effective values of these parameters were determined by comparing calculated values of Bragg peak widths and incoherent vanadium scan widths with the observed values and optimising the overall agreement. The optimised spectrometer parameters were input into a second program RESFLD (written by M T Hutchings and E J Samuelsen), which calculates the scan profile for a sharp excitation and a defined dispersion relation. The shift of the calculated peak, from the position defined by the dispersion relation, was then applied to the observed data. The shifts of the transverse modes were small, but those of the longitudinal modes were appreciable because of the tighter curvature of the dispersion curve. Resolution shifts were insignificant for wavevectors greater than 0.2 reciprocal lattice units (r.l.u.) and for optic modes.

The longitudinal optic phonon was not observed, despite several attempts using the conventional analyser technique and also using a cooled beryllium filter in the scattered beam, with and without an analyser crystal. It therefore appears that a spectrometer having a larger flux of high energy neutrons, such as IN1 or IN8 at ILL Grenoble, is required for this highest energy mode ($\hbar\omega \sim 70$ meV). The observed

phonon energies, corrected for resolution shifts, are tabulated in Appendix A.4 and illustrated in Fig. 5.2.

5.3 MODELS OF PHONON DISPERSION

The most appropriate treatment of the lattice dynamics of ionic solids is that given by the Born-Von Karman formalism (e.g. Born and Huang 1954), a brief outline of which is given here together with its application to two models. The three general assumptions, on which the theory is based, are the following.

1. Cyclic Boundary Conditions

In order to avoid surface effects and yet consider a finite number of atoms, an infinite crystal is divided into identical macrocrystals, all having N atoms. The cyclic boundary condition requires that equivalent atoms on opposite faces of a macrocrystal move in exactly the same way, so that the atomic displacements are periodic with the dimensions of the macrocrystal.

2. The Adiabatic Approximation

Electrons are assumed to have negligible mass, so that the nuclear motion may be considered independently of the electronic motion. (In effect, this means that the electrons follow the nuclei instantaneously.) Its validity depends on the vibrational frequencies being much smaller than electronic transition frequencies.

3. The Harmonic Approximation

For small atomic displacements the crystal potential energy Φ may be expressed as a Taylor expansion of the displacements.

$$\Phi = \Phi_o + \Phi_1 + \Phi_2 + \Phi_3 + \ldots\ldots \qquad (5.1)$$

Φ_o is the static potential energy for all atoms in their equilibrium position.

$$\Phi_1 = \sum_{l\kappa\alpha} \frac{\partial \Phi}{\partial U_\alpha}(l\kappa)\, U_\alpha(l\kappa) \qquad (5.2)$$

$$\Phi_2 = \tfrac{1}{2} \sum_{l\kappa\alpha} \sum_{l'\kappa'\beta} \phi_{\alpha\beta}(l\kappa; l'\kappa')\, U_\alpha(l\kappa)\, U_\beta(l'\kappa') \qquad (5.3)$$

$$\text{with} \quad \phi_{\alpha\beta}(l\kappa; l'\kappa') = \frac{\partial^2 \Phi}{\partial U_\alpha(l\kappa)\partial U_\beta(l'\kappa')} \qquad (5.4)$$

In the harmonic approximation, the higher-order terms, Φ_3, ..., are neglected. $-\phi_{\alpha\beta}(l\kappa; l'\kappa')$ is the force in direction α on atom $(l\kappa)$, the κ'th atom in the l'th unit cell, when atom $(l'\kappa')$ is moved unit distance in the direction β. Clearly Φ_1 must be zero for an equilibrium configuration, and hence the potential energy may be expressed as a quadratic function of the atomic displacements. The equation of motion is then

$$m_\kappa \ddot{U}_\alpha(l\kappa) = -\frac{\partial \Phi_2}{\partial U_\alpha}(l\kappa) = -\sum_{l'\kappa'\beta} \phi_{\alpha\beta}(l\kappa; l'\kappa')\, U_\beta(l'\kappa') \qquad (5.5)$$

where m_κ is the mass of atom κ. A solution is

$$\underset{\sim}{U}(l\kappa) = \sum_{\underset{\sim}{q}} (m_\kappa)^{-\frac{1}{2}}\, \xi(\kappa, \underset{\sim}{q}) \exp\left\{ i\left[\underset{\sim}{q}.\underset{\sim}{r}(l\kappa) - \omega(\underset{\sim}{q})t \right] \right\} \qquad (5.6)$$

which is a summation over plane waves of wavevector $\underset{\sim}{q}$, frequency $\omega(q)$ and polarisation vector $\xi(\kappa, \underset{\sim}{q})$. Substituting (5.6) into (5.5), a set of linear equations is obtained

$$\omega^2(\underset{\sim}{q})\, \xi_\alpha(\kappa, \underset{\sim}{q}) = \sum_{\kappa'\beta} D_{\alpha\beta}(\kappa\kappa', q)\, \xi_\beta(\kappa', q) \quad , \qquad (5.7)$$

where the dynamical matrix D is

$$D_{\alpha\beta}(\kappa\kappa', q) = (m_\kappa m_{\kappa'})^{-\frac{1}{2}} \sum_{l'} \phi_{\alpha\beta}(l\kappa; l'\kappa') \times \exp\left\{ i\underset{\sim}{q}.\left[\underset{\sim}{r}(l\kappa) - \underset{\sim}{r}(l'\kappa') \right] \right\} \qquad (5.8)$$

Equation (5.7) may be solved if

$$\left| D_{\alpha\beta}(\kappa\kappa', \underset{\sim}{q}) - \delta_{\alpha\beta}\, \delta_{\kappa\kappa'}\, \omega^2(\underset{\sim}{q}) \right| = 0 \qquad (5.9)$$

The solution of (5.9) gives the 3s eigenvalues $\omega_j^2(\underset{\sim}{q})$ and eigenvectors $\underset{\sim}{e}_j(\underset{\sim}{q})$, where s is the number of atoms in the unit cell and j = 1, ..., 3s

is an index labelling each branch of the dispersion relation $\omega_j(q)$. For each j, the s polarisation vectors $\underset{\sim}{\xi}_j(K, \underset{\sim}{q})$ are components of the corresponding eigenvector $\underset{\sim}{e}_j(\underset{\sim}{q})$.

5.3.1 RIGID ION MODEL

The energy of a non-metallic crystal may be divided into two parts - one from long-range Coulomb interactions, ϕ^C, and the other, ϕ^R, from an overlap potential which results in a short-range force. Each element of the dynamical matrix may similarly be divided into a short-range component D^R and a Coulombic component D^C through equation (5.8). In the rigid ion model of Kellermann (1940), the forces are considered to be between point charges, neglecting polarisability of the ion. From equation (5.8),

$$D^R_{\alpha\beta}(\kappa\kappa',q) = (m_\kappa m_{\kappa'})^{-\frac{1}{2}} \sum_{l'} \phi^R_{\alpha\beta}(l\kappa;l'\kappa') \times \exp i\underset{\sim}{q}.[\underset{\sim}{r}(l\kappa) - \underset{\sim}{r}(l'\kappa')] \qquad (5.10)$$

and

$$D^C_{\alpha\beta}(\kappa\kappa',\underset{\sim}{q}) = (m_\kappa m_{\kappa'})^{-\frac{1}{2}} Z_\kappa C(\kappa\kappa',q) Z_{\kappa'} \qquad (5.11)$$

with $$C(\kappa\kappa',q) = \sum_l \frac{\partial^2}{\partial\underset{\sim}{r}(\kappa)\,\partial\underset{\sim}{r}(\kappa')} \left\{ \frac{e^2}{r(l\kappa')-r(\kappa)} \right\} \times \exp i\underset{\sim}{q}.[\underset{\sim}{r}(l\kappa') - \underset{\sim}{r}(\kappa)] \qquad (5.12)$$

Evaluation of the Coulomb coefficients $C(\kappa\kappa',q)$ requires the summation of a slowly coverging series, which, once calculated for a given structure, may be used in all subsequent calculations.

Equations (5.10) to (5.12) may be inserted into equation (5.7), giving the equation of motion for a rigid ion crystal,

$$m\omega_j^2(\underset{\sim}{q})\ \xi_{j\alpha}(\underset{\sim}{\kappa},q) = \sum_{\kappa',\beta} [R_{\alpha\beta}(\kappa\kappa',\underset{\sim}{q}) + Z_\kappa C(\kappa\kappa',\underset{\sim}{q}) Z_{\kappa'}]\, \xi_{j\beta}(\kappa',q) \qquad (5.13),$$

where the short-range matrix R is

$$R_{\alpha\beta}(\kappa\kappa',q) = (m_\kappa m_{\kappa'})^{\frac{1}{2}} D^R_{\alpha\beta}(\kappa\kappa',q) \qquad (5.14)$$

Equation (5.13) may be expressed more succinctly in matrix notation as

$$\underset{\approx}{m}\,\underset{\approx}{\omega}^2 e = (\underset{\approx}{R} + \underset{\approx\approx\approx}{ZCZ})e \qquad (5.15)$$

where $\underset{\approx}{m}$ and $\underset{\approx}{Z}$ are diagonal matrices containing the ionic masses and charges respectively.

The rigid ion model has been used successfully to explain many properties of simple ionic crystals, such as elastic constants and cohesive energies, but it has proved inadequate for the understanding of dielectric properties and optic phonon frequencies (e.g. Dolling et.al. 1965). Its main deficiency is its representation of the electrostatic field as arising only from point charges, neglecting polarisation effects.

5.3.2 THE SHELL MODEL

A simple model, which takes into account the distortions of ions due to lattice vibrations, originally proposed by Dick and Overhauser (1958) and later applied to lattice dynamical calculations (Woods et.al. 1960) is now introduced. Each ion κ is assumed to consist of a rigid core, having a charge $X_\kappa e$, and a polarisable shell of outer electrons, having a charge $Y_\kappa e$, the total ionic charge being $Z_\kappa e = (X_\kappa + Y_\kappa)e$. The core and shell are bound together by an isotropic force constant k. Additional short range force constant matrices T and S, which are analogous to the R matrix of equation (5.14), must be introduced. R represents the forces between ion κ and ion κ', T those between core κ and shell κ' and S those between shell κ and shell κ' (Fig. 5.3(a)). Equations of motion may again be expressed for the nuclear displacement $\underset{\sim}{U}$ and the relative displacement of the shell with respect to the core, $\underset{\sim}{W}$:

$$\omega^2_{mU} = (R + ZCZ)U + (T + ZCY)W$$

$$O = (\tilde{T} + YCZ)U + (\delta + YCY)W \qquad (5.16)$$

where $\delta_{\alpha\beta}(\kappa\kappa') = S_{\alpha\beta}(\kappa\kappa') + \delta_{\alpha\beta}\,\delta_{\kappa\kappa'}\{k_\kappa + T_{\alpha\alpha}(\kappa\kappa')_{q=o} - S_{\alpha\alpha}(\kappa\kappa')_{q=o}\}$ (5.17)

The left-hand side of the second equation is zero because of the zero electron mass implied by the adiabatic condition. W may be eliminated between the equations of (5.16) giving

$$\omega^2_{mU} = MU \qquad (5.18)$$

with $M = (R + ZCZ) - (T + ZCY)(\delta + YCY)^{-1}(\tilde{T} + YCZ)$ (5.19)

In order to reduce the number of short-range parameters, the short-range forces may be assumed to act only through the shells, implying that R = T = S (Woods et.al. 1960). The two resulting short-range parameters for each ion are the electrical polarisability α and the short-range mechanical polarisability d, which may be related to the above expressions by

$$\alpha_\kappa = \frac{Y_\kappa^2}{k_\kappa + T_\kappa} \quad \text{and} \quad d_\kappa = -\frac{T_\kappa Y_\kappa |e|}{k_\kappa + T_\kappa} \quad . \qquad (5.20)$$

5.4 DATA ANALYSIS

The application of the rigid ion and shell models to the fluorite structure has been discussed by Axe (1965), Dolling et.al. (1965) and Elcombe and Pryor (1970). The short-range matrices R, T and S are represented by two parameters, A_i and B_i, for the i'th neighbouring pairs, where

$$A_i = \frac{v}{e^2}\frac{\partial^2 \Phi^R}{\partial r^2} \quad , \quad B_i = \frac{v}{e^2}\frac{1}{r}\frac{\partial \Phi^R}{\partial r} \qquad (5.21)$$

and $v = a_o^3/4$ is the volume of the primitive unit cell. Up to four pairs

of neighbours are included: i = 1, (Th - O_1) at a separation of $a_o \cdot \sqrt{3}/4$; i = 2, (O_1 - O_2) at $a_o/2$; i = 3, (Th - Th) at $a_o/\sqrt{2}$; and i = 4, (O_1 - O_1) at $a_o/\sqrt{2}$ (Fig. 5.3(b)). The shell model introduces four additional polarisability parameters α_{Th}, α_o, d_{Th} and d_o. The exact expressions for the dependence of the short-range matrices, elastic constants and dielectric constant ϵ_∞ on the above parameters may be found in the appendix of Elcombe and Pryor (1970).

These variable parameters were optimised by fitting to the experimentally observed phonon frequencies, using the SHELL program written by M H Dickens and M W Wiltshire. This incorporates the Harwell library least-squares fitting subroutines VA02A and SV01A. The phonon frequencies and eigenvectors were calculated by solving the equations of motion of the ions using the Harwell matrix-diagonalisation routine EA06C. The program minimises the quantity

$$\chi^2 = \frac{1}{(n - p)} \sum_{i=1}^{n} \left(\frac{\omega^i_{obs} - \omega^i_{calc}}{\Delta\omega^i_{obs}} \right)^2 \qquad (5.22)$$

where n is the number of data points, p the number of parameters, ω^i_{obs} and ω^i_{calc} the observed and calculated phonon frequencies and $\Delta\omega^i_{obs}$ the estimated accuracy of the observation i. Each data point thus carries relative weight $(\Delta\omega_{obs})^{-2}$ in the fit.

The phonon groups were identified with a particular branch by comparing their frequencies, polarisation and intensities for unambiguous cases. At a given wavevector an observed phonon was associated with a calculated branch by labelling the latter with an index, m, denoting its position in order of increasing energy. Initial fits involved easily identified modes only, which then enabled other groups to be identified and included iteratively. Values for the three

zone-centre modes, as determined by second order Raman scattering (Ishigame and Kojima 1976), were included in the fit in view of their higher accuracy and of the absence of neutron longitudinal optic phonon measurements. Phonon frequencies were calculated at intervals of 0.05 r.l.u. across the zone, therefore the frequencies of phonons observed in constant energy scans were interpolated to the nearest suitable $\underset{\sim}{q}$ value. The program was checked by reproducing the dispersion curves of CaF_2 and UO_2 from the published shell model parameters (Elcombe and Pryor 1970 , Dolling et.al. 1965). (The parameters for UO_2 were corrected, as discussed in the following section.)

Two rigid ion models (1 and 2) and two shell models (3 and 4), all involving short-range interactions out to the fourth nearest neighbours, were fitted to the data. In models 1 and 3, the cation charge Z = 4 was fixed, and in models 2 and 4, Z was treated as a variable parameter. The results of the fits are given in Table 5.1, and the physical quantities which may be derived from the model parameters are compared with direct experimental measurements in Table 5.2.

5.5 DISCUSSION

The results of models 1 and 2 show that the rigid ion model cannot account for the data, particularly optic mode energies, unless the cation charge is allowed to vary. The introduction of polarisability, in models 3 and 4, improves the fit significantly. Model 4 gives a value of Z close of its normal ionic value, used in model 3. The values of the dielectric and elastic constants derived from the fitted parameters (Table 5.2) are in fair agreement with those obtained by direct measurement (Axe and Pettit 1966, Macedo et.al. 1964). However, it is unwise to attach much physical significance to the fitted values of the model parameters - their usefulness is limited to their accurate

TABLE 5.1

RIGID ION AND SHELL MODEL PARAMETERS FOR LEAST SQUARES ANALYSIS OF ThO_2 PHONON DISPERSION DATA

Fitted Parameters	Model 1	2	3	4
A_1 (e^2/v)	42.0(40)	15.90(7)	62.60(12)	60.60(13)
B_1 (e^2/v)	-4.7(22)	1.30(4)	-12.50(4)	-12.20(4)
A_2 (e^2/v)	-7.3(19)	1.90(2)	-5.40(5)	-4.70(4)
B_2 (e^2/v)	3.0(10)	0.90(1)	1.40(2)	1.50(1)
A_3 (e^2/v)	10.9(103)	10.10(10)	1.00(8)	1.20(5)
B_3 (e^2/v)	-2.9(22)	-2.50(2)	2.00(2)	2.30(2)
A_4 (e^2/v)	-2.8(17)	-3.00(1)	-0.90(2)	-1.10(1)
B_4 (e^2/v)	0.4(6)	-0.25(5)	0.16(7)	0.17(7)
α_{Th} ($\AA^3$)	-	-	4.93(8)	4.56(10)
α_O ($\AA^3$)	-	-	0.11(24)	0.01(2)
d_{Th} (e)	-	-	-1.60(4)	-1.42(6)
d_O (e)	-	-	-0.05(3)	-0.03(1)
Z(e)	4.0†	2.46(2)	4.0†	3.82(4)
Shell Properties				
Y_{Th} (e)	-	-	7.0	7.1
Y_O (e)	-	-	2.4	4.8
k_{Th} (e^2/v)	-	-	342	388
k_O (e^2/v)	-	-	2290	640
χ	20.6	2.43	1.71	1.67

Error in last digit(s) shown in parantheses

† Fixed value

TABLE 5.2

QUANTITIES DERIVED FROM FITS OF ThO_2 PHONON DATA - COMPARISON WITH EXPERIMENTAL VALUES

Quantity	Model 1	2	3	4	Expt.
$C_{11}(10^{10}\ Nm^{-2})$	35.8	36.4	37.7	38.1	36.7(4) [a]
$C_{12}(10^{10}\ Nm^{-2})$	6.6	12.9	14.6	15.5	10.6(2) [a]
$C_{44}(10^{10}\ Nm^{-2})$	9.6	7.9	8.9	9.1	7.97(8) [a]
ϵ_∞	-	-	4.16	3.51	4.30(5) [b]
ω_{TO}(meV)	31.3	34.1	33.4	34.1	34.6(3) [c †]
ω_{LO}(meV)	104.0	70.0	70.7	70.4	70.3(3) [c †]
ω_{Raman} (meV)		57.9	58.0	57.9	57.7(1) [c †]
$\epsilon_o = (\omega_{LO}/\omega_{TO})^2\epsilon_\infty$	-	-	18.6	15.0	18.9(4) [b]

[a] Macedo et.al. 1964

[b] Axe and Pettit 1966

[c] Ishigame and Kojima 1976

† Included in fit

description of the phonon dispersion relation (e.g. Cochran 1971).

The dispersion curves of ThO_2 (Fig. 5.2) resemble closely those of UO_2 (Dolling et.al. 1965), thus indicating that their lattice dynamics are very similar. The dispersion relation of CeO_2 (Schnabel 1983) shows a few minor differences (e.g. the Δ'_2 branch at the zone boundary is lower than in UO_2 and ThO_2). The shell model parameters, and their derived quantities, are summarised for the fluorite oxides and halides in Table 5.3, for models which correspond most closely to model 3 of this work. (The values quoted for UO_2 are those of Dolling et.al. (1965) after correction for their value of e, which is a factor of $\sqrt{2}$ too small (Cochran 1971). Thus Dolling's values of A_i, B_i have been divided by 2, and Z, d_u and d_o divided by $\sqrt{2}$.) The dispersion curves for the fluorite halides show a general similarity to those of the oxides. However, they are characterised by a greater degree of overlap between acoustic and optic modes as a result of a smaller disparity between cation and anion masses and of smaller ionic charges.

5.6 CONCLUSIONS

The room temperature phonon dispersion curves of ThO_2 have been measured in the three high symmetry directions. A shell model of the lattice dynamics accounts well for the data. The fitted parameters provide a means of estimating, by interpolation, the phonon energy eigenvalues and eigenvectors at any point in the Brillouin zone, and hence the phonon density of states. The phonon dispersion relation of ThO_2 is very similar to that of UO_2, which is consistent with the observation of similar lattice disorder in both compounds at high temperatures. The dispersion curves of the fluorite halides show a general, but not exact, resemblance to those of UO_2 and ThO_2. The

TABLE 5.3

COMPARISON OF SHELL MODEL PARAMETERS

FOR FLUORITE OXIDES AND HALIDES, MX_2

PARAMETER	ThO_2	UO_2 [a]	CeO_2 [b]	PbF_2 [c]	CaF_2 [d]	SrF_2 [e]
A_1 (e^2/v)	62.6	52.4	56.6	15.3	15.1	16.6
B_1	-12.5	-8.4	-9.5	-2.3	-1.7	-1.9
A_2	-5.4	-4.6	-1.0	-0.02	1.3	0.9
B_2	1.4	0.6	-0.8	0.3	0.1	-0.1
A_3	0.1	-0.3	-4.9	1.4	0.2	-0.4
B_3	2.0	0.4	0.5	-0.3	-0.3	-0.2
A_4	-0.9	0.0†	0.4	-0.2	-0.0	0.05
B_4	0.16	0.0†	0.37	0.03	0.06	-0.06
α_M ($\AA^3$)	4.93	4.34	3.6	2.15	1.63	1.6
α_X ($\AA^3$)	0.11	0.98	0.06	0.65	0.45	0.72
d_M (e)	-1.60	-1.63	-1.11	0.09	-0.25	-0.05
d_X (e)	-0.05	0.18	0.10	0.05	0.06	0.13
Z_{cat} (e)	4.0†	4.0	4.0†	2.0†	2.0†	2.0†
Y_M (e)	7.1	6.9		-13.8		
Y_X (e)	2.4	-14.6		3.7		
k_M (e^2/v)	342	327		4540		
k_X (e^2/v)	2290	15220		1072		
C_{11} (10^{10} Nm^{-2})	37.7	40.4	45.0	11.2	16.5	12.5
C_{12}	14.6	11.6	11.7	5.5	4.5	4.5
C_{44}	8.9	6.0	5.7	2.5	3.4	3.2
ω_{LO} (meV)	70.7	66.0		42.2		
ω_{TO} (meV)	33.4	35.2		12.9		
ϵ_∞	4.12	5.25	2.85	2.19	2.01	2.03
ϵ_o	18.5	18.7	16.6	23.6	6.30	6.21

† Fixed Value

[a] Dolling et.al. 1965

[b] Schnabel 1983

[c] Dickens and Hutchings 1978

[d] Elcombe and Pryor 1970

[e] Elcombe 1972

resulting data and parameters should prove useful in determining the interionic potentials used in molecular dynamics calculations of the high temperature disordered state.

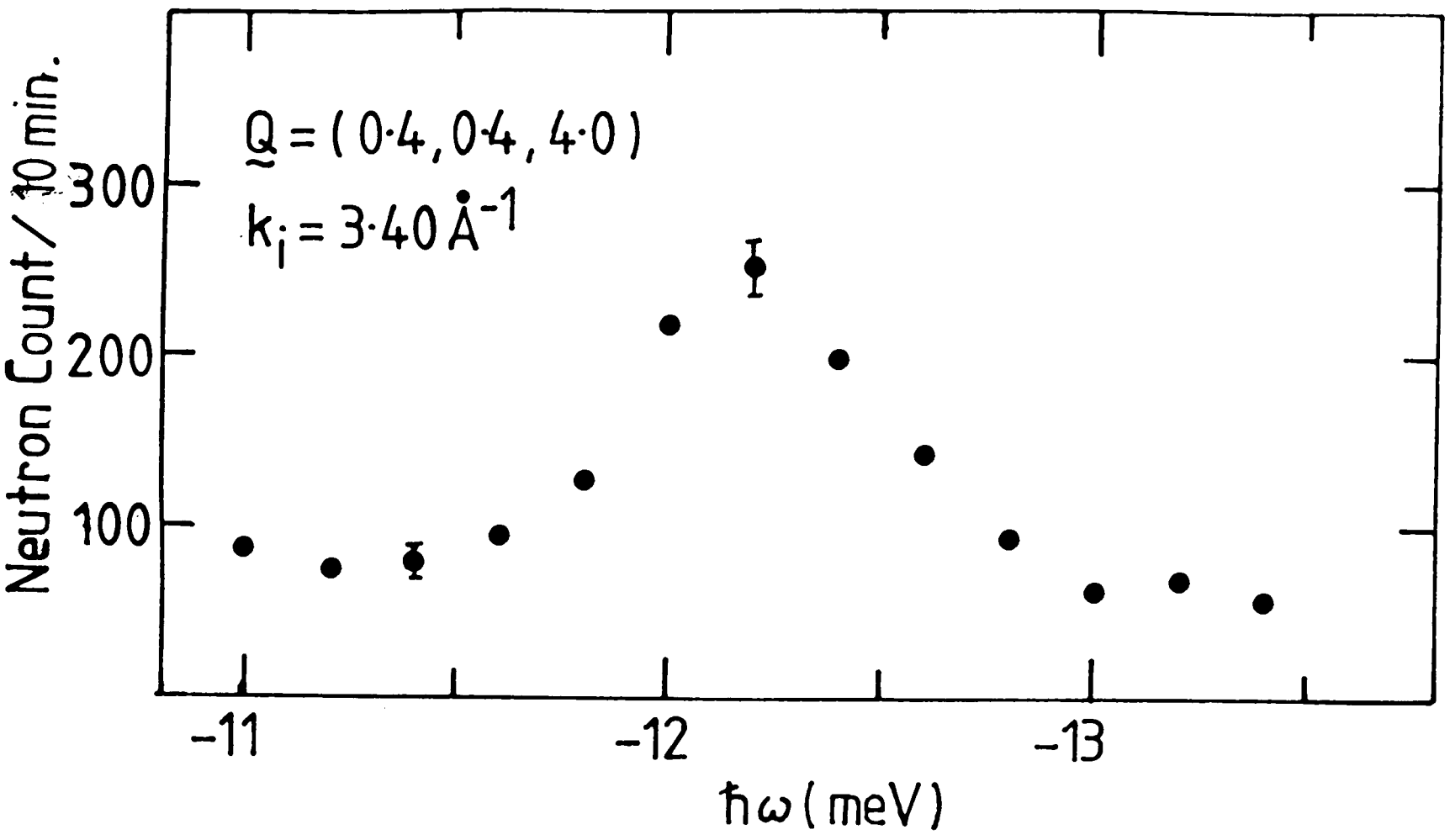

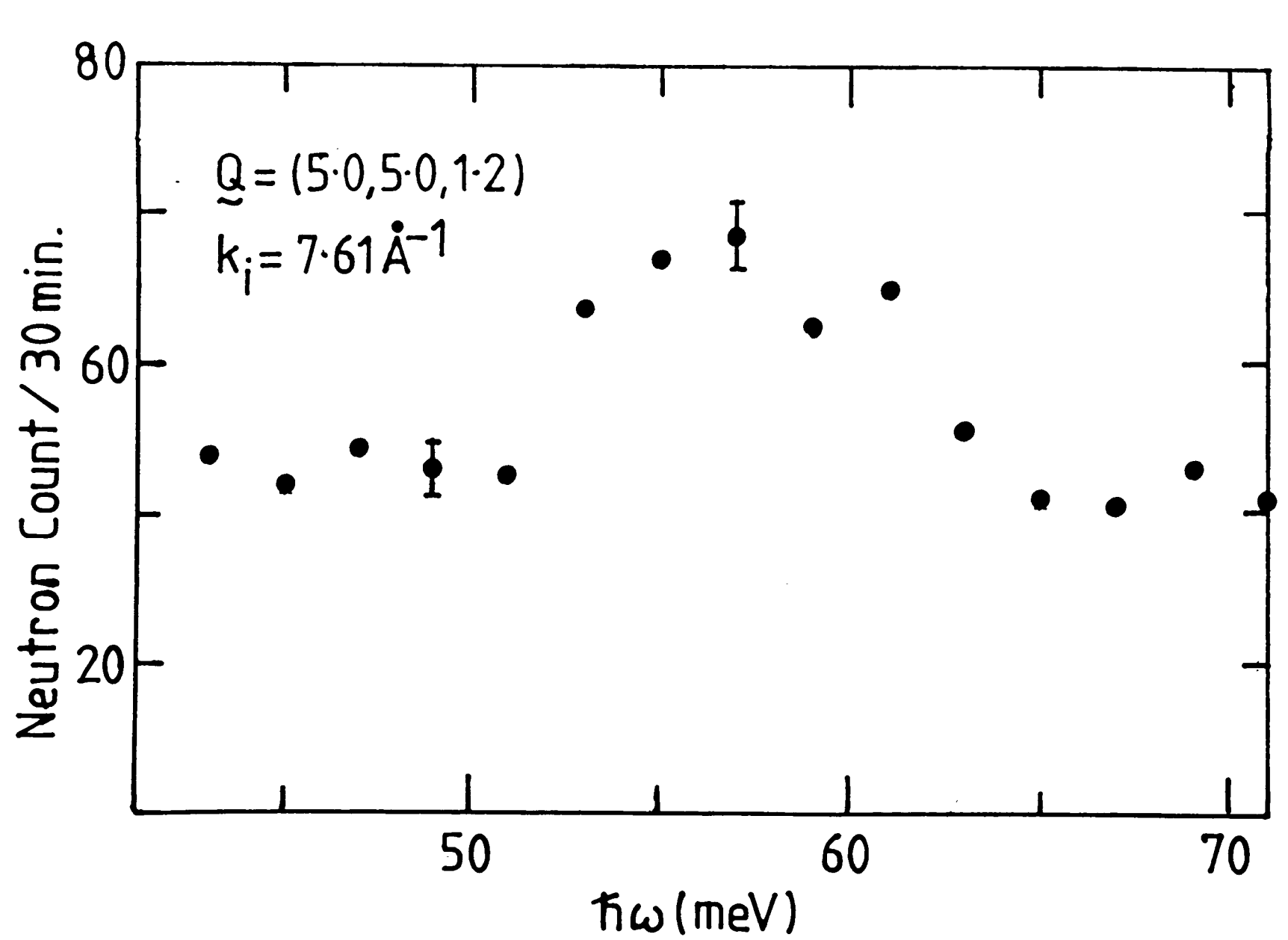

Fig. 5.1 Typical scans of acoustic and optic phonons in ThO_2 at 293K

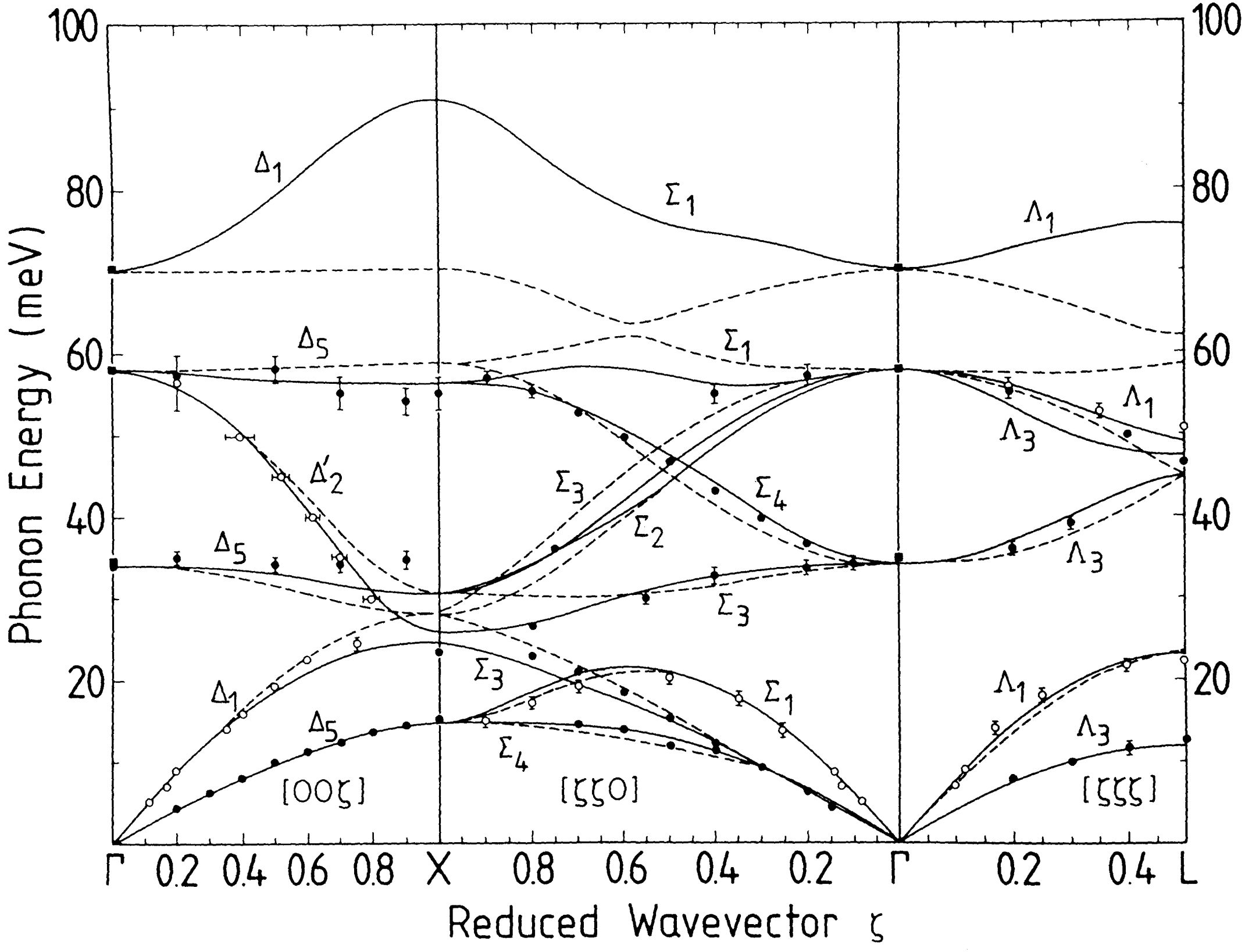

Fig. 5.2 Phonon dispersion relations in the symmetry directions of ThO_2 at 293K. Closed (open) circles are predominantly transverse (longitudinal) modes. The broken curves are calculated from the best fit using model 2, and the full curves from the best fit using model 4. The modes are labelled as in Dickens and Hutchings(1978).

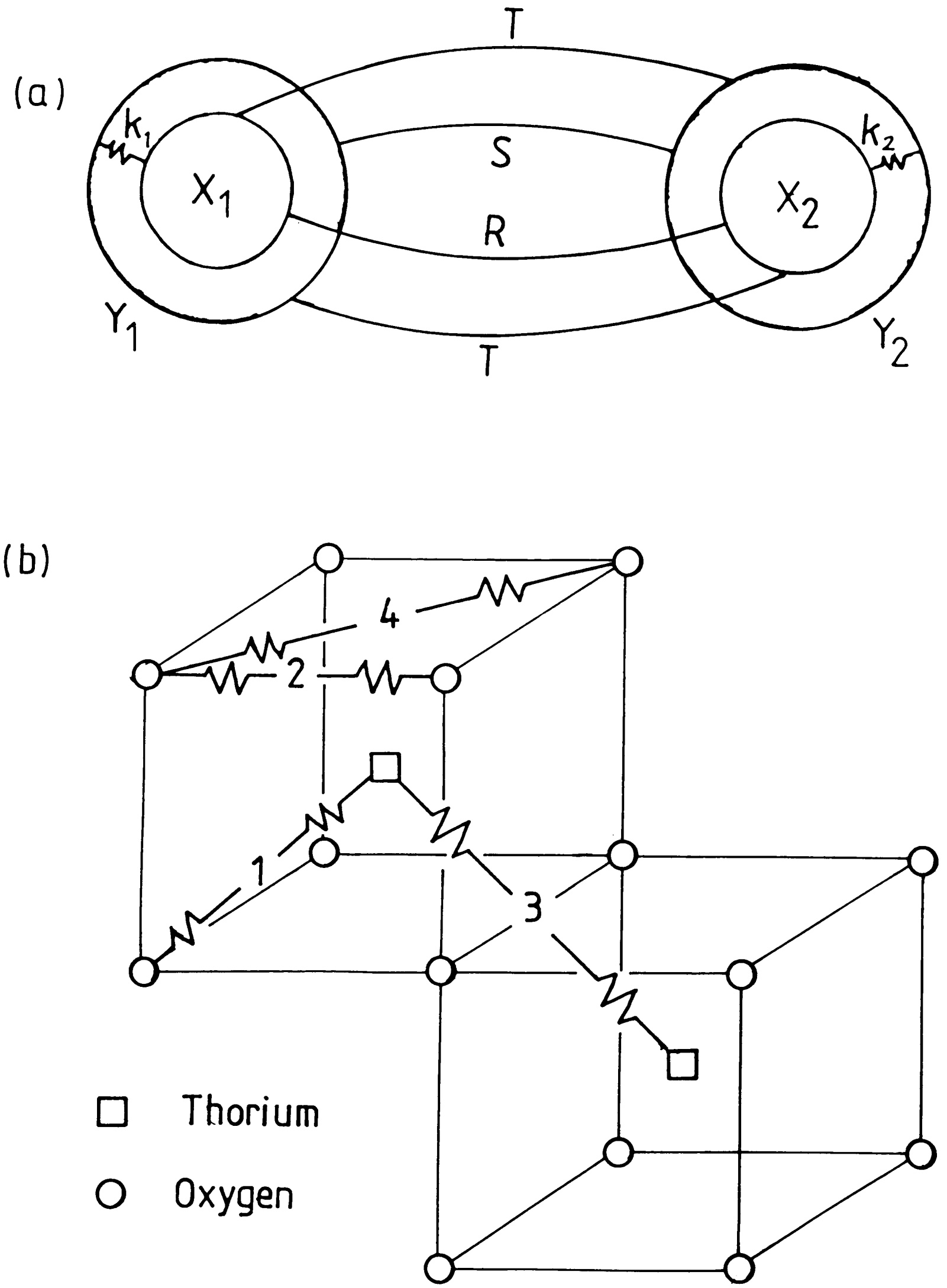

Fig. 5.3 Schematic diagrams of (a) short range forces between two ions in the shell model (b) the four nearest neighbour interactions included in the rigid ion and shell model calculations.

CHAPTER 6

LATTICE DYNAMICS OF UO_2 AT HIGH TEMPERATURES

6.1 INTRODUCTION

Having reported evidence of anion disorder in UO_2 from diffraction results, we now explore the behaviour of its lattice dynamics at high temperatures. We determine the temperature dependence of the elastic constants, acoustic phonon widths and zone-centre optic phonons. The elastic constants C_{ij} describe the slope of the low wavevector acoustic phonons and also enable the determination of the phonon contributions to the heat capacity and thermal conductivity. They are also useful for comparison of theoretical models of interatomic potentials with experimental data. The widths of the acoustic and optic phonons across the Brillouin zone provide information about phonon lifetimes and the effects of anharmonicity. The zone-centre optic mode frequencies may also give information about dielectric properties through the Lyddane - Sachs - Teller relation. Finally, the possible existence of low-energy local modes, predicted to occur at high temperatures on the basis of a small polaron model of electronic disorder (Harding et.al. 1980), is investigated.

6.2 EXPERIMENTAL PROCEDURE

6.2.1 ELASTIC CONSTANTS

The temperature variation of the elastic constants of UO_2 were measured using the PLUTO TAS and the Harwell High Temperature Furnace. Data were taken at a range of temperatures up to 2930K, with room temperature measurements performed both before heating and after the run at 2683K. Supplementary measurements were made using the IN2 TAS at the ILL, but the temperature was limited to 2300K by the performance

of the ILL furnace. One set of elastic constants at 2098K was also determined using the TAS1 spectrometer at Risø National Laboratory, Denmark.

A summary of experimental details is given in Table 6.1, together with those for the other investigations described in this chapter. IN2 differs from a conventional TAS in that the incident beam is monochromatised by Bragg reflection from two identical crystals, the beam emerging parallel with that from the reactor to the monochromator. The advantage of this double monochromator is the improved resolution and reduced background from fast neutrons and γ-rays. However it suffers from a considerable loss of intensity which limits the utilisation of the high neutron flux produced by the reactor.

The UO_2 single crystals were oriented with a $\langle 001 \rangle$ axis vertical, in order to enable the $[110]$ mode polarised along $[1\bar{1}0]$ to be measured and so improve the accuracy of the resulting C_{12} values. The transverse acoustic (TA) phonons were measured in energy loss at $\underset{\sim}{q}$ values of 0.1, 0.15 and 0.2 r.l.u. in $[100]$ and $[110]$ directions at each temperature, using constant Q scans. Because of their steeper gradients, longitudinal acoustic (LA) phonons, in $[100]$ and $[110]$ directions, were measured using constant energy scans at energy transfers of 5, 6 and 7 meV. The $\underset{\sim}{Q}$ values at which the phonons were measured, and the incident neutron wavevectors employed, are summarised in Table 6.2. The larger scattering angles attainable on IN2 permitted the use of $k_i = 2.662 \text{Å}^{-1}$ neutrons for measuring the LA phonons around the (004) reciprocal lattice point, giving better resolution and improving the accuracy of the C_{11} value.

The observed phonon profiles were corrected for resolution shifts using the RESFLD routine, as described in §5.2. The parameters used

TABLE 6.1

SUMMARY OF EXPERIMENTAL DETAILS FOR UO_2 PHONON MEASUREMENTS AT HIGH TEMPERATURES

Date	Spectrometer	Sample	Collimation (M-S/S-A/A-D)	Monochromator (M) Analyser (A)	k_i (A^{-1})	Vanadium Width (meV)	Measurements
Jan. 81	TAS1, Risø	UL1	26′/28′/30′	M:PG(002) A:PG(002)	2.597	0.73	Acoustic Phonons Elastic Constants Local Modes
			26′/61′/66′	M:PG(002) A:Be(002)	2.597	-	Optic Phonons
Jan. 83	IN2, ILL	UL3	40′/40′/40′	M:2xPG(002) A:PG(002)	2.662	0.79	Elastic Constants
Mar. 83	PLUTO TAS, Harwell	UL5	40′/27′/60′	M:PG(002) A:PG(002)	2.673 4.054	1.00 -	Elastic Constants
					4.054	-	Acoustic Phonon Widths

TABLE 6.2

INCIDENT NEUTRON WAVEVECTOR AND MOMENTUM TRANSFER FOR MEASUREMENT OF ELASTIC CONSTANTS OF UO_2

Phonon Branch	k_i ($\AA^{-1}$)	$\underset{\sim}{Q}$(r.l.u.)
PLUTO TAS †		
[ζOO] TA	2.673	(2,2 + ζ ,O)
[ζOO] LA	4.051	(4 + ζ , O, O)
[ζζO] TA	2.673	(2 - ζ , 2 +ζ ,O)
[ζζO] LA	4.051	(2 + ζ , 2 +ζ ,O)
IN2 †		
[ζOO] TA	2.662	(4, ζ , O)
[ζOO] LA	2.662	(4 - ζ , O, O)
[ζζO] TA	2.662	(2 +ζ , 2 - ζ ,O)
RISØ ‡		
[ζOO] TA	2.597	(2, 2, ζ)
[ζOO] LA	2.597	(O, O, 2 + ζ)
[ζζO] LA	2.597	(2 - ζ ,2 - ζ , O)

† ⟨OOl⟩ Axis vertical

‡ ⟨1$\bar{1}$O⟩ Axis vertical

to define the resolution function in RESFLD are given in Table 6.3. The shifts were small for the IN2 data, but they were appreciable for the LA phonons measured on PLUTO TAS because of the large resolution volume, resulting from the high incident neutron wavevector. The resolution shifts and the corrected phonon energies are tabulated in Appendix A.5.

6.2.2 ACOUSTIC PHONON WIDTHS

The [ζ00] TA phonons were scanned at constant Q = (ζ,4,0) for ζ = 0.2, 0.4, 0.6 and 0.8 r.l.u.. The scans were performed using PLUTO TAS in neutron energy loss with $k_i = 4.05 Å^{-1}$. The measurements were made concurrently with those of the elastic constants described above and with those of coherent QES reported in chapter 7.

6.2.3 ZONE-CENTRE OPTIC PHONONS

The temperature variation of the energies and line-widths of the zone-centre transverse optic (TO) and Raman-active phonon modes have been investigated. Scans were performed at four temperatures between 160OK and 230OK, using the TAS1 spectrometer at Risø, by M.T. Hutchings and K. Clausen; an analysis of their data is presented here. Neutrons of $k_i = 2.662 Å^{-1}$ were monochromated using the pyrolytic graphite (002) plane and scattered in energy gain, by virtue of the large phonon populations at these temperatures. A Be(002) plane, which has a small interplanar spacing, was used to analyse the high scattered neutron energies.

Several attempts have also been made to detect the longitudinal optic (LO) phonon in UO_2 between room temperature and 160OK, but without success. Using the PLUTO TAS, scans were made in energy gain

TABLE 6.3

PARAMETERS USED TO DEFINE THE SPECTROMETER RESOLUTION FUNCTION IN THE RESFLD PROGRAM

Parameter	PLUTO TAS (March 1983)	IN2, ILL (Jan. 83)
α_{R-M}	60′	30′
α_{M-S}	40′	40′
α_{S-A}	27′	40′
α_{A-D}	60′	40′
β_{R-M}	100′	100′
β_{M-S}	100′	100′
β_{S-A}	100′	100′
β_{A-D}	100′	100′
η_M	50′	10′
η_S	30′	17′
η_A	25′	25′
k_i	$2.673\,\text{Å}^{-1}$	$2.662\,\text{Å}^{-1}$
Configuration	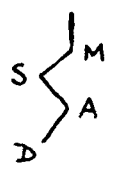	
Observed and Calculated FWHM of Bragg and Vanadium peaks		
Bragg peak	(200)	(400)
$FWHM_{\perp}$ Bragg (Observed)	$0.022\,\text{Å}^{-1}$	$0.026\,\text{Å}^{-1}$
$FWHM_{\perp}$ Bragg (Calculated)	$0.022\,\text{Å}^{-1}$	$0.027\,\text{Å}^{-1}$
$FWHM_{//}$ Bragg (Observed)	$0.038\,\text{Å}^{-1}$	$0.056\,\text{Å}^{-1}$
$FWHM_{//}$ Bragg (Calculated)	$0.028\,\text{Å}^{-1}$	$0.051\,\text{Å}^{-1}$
FWHM Vanadium (Observed)	1.00meV	0.79meV
FWHM Vanadium (Calculated)	1.05meV	0.84meV

R: reactor M: monochromator S: sample A: analyser

D: detector α: Horizontal collimation β: vertical collimation

$FWHM_{//}$: width of radial scan $FWHM_{\perp}$: width of tangential scan

and loss using suitable analyser crystals (graphite for energy loss, beryllium and zinc for energy gain). A cooled beryllium filter, which transmits neutrons of energy less than 5 meV, was also used to analyse the scattered beam, both with and without a conventional analyser crystal. Because of the LO phonon's high energy (60 - 70 meV), a spectrometer having a greater flux of high energy neutrons, such as IN1 or IN8 at ILL, is needed to observe it, provided that its width is not excessively large at these temperatures. Knowledge of the LO phonon's behaviour could shed light on the nature of electronic defects. For instance, if the conduction electrons are de-localised as in a semiconductor, then the splitting of the zone-centre TO and LO phonons may be reduced by screening effects.

6.2.4 LOCAL MODES

On the basis of the small polaron model of electronic disorder, discussed in §1.3, Harding et.al.(1980) predicted the existence of local modes at 2.4 meV, 6.1 meV and 6.9 meV, due to a twisting motion of the oxygen sub-lattice. A thorough search was made for these local modes during the experiment performed at Risø, described in the previous sub-section. Scans were made at 2098K in regions unaffected by phonons, and the $[\zeta 00]$ TA phonon widths were also determined near the predicted local mode energies in order to assess any broadening brought about by interactions between the modes. No evidence was found for the existence of such local modes, but it should be noted that polaron concentrations of only about 1% are predicted to occur at this temperature (Harding et.al. 1980).

6.2.5 PLASTIC DEFORMATION OF UO_2

During crystal alignment at 293OK for the elastic constants measurements it was noted, from photographs of the diffracted beam,

that the axis of the cylindrical UO_2 crystal was always vertical regardless of the tilt of the furnace on the goniometer arcs. This indicated that the tungsten tube, in which the sample was encapsulated, had softened and could not support the weight of the crystal. On opening the furnace, it was found that the tungsten tube, which had been sealed in vacuo, had partially collapsed under the ~25 p.s.i. pressure exerted by the argon atmosphere in the furnace. The tube was also punctured as a result of the deformation. After opening the tube, the UO_2 crystal (sample UL5) was found to have deformed and taken the shape of the tungsten tube! Similar deformation of both the tungsten tube and the UO_2 crystal was also observed in sample UL4 after cooling from 2793K during QES measurements (chapter 7, experiment 3). No such deformation was observed in sample UL2 after heating to 2100K.

Similar deformation effects may have led Ackermann (1955) to report that the melting point of UO_2 was between 2661K and 2699K, based on the appearance of residues from two experiments for which these were the maximum temperatures. The deformation of UO_2 at high temperatures has also been investigated by Slagle (1978) who reported rapid increases in its creep rate between 2500K and 2900K.

Chemical tests of the stoichiometry of fragments from the centre of sample UL4, performed using the gas equilibration technique, gave a U:O ratio of 1.93 (G Phillips and I Jones, private communication). (Tests of the crystal surface were prohibited by the risk of tungsten contamination of the apparatus.) X-ray diffraction analysis of the surfaces of the tungsten sample tube and of the UO_2 crystal showed no traces of tungsten oxides (M D Fones, private communication). Hence the deviation from stoichiometry cannot be attributed to a chemical

reaction between the UO_2 and the sample tube. It may possibly have been caused by the fracture of the sample tube at high temperatures as described above. Tests of the stoichiometry of the other UO_2 samples cannot be performed at Harwell at present (G. Phillips, private communication), therefore enquiries are being made concerning the possible execution of these tests at other establishments. Further detailed investigations of the deformation of UO_2 and of its stoichiometry at high temperatures are clearly required.

6.3 ANALYSIS AND RESULTS

6.3.1 ELASTIC CONSTANTS

The resolution-corrected acoustic phonon energies were fitted with a sinusoidal function,

$$\hbar\omega(\underset{\sim}{q}) = \frac{2}{\pi}\gamma \sin(\tfrac{1}{2}\pi q) \quad , \tag{6.1}$$

in order to determine the slope γ of each branch at $q = 0$. The phonon velocity v is related to γ by

$$v(ms^{-1}) = \frac{151.92}{a^*(\mathring{A}^{-1})} \cdot \gamma\ (meV/r.l.u.) \tag{6.2}$$

where $a^* = 2\pi/a_o$. The elastic constants for each branch were calculated from the values of v and the density ρ at each temperature, using the expressions given in Table 6.4. The density was calculated from the atomic masses, $m_u = 238.03$ and $m_o = 16.00$, and the lattice constants at each temperature (Table 6.5).

The resulting values of the elastic constants are given in Table 6.6 and illustrated in Fig. 6.1. The consistency of the results may be judged by comparing the values of $\frac{1}{2}(C_{11} + C_{12} + 2C_{44})$ obtained by direct measurement of the $[\zeta\zeta 0]$ LA branch with those calculated from the values of the three individual elastic constants. These are

TABLE 6.4

THE ELASTIC CONSTANTS WHICH MAY BE EQUATED TO THE QUANTITY ρv^2 FOR LONG WAVELENGTH ACOUSTIC PHONONS IN CUBIC CRYSTALS (KITTEL 1971)

Phonon Branch		ρv^2
[ζ00]	LA	C_{11}
[ζ00]	TA	C_{44}
[ζζ0]	LA	$\frac{1}{2}(C_{11} + C_{12} + 2C_{44})$
[ζζ0]	TA †	C_{44}
[ζζ0]	TA ‡	$\frac{1}{2}(C_{11} - C_{12})$
[ζζζ]	LA	$1/3(C_{11} + 2C_{12} + 4C_{44})$
[ζζζ]	TA	$1/3(C_{11} - C_{12} + C_{44})$

† $(1\bar{1}0)$ plane

‡ (001) plane

TABLE 6.5

TEMPERATURE VARIATION OF THE LATTICE CONSTANT AND DENSITY OF UO_2

T(K)	a_o (Å)	$\rho(10^3 kg\ m^{-3})$
PLUTO TAS		
293	5.470	11.04
2081	5.593	10.33
2271	5.612	10.22
2390	5.625	10.15
2478	5.634	10.10
2589	5.649	10.02
2683	5.659	9.97
2771	5.672	9.90
2929	5.690	9.81
IN2, ILL		
293	5.470	11.04
1211	5.524	10.72
1963	5.575	10.43
2198	5.594	10.32
TAS1, RISO		
2098	5.595	10.32

TABLE 6.6

TEMPERATURE VARIATION OF THE ELASTIC CONSTANTS OF UO_2 (IN UNITS OF $10^{10} Nm^{-2}$)

(Error in last digit(s) shown in parentheses)

T(K)	C_{11}	C_{44}	$\frac{1}{2}(C_{11}-C_{12})$	C_{12}	$\frac{1}{2}(C_{11} + C_{12} + 2C_{44})$ measured	calculated
PLUTO TAS						
293[a]	34.4(34)	6.80(37)	12.8(8)	8.8(38)	30.7(29)	28.4(26)
293[b]	34.4(26)	6.71(21)	11.7(16)	11.0(40)	28.6(12)	29.4(24)
2081	26.0(25)	4.91(18)	8.2(6)	9.6(28)	19.6(22)	22.7(19)
2271	23.3(11)	4.85(20)	7.6(11)	8.0(25)	19.8(18)	20.5(14)
2390[b]	22.0(14)	4.27(13)	6.5(5)	9.0(17)	17.9(15)	19.7(11)
2478	21.9(15)	4.28(10)	6.2(6)	9.6(19)	18.2(6)	20.0(12)
2589	21.4(11)	4.04(6)	6.0(3)	9.4(13)	17.9(7)	19.4(9)
2683	19.8(16)	3.54(26)	5.2(1)	9.5(16)	16.6(8)	18.2(12)
2771	17.9(6)	3.21(16)	4.3(4)	9.3(9)	15.5(4)	16.8(6)
2929	14.7(21)	2.69(16)	3.5(4)	7.7(22)	12.7(48)	13.9(15)
IN2, ILL						
293	41.6(29)	6.28(13)	11.5(9)	18.6(34)	-	36.4(22)
1211	32.1(16)	5.90(22)	10.2(2)	11.8(16)	-	27.9(12)
1963	27.9(16)	5.12(32)	8.1(8)	11.8(22)	-	25.0(26)
2198	28.9(10)	4.89(58)	7.7(5)	13.5(15)	-	26.1(11)
TAS1, RISØ						
2098	23.4(20)	5.25(20)	-	9.6(50)	-	19.1(27)
ULTRASONICS						
293[c]	39.6(2)	6.41(2)	13.8(2)	12.1(2)	-	32.3(2)
293[d]	38.9(2)	5.97(3)	13.5(3)	11.9(2)	-	31.4(2)
SHELL MODEL						
293[e]	40.1(9)	6.7(6)	14.7(5)	10.8(20)	-	32.0(33)

[a] before heating [b] after 2683K run [c] Wachtman et.al. 1965 [d] Fritz 1976 [e] Dolling et.al. 1965

also shown in Table 6.6, from which it may be seen that the measured values are systematically smaller than the calculated values. Agreement between data from different experiments is good for the shear modes, but rather poor for C_{11}. The values of C_{12} are particularly imprecise because its evaluation involves the velocities of two phonon modes. Also given in Table 6.6 are the values of the elastic constants at room temperature, determined by ultrasonic techniques (Wachtman et.al. 1965, Fritz 1976) and by a shell model fit to the full dispersion curves (Dolling et.al. 1965).

All the elastic constants decrease smoothly with increasing temperature up to 245OK, above which C_{11}, C_{44} and $\frac{1}{2}(C_{11} - C_{12})$ show a more rapid rate of decrease. However, there is no evidence for anomalous softening of any branches. The temperature variations of the anisotropy factor $A = 2C_{44}/(C_{11} - C_{12})$ and the bulk modulus $B = {}^{1}/_{3}\ (C_{11} + 2C_{12})$, deduced from the data, are also shown in Table 6.7 and Fig. 6.2. The extrapolation of previous data of the bulk modulus below 160OK by Fink et.al. (1981), used by Browning et.al. (1983) to calculate the dilation contribution to the enthalpy of UO_2, is in reasonable agreement but is a little below the measured values (Fig. 6.2). More accurate values of the bulk modulus may be obtained from the combination of C_{44} and the slope of the [ξξξ] LA branch which is related to ${}^{1}/_{3}(C_{11} + 2C_{12} + 4C_{44})$.

6.3.2 ACOUSTIC PHONON WIDTHS

In order to determine the widths of the acoustic phonons as a function of wavevector and temperature, the observed intensity at each point in the constant - $\underset{\sim}{Q}$ scans must be fitted with a function describing the scattering from several sources, which are now discussed in turn. Noise in the detector, background radiation and multiphonon scattering,

TABLE 6.7

VALUES OF THE BULK MODULUS AND ANISOTROPY PARAMETER OF UO_2 (DERIVED FROM THE ELASTIC CONSTANTS)

Errors in last digit(s) shown in parentheses

T(K)	$B(10^{10}\ Nm^{-2})$	$A = \frac{2C_{44}}{(C_{11} - C_{12})}$
PLUTO TAS		
293[a]	17.3(28)	0.53(4)
293[b]	18.8(28)	0.57(8)
2081	15.1(20)	0.60(5)
2271	13.1(17)	0.63(10)
2390[b]	13.3(12)	0.66(5)
2478	13.7(14)	0.69(6)
2589	13.4(9)	0.67(4)
2683	12.9(12)	0.68(5)
2771	12.2(6)	0.75(7)
2929	10.0(16)	0.77(9)
IN2, ILL		
293	26.3(25)	0.55(5)
1211	18.6(12)	0.58(2)
1963	17.2(16)	0.63(7)
2198	18.6(11)	0.64(9)
TAS1, RISO		
293	14.2(34)	-
ULTRASONICS		
293[c]	21.3(2)	0.47(1)
293[d]	20.9(1)	0.44(1)
SHELL MODEL		
293[e]	20.6(14)	0.46(8)

[a] before heating [b] after 2683K run [c] Wachtman et.al. 1965

[d] Fritz 1976 [e] Dolling et.al. 1965

which is strong at high temperatures, produce a background contribution I_B which may be approximated by a sloping linear function of energy.

$$I_B(\omega) = B_o + B_s\omega \qquad (6.3)$$

The tungsten sample can and furnace components produce a significant amount of incoherent elastic scattering (IES) at zero energy transfer. The IES contribution I_{IES} may be represented by a Gaussian function having the resolution width of the spectrometer and centred on $\omega = 0$.

$$I_{IES}(\omega) = S_G e^{-a^2\omega^2} \qquad (6.4)$$

The parameters S_G and a were obtained by fitting to an energy scan of the IES at room temperature. The values of S_G at higher temperatures were then corrected for thermal effects by assuming that the Debye-Waller factor of tungsten is equal to that of the uranium ion, B_u, which was determined up to 2900K from diffraction results (chapter 4).

The one-phonon scattering function was represented by a damped simple harmonic oscillator (DSHO) function (Dorner 1982),

$$S_{DSHO}(\underset{\sim}{Q},\omega) = S\left[1 - \exp(-\frac{\hbar\omega}{k_B T})\right]^{-1} \frac{\omega\Gamma}{(\omega^2 - \Omega^2)^2 - \omega^2\Gamma^2} \qquad (6.5)$$

where S is a scale factor, $\Gamma(\underset{\sim}{q})$ is the HWHM of the broadened phonon and $\Omega(q)$ is the phonon 'natural' frequency, defined as

$$\Omega(q) = \frac{2}{\pi}\gamma \sin(\tfrac{1}{2}\pi q) \qquad (6.6)$$

The first term in (6.5) represents a Bose population factor. The phonon intensity at an energy ω_o is then given by

$$I_{DSHO}(\omega_o) = \iint S_{DSHO}(Q,\omega)\, R(\underset{\sim}{Q} - \underset{\sim}{Q}_o, \omega - \omega_o; \underset{\sim}{Q}_o, \omega_o)\, d\underset{\sim}{Q}d\omega \qquad (6.7)$$

where the resolution function R must be calculated at each point in the scan from the parameters given in Table 6.3. It should be noted that

the approximation given in equation (3.41) is not valid here because of the rapid $\underset{\sim}{Q}$ - variation of the scattering function.

The total calculated scattered intensity at a point ω_o in a constant - $\underset{\sim}{Q}$ scan is then

$$I_c(\omega_o) = I_B(\omega_o) + I_{IES}(\omega_o) + I_{DSHO}(\omega_o). \qquad (6.8)$$

This function has been fitted to the observed intensity at each point of the spectra using the routing FITSQW (written by M T Hutchings). This program takes a considerable time to fit the data because it involves the repeated evaluation of the resolution function and the convolution integral. The resulting values of the fitted parameters S, Y , B_o, B_S and $\Gamma(\underset{\sim}{q})$ are given in Table 6.8. Scans of the [.8,0,0] TA phonon at three temperatures, together with the fitted profiles, are shown in Fig. 6.3.

The temperature variation of $\Gamma(\underset{\sim}{q})$ at $\underset{\sim}{q}$ = 0.4, 0.6 and 0.8 r.l.u. is shown in Fig. 6.4. It may be seen that the phonon width increases monotonically with wavevector and temperature. The $\underset{\sim}{q}$ - variation of $\Gamma(\underset{\sim}{q})$ at each temperature, shown in Fig. 6.5, does not show a definite deviation from the linear dependence predicted for anharmonic effects up to 2478K. There is some evidence of a q^2 dependence at 2589K and 2683K, similar to that observed in the fast-ion region of PbF_2 (Dickens et.al. 1979b). However, the data show a fair degree of scatter and no firm, quantitative conclusions can be drawn from this investigation.

6.3.3 OPTIC PHONONS

The spectrometer resolution function was determined by comparison of calculated and observed widths of Bragg and vanadium incoherent peaks, as described in §5.2. Following the procedure given in the preceding section, the intensity at each point in the

TABLE 6.8

RESULTS OF FITTING A DAMPED SIMPLE HARMONIC OSCILLATOR FUNCTION TO CONSTANT-$\underset{\sim}{Q}$ [q,0,0] TA PHONONS

Errors in last digit(s) shown in parentheses

T(K)	q(r.l.u.)	S	γ(meV/r.l.u.)	Γ(meV)	χ^2
293	0.4	50.3(6)	19.02(2)	0.18(2)	2.27
	0.6	39.7(7)	19.95(3)	0.45(3)	5.36
	0.8	21.8(16)	20.35(3)	0.26(6)	3.04
2081	0.4	102(7)	16.79(4)	0.29(6)	0.85
	0.6	69(3)	17.22(5)	0.75(8)	2.19
	0.8	-	-	-	-
2271	0.4	113(4)	16.48(4)	0.44(6)	1.30
	0.6	71(4)	16.64(6)	1.12(14)	1.57
	0.8	39(4)	17.48(13)	1.38(27)	1.59
2390	0.4	84(4)	15.33(6)	0.39(8)	3.64
	0.6	44(3)	16.01(9)	0.63(15)	1.20
	0.8	-	-	-	-
2478	0.4	93(4)	15.46(7)	0.60(9)	2.75
	0.6	60(7)	15.70(14)	1.34(29)	1.30
	0.8	23(4)	16.26(25)	1.54(61)	0.77
2589	0.4	72(4)	15.08(7)	0.46(9)	2.17
	0.6	51(7)	15.26(18)	1.56(40)	0.96
	0.8	18(5)	15.40(36)	1.81(92)	0.76
2683	0.4	52(3)	14.73(10)	0.49(10)	1.56
	0.6	30(4)	14.75(20)	1.04(35)	1.26
	0.8	22(4)	14.31(54)	3.90(10)	1.66

The scale factor S has been normalised to the neutron monitor count.

spectra was fitted with a function of the form

$$I_c(\omega_o) = I_B(\omega_o) + I_{ph}(\omega_o), \qquad (6.9)$$

where the phonon contribution $I_{ph}(\omega_o)$ is

$$I_{ph}(\omega_o) = \int S_L \frac{\Gamma(Q)}{(\omega - \Omega)^2 + \Gamma(Q)^2} R_o \exp\left\{-a^2(\omega - \omega_o)^2\right\} d\omega . \qquad (6.10)$$

A Lorentzian line-shape was chosen for $S(\underset{\sim}{Q},\omega)$ since it is the Fourier transform of an exponential time-decay term. The zone-centre optic modes were assumed to be non-dispersive over the extent of the resolution function, and therefore the approximations embodied in equations (3.41 - 3.43) were applied. The parameters S_L, B_o, B_S, Ω and $\Gamma(Q)$ were fitted to the data using the PKFIT routine (written by R.Vaughan-Watkins of the Polytechnic of Central London).

The scans and the fitted profiles at each temperature are illustrated for the TO zone-centre phonon in Fig. 6.6. The resulting phonon frequencies and widths are given in Table 6.9 and the temperature variation of the phonon widths 2Γ are illustrated in Fig. 6.7. Both the TO and Raman modes broaden with increasing temperature, dramatically so above 2000K - the Raman mode was unobservable at 2323K.

6.4 DISCUSSION AND CONCLUSIONS

Inelastic neutron scattering techniques have been used to investigate the lattice dynamics of UO_2 at temperatures up to 2930K. The elastic constants and bulk modulus of UO_2, which are important for theoretical analyses and for the interpretation of thermophysical data, have also been determined at these temperatures. The elastic constants all decrease with increasing temperature up to ~2450K, behaviour which is typical of most solids. Above this temperature, the rates of decrease of C_{11}, C_{44} and $\frac{1}{2}(C_{11} - C_{12})$ become more rapid

TABLE 6.9

TEMPERATURE VARIATION OF RAMAN AND TRANSVERSE OPTIC ZONE-CENTRE MODE ENERGIES AND PHONON LINEWIDTHS IN UO_2 (UNITS ARE IN meV)

Errors in last digit(s) shown in parentheses

	Raman mode		TO mode	
T(K)	$\hbar\Omega$	2Γ	$\hbar\Omega$	2Γ
293	55.5(7)	~0	35.2(5)	~0
1673	52.0(2)	7.5(13)	29.8(2)	5.0(3)
1873	51.1(4)	8.5(15)	28.7(2)	5.7(4)
2073	50.3(7)	9.7(23)	27.8(2)	7.0(5)
2323	50.0(10)	'∞'	26.2(4)	14.5(15)

but no soft modes were observed. This behaviour is similar to that of the elastic constants of PbF_2 (Dickens et.al. 1979b).

Whereas the low wavevector acoustic phonons are sharp and well-defined up to 293OK, the widths of the [ζOO] TA phonons increase with increasing wavevector and temperature. However the data are not of sufficient quality to determine the $\underset{\sim}{q}$ - dependence of the phonon widths. Dramatic broadening of the zone-centre TO and Raman phonons occurs above 2000K. The widths of optic and large wavevector acoustic phonons are sensitive to anharmonicity and defect formation because neighbouring ions move approximately in antiphase. Indeed, thermally-induced broadening of optic modes is readily observable at room temperature in PbF_2 (Dickens and Hutchings 1978).

Attempts to investigate possible electronic disorder in UO_2 have been inconclusive. No evidence of local modes, predicted to occur as a consequence of small polaron behaviour, was seen up to a temperature of 2100K. However, no estimates are yet available for the scattering cross-sections and lifetimes of these local modes and it should be noted that the concentration of small polarons is predicted to be $\lesssim$ 1% below 2400K (Harding et.al. 1980). Failure to observe the LO phonon has also thwarted attempts to investigate the zone-centre LO - TO phonon splitting, which could give information on electronic screening effects.

The deformation of UO_2 crystals, observed after cooling from $\sim$ 2700K, requires further investigation. This behaviour may probably be identified with the creep phenomenon, investigated by Slagle (1978) and others. The changes in textural appearance reported by Ackermann (1955) are also consistent with our observations.

The general behaviour of the phonon modes investigated in UO_2 at high temperatures is reminiscent of that observed in the fluorite halides PbF_2 (Dickens et.al. 1979b), $SrCl_2$ and BaF_2 (M H Dickens and M T Hutchings, private communication). This suggests that the effects observed above 220OK are probably due to the onset of Frenkel disorder, as observed directly by diffraction measurements.

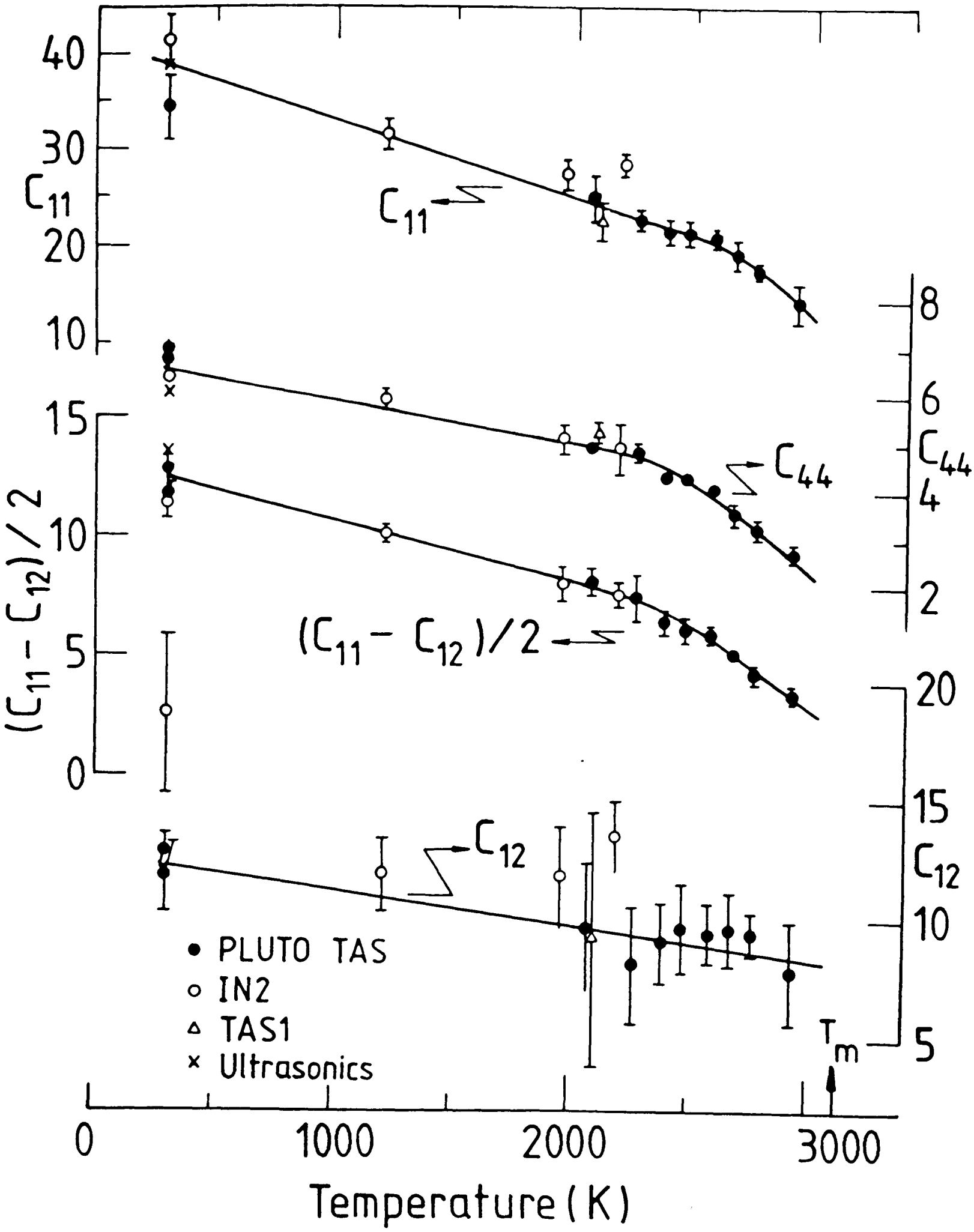

Fig. 6.1 Temperature variation of the elastic stiffness constants of UO_2. Also shown are the room temperature values obtained using ultrasonic techniques. Solid lines are guides to the eye.

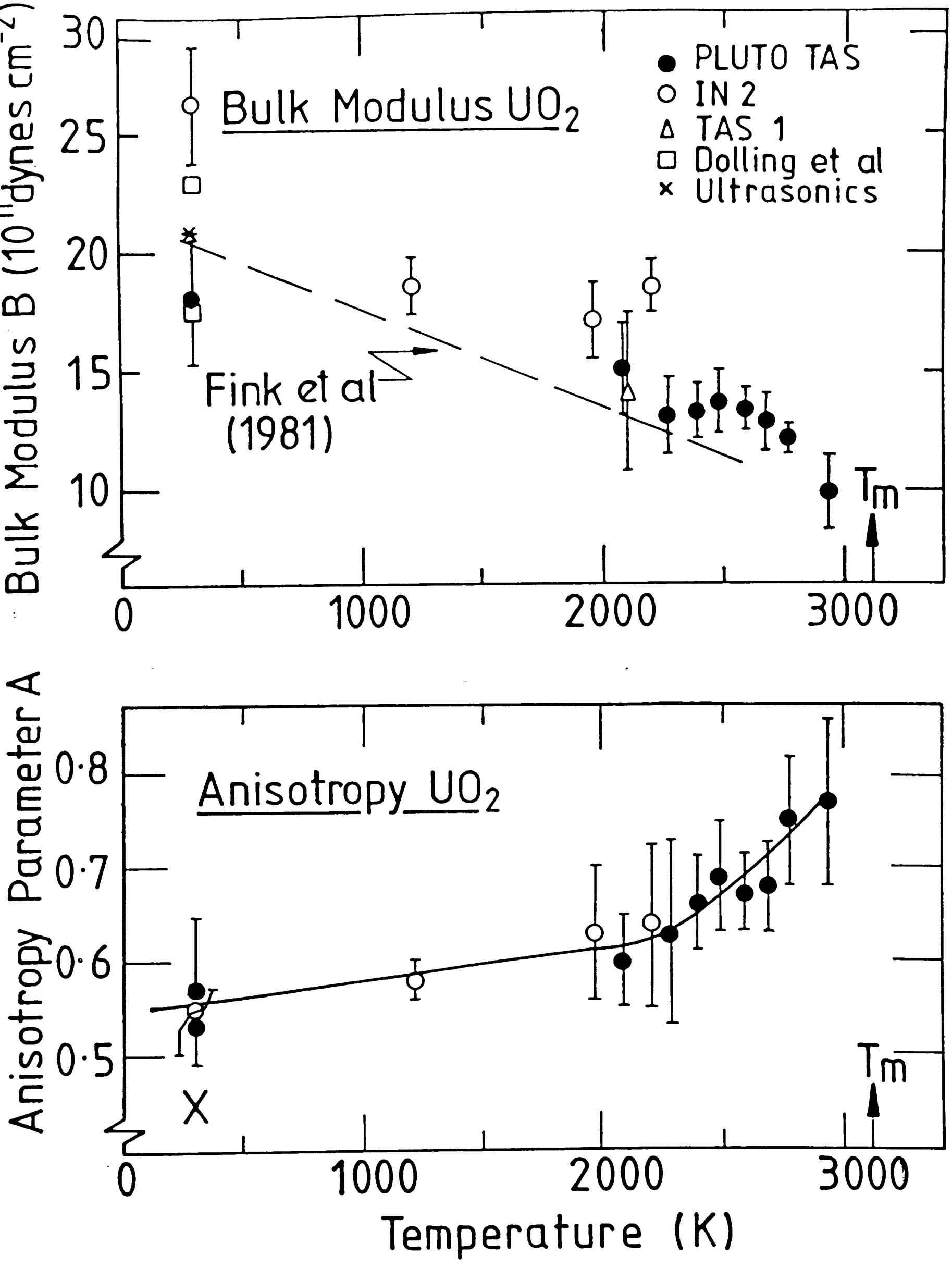

Fig. 6.2 Temperature variation of the bulk modulus $B = \frac{1}{3}(C_{11}+2C_{12})$ and anisotropy parameter $A = 2C_{44}/(C_{11}-C_{12})$ of UO_2. The broken line represents an extrapolation from data at lower temperatures (Fink et.al. 1981). The solid line is a guide to the eye.

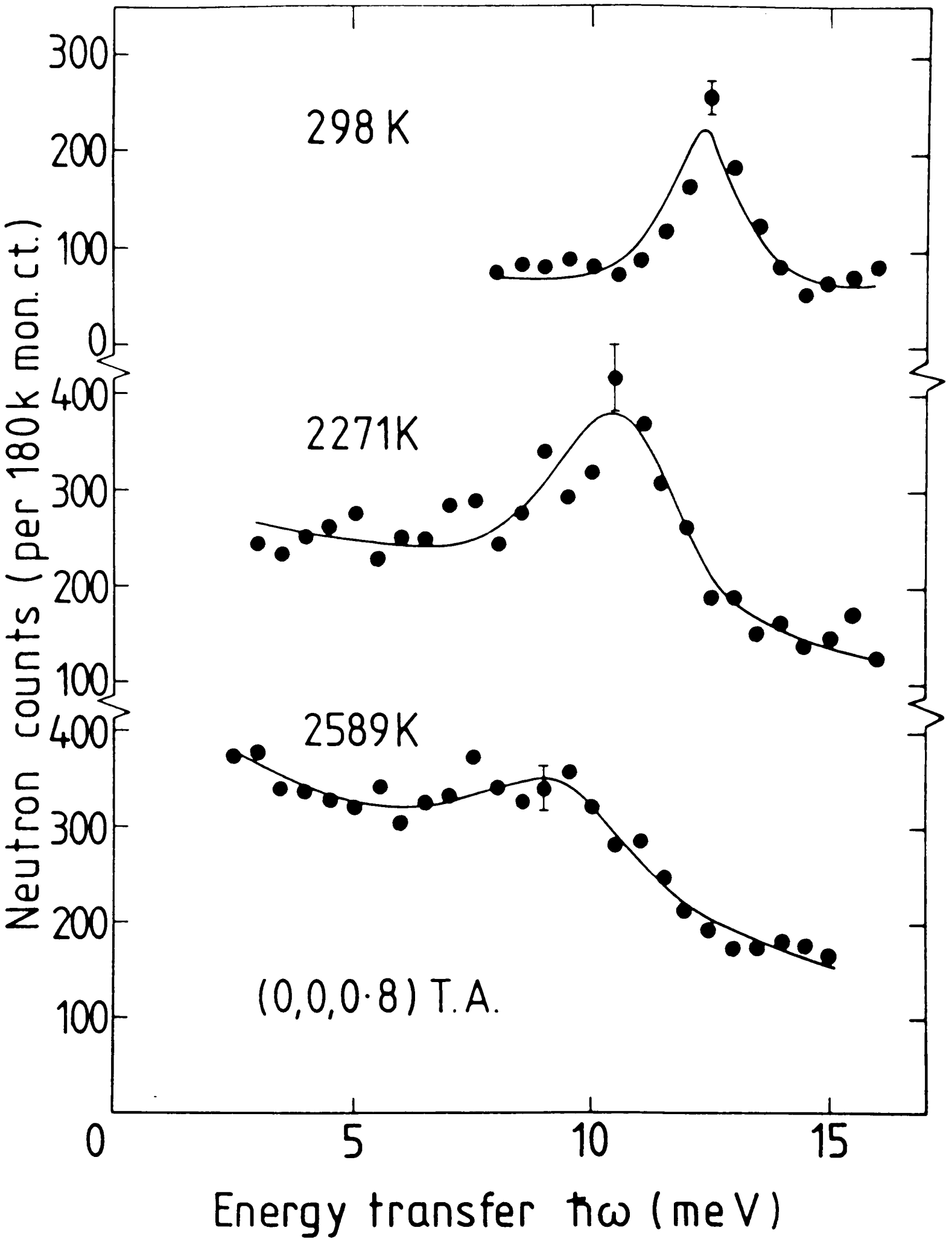

Fig. 6.3 Neutron groups for constant Q scans of the (0,0,0.8)TA phonon mode in UO_2 at three temperatures. Solid lines are the scan profiles fitted using the FITSQW routine.

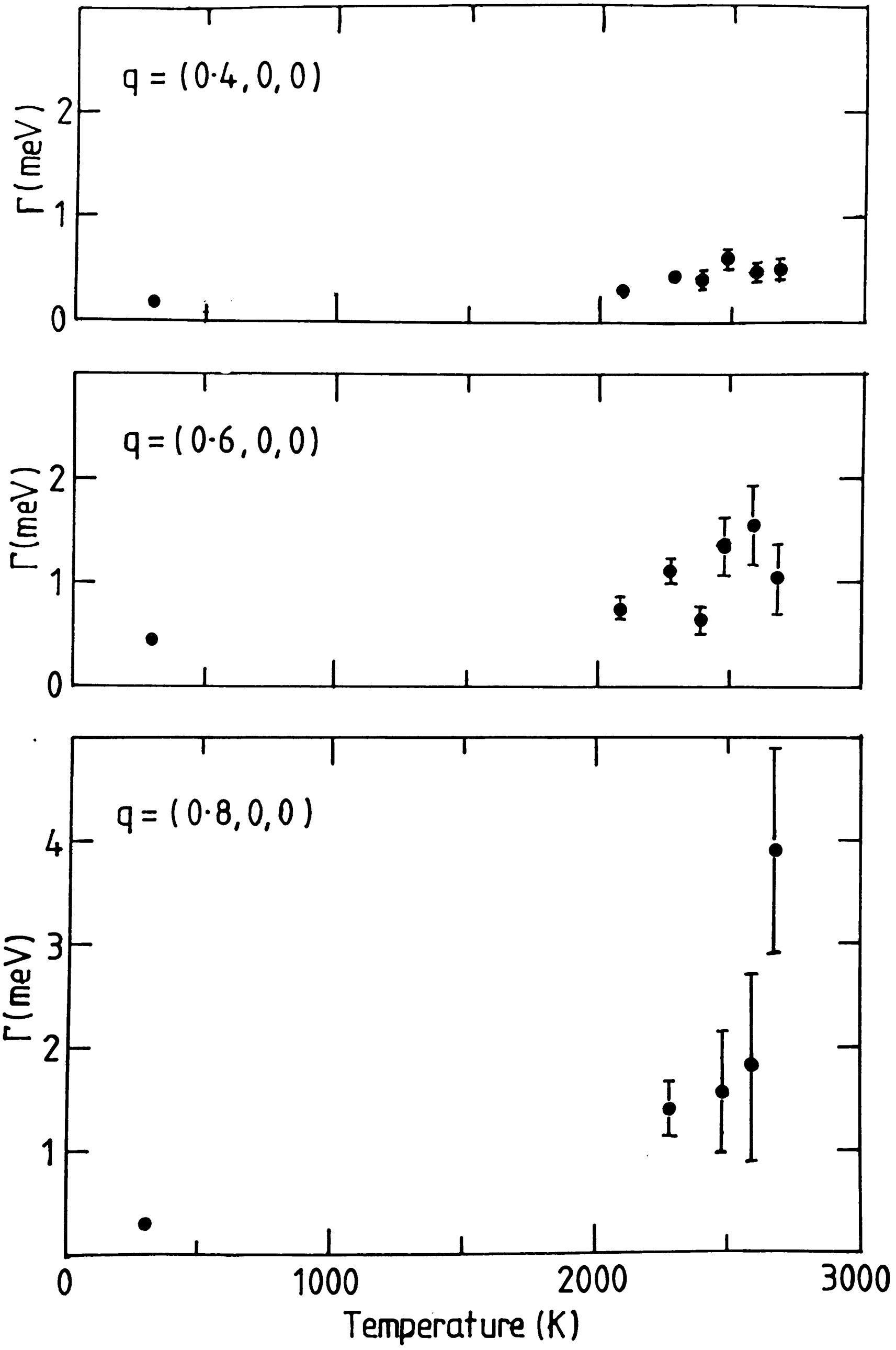

Fig. 6.4 Temperature variation of the intrinsic phonon widths (HWHM) Γ at three wavevectors in UO_2.

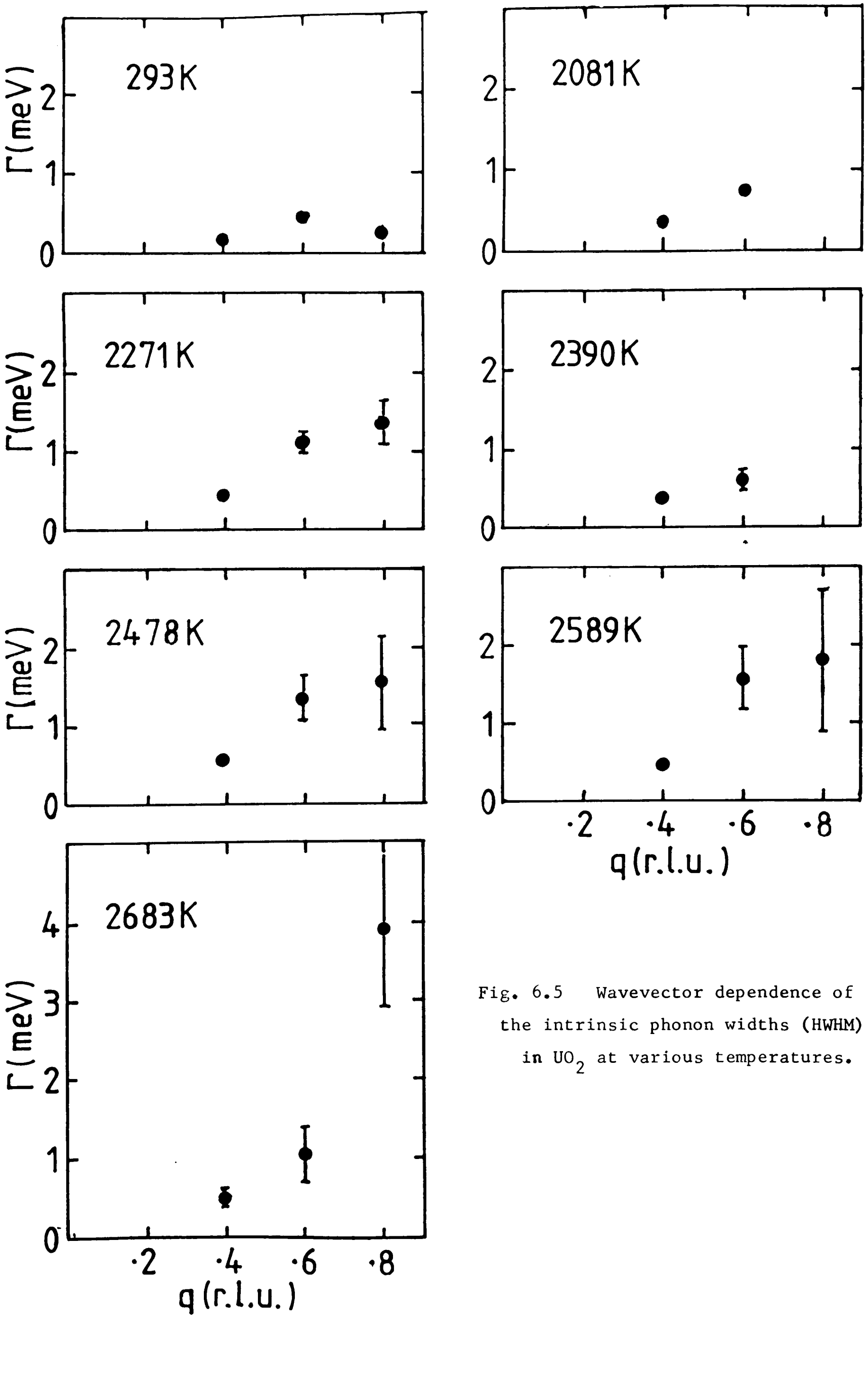

Fig. 6.5 Wavevector dependence of the intrinsic phonon widths (HWHM) in UO_2 at various temperatures.

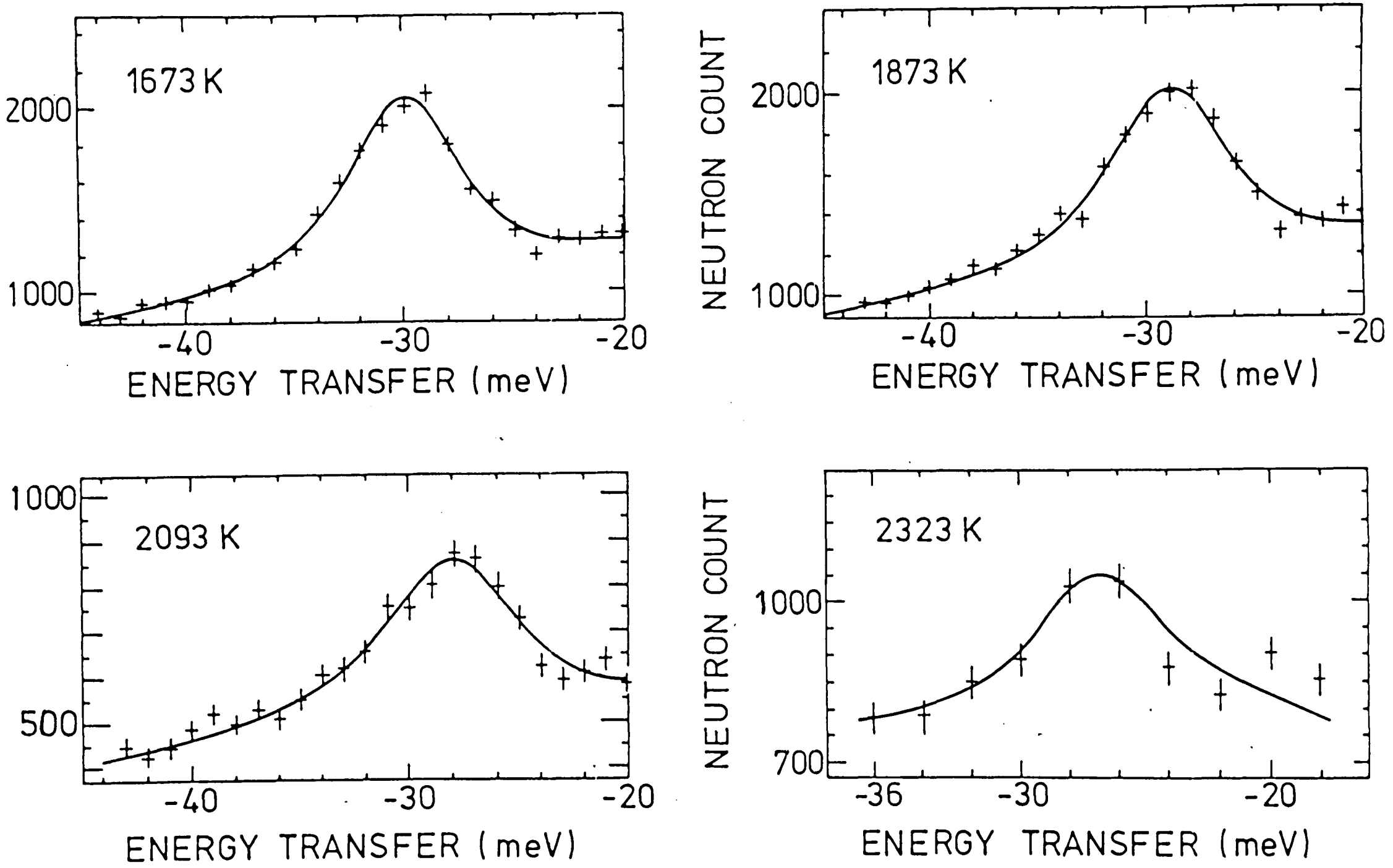

Fig. 6.6 Neutron groups at four temperatures from deexcitation of the $\underset{\sim}{q} = 0$ TO phonon mode in UO_2. The solid lines are best fits of a Lorentzian phonon lineshape convolved with a Gaussian resolution function.

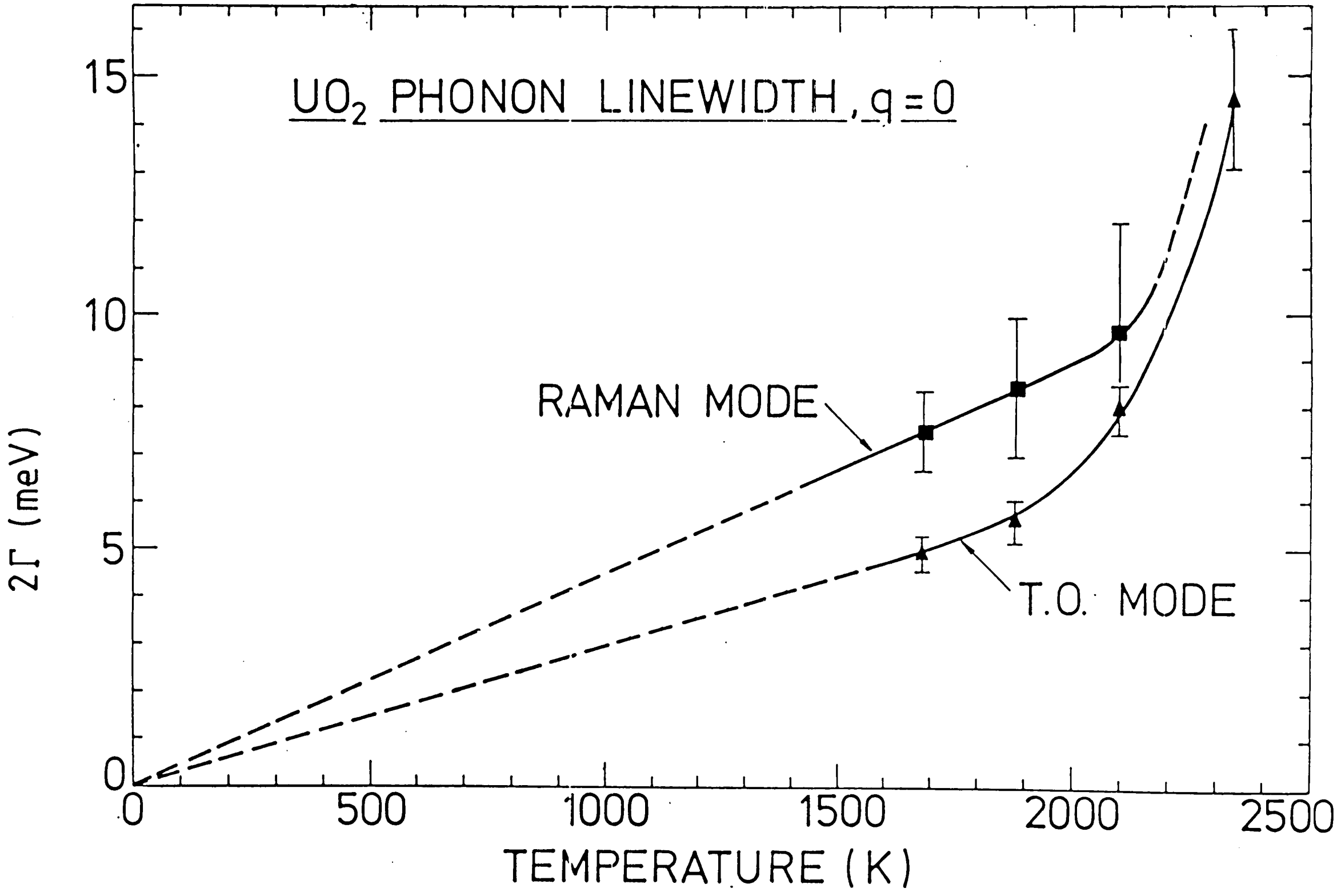

Fig. 6.7 Temperature variation of the intrinsic phonon linewidth 2Γ of the zone centre TO and Raman modes in UO_2.

CHAPTER 7

COHERENT DIFFUSE QUASIELASTIC SCATTERING STUDIES OF UO_2

7.1 INTRODUCTION

Coherent diffuse QES provides valuable information concerning correlations within disordered structures. In dynamically-disordered materials, the energy dependence of the scattering leads to the temporal correlations between nuclei. Such measurements thus complement diffraction experiments, from which the time-averaged structure may be obtained. The results of previous QES investigations of the fluorite halides is summarised in the next section. The present measurements on UO_2 are then described and the results are compared with those for the fluorite halides.

7.2 QES INVESTIGATIONS OF FLUORITE HALIDES

The coherent diffuse QES from PbF_2, CaF_2 and $SrCl_2$ has been investigated in detail over recent years (Clausen et.al. 1981, Schnabel 1983, Hutchings et.al. 1984). All three materials show a rapid increase in the QES intensity along the axis beyond the (002) reciprocal lattice point at temperatures in the region of T_c, as shown in Fig. 7.1 for CaF_2. The scattering observed in this region of reciprocal space energy-broadened, corresponding to a life-time $\tau \sim 3 \times 10^{-2}$ sec, i.e. a few phonon vibration periods. Its line-shape was best described by a Lorentzian function in energy transfer, consistent with an exponential temporal decay of the correlations of the form exp $(-t/\tau)$

$$S(\underset{\sim}{Q},\omega) = S^{D}(Q) \frac{\Gamma(Q)}{\Gamma(\underset{\sim}{Q})^2 + \omega^2} \qquad (7.1)$$

$$\tau(ps) = \frac{4.14}{\pi [2\Gamma(\underset{\sim}{Q})]} \qquad (7.2)$$

where $\Gamma(\underset{\sim}{Q})$ is the HWHM of the Lorentzian (in meV). The evolution of the energy-broadened scattering in CaF_2 is illustrated in Fig. 7.2. The variation of the integrated diffuse QES in the $(1\bar{1}0)$ and (001) planes

has been determined for $SrCl_2$, CaF_2 and PbF_2 (Dickens et.al. 1978, Dickens et.al. 1979a, Schnabel 1983). A contour diagram of the integrated diffuse scattering, $S^D(\underset{\sim}{Q})$, for CaF_2 is shown in Fig. 7.3(a). $S^D(\underset{\sim}{Q})$ has been calculated for the cluster model of §1.4.1 and the resulting contour diagram, shown in Fig. 7.3(b), agrees well with the observed data (Hutchings et.al. 1984). Comparison of the magnitude of the observed and calculated $S^D(\underset{\sim}{Q})$ at a particular $\underset{\sim}{Q}$ near the peak intensity gave a value for the fraction of defective anions in reasonable agreement with that obtained from diffraction measurements (Smith 1980).

7.3 EXPERIMENTAL PROCEDURE

TAS techniques may be used to determine the energy width of scattering at a given $\underset{\sim}{Q}$ and to investigate the distribution of diffuse scattering in reciprocal space. By analysing the scattered neutron energies, diffuse scattering may be distinguished from Bragg and phonon scattering. The latter is particularly important at high temperatures in view of the large phonon population. Diffuse QES in UO_2 has been investigated over four experiments: one preliminary study performed at Risø by K. Clausen and M. T. Hutchings, and three sets of measurements made using the PLUTO TAS at Harwell. These are labelled 1 to 4 respectively, and the experimental details are summarised in Table 7.1. Measurements were confined to the region around the (002) point in reciprocal space, in which the most pronounced QES was observed in the halides, because of the limited life-time of furnace components at high temperatures. Elastic $\underset{\sim}{Q}$ scans ($\omega = 0$), and energy scans at various $\underset{\sim}{Q}$ points in this region were performed during each experiment.

No unambiguous evidence of diffuse scattering was seen up to 2320K during the Risø experiment (Clausen et.al. 1983). During experiments 2 and 3, performed using PLUTO TAS, elastic scans along

TABLE 7.1

EXPERIMENTAL DETAILS OF UO_2 DIFFUSE SCATTERING MEASUREMENTS

Experiment Number	Date	Instrument	Sample	Monochromator Analyser	Collimation M-S, S-A, A-D	Temperatures	Comments
1	Jan. 81	TASI, RISØ	UL1 $(1\bar{1}0)$ plane	M:PG(002) A:PG(002)	26′- 61′- 66′	293K 1286K 1693K 2098K 2298K	Preliminary run with Risø High Temperature Furnace W/5%Re - W/25%Re thermocouples.
2	July 82	PLUTO TAS	UL2 $(1\bar{1}0)$ plane	M:PG(002) A:PG(002)	60′- 27′- 60′	293K 247OK 2536K 2688K	First run above 25OOK with AERE High Temperature Furnace. Crack in sample tube led to a rapid loss of crystal due to evaporation.
3	Feb. 83	PLUTO TAS	UL4 $(1\bar{1}0)$ plane	M:PG(002) A:PG(002)	40′- 27′- 60′	293K 2148K 2398K 2688K 2793K	Several crystallites formed on heating to 2793K. Crystal severely deformed after cooling. Stoichiometry of centre was $UO_{1.93}$ after experiment.
4	March 83	PLUTO TAS	UL5 (001) plane	M:PG(002) A:PG(002)	40′- 27′-60′	293K 2081K 229OK 2478K 2589K 2683K 293K 239OK 2778K 293OK	Detailed measurement of temperature variation of $S^D(Q,\omega)$. Crystal loss due to evaporation above 26OOK. Measurements performed concurrently with those of acoustic phonons described in chapter 6.

the $[\zeta 00]$ direction and energy scans at ζ = 1.8, 2.2 and 2.4 r.l.u. were performed at about 230OK and 268OK. In both experiments an increase in intensity in the region (0, 0, 1.8) to (0, 0, 2.4) was seen at the higher temperature. Transverse elastic scans through (ζ, ζ, 2.15) showed that the scattering was localised on the axis having a width of $\sim 0.8\text{Å}^{-1}$. The energy scans showed some evidence of intrinsic broadening, giving an energy width $2\Gamma \sim$ 0.6 meV at 268OK. Experiment 2 was curtailed after two days at 268OK when the pyrometer sighting tube, on which the sample was mounted, broke due to internal stresses. Experiment 3 was also cut short as a result of sample degradation on further heating to 278OK. The intensity of Bragg and phonon peaks were suddenly reduced by 60% and several other weak Bragg peaks were detected, indicating the break-up of the crystal into small crystallites. On opening the furnace after the experiment, the tungsten sample tube and the UO_2 crystal were found to be badly deformed, as described in §6.2.5. The break-up of the crystal was probably the result of stresses set up during the sample deformation.

On the basis of these brief exploratory measurements, the development of diffuse scattering with increasing temperature was carefully monitored in experiment 4. These measurements were performed concurrently with those of the elastic constants and acoustic phonon widths described in chapter 6. Neutrons of fixed incident wavevector $k_i = 2.673\text{Å}^{-1}$ were monochromated by a pyrolytic graphite crystal and a graphite filter was used to remove higher order wavevectors. The energy resolution was 1.0 meV as determined by the FWHM of scans of elastic incoherent scattering from a vanadium sample and from the furnace and UO_2 sample at low temperature. The sample was orientated with its $\langle 001 \rangle$ axis vertical. The scans performed at each temperature were:

1. Radial elastic scans along (ζ, 0, 0), ζ ranging from 0.5 to 3.0 r.l.u.

2. Transverse elastic scans through the maximum diffuse intensity, (2.15, ζ, 0), ζ ranging from -1.0 to +1.0 r.l.u.

3. Energy scans at constant $\underset{\sim}{Q}$ values of (1.85, 0, 0), (2.15, 0, 0) and (2.4, 0, 0).

4. Frequent energy scans of the (.15, .15, 0)TA phonon at Q = (2.15, 1.85, 0) in order to monitor the crystal quality and alignment. (A phonon peak was preferred to a Bragg peak in order to avoid changing extinction levels.)

The background levels for these measurements were rather high as a consequence of contributions from multi-phonon scattering and incoherent elastic scattering from tungsten components in the furnace. These could not be completely shielded because of the lack of a neutron absorber having a sufficiently high melting temperature. The FWHM of the energy scans increased from 1.0 meV below 2200K to 1.2 meV at 2600K, indicating an intrinsic energy width $2\Gamma \sim$ 0.7 meV. Better resolution, as afforded by the use of low energy ($\sim$ 5 meV) neutrons, is required to determine the energy width accurately. The low flux of 5 meV neutrons from the PLUTO reactor prevented high resolution measurements - spectrometers situated on a cold neutron source, such as IN12 at ILL Grenoble, are needed.

The development of the diffuse scattering in UO_2 between 2081K and 2590K is shown in Fig. 7.4 for the radial elastic scans and in Fig. 7.5 for the transverse elastic scans. On comparison of Fig. 7.4 with the corresponding scan for CaF_2, shown in Fig. 7.1, it may be seen that the excess scattering at high temperatures shows similar characteristics in both compounds. The total integrated intensity, $\mathcal{I}(T)$,

of the three energy scans performed at each temperature were calculated by summing the experimental counts over the peak and subtracting a sloping background estimated from the wings of the scan. The diffuse scattering intensity $\mathcal{I}^D(T)$ at each $\underset{\sim}{Q}$ - point was assumed to be negligible at 2081K, as suggested by the temperature variation of the elastic scans. $\mathcal{I}^D(T)$ was then obtained by subtracting the Debye-Waller - corrected intensity $\mathcal{I}(2081K)$ from $\mathcal{I}(T)$.

$$\mathcal{I}^D(T) = \mathcal{I}(T) - \mathcal{I}(2081K).\exp\left\{-2\left[W_u(T) - W_u(2081)\right]\right\} \qquad (7.3)$$

Since the non-diffuse intensity is mainly due to incoherent scattering by the tungsten furnace components, its Debye-Waller factor was approximated to that of the uranium ion, $\exp(-W_u)$, as determined by diffraction. This gave good agreement between the values of $\mathcal{I}(T)$ at 293K and 2081K.

7.4 ANALYSIS AND RESULTS

7.4.1 EVALUATION OF $S^D(Q)$

On the assumption that the observed diffuse scattering is due solely to disorder in the anion sub-lattice, equation (3.29) may be expressed in the form

$$\left(\frac{d\sigma}{d\Omega}\right)^D_{coh} = \frac{\sigma^a_{coh}}{4\pi} N_a S^D(\underset{\sim}{Q}) = \frac{\sigma^a_{coh}}{4\pi} N_a \exp\left[-2W_a(\underset{\sim}{Q})\right] X^D(\underset{\sim}{Q}) \qquad (7.4)$$

where N_a is the number of anions with coherent cross-section σ^a_{coh} and Debye-Waller factor $\exp\left[-W_a(\underset{\sim}{Q})\right]$. $X^D(\underset{\sim}{Q})$ is the diffuse scattering per anion with the temperature factor removed. $X^D(\underset{\sim}{Q})$ may be calculated for an assembly of small, uncorrelated non-interacting defect clusters of differing kinds (Hutchings et.al. 1984). Assuming that the scattering is due to one kind of cluster, $X^D(\underset{\sim}{Q})$ may be expressed as

$$X^D(\underset{\sim}{Q}) = n_d \, . \, Y^D(\underset{\sim}{Q}) \qquad (7.5)$$

where $Y^D(Q)$ is the scattering per defective anion (interstial or relaxed ion) in the cluster, averaged over N_o possible orientations of the cluster relative to the lattice, n_d is the fraction of defective anions and N_d is the number of defective anions per cluster.

$$Y^D(Q) = \frac{1}{N_d}\frac{1}{N_o}\sum_{j=1}^{N_o} \mathcal{F}_j(Q)\,\mathcal{F}_j^*(Q) \qquad (7.6)$$

where $\mathcal{F}_j(Q) = \sum_{R_j^I} e^{iQ.R_j^I} - \sum_{R_j^V} e^{iQ.R_j^V}$

is the structure factor for the cluster in orientation j. The summation is made over all interstitials and vacancies, due to true Frenkel pairs or due to relaxations within the cluster, R_j^I and R_j^V being their site locations relative to the cluster centre. Equation (7.6) shows that the diffuse scattering originates from deviations of ionic positions from the regular structure.

7.4.2 QUALITATIVE FEATURES OF $S^D(\underset{\sim}{Q})$

The variation of $S^D(\underset{\sim}{Q})$ in the $(1\bar{1}0)$ and (001) reciprocal lattice planes, arising from a given cluster, may be calculated using a suite of programs written by K. Clausen. The co-ordinates of the vacancies and interstitials in the cluster are input into the first program, DATAGEN, which generates the symmetry-related orientations of the cluster by 4-fold rotation and inversion. A second program, SQWDIF, calculates $S^D(\underset{\sim}{Q})$ from the co-ordinates produced by DATAGEN, using equation (7.6). The scattering from different orientations of the cluster are thus summed incoherently. A contour diagram of $S^D(\underset{\sim}{Q})$ in either plane may be produced using a third program SQPLOT.

Contour diagrams of $S^D(\underset{\sim}{Q})$ for UO_2 have been calculated for models based on those fitted to the diffraction data. The models considered

are denoted III, IV, VA, VB, VIA, VIB and VII. The nomenclature is consistent with that of §4.4.2, where a detailed description of the models is given. Model III represents a Frenkel interstitial occupying an empty cube-centre. Model IV consists solely of interstitial ions situated at the I sites. Relaxations of all eight nearest neighbour anions in the (111) directions towards the cation and away from the cation are represented in models VA and VB respectively. Such relaxations might occur around U^{5+} and U^{3+} ions respectively. Models VIA and VIB represent 3:1:2 clusters comprising one interstitial ion at an I site with its two nearest neighbours relaxed off in (111) directions (R sites). In model VIA the positional parameters x and y were set to the refined values obtained from the diffraction measurements of chapter 4. For model VIB, x and y were determined using a hard sphere model of the ions, assuming that the cation displacement is negligible. Cation - anion distances only were considered, since they are independent of the effects of covalency on the ionic radii. Model VII represents a 4:2:2 cluster in which two interstitial ions occupy I sites equidistant from the same mid-anion position.

Initially the vacancy associated with the true interstitial ion was positioned at (0, 0, 1.25) along the axis of the cluster relative to the mid-anion position, as suggested by static energy calculations for a 3:1:2 cluster (Catlow and Hayes, 1982). This gave rise to an additional peak in $S^{D}(\underset{\sim}{Q})$ at about (0, 0, 2.7), which does not agree with the observed data (Fig. 7.4). For the calculations given here, the vacancy was positioned away from the cluster axis at (.5, .5, 1.25) with respect to the mid-anion position. The scattering was found to be insensitive to the position of the vacancy, provided that it is situated away from high symmetry positions e.g. along the axis of a 3:1:2 cluster.

The values of the positional parameters x, y used in the these calculations are summarised in Table 7.2 and the resulting contour diagrams of $S^D(\underset{\sim}{Q})$ are shown in Fig. 7.6.

The calculated contour diagrams may be compared with the elastic scans shown in Figs. 7.4 and 7.5. These scans approximate well to $S^D(Q) = \hbar \int S(Q,\omega)d\omega$ since the energy resolution is broader than the energy width of the scattering. Despite the limited extent of the data, certain conclusions may be drawn from such a comparison. Models III (cube-centre) and IV (I-sites only) may be discounted because of the additional peaks which they give along the (00ζ) axis. Model VA ((111) relaxations towards U^{5+} ions) gives a large peak at (0, 0, 1.5) which is also inconsistent with the data. Model VB ((111) relaxations away from U^{3+} ions) gives an intense peak at (0, 0, 2.4) having a Q-width of $\sim 0.8\mathring{A}^{-1}$. The peak is consistent with the data, but it is situated at slightly too large a Q-value and it also gives a weak additional peak at (0, 0, 1.0). Models VIA and VIB (3:1:2 cluster) do give a peak at (0, 0, 2.15) in agreement with the data. However for model VIA, in which the diffraction values of x and y are used, the intensity is very weak and there are additional peaks at (0, 0, 0.9) and (0, 0, 2.4). The use of hard-sphere parameters in model VIB results in a correctly-positioned peak at (0, 0, 2.15) with no additional peaks along the axis. Increased peak intensity but no basic change of pattern results from the introduction of (100) relaxations around the true vacancy at (.5, .5, 1.25). Model VII (4:2:2 cluster with hard-sphere parameters) gives a similar distribution of $S^D(\underset{\sim}{Q})$ to model VIB with a larger peak intensity.

We conclude from this comparision that the 3:1:2 cluster model, which accounted best for the diffraction results, is also consistent

TABLE 7.2

CLUSTER MODEL PARAMETER FOR $S^{D}(\underset{\sim}{Q})$ CALCULATIONS

Model	III	IV	VA	VB	VIA	VIB	VII
Number of Defective Anions	1	1	8	8	3	3	4
Number of Frenkel Interstitials	1	1	0	0	1	1	2
x	0.50	-	0.16	0.39	0.34	0.39	0.39
y	-	0.16	-	-	0.04	0.16	0.16
$Y(\underset{\sim}{Q}_{o})$	2.5	2.0	-	9.8	1.1	3.7	5.2

$\underset{\sim}{Q}_{o}$ is the value of $\underset{\sim}{Q}$ at the maximum calculated QES intensity in the near vicinity of (0, 0, 2.15)

with the QES data described here, but the QES results do indicate a larger value of the positional parameter y than obtained from diffraction. However, detailed investigation of the variation of $S^D(Q)$ in the $(1\bar{1}0)$ and (001) planes is needed to provide further information about the exact nature of the cluster. It is unclear why the hard-sphere model values of x and y are preferable to those obtained from the diffraction analysis. Such a discrepancy was also seen in the halides CaF_2, $SrCl_2$ and PbF_2 (Hutchings et.al. 1984). The two sets of relaxation values for UO_2 and the halides, obtained from the diffraction results and from the hard-sphere model, are summarised in Table 7.3.

7.4.3 $S^D(Q)$ ON AN ABSOLUTE SCALE

Having compared the form of the calculated $S^D(\underset{\sim}{Q})$ with the observed data, we now determine the observed $S^D(\underset{\sim}{Q})$ on an absolute scale. The integrated intensity, $\mathcal{I}^D(T)$, may be compared with that of a given phonon peak, $\mathcal{I}^{ph}(T)$, in order to remove the unknown constants, namely the spectrometer parameters and the number of atoms in the crystal. This also corrects for the loss of crystal experienced at the higher temperatures. The procedure and details of the normalisation are described in Appendix A.6. The resulting temperature variation of $X^D(Q)$ at $Q = (\zeta, 0, 0)$ for $\zeta = 1.85$, 2.15 and 2.4 is shown in Fig. 7.7. The diffuse intensity increases dramatically at about 240OK for $\zeta = 2.15$, whereas the increase is far less marked for $\zeta = 1.85$ and 2.4.

A comparison of the experimentally determined $X^D(Q)$ at $Q = (2.15,0,0)$ with the scattering per defective ion $Y^D(Q)$ at the corresponding peak intensity near $Q = (2.15, 0, 0)$, calculated in the previous section, yields the fraction of defective anions n_d via equation (7.5). The values of $X^D(Q)$ and the corresponding values of $Y^D(Q)$ and n_d for the various models are listed in Table 7.4. In Fig. 7.8, a comparison is

TABLE 7.3

COMPARISON OF THE POSITIONAL PARAMETERS x, y OF RELAXED AND INTERSTITIAL IONS IN THE 3:1:2 CLUSTER MODEL

	Hard Sphere Model		Diffraction	
Material	x	y	x	y
CaF_2 †	0.37	0.15	0.33	-
$SrCl_2$ †	0.40	0.14	0.38	0.04
PbF_2 †	0.36	0.16	0.37	0.07
UO_2	0.39	0.16	0.34	0.04

† Hutchings et.al. 1984

TABLE 7.4

VALUES OF $X^D(\underset{\sim}{Q})$ FOR THE THREE $\underset{\sim}{Q}$ VALUES INVESTIGATED, AND THE RESULTING VALUES OF $n_d = X^D(\underset{\sim}{Q})/Y^D(\underset{\sim}{Q})$ EVALUATED AT $\underset{\sim}{Q} = (2.15, 0, 0)$ FOR VARIOUS CLUSTER MODELS

Error in last digit(s) shown in parentheses

	$X^D(\zeta, 0, 0)$ for $\zeta =$			n_d evaluated for Model					
T(K)	1.85	2.15	2.4	III	IV	VB	VIA	VIB	VII
293	-0.003(29)	-0.028(18)	-	-0.01	-0.01	-0.00	-0.02	-0.01	-0.01
2081	0.0	0.0	0.0						
2271	0.100(30)	0.095(32)	-0.081(33)	0.03	0.04	0.01	0.07	0.02	0.01
2390	-	0.080(54)	0.157(60)	0.03	0.03	0.01	0.06	0.02	0.01
2478	0.183(45)	0.365(57)	-0.004(50)	0.11	0.14	0.03	0.26	0.08	0.05
2589	0.251(56)	0.457(74)	0.068(63)	0.14	0.18	0.04	0.33	0.10	0.07
2683	0.069(50)	0.373(72)	0.012(64)	0.12	0.14	0.03	0.27	0.08	0.06
2771		0.444(99)	0.114(90)	0.14	0.17	0.04	0.32	0.09	0.07
		$Y^D(2.15, 0, 0)$		3.2	2.6	12.6	1.4	4.8	6.7

made of the variations of n_d, obtained using models VB, VIA, VIB and VII to calculate $Y^D(Q)$, with that obtained from the diffraction measurements. Of the models postulated, model VIB (3:1:2 cluster with hard-sphere model relaxations) is preferred since it gives the best overall agreement for the contour diagrams of $S^D(\underset{\sim}{Q})$ and for the temperature variation of n_d.

7.4.4 ENERGY WIDTH OF $S^D(Q)$

In order to gain information on the dynamic nature of the disorder, the temperature variation of the energy width of the QES is needed. As explained in §6.3.2, this involves fitting the energy scans at constant $\underset{\sim}{Q}$ with a function representing a sum of contributions to the observed intensity. In this analysis, the diffuse peak was represented by a Lorentzian function, which gave the best description of $S^D(\underset{\sim}{Q},\omega)$ for the halides (Schnabel 1983). A function of the form

$$\mathcal{J}(\underset{\sim}{Q}_o,\omega_o) = (B_o + B_S\omega_o) + S_G \exp(-a^2\omega_o^2) + \int S_L \frac{\Gamma(Q_o)}{\Gamma(Q_o)^2 + \omega^2} \cdot R'_o \exp\left\{-a^2(\omega - \omega_o)^2\right\} d\omega \qquad (7.7)$$

was fitted to the observed intensities at each point $(\underset{\sim}{Q}_o,\omega_o)$ in the spectra. The first term represents a sloping background, the second term the resolution-limited incoherent scattering from furnace components, and the third term the Lorentzian QES peak, convoluted with the resolution function. Since $S^D(\underset{\sim}{Q},\omega)$ varies slowly with $\underset{\sim}{Q}$, use was made of the simplified expression for the resolution function, described in equations (3.41 - 3.43). The value of $a = 1.67\ meV^{-1}$ was determined by fitting the first two terms of equation (7.7) to a vanadium scan. The value of the Gaussian scale factor S_G was fixed at each temperature to $S_G(2081K) \exp\left\{-2\left[W_u(T) - W_u(2081)\right]\right\}$, as in equation (7.3), where $S_G(2081K)$ was obtained from a fit to the 2081K data with $S_L = 0$. The fitted parameters at higher temperatures were B_o, B_S, the Lorentzian

scale factor S_L and FWHM $2\Gamma(Q_o)$, and a parameter $\Delta\omega \approx 0$ which accounts for small spectrometer misalignments.

The diffuse intensity in the spectra at $\underset{\sim}{Q}$ = (1.85, 0, 0) and (2.4, 0, 0) proved to be too weak to obtain reliable fits of its intensity and width. For the (2.15,0,0) spectra, both S_L and $\Gamma(Q_o)$ increase with temperature up to 2600K and then seem to decrease at higher temperatures. The fit to the 2478K data is shown in Fig. 7.9. The results are summarised in Table 7.5 and the temperature variation of 2Γ is shown in Fig. 7.10. At 2600K, 2Γ is about 0.7 meV, which corresponds, by equation (7.2), to a life-time $\tau \sim 2$ ps, i.e. a few phonon periods. This value agrees with the corresponding lifetimes for the halides, which range from 0.8 ps to 2.7 ps for PbF_2, $SrCl_2$ and CaF_2 (Schnabel 1983).

The decrease in the Lorentzian intensity above 2600K is due to crystal loss and may be corrected by the normalisation procedure described in the previous section. The apparent decrease in 2Γ is more difficult to understand. It may be due to the wings of the broadened Lorentzian being included in the background contribution, thus increasing B_o and decreasing 2Γ. (It should be noted that there is also a growing multiphonon contribution to B_o at high temperatures.) High-resolution studies are clearly needed in order to resolve the diffuse QES and to investigate more accurately the evolution of its intensity and width.

7.4.5 ROOM TEMPERATURE SCANS

An interesting effect was noticed in sample UL5 (experiment 4) on cooling from high temperatures. During the [ζ, 0, 0] elastic $\underset{\sim}{Q}$ scan performed at room temperature after cooling from 2683K, a puzzling

TABLE 7.5

RESULTS OF FITS TO ENERGY SCANS AT $\underset{\sim}{Q}$ = (2.15, 0, 0) OF QES IN UO_2

Error in last digit(s) shown in parentheses

T(K)	S_G	B_o	B_S	S_L	2Γ (meV)	$\Delta\omega$(meV)	χ^2
293[a]	100.1(54)	21.2(10)	-1.3(5)	0[†]	-	0.12(3)	1.79
2081	93.0(54)	25.8(12)	-2.4(5)	0[†]	-	0.11(3)	1.41
2271	90.5[†]	27.9(23)	-1.7(7)	27(14)	0.39(67)	0.11(3)	1.80
2390[b]	88.7[†]	29.9(26)	-2.5(8)	15(16)	0.44(144)	0.03(3)	1.34
2478	87.0[†]	31.5(28)	-2.5(8)	99(19)	0.63(27)	0.09(3)	1.24
2589	84.4[†]	34.3(38)	-2.2(9)	126(29)	1.14(40)	0.08(3)	1.41
2683	81.8[†]	41.9(35)	-1.6(9)	81(24)	0.81(44)	0.16(3)	1.28
2771	79.3[†]	40.9(27)	-2.6(9)	54(15)	0.28(34)	0.09(3)	1.25

[†] fixed value

[a] before heating

[b] performed after 2683K run

additional sharp peak was noticed at (2.18, 0, 0) which was not present in the initial room temperature run before heating. It was not seen at high temperatures (>2000K) before or after its observation at room temperature, but it reappeared on subsequent cooling. Radial and transverse $\underset{\sim}{Q}$ - scans and an energy scan, shown in Fig. 7.11, demonstrated that the peak was elastic and situated exactly on the symmetry axis, thus indicating that it originated from the crystal.

This peak may be due either to a surface reaction, forming compounds which vaporise or dissociate on heating, or to the formation of other phases of uranium oxide, such as U_4O_9, on cooling from ~2700K. However in view of the similarity between the lattice constants of UO_2 and other oxides, Bragg peaks from other oxides would be expected to occur nearer to the (002) Bragg point. This effect clearly requires further investigation.

7.5 SUMMARY AND CONCLUSIONS

In this chapter, a preliminary investigation of diffuse quasielastic scattering from UO_2 has been reported. Elastic scans and energy scans at constant $\underset{\sim}{Q}$ indicate that a diffuse peak, which shows evidence of energy broadening, develops around $\underset{\sim}{Q}$ = (0, 0, 2.15) at temperatures above 2000K. It occurs in the same region of reciprocal space as the diffuse QES which characterises the halides CaF_2, PbF_2 and $SrCl_2$ in their fast-ion phase. Good qualitative agreement for the wave-vector dependence of the scattering is given by a 3:1:2 cluster model, similar to that deduced from the diffraction data. Estimates of the fraction of defective anions n_d for this model are also in reasonable agreement with the values obtained from diffraction. The limited data do suggest that the scattering is of a similar nature to that occuring in the halides, and indicate the existence of dynamic anion disorder in

UO_2 above 2300K. However it should be stressed that the disordered state is complex and highly dynamic and that the cluster model, developed to account for the diffraction and QES data, may ultimately prove to be an oversimplification of the true nature of the anion disorder.

Further measurements are required of $S^D(Q)$ throughout the $(1\bar{1}0)$ and (001) planes, and of the energy width as a function of $\underset{\sim}{Q}$ and temperature, using a high resolution spectrometer. An anomalous peak at (2.18, 0, 0), observed at room temperature after cooling from 2683K, also requires further investigation.

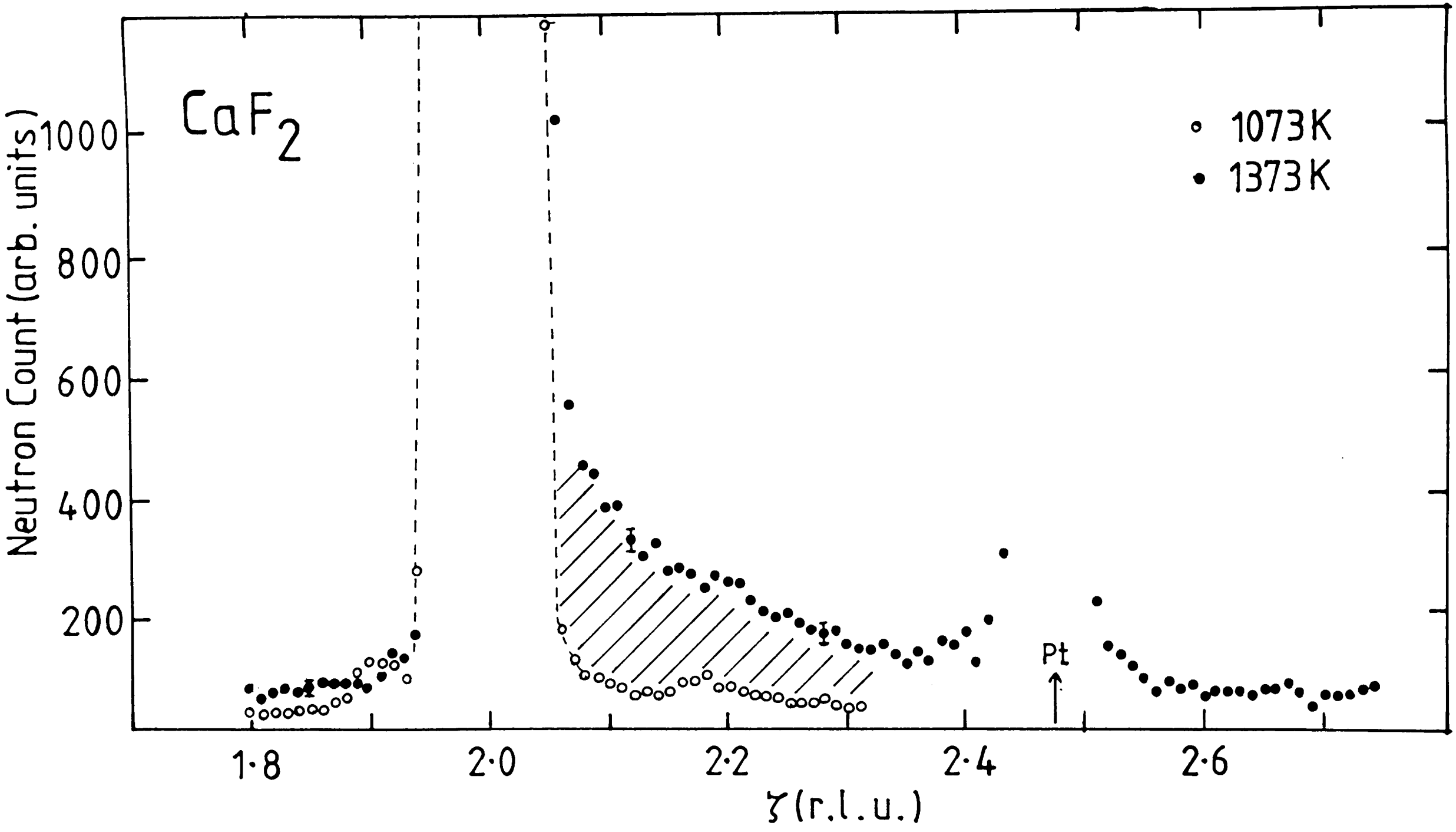

Fig. 7.1 Elastic diffuse scattering along [ζ00] at two temperatures in CaF_2. The shaded area indicates the increase in diffuse scattering as the temperature is raised. Also shown are the (002) Bragg peak and a platinum (111) Bragg peak from the sample can.

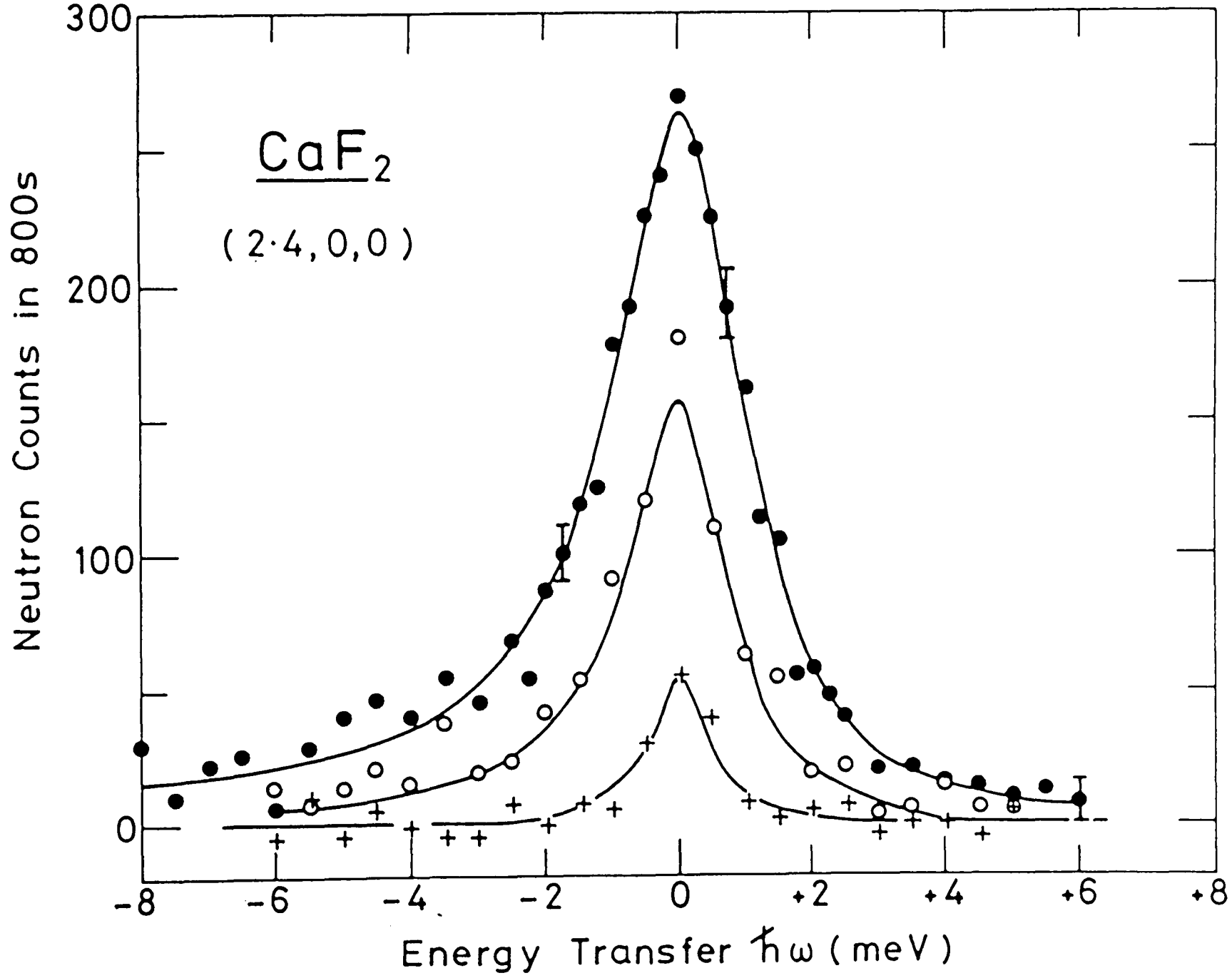

Fig. 7.2 Typical coherent diffuse QES in CaF_2 observed by constant $\underset{\sim}{Q}$ scans of energy transfer at different temperature
+ 1273K **O** 1373K **●** 1473K .

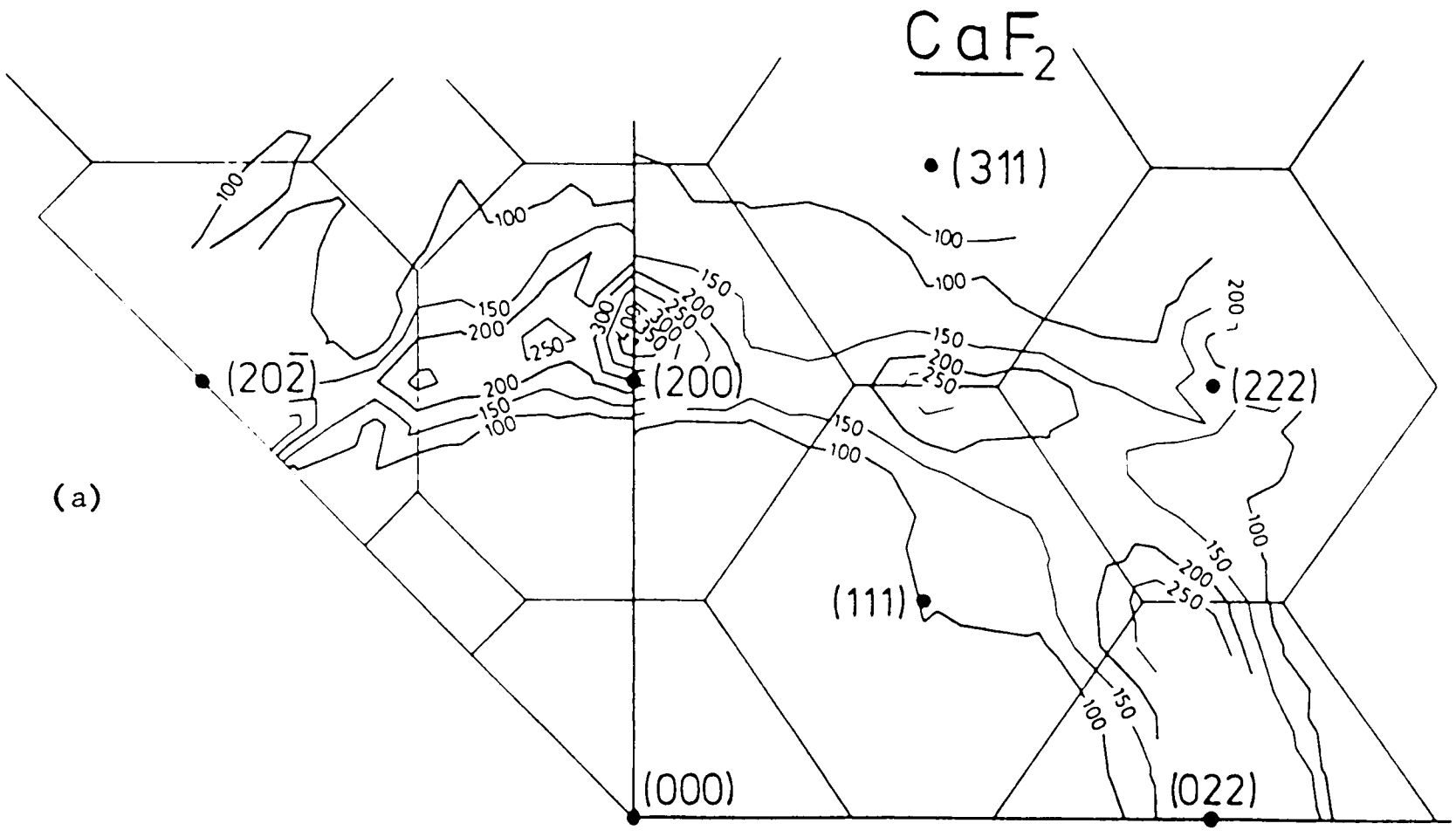

Fig. 7.3 (a) Contour diagram of observed diffuse QES intensity $S^D(Q)$ in the (110) and (010) planes of CaF_2 at 1473K. (b) Contour diagram of $S^D(Q)$ calculated using a 9:1:8 cluster model, which consists of a 3:1:2 cluster with relaxation of nearest neighbours around the 'R' site anions of the 3:1:2 cluster.

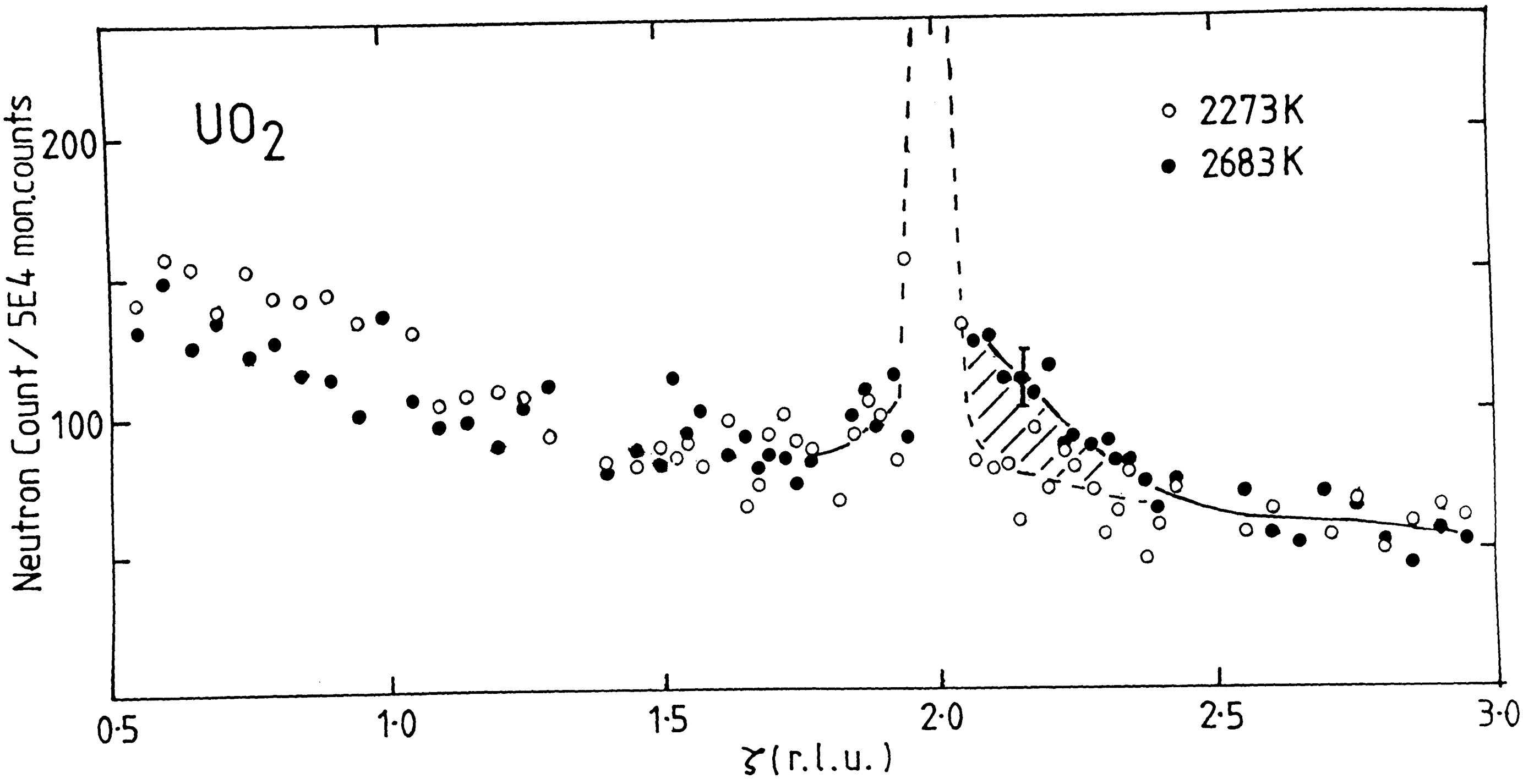

Fig. 7.4 Elastic diffuse scattering along [ζ00] at two temperatures in UO_2. The shaded area indicates the evolution of diffuse scattering as the temperature is raised, which is similar to that observed in CaF_2 (Fig. 7.1). The solid and broken lines are guides to the eye.

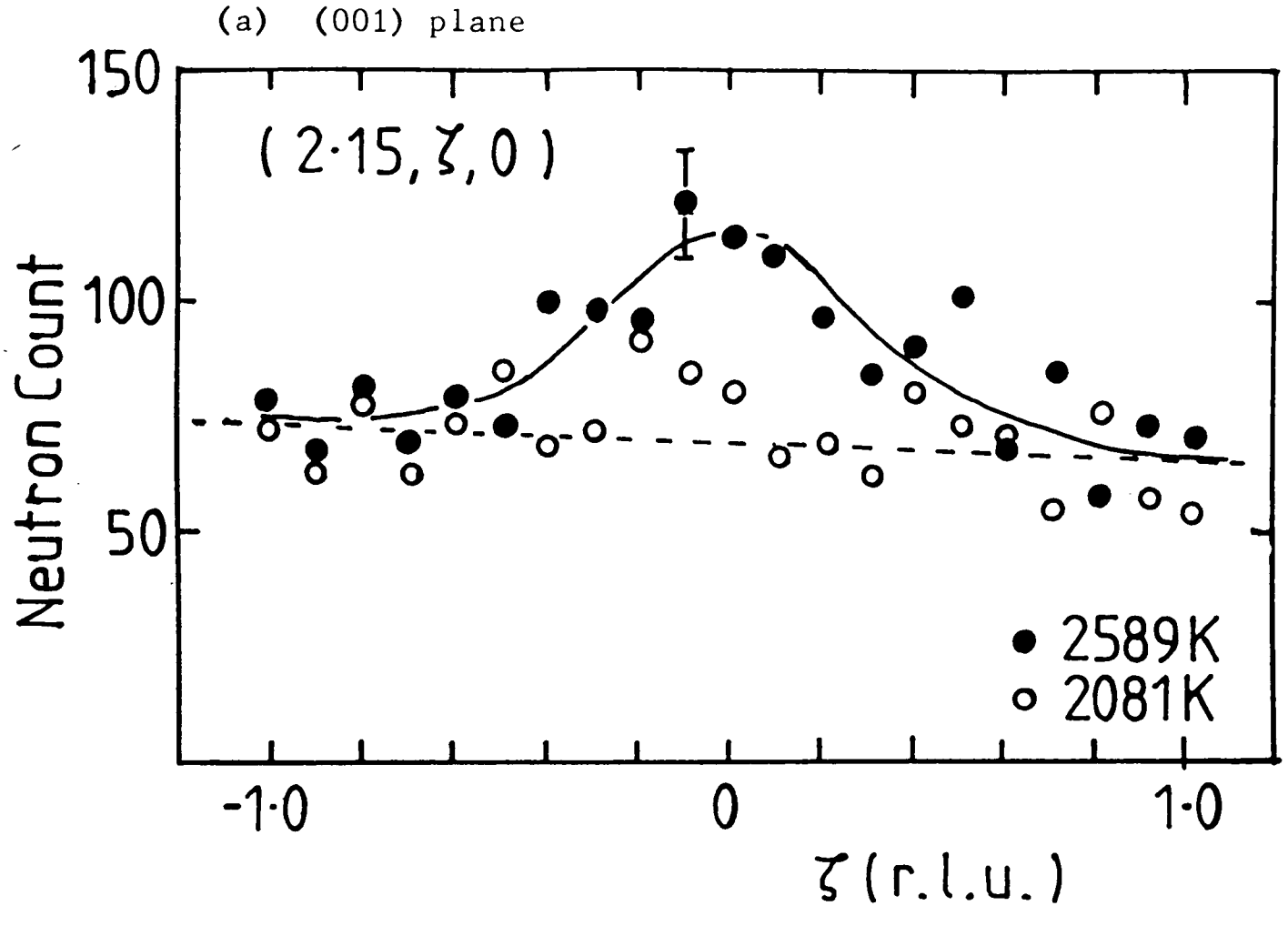

Fig. 7.5 Tranverse elastic scans through the diffuse peak at (0,0,2.15) in UO_2 in the (a) (001) plane (b) (1$\bar{1}$0) plane. The lines are guides to the eye.

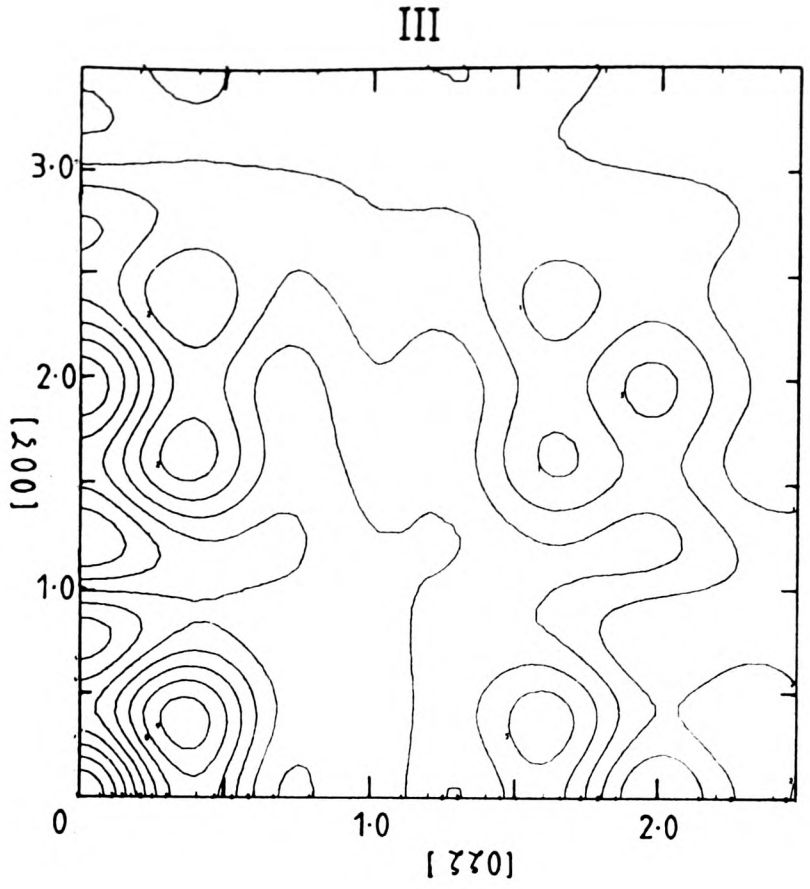

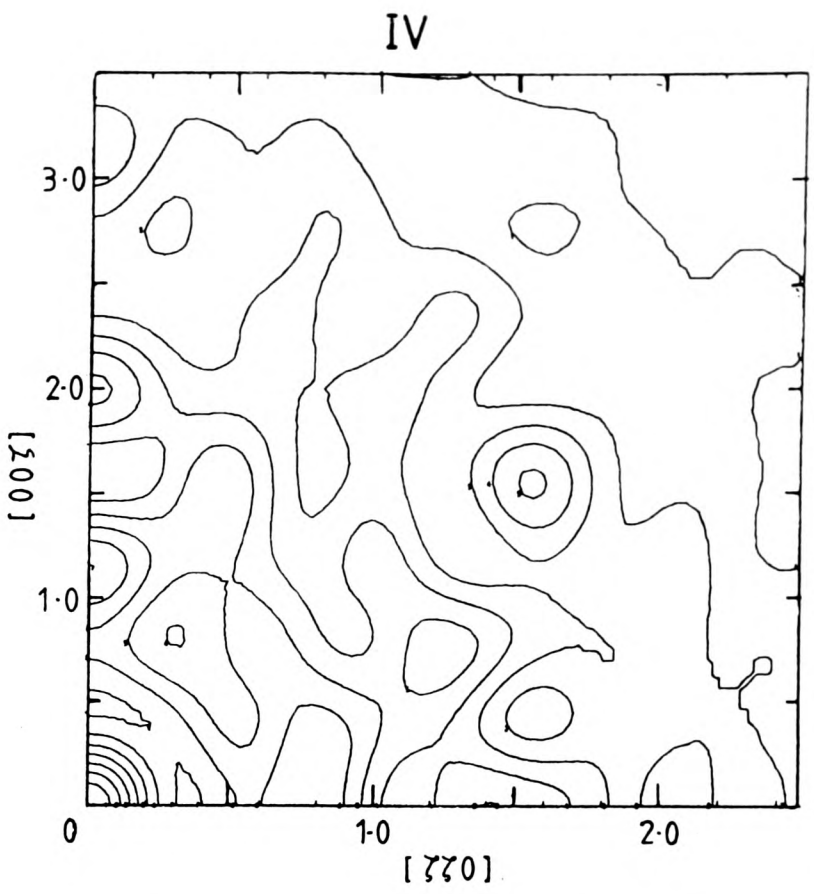

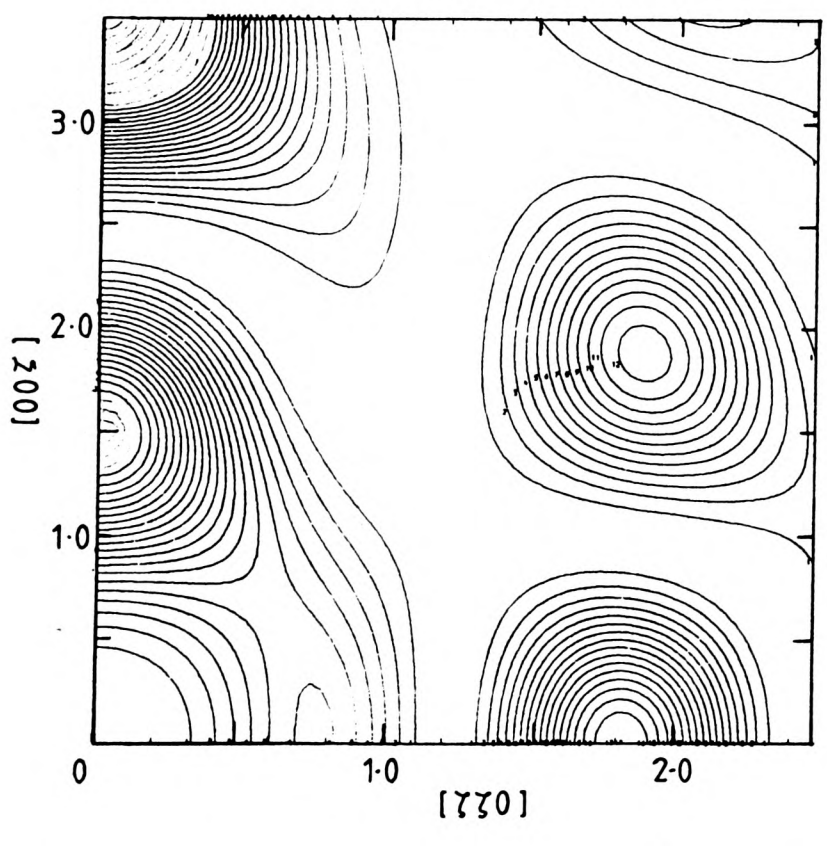

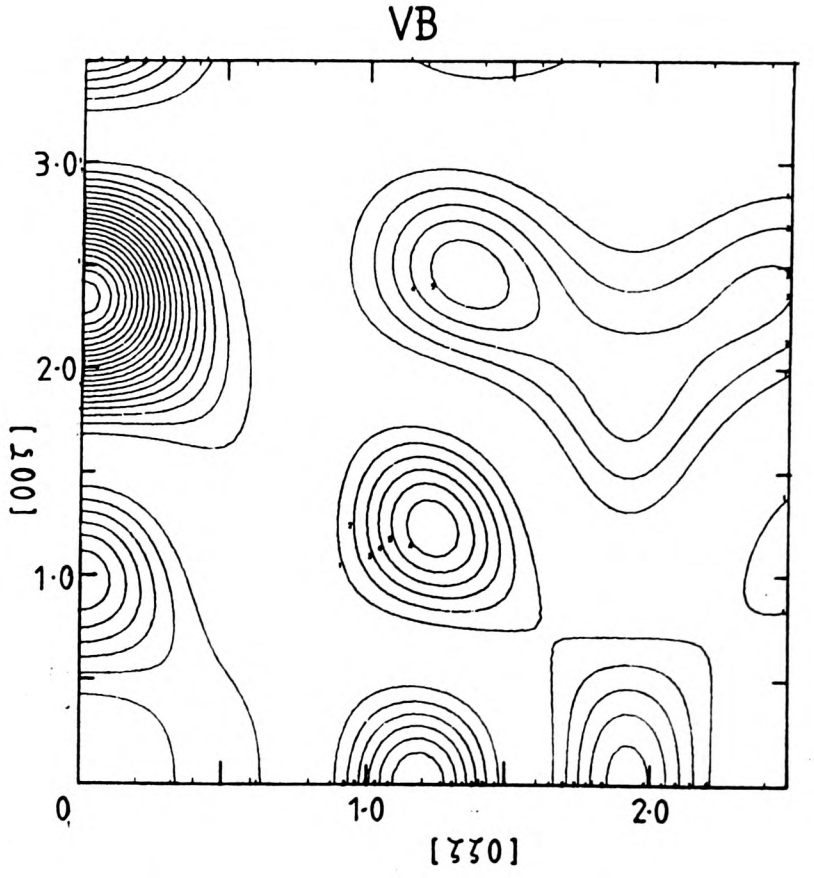

Fig. 7.6 Contour diagrams of $S^{D}(\underset{\sim}{Q})$ in UO_2 calculated for various models of the disordered structure. The models are : III - cube-centre interstitial, IV - 'I' site interstitial, VA - 8 nearest neighbour anions relaxed in [111] directions towards a cation, VB - 8 nearest neighbour anions relaxed in [111] directions away from a cation, VIA - 3:1:2 cluster(diffraction values of relaxations), VIB - 3:1:2 cluster (rigid sphere model values of relaxations), VII - 4:2:2 cluster (rigid sphere model values of relaxations).

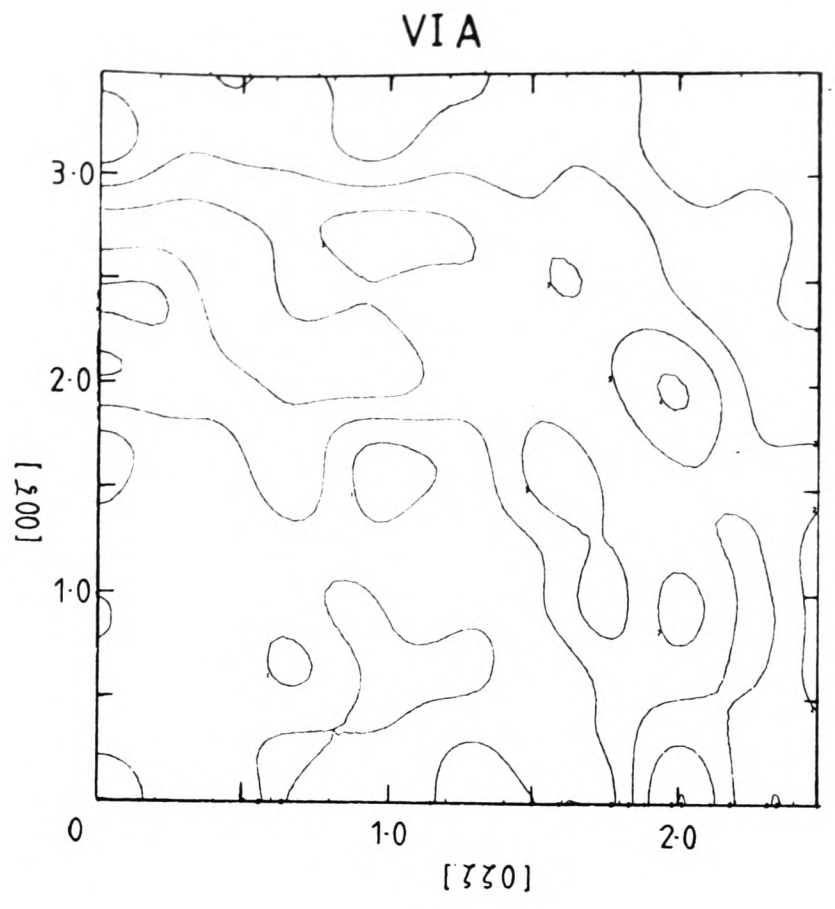

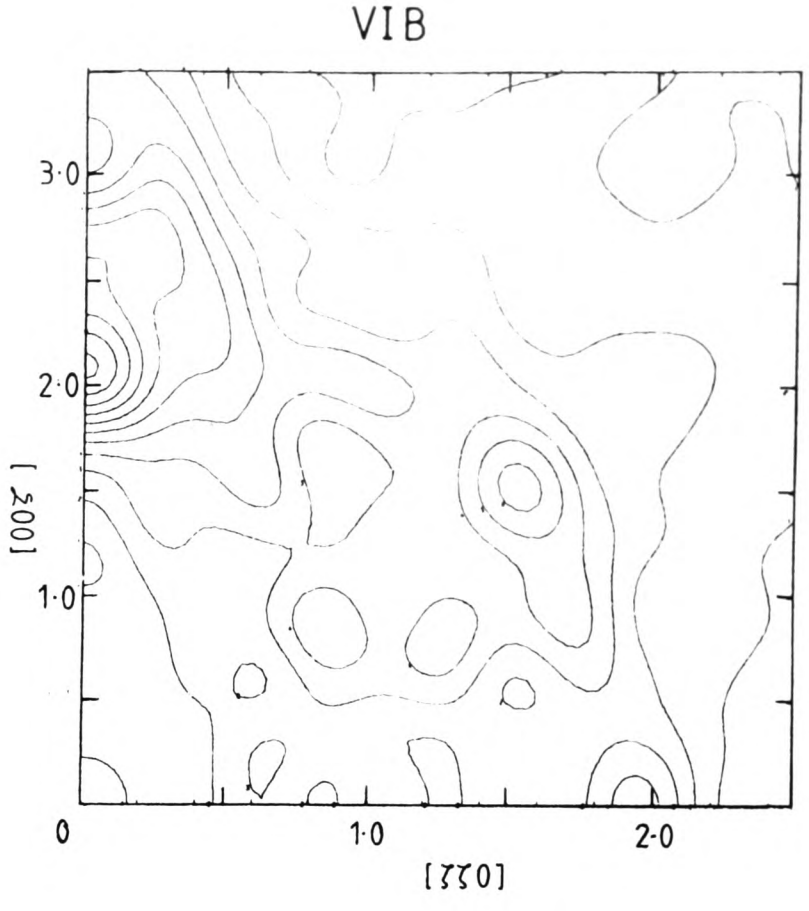

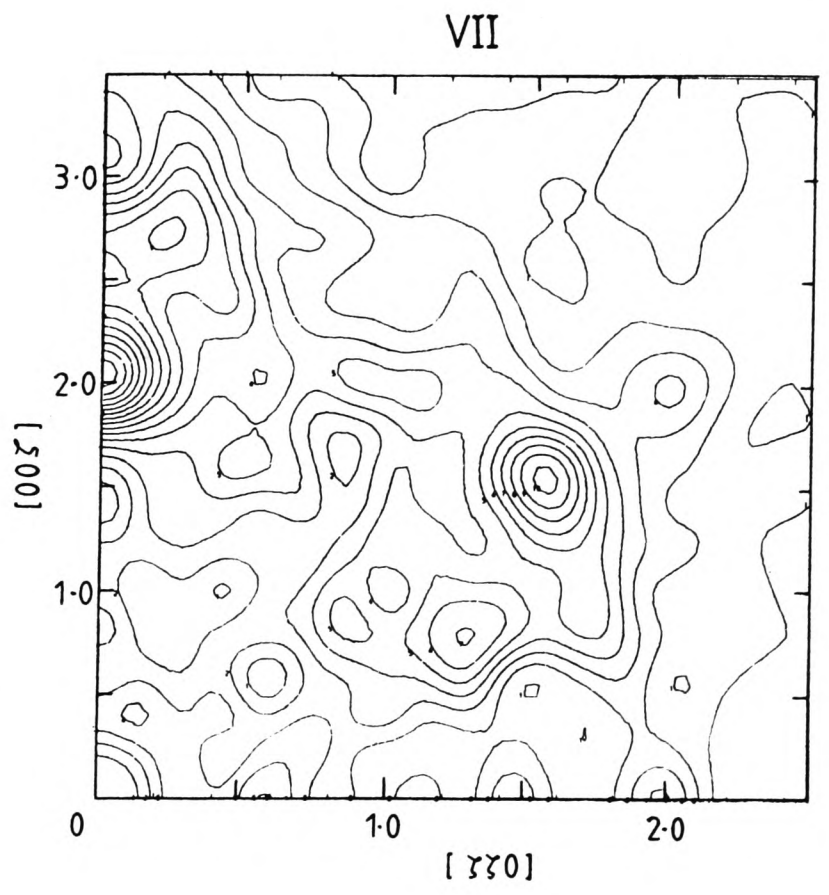

Fig. 7.6 (continued)

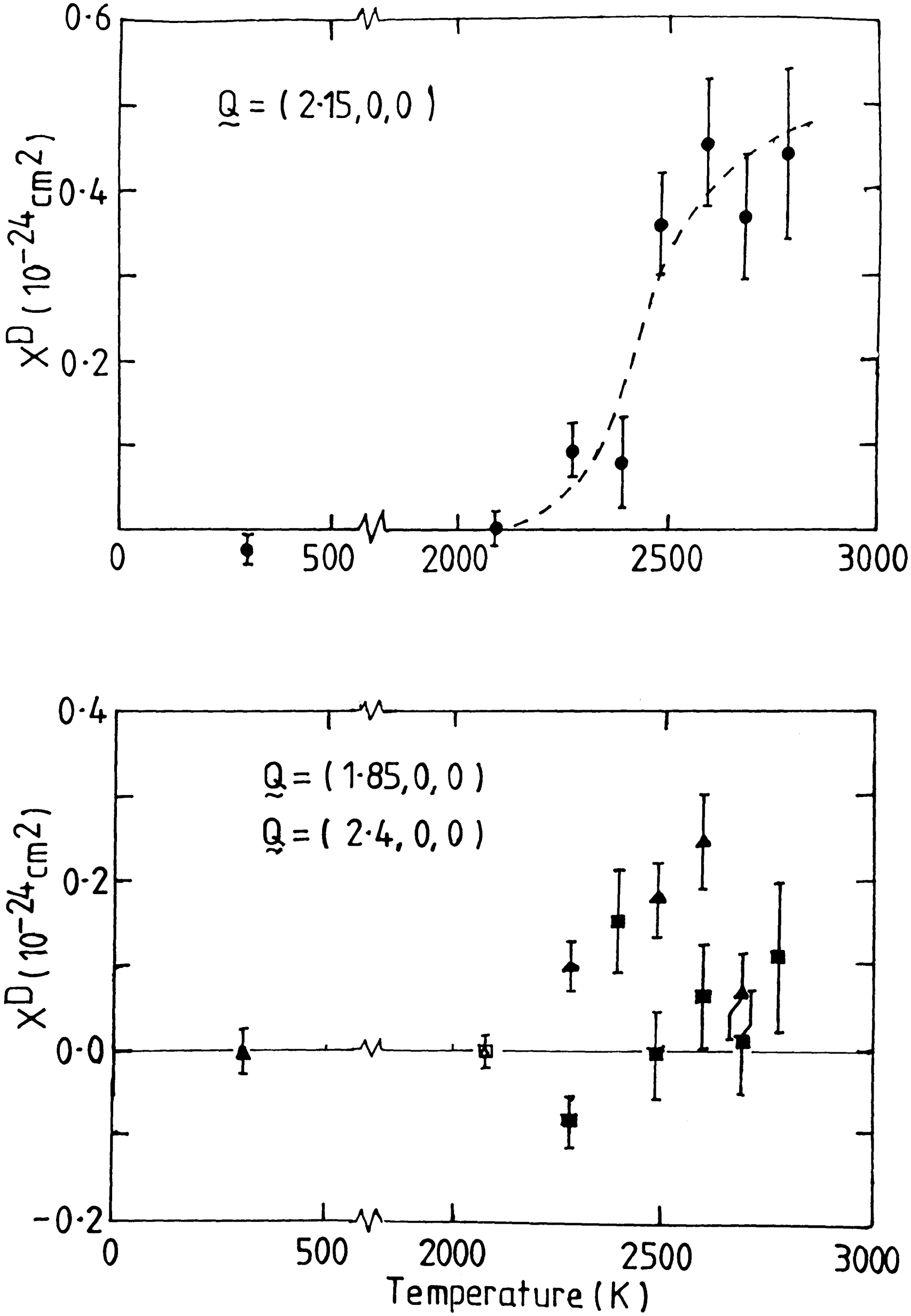

Fig. 7.7 Temperature variation of the diffuse scattering per anion $X^D(\underset{\sim}{Q})$ in UO_2 at three $\underset{\sim}{Q}$ values.

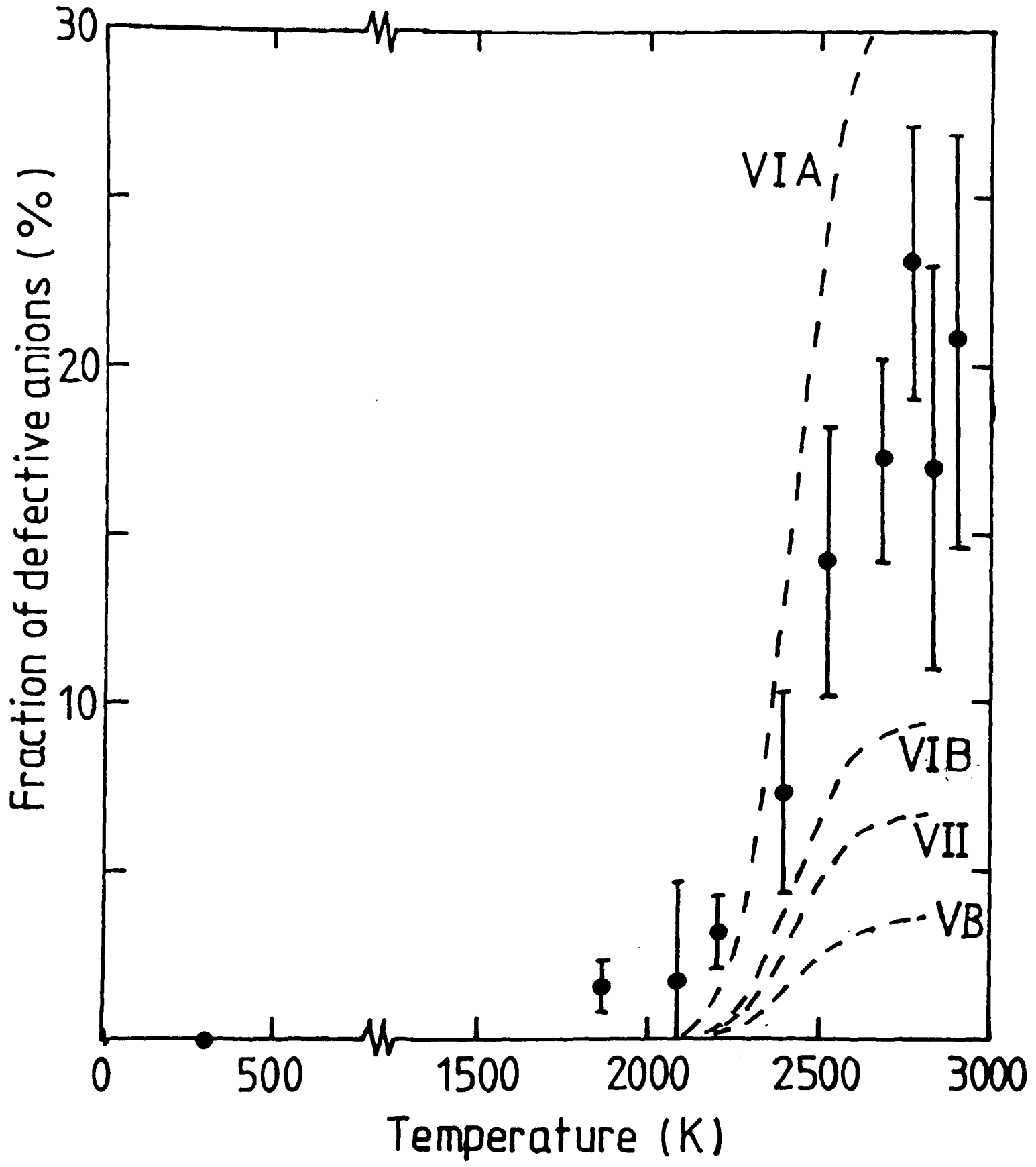

Fig. 7.8 A comparison of the temperature variation of n_d obtained from diffraction results with those deduced from the diffuse QES data using different models of the disordered structure.

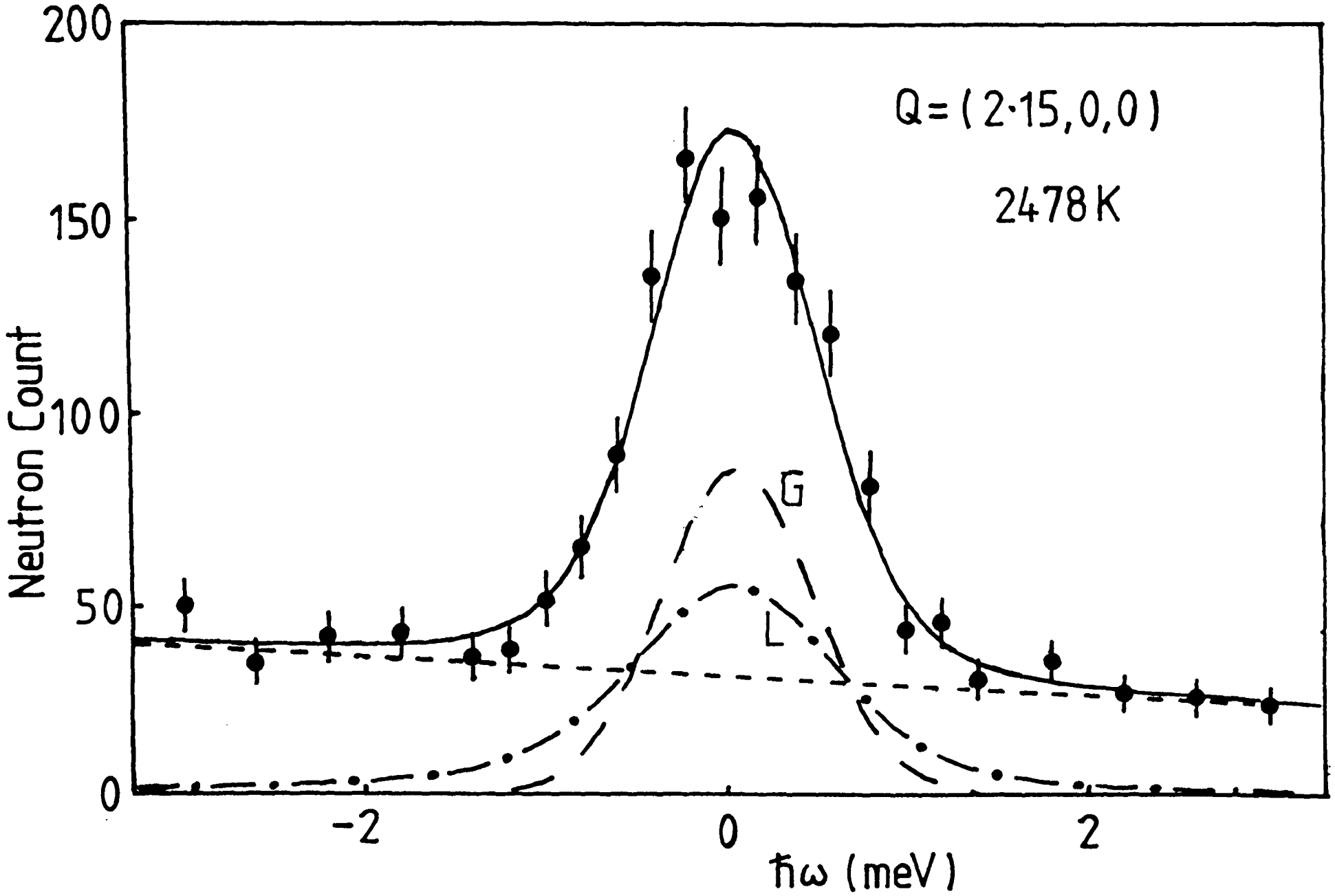

Fig. 7.9 A typical energy scan at constant $\underset{\sim}{Q}$ of the quasielastic peak in UO_2 at 2478K. The fitted function (____) consists of a sum of a sloping background (_ _ _), a Lorentzian convolved with a Gaussian resolution function (__ . __ .) and a resolution-limited Gaussian representing the incoherent elastic scattering (__ __ __).

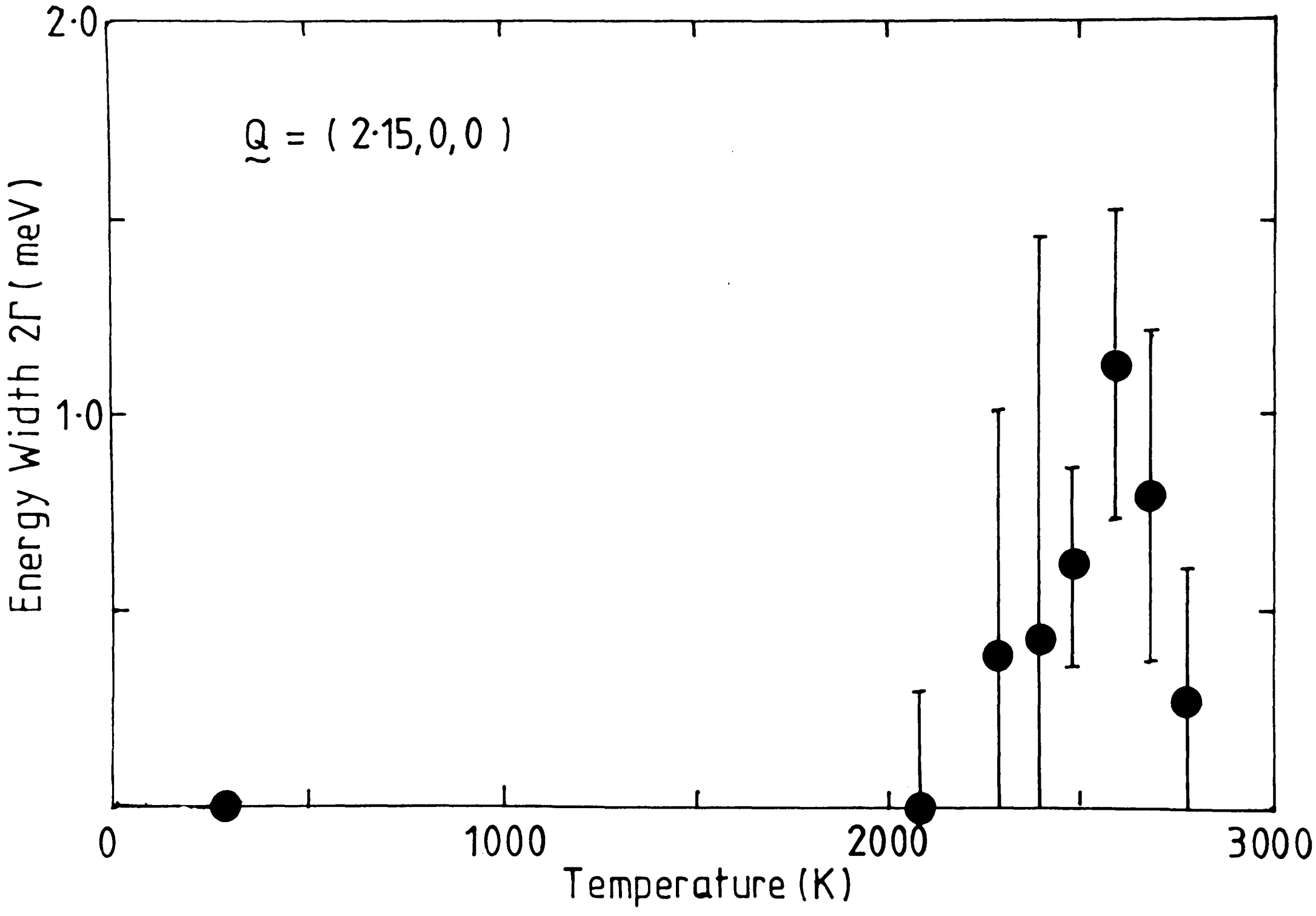

Fig. 7.10 Temperature variation of the Lorentzian FWHM 2Γ of the diffuse QES peak at (0,0,2.15) in UO_2.

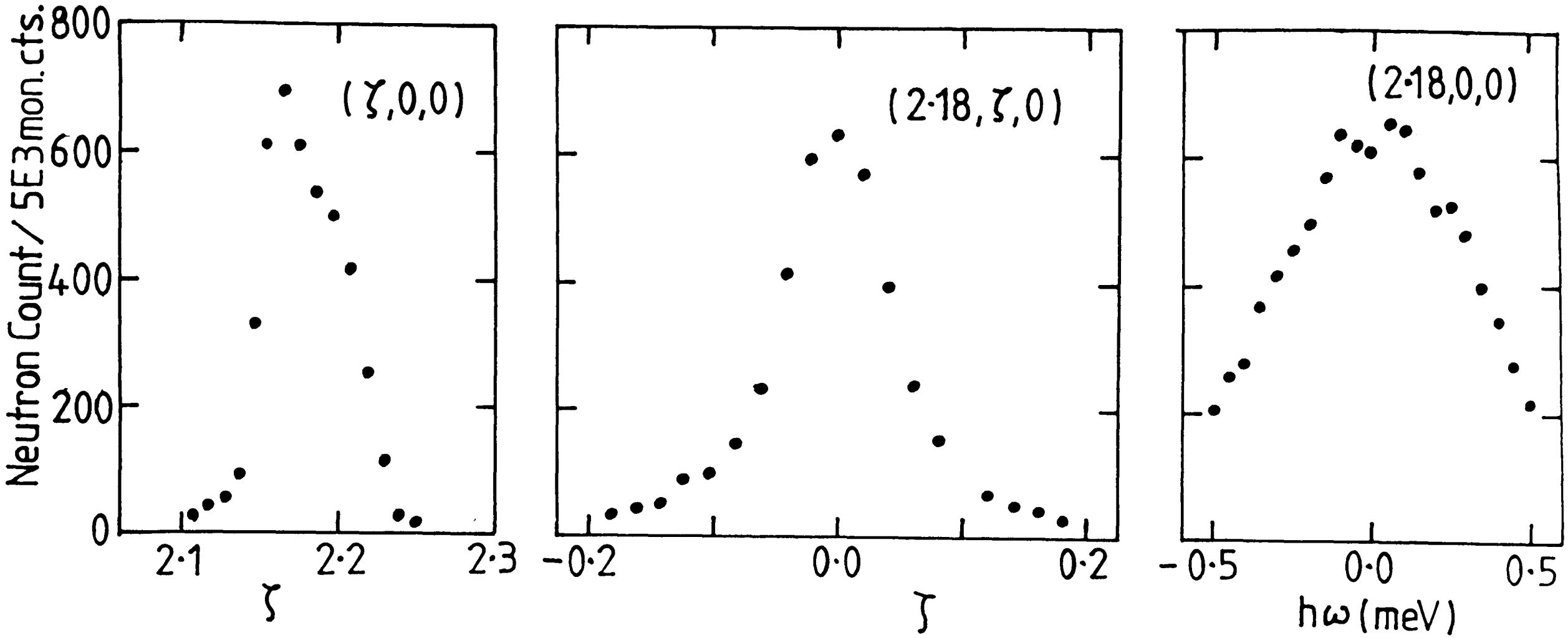

Fig. 7.11 Radial and transverse elastic scans and an energy scan of the additional peak observed at (2.18,0,0) in UO_2 at room temperature after cooling from 2930K. Note the intensity and width of this peak relative to the diffuse peak at (2.15,0,0) observed at high temperatures (Fig. 7.4).

CHAPTER 8

A QUASIELASTIC NEUTRON SCATTERING STUDY OF Y_2O_3 - STABILISED ZIRCONIUM DIOXIDE

8.1 INTRODUCTION

Considerable industrial interest has been shown in zirconia, ZrO_2, over recent years because of its hardness and high melting point (T_m = 2988K). Pure ZrO_2 has a monoclinic structure at temperatures up to 1370K, above which it assumes a tetragonal structure. At 2640K, ZrO_2 transforms into the cubic fluorite structure (Viechnicki and Stubican 1965).

The fluorite structure may be stabilised at room temperature by the addition of oxides such as Sc_2O_3, Y_2O_3 and CaO. For ZrO_2 - Y_2O_3 solid solutions, the fluorite phase is stable for Y_2O_3 molar concentrations of between 7% and 40%. For Y_2O_3 concentrations of less than 7% the structure is tetragonal, and for concentrations greater than 40%, the ordered phase $Zr_3Y_4O_{12}$ is formed (Stubican et.al. 1978). Investigations of the transport properties of ZrO_2:xY_2O_3, for x between 7 and 25 mol%, indicate that the electrical conductivity is enhanced above ~1100K (Suzuki et.al. 1981). This may be due to the onset of anion hopping as a result of the large concentration of oxygen vacancies induced by doping with a trivalent metal oxide (Morinaga et.al. 1979).

In this chapter, we report an investigation of the nature of the disorder in Y_2O_3 - doped ZrO_2 at ambient and elevated temperatures, using QES techniques. Firstly, contour diagrams of the diffuse scattering intensity at room temperature are determined for varying concentrations of Y_2O_3. These are interpreted in terms of the local structure around oxygen vacancies and dopant cations. The development of the diffuse scattering with increasing temperature is then described

for ZrO_2 (9.4 mol% Y_2O_3). Finally, a model of the dynamic disorder above 1100K is discussed. The work reported in this chapter was performed in collaboration with K. Clausen, R.Osborn and N. H. Andersen.

8.2 Y_2O_3 - DOPED ZrO_2 AT ROOM TEMPERATURE

8.2.1 EXPERIMENTAL PROCEDURE

The large single crystals of ZrO_2, doped with 9.4, 12, 15 and 18 mol% Y_2O_3, used for these measurements were supplied by J. Wenckus of Ceres Corporation, U.S.A.. The experiments were all performed using DIDO TAS at Harwell. Neutrons of wavelength 1.55Å were monochromated using the (111) plane of an aluminium crystal, the higher order wavelengths being minimised by a pyrolytic graphite filter in the incedent beam. Although the scattering at room temperature is purely elastic, a graphite (002) analyser crystal was used in order to reduce the background level and to discriminate against phonon scattering.

The scattered elastic intensity was determined at scattering vectors $\underset{\sim}{Q}$ lying on a fine mesh of points in the $(1\bar{1}0)$ reciprocal lattice plane, with increments of 0.05 r.l.u. in the (001) direction and 0.1 r.l.u. in the (110) direction. Scattering at Bragg points were omitted. Contour diagrams of the diffuse intensity were obtained for each crystal from the unsmoothed experimental data using the GHOST80 CONTRA routine (except that for the ZrO_2(9.4 mol% Y_2O_3) crystal, which was produced manually). The contour diagrams for the various dopant concentrations are shown in Fig. 8.1..

8.2.2 GENERAL FEATURES OF THE DIFFUSE SCATTERING

The contour diagrams of the scattering for all four dopant concentrations show a similar overall pattern. They consist of a broad shell of scattering emanating from the (220) Bragg peak towards the

(002) peak and another more intense shell emanating from the (004) peak. Both shells display a fair degree of structure, especially around (1.8, 1.8, 1.0) and (1.0, 1.0, 4.0). The diffuse scattering becomes progressively sharper and more intense with increased dopant concentration, indicating greater correlations in the disordered structure. The contour diagram for ZrO_2 (9.4 mol% Y_2O_3) shows fairly sharp peaks at (112) and (114), which are consistent with an internal shear deformation, in which neighbouring oxygen ions are displaced a small amount in opposite [100] directions (Faber et.al. 1978). With increased dopant concentration, the (114) peak disappears and the two adjacent peaks at (0.6, 0.6, 3.8) and (1.4, 1.4, 3.8) intensify.

Less extensive diffuse neutron scattering investigations of ZrO_2 (~10 mol% Y_2O_3) (Feinberg and Perry 1981) are consistent with those described here. The X-ray diffuse scattering measurements of Morinaga et.al. (1980) are difficult to compare with the neutron data since their investigation covers a small area in reciprocal space, in which the scattering is rather weak. The X-ray data are in substantial agreement with the neutron results, but they do show some additional peaks. It should be noted that X-ray scattering is more sensitive to the distribution of cations than to that of the lighter anions.

8.2.3 INTERPRETATION OF THE DIFFUSE SCATTERING

Bragg diffraction experiments, performed with neutrons and X-rays by several workers, have shown that the room temperature structure of Y_2O_3 and CaO - doped ZrO_2 cannot be accounted for adequately by the simple introduction of oxygen vacancies into the regular fluorite model. The results have been interpreted in terms of either local ionic displacements or of the formation of fine precipitates of compounds such as Zr_4CaO_9. In their diffraction analysis of CaO-doped ZrO_2,

Carter and Roth (1968) proposed that each regular oxygen site should be replaced by four equivalent, statistically-occupied sites, displaced in [111] directions. However Steele and Fender (1974) concluded that about 45% of oxygen ions are displaced by $0.073a_o$ in [100] directions in Y_2O_3 - doped ZrO_2 and suggested that these displacements were towards an oxygen vacancy by its nearest neighbours. Similar results were obtained for Y_2O_3 - doped ZrO_2 by Faber et.al. (1978) and by Morinaga et.al. (1979), who also reported [100] oxygen displacements in CaO-doped ZrO_2. The latter authors also found that the fits were improved by introducing small [111] displacements of $0.015a_o$ for all cations. In contrast, Allpress and Rossell (1975) explained their results on CaO-doped ZrO_2 in terms of domains of Zr_4CaO_9, having dimensions of about 30Å.

Complementary X-ray diffuse scattering investigations of ZrO_2 (13.6 mol% Y_2O_3) and ZrO_2 (15.5 mol% CaO) were found to be consistent with [100] displacements of oxygen ions, occuring without long-range correlations (Morinaga et.al. 1980). No evidence was seen of many of the strong diffuse peaks predicted by the precipitate model of Allpress and Rossell (1975). However this investigation was limited to the region (hhl) in the $(1\bar{1}0)$ plane, for h between 0 and 2 and l between 2 and 4. Comparison with Fig. 8.1 shows that this area does not include the most intense regions of diffuse scattering.

In this study we follow the procedure outlined in § 7.4.2 to calculate the integrated scattering function $S^D(Q)$, excluding Bragg scattering. We consider a cluster model representing the short-range ordering around the Y^{3+} cations. Since this procedure neglects interactions between clusters it is necessary to consider the extent of inter-cluster correlations. Assuming an exponentially-decaying inter-

action between clusters, of the form $\exp(-r/\xi)$, an estimate of the correlation length ξ may be obtained from the HWHM Δq of the diffuse peak at (1.0, 1.0, 1.8).

$$\xi = \frac{1}{\Delta q} \qquad (8.1)$$

where ξ and Δq are in units of $\mathring{A}$ and $\mathring{A}^{-1}$ respectively. The correlation length may be compared with the average separation of Y^{3+} ions, $\bar{d}_Y$, (assuming that the Y^{3+} ions are randomly distributed on regular cation sites).

$$\bar{d}_Y = \frac{a_o}{(8x)^{1/3}} \qquad (8.2)$$

where x is the molar concentration of Y_2O_3. The variation of Δq, ξ and $\bar{d}_Y$ with dopant concentration is summarised in Table 8.1. As x is increased from 9.4 to 18 mol%, the correlation length is found to increase from 3.1$\mathring{A}$ to 4.8$\mathring{A}$ whereas the average separation of Y^{3+} ions decreases from 5.6$\mathring{A}$ to 4.5$\mathring{A}$. Thus inter-cluster correlations play an increasingly significant part in the diffuse scattering with increasing dopant concentration.

In order to account for the observed scattering, the distribution of diffuse intensity in the $(1\bar{1}0)$ plane has been calculated for a simple cluster (Fig. 8.2) comprising two Y^{3+} ions occupying regular cation sites at the origin and at (½, ½, 0), and an oxygen vacancy at (¼, ¼, ¼), with subsequent relaxations of its neighbouring ions. The six nearest-neighbour oxygen ions were displaced by $0.075a_o$ in [100] directions and the two nearest-neighbour Zr^{4+} ions displaced by $0.038a_o$ in [111] directions towards the vacancy, in view of the Zr^{4+} ion's small ionic radius (r_{Zr} = 0.72$\mathring{A}$, r_Y = 0.89$\mathring{A}$, Shannon and Prewitt 1969). The magnitude of the displacements were taken from the diffraction analysis of Steele and Fender (1974). The positions and

TABLE 8.1

THE VARIATION OF THE HWHM OF THE (1.8, 1.8, 1.0) DIFFUSE PEAK IN Y_2O_3 - DOPED ZrO_2

x(mol%)	Δq(r.l.u.)	ξ(Å)	d_Y(Å)
9.4	0.26	3.1	5.65
12	0.23	3.6	5.29
15	0.19	4.3	4.83
18	0.17	4.8	4.52

scattering lengths of the ions in the cluster are summarised in Table 8.2, and the resulting contour map for the $(1\bar{1}0)$ plane is shown in Fig. 8.3. Its general features resemble those of the contour maps of observed intensity shown in Fig. 8.1 - the model does predict the shells of scattering emanating from the (220) and (004) Bragg points. However the model fails to reproduce much structural detail within the shells of observed scattering, such as the two peaks at (0.6, 0.6, 3.8) and (1.4, 1.4, 3.8).

The general agreement between the data and the simple cluster model adopted indicates that the scattering is dominated by short-range order. However, extended clusters or inter-cluster correlations must be considered in any attempt to simulate the detailed structure of the scattering. It should be noted that Y_2O_3-doped ZrO_2 contains twice as many Y^{3+} ions as oxygen vacancies, so each vacancy is shared between two Y^{3+} ions. However because of the similarity between the scattering lengths of zirconium and yttrium, (b_{Zr} = 7.16fm, b_Y = 7.75fm), the scattering is insensitive to the positions of the Y^{3+} ions, provided that they occupy regular cation sites, an assumption which is supported by the diffraction measurements (Steele and Fender 1974, Morinaga et.al. 1979).

8.3 ZrO_2 (9.4 mol% Y_2O_3) AT HIGH TEMPERATURE

8.3.1 SUMMARY OF EXPERIMENTAL DETAILS

The measurements of the development of the diffuse scattering at elevated temperatures, reported in this section, were performed at Risø National Laboratory, Denmark in collaboration with K. Clausen and N. H. Andersen. A cylindrical single crystal ZrO_2 (9.4 mol% Y_2O_3), having a diameter of 14mm and sealed in a machined molybdenum tube, was

TABLE 8.2

IONIC POSITIONS AND SCATTERING LENGTHS FOR THE Y_2O_3 - DOPED ZrO_2 CLUSTER MODEL

Ion	Ion Position			Vacancy Associated with relaxed ion		
Y^{3+}	0.0	0.0	0.0			
	0.5	0.0	0.0			
O^{2-} vacancy	0.25	0.25	0.25			
Zr^{4+} (relaxed)	0.478	0.022	0.478	0.5	0.0	0.5
	0.022	0.478	0.478	0.0	0.5	0.5
O^{2-} (relaxed)	-0.175	0.25	0.25	-0.25	0.25	0.25
	0.675	0.25	0.25	0.75	0.25	0.25
	0.25	-0.175	0.25	0.25	-0.25	0.25
	0.25	0.675	0.25	0.25	0.75	0.25
	0.25	0.25	-0.175	0.25	0.25	-0.25
	0.25	0.25	0.675	0.25	0.25	0.75

Ion	b(10^{-14}m)
Zr^{4+}	0.716
Y^{3+}	0.775
O^{2-}	0.5805

used for all four experiments, labelled 1 - 4. The sample was heated under a dynamic vacuum in the Risø high temperature furnace, the temperature of which was monitored and controlled using two W/3% Re - W/25% Re thermocouples.

Triple axis spectrometers were used to examine the temperature variation of the diffuse quasielastic intensity $S^{D}(\underset{\sim}{Q})$ and of the quasielastic energy width. In order to attain the large $\underset{\sim}{Q}$ values required to investigate both observed shells of scattering, thermal neutrons of energy 34.0 meV were employed on the TAS4 spectrometer. Conversely, the high resolution required to investigate energy-broadening entailed the use of the cold-moderated 5meV incedent neutrons available on the TAS1 and TAS6 spectrometers. The (002) plane of pyrolytic graphite was used for monochromator and analyser crystals in all experiments. The higher-order wavelengths were suppressed using filters in the incoming beam - a Be filter for 5meV neutrons and a pyrolytic graphite filter for 14.4meV and 34.0meV neutrons. These also served to reduce the background levels. The details of the individual experiments are summarised in Table 8.3. In the next two sections the experimental procedures and results are presented in a systematic, rather than chronological, order.

8.3.2 QES INTENSITY

In experiment 1, the intensities of several diffuse peaks were determined at several temperatures up to 2100K. Time considerations and software limitations constrained the measurements to three scans at each temperature. These were chosen to be the elastic $\underset{\sim}{Q}$-scans (1.4, 1.4, ζ), (1.0, 1.0, ζ) and (ζ, ζ, 1.0) in order to monitor the temperature evolution of the diffuse peaks at (1.4, 1.4, 1.8),

TABLE 8.3

SUMMARY OF EXPERIMENTAL DETAILS FOR HIGH TEMPERATURE INVESTIGATIONS OF ZrO_2 (9.4 mol% Y_2O_3)

Experiment Number	Date	Spectrometer	Collimation R-M/M-S/S-A/A-D	k_i ($\AA^{-1}$)	Vanadium Scan FWHM (meV)	Scans
1	Nov 82	TAS4 (thermal)	60′/44′/54′/106′	4.05	4.25	Elastic Q-scans (broad resolution) 290 - 2100K
2	Nov/Dec 82	TAS6 (cold)	60′/37′/61′/104′	1.553	0.20	Energy scans at constant $\underset{\sim}{Q}$ 290 - 1720K: $\underset{\sim}{Q}$ = (0, 0, 1.9) 1720K: $\underset{\sim}{Q}$ = [0, 0, ζ] and [ζ, ζ, 0]
3	May/June 83	TAS1 (cold)	60′/33′/28′/30′	1.553	0.135	Energy scans at constant Q 1720K: Q points in (1$\bar{1}$0) plane
4	Aug 83	TAS6 (cold)	30′/23′/26′/29′	2.636	0.51	Contour map of diffuse intensity at 1720K. Energy scans in regions of diffuse intensity at 1720K.

(1.4, 1.4, 3.8) and (1.8, 1.8, 1.0) and the sharp Bragg peaks at (112) and (114). The resolution width of 4.25meV for the 34.0meV neutrons employed was assumed to be much broader than the QES, so that the observed intensity represents the integrated scattering function $S^{D}(\underset{\sim}{Q})$. This assumption is amply justified in §8.3.3.

All the monitored peak intensities decreased gradually with increasing temperature without showing any dramatic effects. From the ratio of the integrated peak intensity at temperature T to that at 293K, $\int(T)/\int(293)$, an estimate of the isotropic thermal vibration parameter, B(T) - B(293) may be obtained (from equations 3.17 - 3.19).

$$B(T) - B(293) = -\tfrac{1}{2}\left(\frac{4\pi}{Q}\right)^{2} \ln\left\{\frac{\int(T)}{\int(293)}\right\} \qquad (8.3)$$

The resulting thermal parameters for the three diffuse peaks are summarised in Table 8.4 and shown in Fig. 8.4 (except the (1.4, 1.4, 1.8) peak, for which the relative errors are very large). The behaviour of B(T) - B(293) is similar to that of the oxygen ion isotropic vibration parameter B_o for UO_2 and ThO_2, shown in Fig. 4.4. Since the diffuse scattering intensity at room temperature is mainly due to the relative positions of oxygen ions, as was seen in §8.2.3, we may deduce from this similarity that the diffuse scattering per anion (with the thermal factor removed), $X(\underset{\sim}{Q})$, does not change substantially with temperature up to 210OK. More recently, a complete contour diagram of $S^{D}(\underset{\sim}{Q})$ at 172OK has been measured by K Clausen and N H Andersen (experiment 4). This is shown in Fig. 8.5, from which it can be seen that the distribution of diffuse intensity in the $(1\bar{1}0)$ plane at 172OK resembles closely that observed at room temperature (Fig. 8.1(a)).

This result indicates that the clusters responsible for the diffuse QES at room temperature occur at temperatures up to 210OK, well

TABLE 8.4

VALUES OF $(B_T - B_{293K})$ DEDUCED FROM THE TEMPERATURE VARIATION OF DIFFUSE PEAK INTENSITIES

Error in last digit(s) shown in parentheses

T(K)	$B_T - B_{293K}$ FOR Q - VALUES OF: (1.4,1.4,3.78)	(1.4,1.4,1.74)	(1.77,1.77,1.0)
293	0.0	0.0	0.0
1028	1.14(31)	0.6(11)	-
1063	1.32(31)	0.7(9)	1.65(65)
1108	1.41(27)	-	1.65(66)
1147	1.61(29)	1.0(9)	2.03(67)
1187	1.56(33)	1.1(9)	1.93(67)
1228	1.66(30)	1.0(9)	2.23(69)
1313	2.27(42)	1.2(11)	2.53(52)
1393	2.55(46)	1.0(11)	2.53(60)
1530	3.37(49)	2.3(10)	3.18(57)
1676	3.73(55)	2.9(10)	3.41(59)
1806	4.05(59)	3.2(11)	-
1903	4.26(43)	4.9(12)	3.90(62)
2003	4.60(59)	6.5(11)	4.83(71)
2103	5.00(64)	7.1(10)	4.98(58)

in excess of the temperature range 1200K - 1600K in which anomalous conductivity behaviour was observed (Suzuki et.al. 1981). However it should be noted, from Table 8.4 and Fig. 8.4, that there are indications of more rapidly increasing thermal parameters at about 1300K for the (1.4, 1.4, 1.8) and (1.4, 1.4, 3.8) diffuse peaks.

8.3.3 QES ENERGY DEPENDENCE

In order to probe the dynamic nature of ZrO_2 (9.4 mol % Y_2O_3) at high temperature, the energy dependence of the QES was investigated with low energy neutrons. During experiment 2, energy scans at constant $\underset{\sim}{Q}$ values along the [001] and [110] directions, performed at 1720K, showed energy-broadening in the region (0, 0, 1.5) to (0, 0, 2.0). No broadening was observed along the [110] axis. The incident neutron energy E_i = 5meV, chosen to be just below the cut-off energy of the beryllium filter, was too low to access the regions of strong diffuse intensity.

The evolution of the energy width with increasing temperature was followed for $\underset{\sim}{Q}$ = (0, 0, 1.9). The peaks were fitted with a Lorentzian function, convoluted with a Gaussian resolution aperture, using the Risø least squares fitting routine.

$$I_c(\omega_o) = B_o + \int S_L \frac{\Gamma(Q_o)}{\Gamma(Q_o)^2 + \omega^2} \cdot \frac{a}{\sqrt{\pi}} \exp\left\{ - a^2(\omega - \omega_o)^2 \right\} d\omega \qquad (8.4)$$

This expression for the calculated intensity is equivalent to that given in (7.7) with $B_S = S_G = 0$ and $R_o = \left[\int \exp\left\{ - a^2\omega^2 \right\} d\omega \right]^{-1} = a/\sqrt{\pi}$. The value of a = 13.4mev^{-1} was determined from a vanadium scan as usual. The fitted parameters were the background B_o, the Lorentzian intensity S_L, the Lorentzian FWHM 2Γ and a parameter $\Delta\omega$ giving the spectrometer

misalignment. The results of the fits are given in Table 8.5 and the temperature variation of 2Γ and S_L are shown in Fig. 8.6. In the fitting routine, the convolution was evaluated by reference to internal tables. This caused problems for non-broadened peaks and gave a minimum value for 2Γ of 0.03meV. The resulting values of 2Γ and S_L below 110OK are therefore suspect and are denoted by open circles in Fig. 8.6.

In experiment 3, the energy scans along the [001] axis were repeated at 172OK with broader scans and more data points per scan. These revealed a broad Lorentzian peak together with a resolution-limited Gaussian peak from the incoherent elastic background, as may be seen from the energy scan at (0, 0, 1.7) shown in Fig. 8.7. These spectra were fitted with the function described in equation (7.7), representing a Lorentzian convoluted with a Gaussian resolution aperture plus a resolution-limited Gaussian, using the PKFIT routine. The fitted parameters were B_o, B_S, S_G, S_L, 2Γ and $\Delta\omega$. The results are given in Table 8.6 and the Lorentzian FWHM 2Γ and intensity S_L are plotted in Fig. 8.8. The $\underset{\sim}{Q}$ - dependence of 2Γ ($\underset{\sim}{Q}$) is interesting - it increases with $\underset{\sim}{Q}$ up to a maximum value of 0.46meV at (0, 0, 1.7) then decreases on approaching the (002) Bragg peak. The fits also show large values of 2Γ beyond the (002) peak, but the data in this region contain large uncertainties because the much greater Gaussian intensity made it difficult to distinguish the Lorentzian contribution from the background. More recent measurements confirm that 2Γ does indeed tend to zero at the (002) Bragg peak and also indicate that 2Γ beyond (002) is less than that shown in Fig. 8.8 - about 0.4meV at (0, 0, 2.1) (M T Hutchings and R Osborn, private communication).

In experiments 3 and 4, the energy scans were extended to the first shell of intense diffuse scattering using incident neutron energies of 7.2 and 14.4meV. Energy broadening was again observed

TABLE 8.5

RESULTS OF FITS TO ENERGY SCANS AT Q = (0, 0, 1.9)

Error in last digit(s) shown in parentheses

T(K)	B_o(counts)	S_L	2Γ (meV)	$\Delta\omega$(meV)	χ^2
293*	7.7(28)	145.6(45)	0.031(4)	0.013(2)	3.70
933*	32.8(33)	121.8(40)	0.033(4)	0.011(2)	2.75
1023*	36.3(40)	112.9(40)	0.039(6)	0.011(2)	1.87
1063	46.5(28)	105.0(30)	0.039(5)	0.012(2)	1.22
1148	54.2(25)	95.2(26)	0.040(5)	0.011(2)	0.89
1233	53.4(37)	94.5(40)	0.055(9)	0.012(3)	1.28
1283	54.8(38)	90.3(41)	0.074(10)	0.012(2)	1.03
1348	53.5(22)	72.4(32)	0.073(11)	0.011(3)	0.68
1418	60.1(31)	63.4(43)	0.069(17)	0.009(5)	1.33
1483	55.3(38)	74.5(58)	0.143(23)	0.015(6)	1.33
1543	57.7(38)	65.8(57)	0.131(25)	0.015(6)	1.45
1603	65.7(41)	59.4(59)	0.130(29)	0.007(7)	1.55
1673	64.5(31)	61.3(46)	0.141(22)	0.011(5)	0.81
1723	65.0(39)	76.7(64)	0.208(27)	0.013(6)	0.87

* The results at these temperatures are doubtful because of convolution problems for a non-broadened Lorentzian in the fitting routine.

TABLE 8.6

RESULTS OF FITS TO ENERGY SCANS AT RECIPROCAL LATTICE POINTS Q = (0, 0, ζ) AT 172OK

Error in last digit(s) shown in parentheses

ζ	S_G	S_L	2Γ (meV)	$\Delta\omega$ (meV)	χ^2
0.9	81(15)	20.0(23)	0.07(2)	.020(3)	1.73
1.3	108(30)	25.6(42)	0.21(11)	.017(3)	1.38
1.6	67(18)	50.1(58)	0.32(7)	.008(4)	1.67
1.7	69(14)	73.4(89)	0.45(9)	.016(5)	1.35
1.8	36(18)	78.7(70)	0.36(6)	.021(6)	1.33
1.9	58(22)	72.5(59)	0.29(5)	.017(5)	1.30
2.1	603(16)	68.6(239)	0.74(24)	.012(1)	2.05
2.18	194(16)	68.6(654)	0.75(49)	.039(3)	1.36

above 1000K and its development with temperature at (1.8, 1.8, 0.8) was monitored in the same way as for Q = (0, 0, 1.9). The results, given in Table 8.7 and Fig. 8.9, indicate similar behaviour to that observed at (0, 0, 1.9), as shown in Fig. 8.6. Further scans were performed at 1720K, fitted with expression (8.4) and a map of energy widths at a number of points in the $(1\bar{1}0)$ plane was produced. This is superimposed on the contour diagram of diffuse intensity in Fig.8.5, from which it can be seen that the energy broadening occurs in the regions of intense diffuse scattering. There are, however, some regions of intense diffuse scattering in which the broadened Lorentzian contribution is small, the main contribution coming from non-broadened elastic scattering (Fig. 8.10). In the regions of weak or negligible diffuse intensity no energy broadening was observed, except in the region around (0, 0, 1.7) as described above.

8.4 DISCUSSION AND CONCLUSIONS

The overall picture that emerges of the QES from ZrO_2 (9.4 mol%Y_2O_3) is the following. In the region of the $(1\bar{1}0)$ plane investigated, two concentric anisotropic shells of scattering occur at room temperature. On heating, the integrated diffuse intensity (after removing thermal vibration factors), $X^D(Q)$, remains substantially unchanged up to 2100K. However the scattering broadens in energy above 1000K to values of $2\Gamma \sim$ 0.4meV at 1720K. In some regions of intense diffuse scattering, where the elastic background is negligible, there is evidence of a broadened Lorentzian and resolution-limited Gaussian contribution to the spectrum. In regions of very weak diffuse scattering there is no evidence of energy broadening, except along the $[00\zeta]$ axis. In this region, the energy width 2Γ has a maximum value of 0.4meV at (0, 0, 1.7) and decreases to zero at the (002) Bragg peak.

TABLE 8.7

RESULTS OF FITS TO ENERGY SCANS AT Q = (1.8, 1.8, 0.8)

Error in last digit(s) shown in parentheses

T(K)	B_o	S_L	2Γ (meV)	$\Delta\omega$(meV)	χ^2
613*	-11(5)	2244(59)	0.078(6)	0.065(3)	12.9
743*	-9(5)	2171(53)	0.086(7)	0.064(3)	10.5
873*	-2(4)	2040(43)	0.088(6)	0.064(3)	7.3
1003*	8(4)	1890(30)	0.103(6)	0.061(3)	3.55
1118*	15(4)	1773(28)	0.101(6)	0.063(3)	3.26
1233	26(4)	1619(23)	0.127(7)	0.067(3)	2.04
1343	34(4)	1506(19)	0.161(8)	0.072(3)	1.40
1448	36(4)	1425(21)	0.225(10)	0.065(3)	1.36
1548	48(4)	1312(18)	0.280(11)	0.075(3)	0.88
1663	44(6)	1177(26)	0.383(19)	0.063(3)	0.95

* The results at these temperatures are doubtful because of convolution problems for a non-broadened Lorentzian in the fitting routine.

As was shown in §8.2.3, the diffuse scattering at room temperature may be interpreted in terms of short-range clustering around oxygen vacancies. The constancy of $X^D(\underset{\sim}{Q})$ with increasing temperature indicates that the clusters occur up to 2100K. The energy broadening of $S(Q,\omega)$ in the shells of intense scattering above 1000K implies that these clusters acquire a finite lifetime (~3ps at 1720K). This behaviour may be explained in terms of vacancy hopping, causing the break-up of the original cluster and the formation of a similar cluster around the new vacancy site. Such a mechanism would also account for the enhanced conductivity observed in this temperature range (Suzuki et.al. 1981). The non-broadened scattering in the shells of intensity could reflect static clustering, as may occur around Y^{3+} ions.

The cause of the energy broadening along the [001] direction is more difficult to establish since the diffuse intensity is very weak in this region. One rather speculative explanation is that the $\underset{\sim}{Q}$-dependence of the energy width 2Γ is analogous to that observed in the incoherent scattering from $SrCl_2$ in its fast ion phase (Schnabel 1983). The $SrCl_2$ data were analysed successfully in terms of anion hopping between regular sites in [100] and [110] directions, using the model of Chudley and Elliott (1961) discussed briefly in § 3.3.4. Since the incoherent scattering cross-section σ_{inc} of oxygen is zero, the second (incoherent) summation in equation (3.11) is zero for zirconia. However the self-term (m = m′) in the first (coherent) summation gives a self-correlation function similar to $S_S(\underset{\sim}{Q},\omega)$ given in equation (3.33). The resulting form of the coherent scattering function $S(\underset{\sim}{Q},\omega)$ for a system of hopping ions is

$$S^D(\underset{\sim}{Q},\omega) = S^D(\underset{\sim}{Q}).\ S_S(\underset{\sim}{Q},\omega).e^{2W(\underset{\sim}{Q})} \qquad (8.5)$$

(Vineyard 1958, Hutchings et.al. 1984). For the Chudley and Elliott (1961) model of [100] hops between regular anion sites, the width function $\Gamma(\underset{\sim}{Q})$ of equation (3.34) increases from zero to a maximum at (0, 0, 1) and decreases to zero again at (0, 0, 2). However it may be objected that, whereas $\Gamma(\underset{\sim}{Q})$ does tend to zero at (0, 0, 2), its maximum value occurs at (0, 0, 1.7) in Y_2O_3 - doped ZrO_2.

Clearly, more work is needed to resolve fully the nature of the dynamic disorder in Y_2O_3 - doped ZrO_2 at high temperatures. The main difficulty associated with this work is the separation of contributions to the observed coherent scattering from the following sources.

<u>At room temperature</u>:

1. Bragg scattering.
2. Diffuse elastic scattering from the static disorder.

<u>At high temperature</u>:

1. Bragg scattering.
2. Diffuse elastic scattering from static disorder.
3. Diffuse energy-broadened scattering from dynamic disorder.

Bragg scattering represents a nuclear distribution which is averaged over time and over all unit cells. Troublesome additional scattering from furnace components is also observed: elastic incoherent scattering, which is isotropic except for thermal vibration effects, and coherent Bragg and phonon scattering. For the undoped fluorites, such as UO_2, the task is simplified by the absence of a diffuse elastic contribution from the time-averaged structure. As a consequence of the purely dynamic nature of the disorder, the time-averaged nuclear distribution has the same periodicity as the lattice, and hence $I(\underset{\sim}{Q},\infty)$ (euqations 3.14c and 3.31) is non-zero only at the reciprocal lattice

points. However, in Y_2O_3 - doped ZrO_2 the clustering is probably connected to the positions of the Y^{3+} ions, which do not have the lattice periodicity.

An interesting extension of the work would be the study of diffuse QES at high temperatures from the ZrO_2 crystals containing greater concentrations of Y_2O_3. As was noted in §8.2.3, these show longer-range correlations at room temperature than in the ZrO_2 (9.4 mol% Y_2O_3) investigated here. An investigation of the extent of correlations in these crystals at high temperature could shed more light on the nature of disorder in Y_2O_3 - doped ZrO_2.

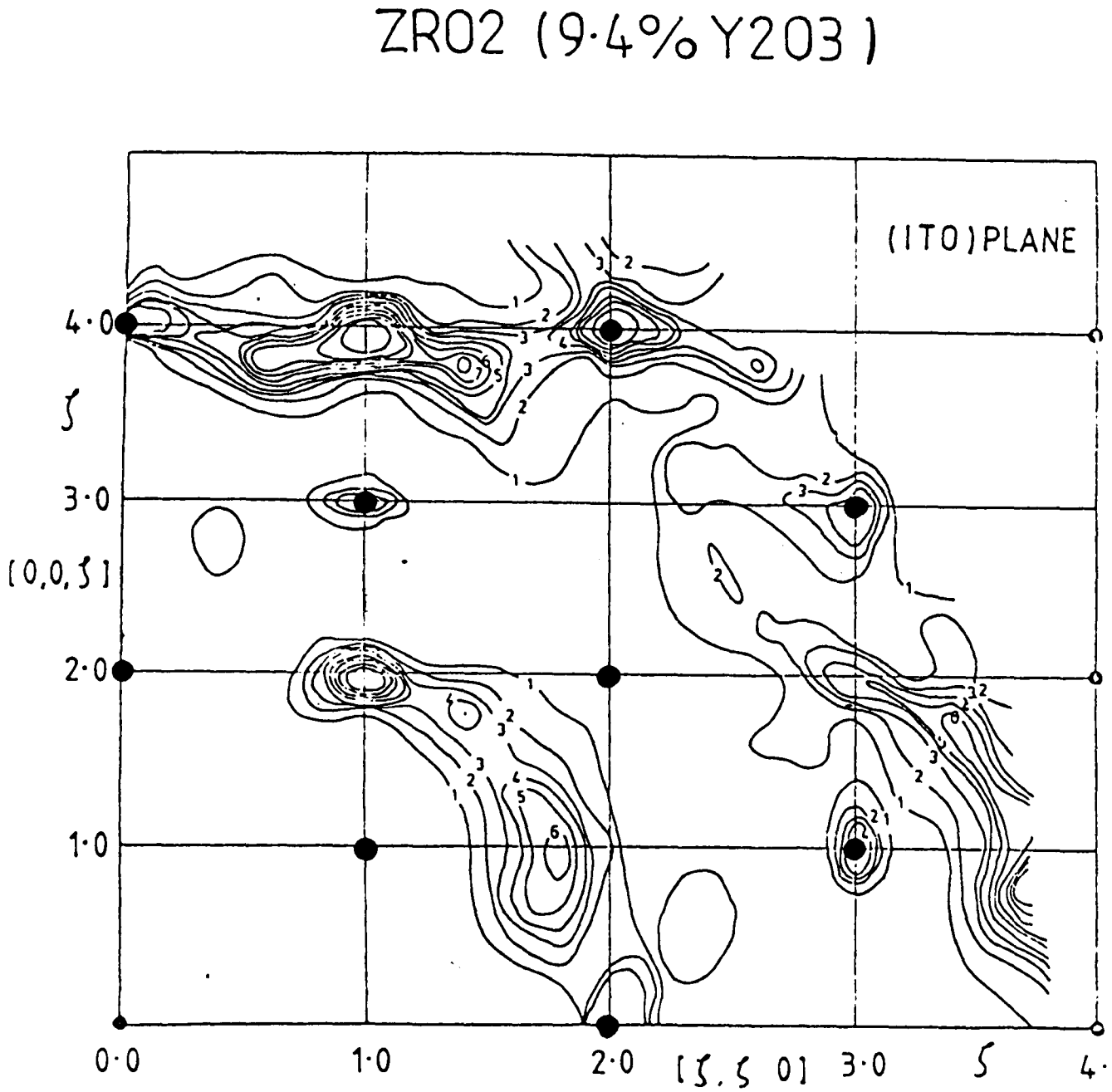

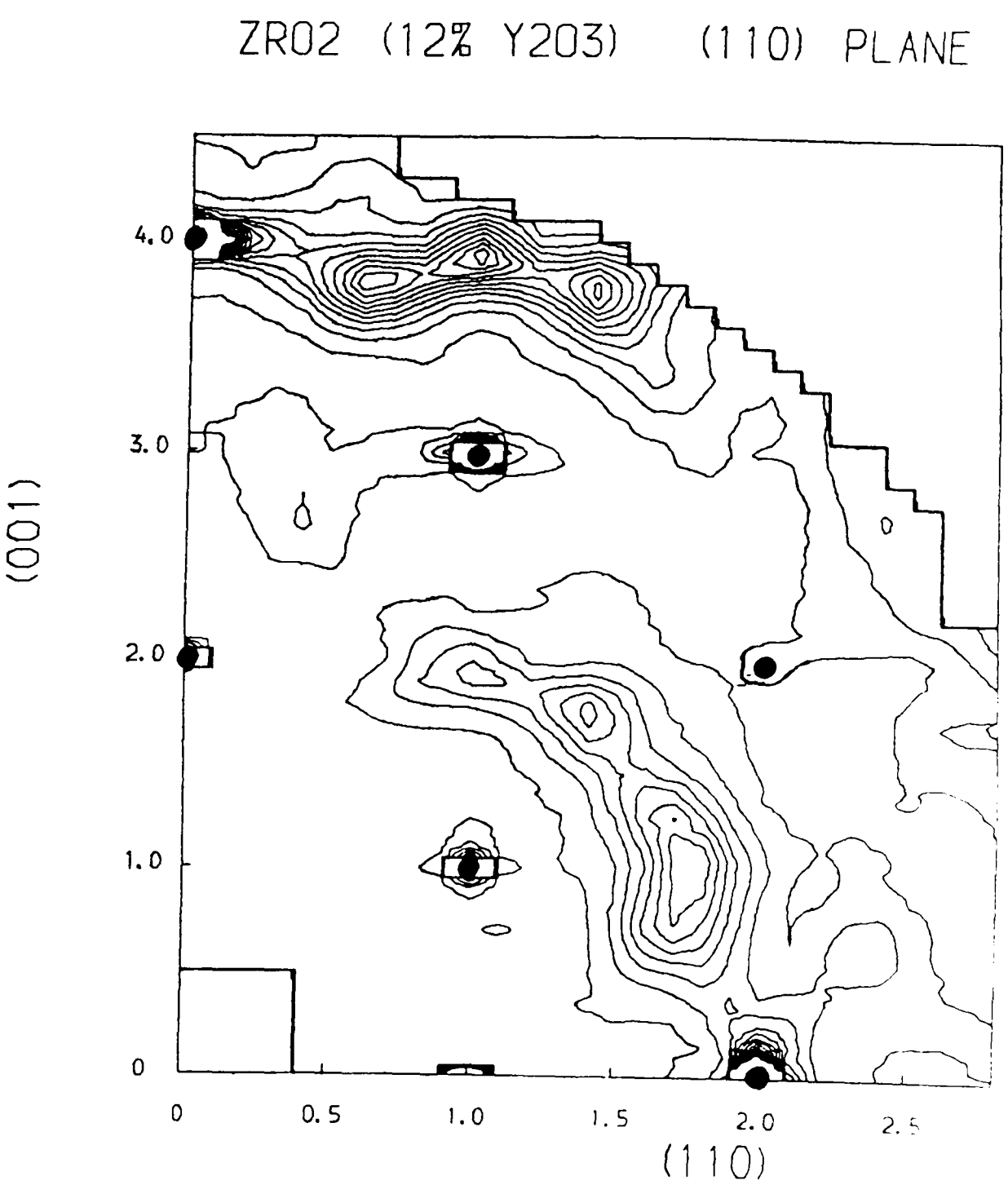

Fig. 8.1 Contour diagrams of the diffuse elastic intensity (in arbitrary units) at room temperature in the $(1\bar{1}0)$ plane of ZrO_2 (x mol% Y_2O_3) for x = 9.4, 12, 15 and 18 mol%.

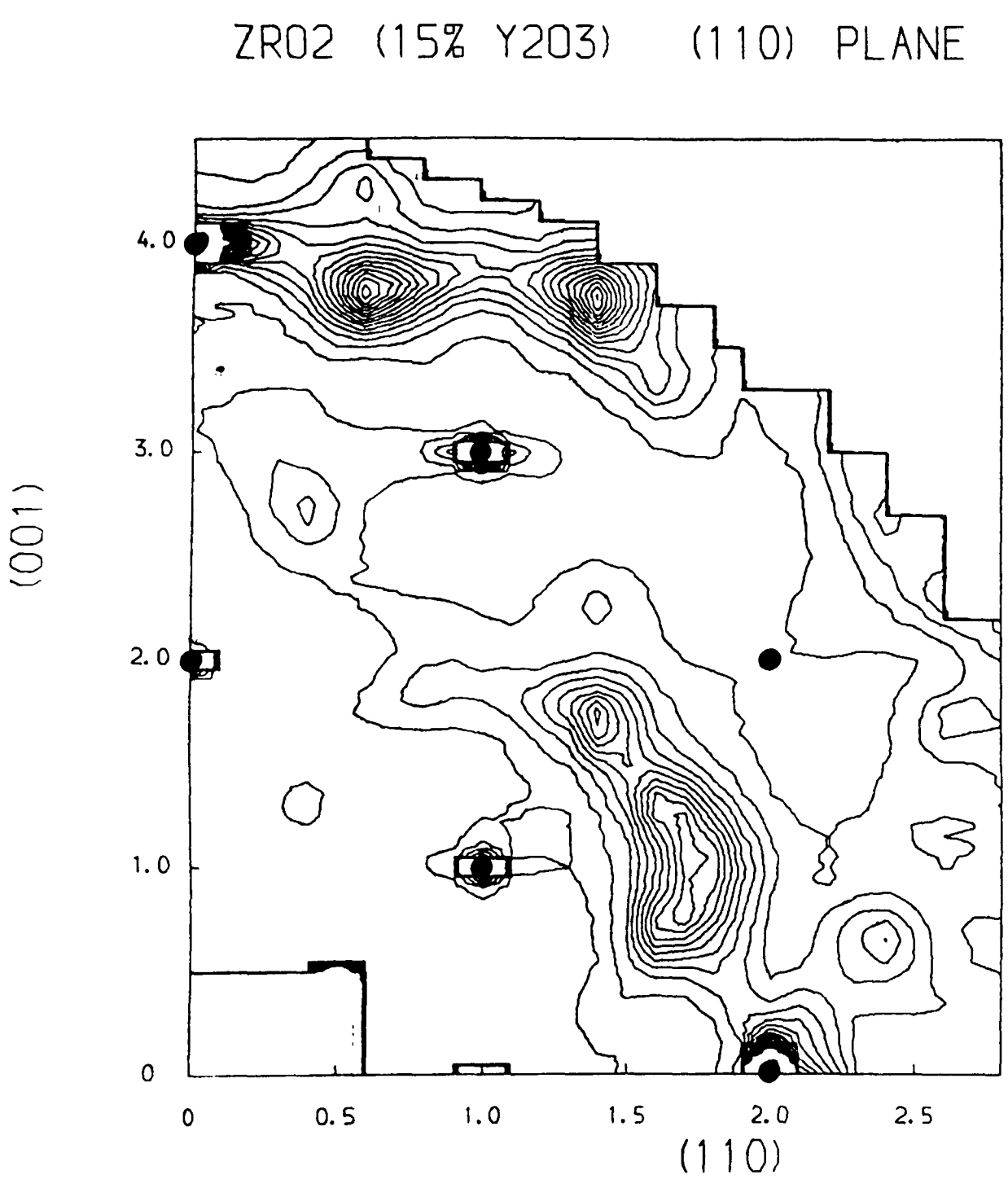

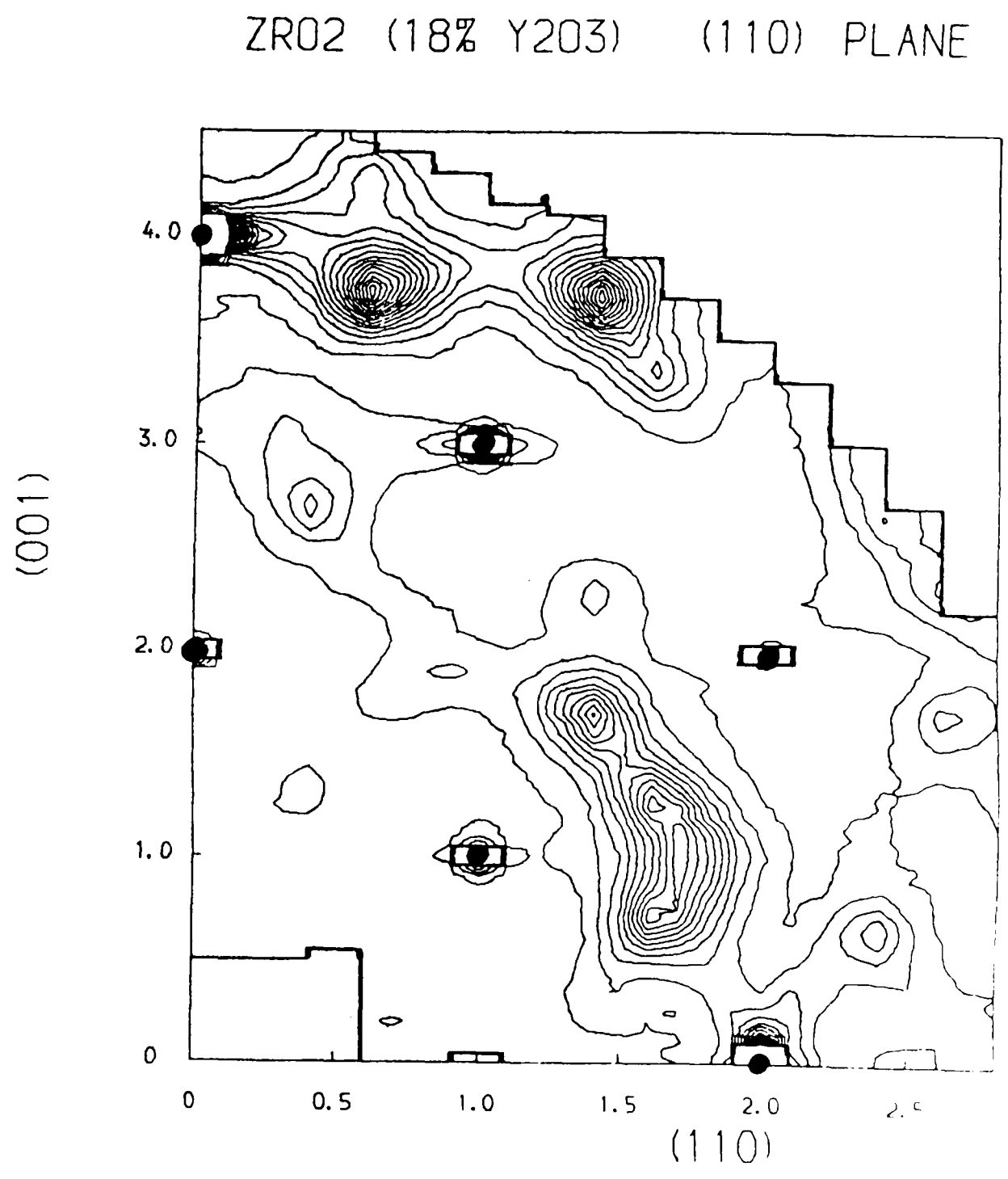

Fig. 8.1 (continued)

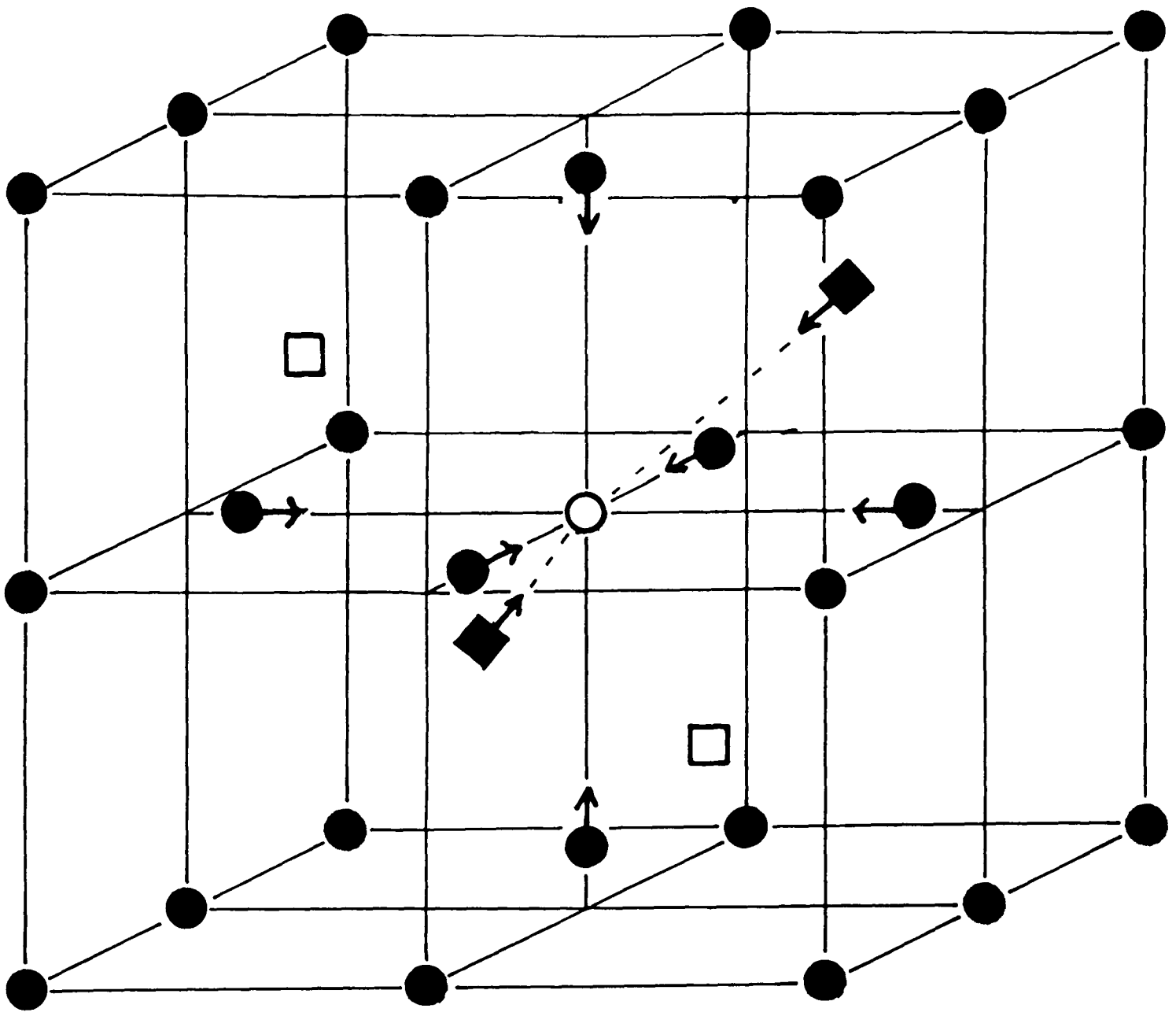

Oxygen ion (regular site)

Oxygen vacancy

Relaxed Oxygen ion

Zirconium ion (regular site)

Relaxed Zirconium ion

Yttrium ion

Fig. 8.2 Proposed cluster model of the relaxations around an oxygen vacancy in Y_2O_3-doped ZrO_2. The magnitude of the relaxations may be taken from the diffraction analysis of Steele and Fender (1974).

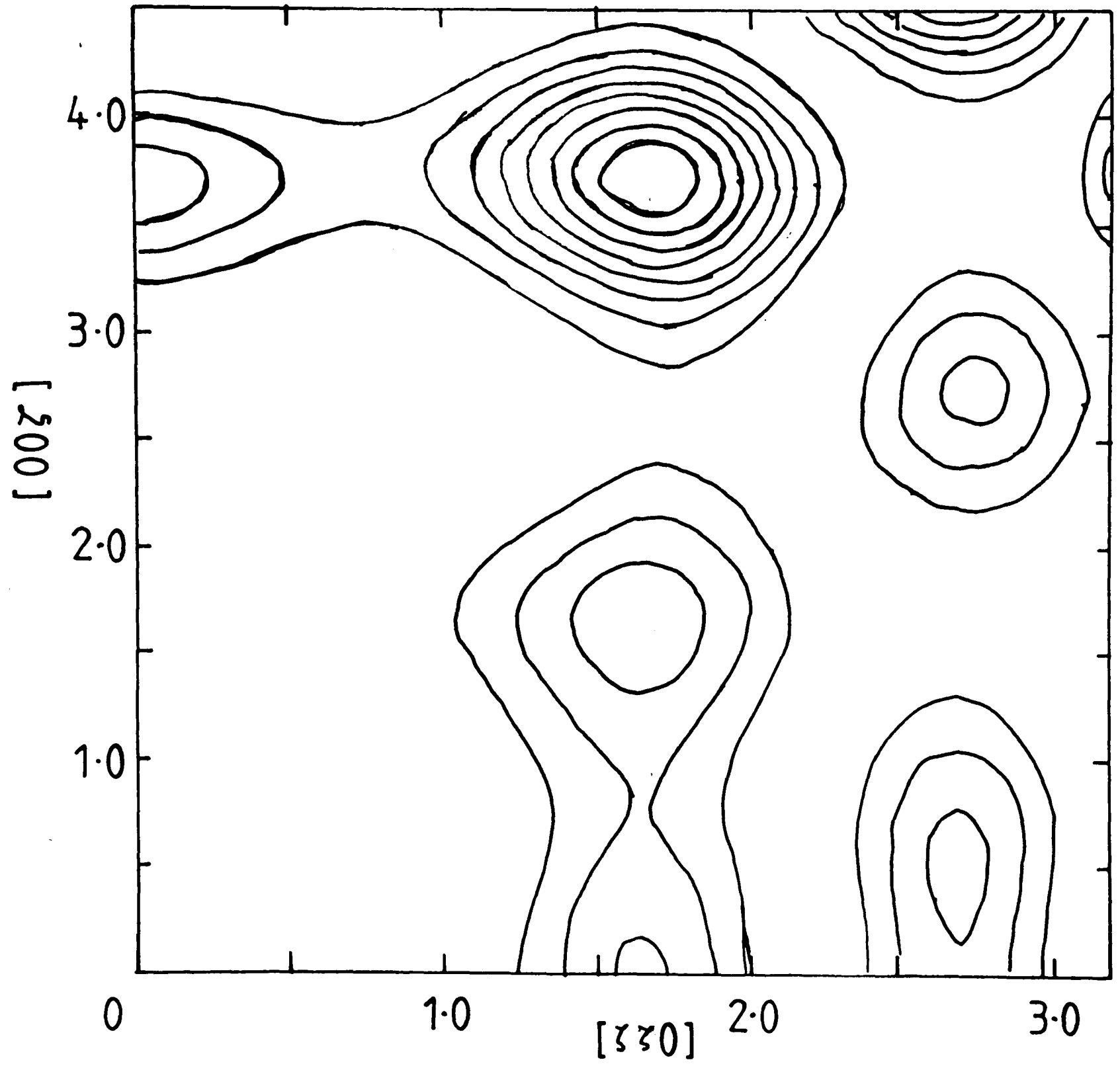

Fig. 8.3 Contour diagram of $S^{D}(Q)$ in Y_2O_3-doped ZrO_2 calculated using the cluster model shown in Fig. 8.2 .

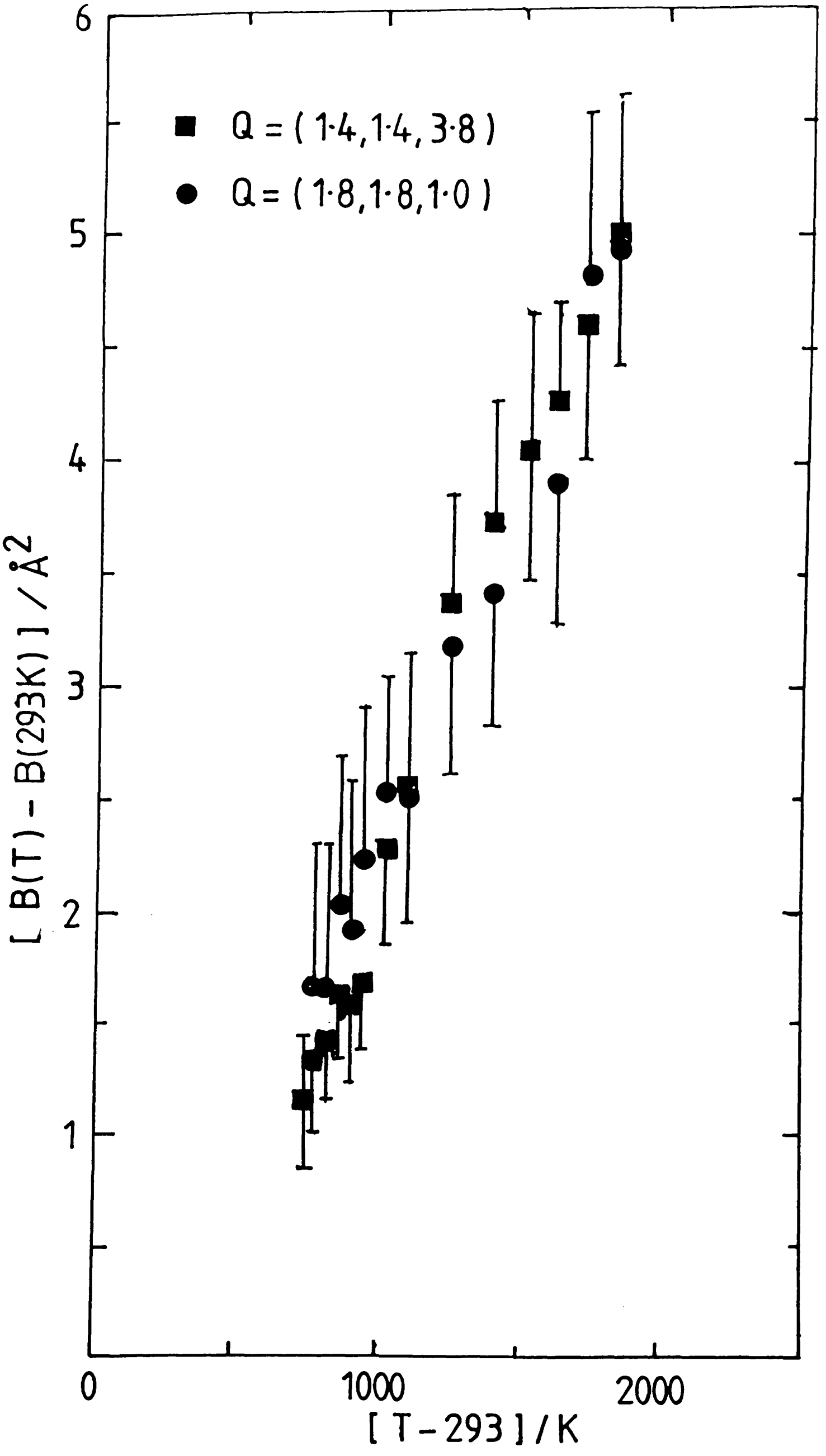

Fig. 8.4 Temperature variation of the isotropic thermal parameter B_0 deduced from the intensities of the diffuse peaks at (1.4,1.4,3.8) and (1.8,1.8,1.0) in ZrO_2 (9.4 mol% Y_2O_3).

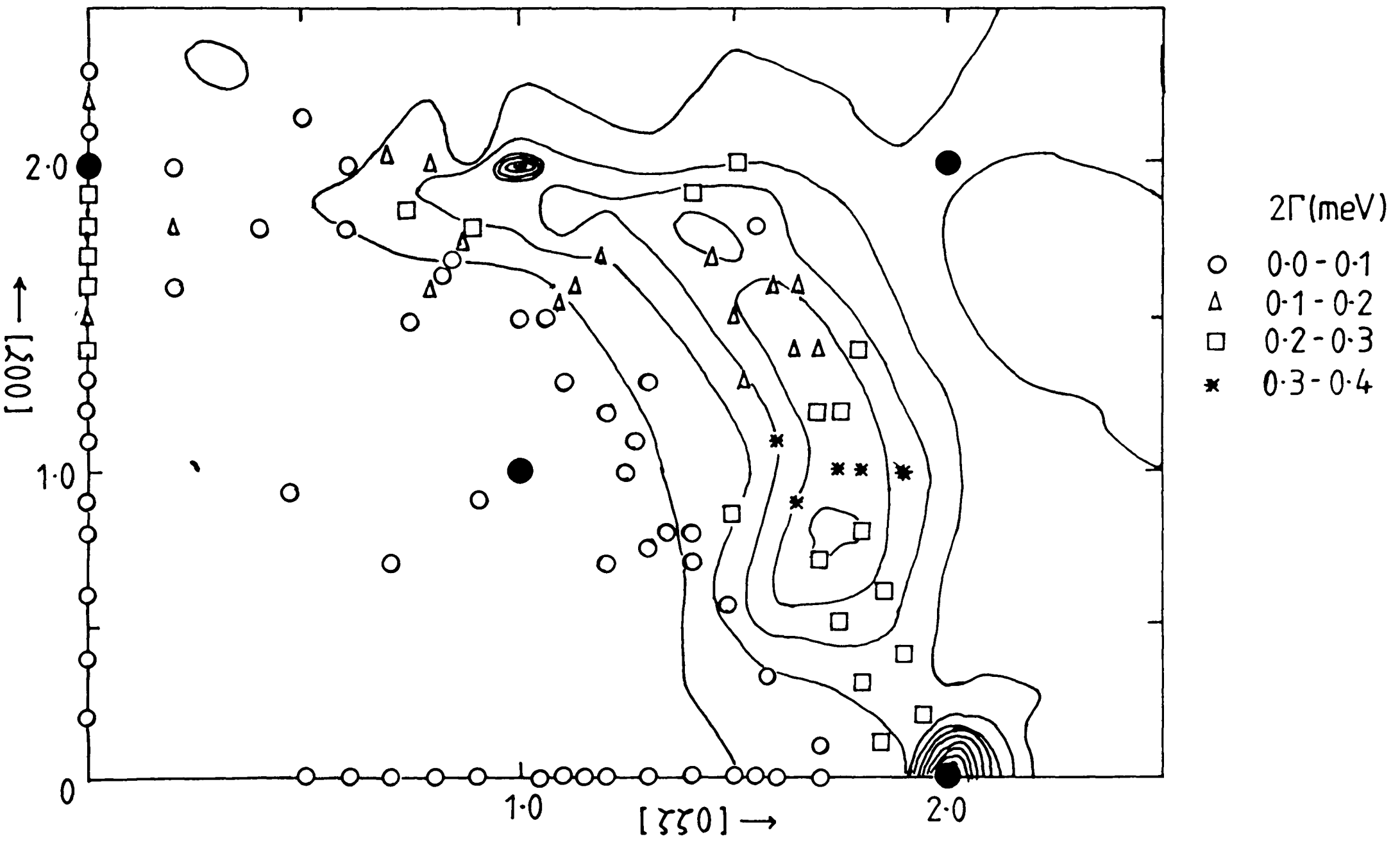

Fig. 8.5 Contour diagram of the observed diffuse QES intensity in the $(1\bar{1}0)$ plane of ZrO_2 (9.4 mol% Y_2O_3) at 1720K. The FWHM 2Γ of a Lorentzian convolved with a Gaussian resolution function, fitted to energy scans at various Q points, are superimposed on the contour map.

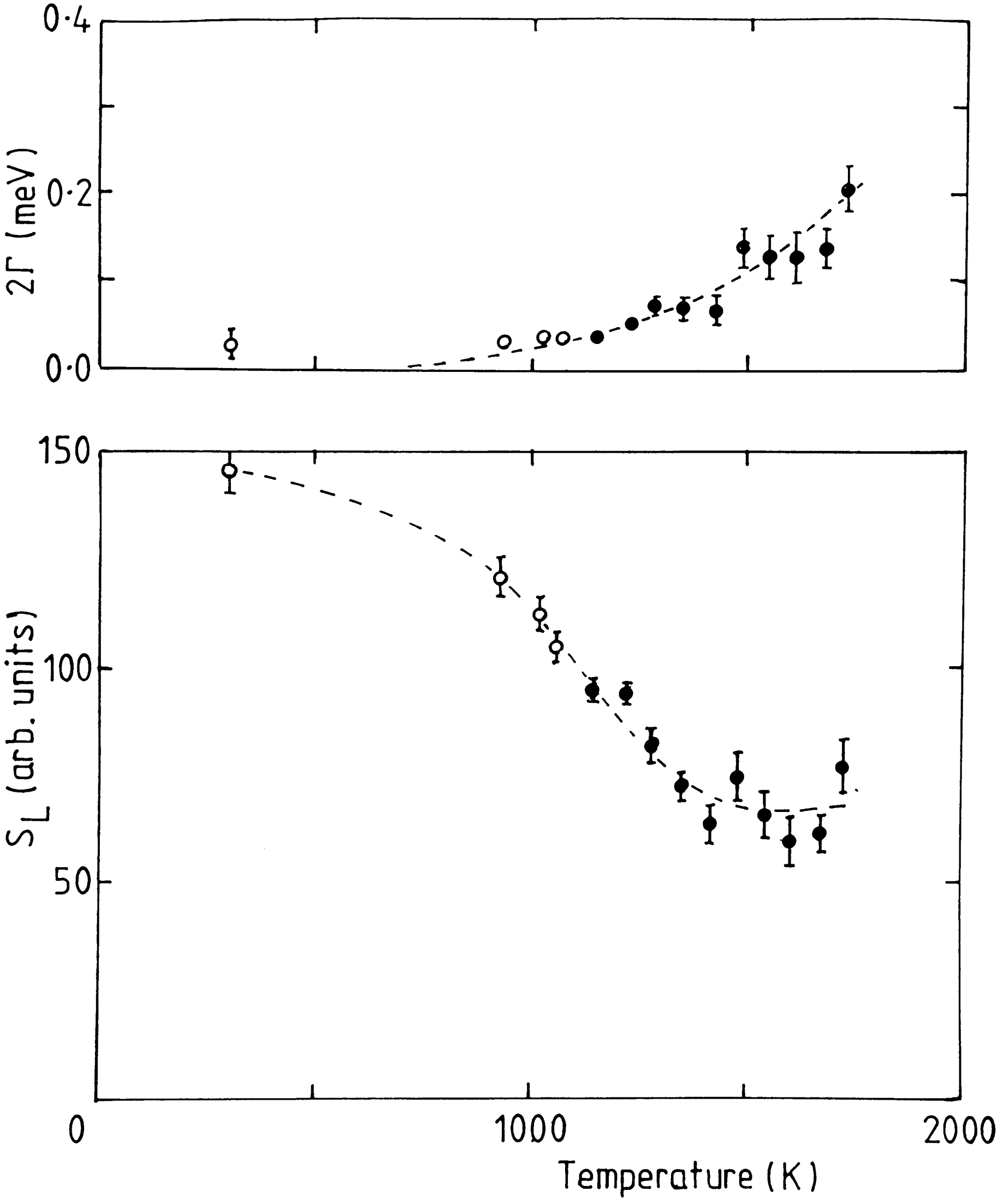

Fig. 8.6 Temperature variation of S_L and 2Γ from fits to energy scans of QES at (0,0,1.9) in ZrO_2 (9.4 mol% Y_2O_3). Open circles denote fits which gave problems with the convolution routine.

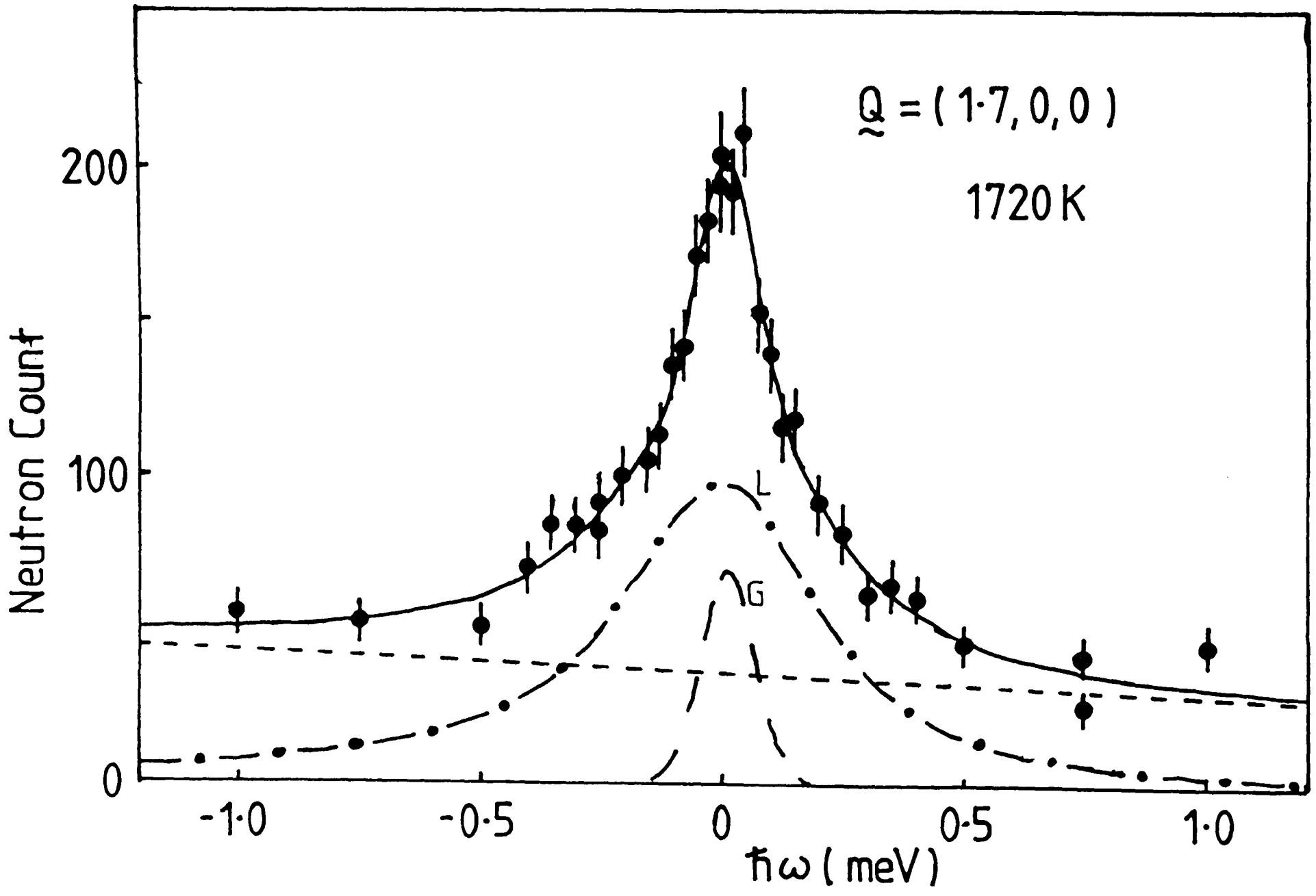

Fig. 8.7 Energy scan at Q = (0,0,1.7) of QES in ZrO_2 (9.4 mol% Y_2O_3) at 1720K. The fitted function (_____) consists of a sum of a sloping background (_ _ _), a Lorentzian convolved with a Gaussian resolution function (__ . __ . __) and a resolution-limited Gaussian representing the incoherent elastic scattering (__ __ __).

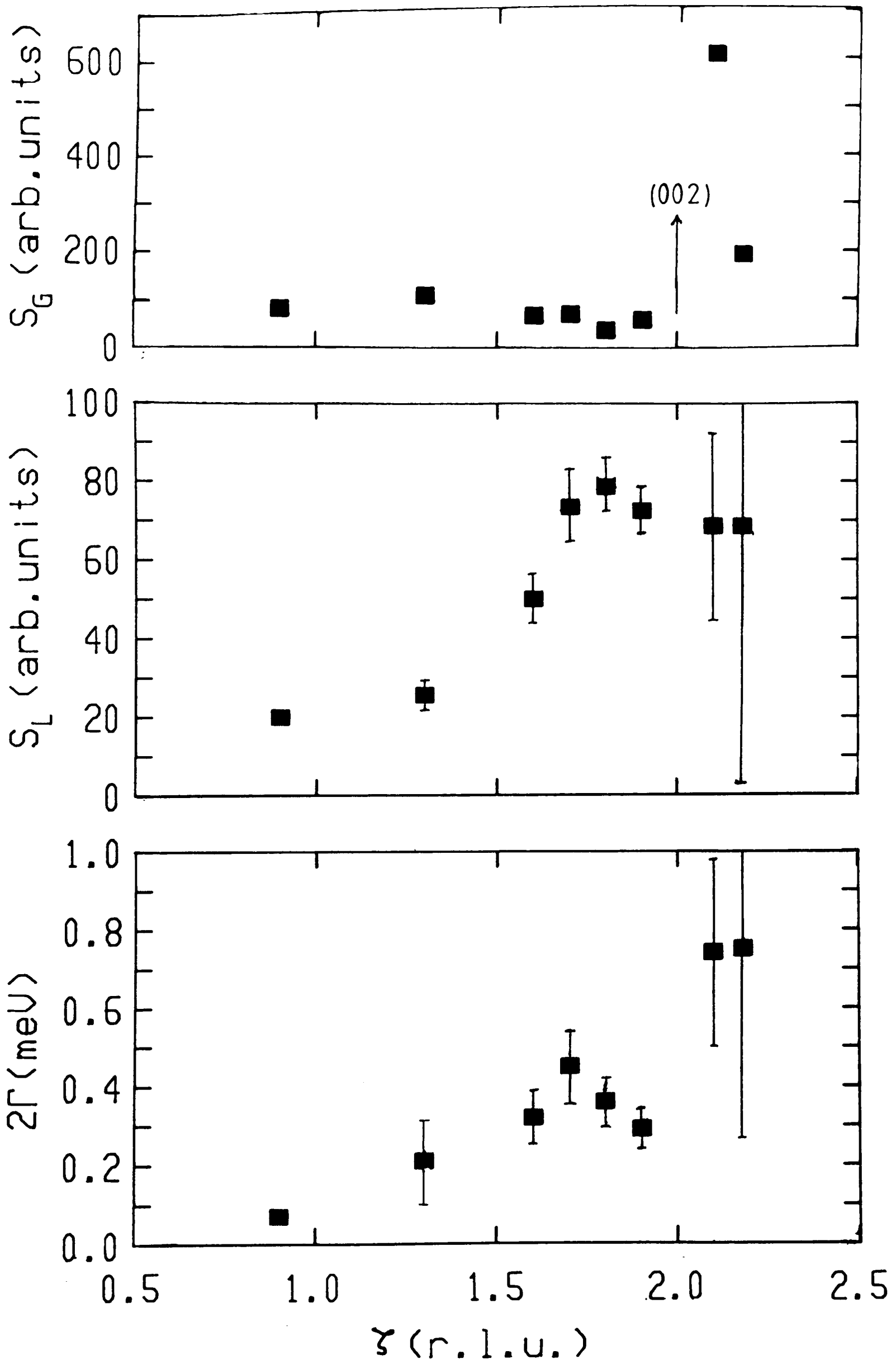

Fig. 8.8 Values of S_G, S_L and 2Γ resulting from fits of energy scans at constant $\underset{\sim}{Q} = (0,0,\zeta)$ in ZrO_2 (9.4 mol% Y_2O_3) at 1720K.

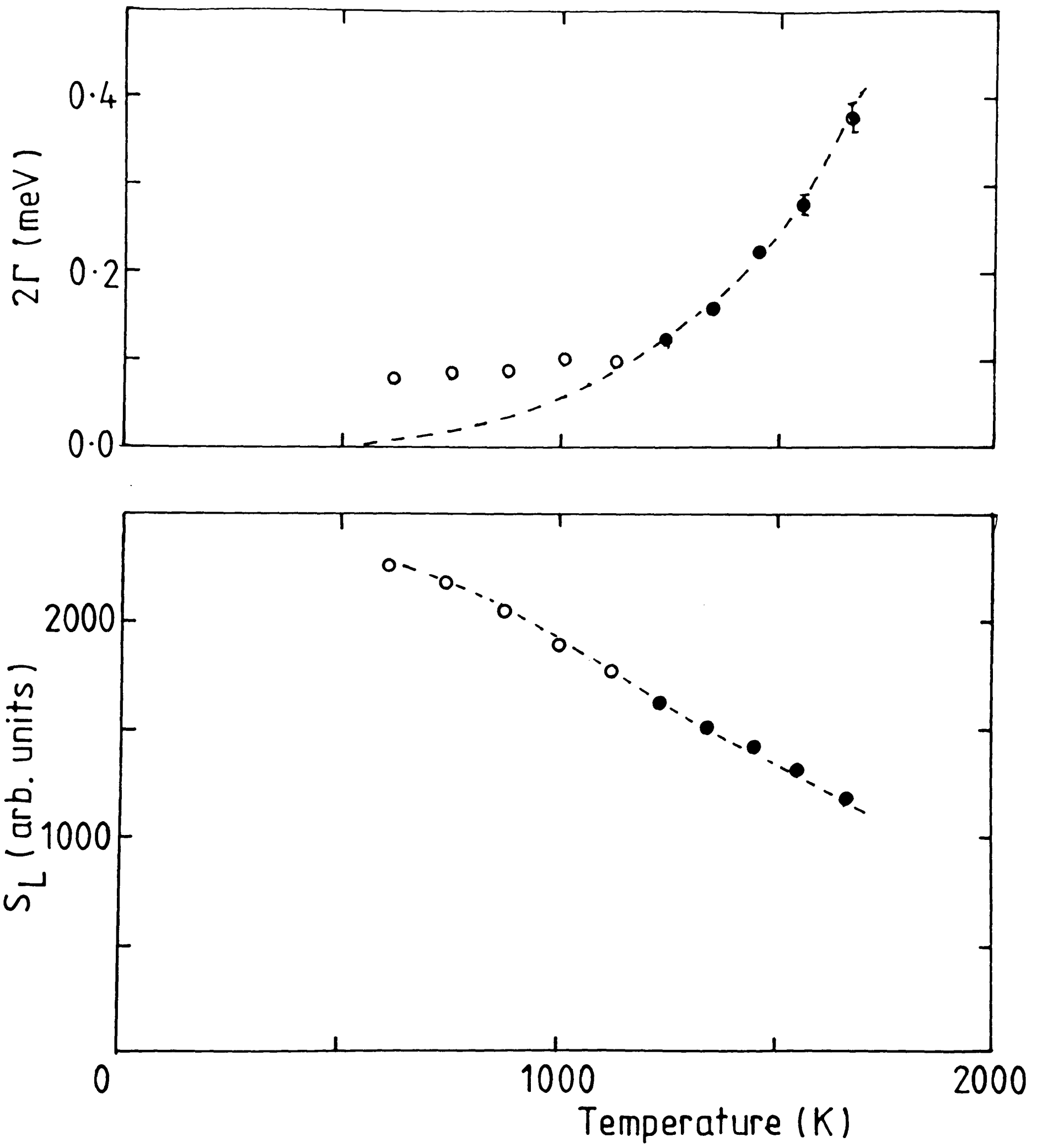

Fig. 8.9 Temperature variation of S_L and 2Γ from fits to energy scans of QES at $Q = (1.8,1.8,0.8)$ in ZrO_2(9.4 mol% Y_2O_3). Open circles denote fits which gave problems with the convolution routine.

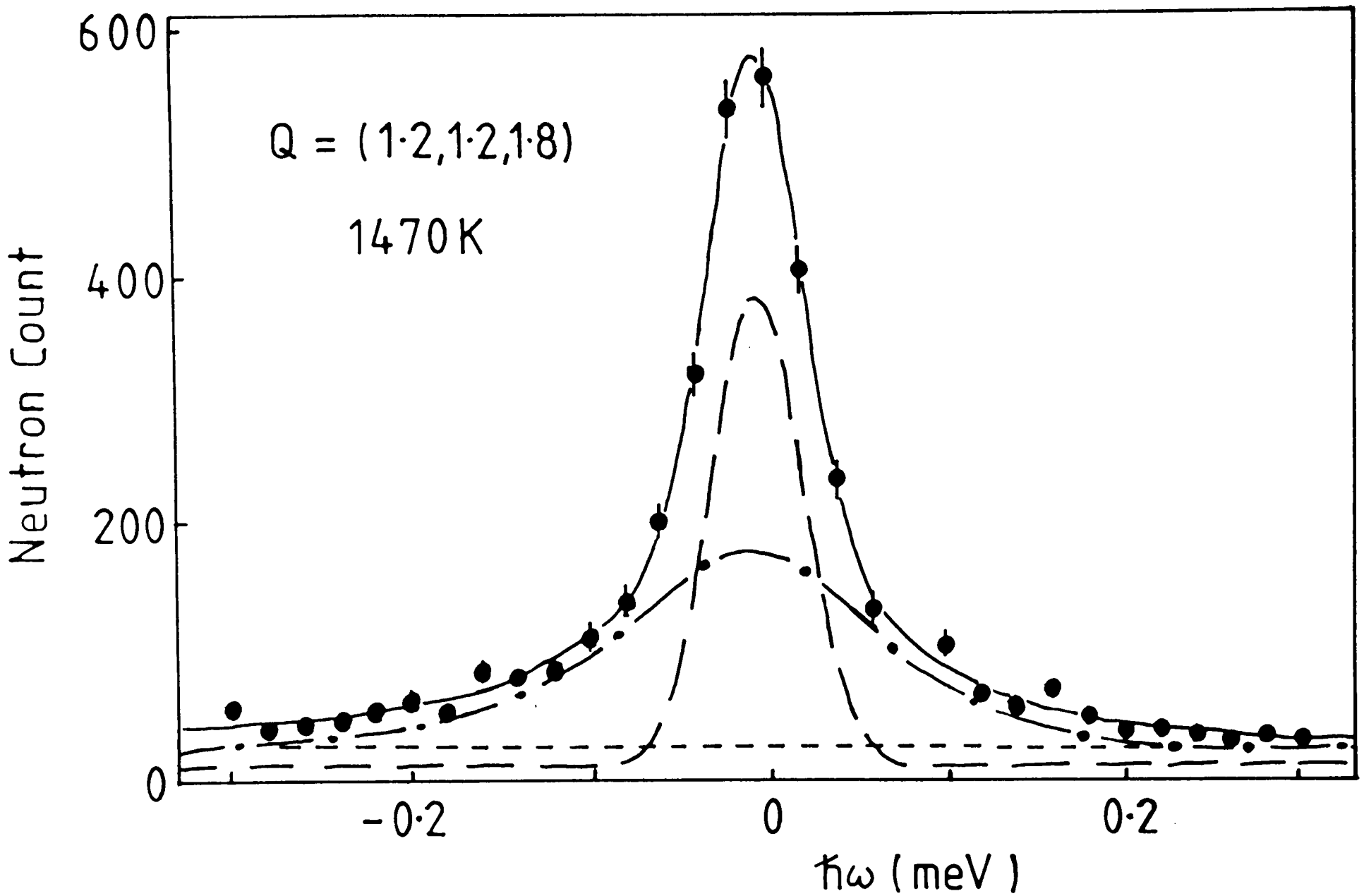

Fig. 8.10 Energy scan at Q = (1.2,1.2,1.8) of QES in ZrO_2 (9.4 mol% Y_2O_3) at 1470K. The fitted function (_____) consists of a sum of a sloping background (_ _ _), a Lorentzian convolved with a Gaussian resolution function (__ . __ . __) and a resolution-limited Gaussian reresenting the coherent elastic scattering (__ __ __).

CHAPTER 9

SUMMARY AND CONCLUSIONS

In this thesis we have described an experimental investigation of the high temperature behaviour of the fluorite oxides UO_2, ThO_2 and Y_2O_3 - doped ZrO_2 using a variety of neutron scattering techniques. Its main aim has been the elucidation of the cause of the anomalously large enthalpy of UO_2 above 1500K, a question of crucial importance for the safety analysis of fast reactors. Thermophysical measurements of macroscopic quantities such as enthalpy, electrical and thermal conductivity have led to two contrasting interpretations. Early workers (e.g. Szwarc 1969) attributed the anomalous behaviour of UO_2 to the formation of Frenkel defects, whereas Catlow (1977) and MacInnes (1978) suggested that it is caused by electronic defects, arising from the uranium ion's multiplicity of possible oxidation states. ThO_2 should have similar lattice dynamical behaviour to UO_2 as a consequence of the comparable atomic masses of U and Th, but the oxides differ in that the Th^{4+} ion is electronically stable. Consequently, a comparison of the results for both materials should help to identify the cause of the excess enthalpy observed in UO_2 at high temperatures. Apart from its technological importance, Y_2O_3 - doped ZrO_2 may also serve as a model of possible small polaron behaviour in UO_2 as a result of the introduction of Y^{3+} ions into a host sub-lattice of Zr^{4+} ions.

The investigation of the properties of these oxides at temperatures above 2000K has required the development of single crystal neutron scattering techniques to higher temperatures than they have hitherto been employed. Pertinent issues concerning the design of furnaces for

high temperature neutron scattering experiments are discussed in the thesis, and a detailed description is given of a furnace which was designed and constructed for these experiments. The furnace has a maximum operating temperature of 2930K and operates continuously at 2700K for over ten days. An account is also given of problems encountered during the experiments, such as evaporation of the crystalline samples and the recrystallisation of the samples and of the metal tubes in which they were encapsulated.

Bragg diffraction measurements, which yield the time-averaged distribution of nuclei in the unit cell, have been performed on UO_2 and ThO_2 at a series of temperatures up to 2900K. It was found that the regular defect-free fluorite structure is inadequate to account for the data at temperatures above 2400K in UO_2 and above 2600K in ThO_2. Various models of the defective structure were fitted to the observed Bragg intensities for both materials. The results indicate that cube-centre sites are not appreciably occupied by anions at high temperatures. The best fit to the data is given by a 3:1:2 cluster model of interstitial and relaxed ions, which is similar to that deduced from diffraction data on PbF_2 and CaF_2. The concentration of defective anions n_d increases with temperature above 2000K in UO_2 and 2200K in ThO_2 to levels of $\sim$20% at $\sim$2800K in both materials. The onset of anion disorder is accompanied by an accelerated rate of increase of the lattice spacing and of the isotropic and anisotropic ionic vibrations.

The full phonon dispersion curves of ThO_2 have been measured in the three symmetry directions and the data fitted with rigid ion and shell models of the atomic vibrations. The elastic and dielectric constants have been deduced from the fitted parameters, which may also

be used to determine the phonon density of states. The phonon dispersion relation of ThO_2 is very similar to that of UO_2, which implies that the interatomic potentials are similar in both oxides. This is consistent with the observation of analagous anion disorder at high temperatures in both compounds using diffraction techniques.

The lattice dynamics of UO_2 have also been investigated at temperatures up to 293OK. Measurements of the low wavevector acoustic phonons, which are sharp and well-defined at all temperatures, give the elastic constants C_{11}, C_{12} and C_{44}. The elastic constants all decrease steadily with increasing temperature, behaviour which is typical of most solids. Above this temperature, the rates of decrease of C_{11}, C_{44} and $\frac{1}{2}(C_{11} - C_{12})$ become more rapid, but no soft modes were observed. The energy widths of the $[\zeta 00]$ TA phonons increase monotonically with increasing wavevector and temperature, but the quality of the data does not allow the determination of the exact q-dependence of the widths. The zone-centre transverse optic and Raman-active phonons broaden dramatically at about 220OK, which is again consistent with increasing anharmonicity and the onset of disorder. The general behaviour of phonons in UO_2 at high temperatures resembles that observed in PbF_2 in its fast-ion region (Dickens et.al. 1979b).

The onset of lattice disorder at high temperatures might be expected to be accompanied by the development of diffuse scattering away from Bragg peaks. Elastic scans show that a diffuse scattering peak, having a width of 0.7Å^{-1}, evolves around (0, 0, 2.15) above 210OK in UO_2. This peak is similar to the diffuse peak which characterises the fluorite halides in their fast-ion phase. The scattering in this region of reciprocal space is energy-broadened at

high temperatures, signifying a lifetime of ~2ps. This quasi-elastic peak may be reproduced in calculations of the diffuse intensity for the 3:1:2 cluster model of the defective structure, which also accounted well for the diffraction data. The values of n_d, which may be deduced by comparing the observed quasi-elastic intensity with the observed intensity of a phonon peak, are also in reasonable agreement with diffraction results. Further detailed investigations are required of the distribution of quasi-elastic intensity in reciprocal space and of its energy width using finer spectrometer resolution.

Comparison of the results of diffraction, quasi-elastic and phonon scattering experiments for the fluorite oxides and halides suggest a value of T_c = 2400K for UO_2 and 2600K for ThO_2. However it should be emphasised that T_c does not represent a critical temperature for a true phase transition. There are no abrupt changes in the lattice spacing, scattered intensity or energy width near T_c - the onset of lattice disorder is a gradual, thermally-induced phenomenon. As has been noted repeatedly throughout the thesis, the results of the various neutron scattering experiments of UO_2 and ThO_2 resemble closely those obtained from corresponding investigations of the fluorite halides CaF_2, PbF_2 and $SrCl_2$. This similarity strongly suggests that the onset of anion disorder in the oxides is analagous to that observed in the fast-ion regime of the halides. This resemblance is further underlined by a comparison of the ratios T_c/T_m and E_F/T_c for the oxides and halides (Table 9.1).

An interesting observation which demands further investigation is the plastic deformation of UO_2 at high temperatures. After cooling two large UO_2 crystals to room temperature, from 2793K and 2930K respectively, it was found, in both experiments, that the tungsten

TABLE 9.1

A COMPARISON OF THE PROPERTIES OF FLUORITE OXIDES AND HALIDES

Compound	T_m(K)	T_c(K)	E_F(eV)	T_c/T_m	$\frac{0.1\ E_F}{k_B T_c}$
CaF_2	1696	1423	2.71	0.84	2.1
SrF_2	1746	1450	2.28	0.83	1.7
BaF_2	1628	1235	1.91	0.76	1.7
PbF_2	1128	705	1.0	0.63	1.6
$SrCl_2$	1148	993	1.70	0.86	1.9
UO_2	3120	2400	4.6	0.77	2.1
ThO_2	3640	2600	-	0.71	-

sample encapsulation tubes had partially collapsed under the external excess pressure of ~25p.s.i.. On opening the sample tubes, the UO_2 crystals were found to have deformed and assumed the shape of the tube. This effect can probably be identified with the large increase in the creep rate observed in UO_2 between 2500K and 2900K (Slagle 1978) and with the change in the textural appearance of UO_2 reported to occur between 2661K and 2699K (Ackermann 1955). It is unclear whether this phenomenon is directly related to the onset of anion disorder which develops above 2000K. In this respect, it should be noted that there have been no reports of such deformation in the fluorite halides.

Quasi-elastic scattering techniques have also been used to investigate the defect structure of Y_2O_3 - stabilised ZrO_2, a material of considerable technological importance. Contour diagrams of the observed quasi-elastic intensity in the $(1\bar{1}0)$ plane at room temperature, for Y_2O_3 molar concentrations of 9 - 18%, show concentric, anisotropic shells of scattering which contain a fair degree of structure. The $\underset{\sim}{Q}$ - width of the diffuse scattering decreases with increasing Y_2O_3 concentration, signifying an increase in the correlation length. A simple defect cluster model of an oxygen vacancy with [100] relaxations of neighbouring oxygen ions and [111] relaxations of neighbouring cations towards the vacancy may be used to reproduce the general features of the scattered intensity, but it fails to account for the detailed structure of the scattering. This failure is probably partly due to the neglect of interactions between defect clusters and of long range correlations.

Investigation of the development of the quasi-elastic scattering at elevated temperatures for ZrO_2(9.4 mol% Y_2O_3) shows that the distribution and intensity of the scattering do not change substantially

up to 2100K, after correction for Debye-Waller factors. However the diffuse scattering broadens in energy above 1000K in the region of intense scattering near (1.0, 1.0, 0.8). This indicates that, although the defect clusters occur at temperatures up to 2100K, these clusters have finite lifetimes of ~5ps at 1500K. One plausible interpretation of the data is that the oxygen vacancies become mobile above 1000K, giving rise to the enhanced electrical conductivity observed at ~1300K (Suzuki et.al. 1981). As the vacancy hops from one site to another, the original cluster of relaxed ions is broken up and another similar cluster forms around the new vacancy site. The energy broadening observed in the region of intense diffuse scattering above 1000K is accompanied by the evolution of weak energy-broadened scattering along the $[00\zeta]$ axis near $\zeta = 1.7$, where the elastic diffuse scattering at room temperature is very weak. The origin of the broadening in this region of reciprocal space is difficult to ascertain and requires further investigation. Another possible extension of the work is the investigation of the high temperature behaviour of samples containing larger concentrations of Y_2O_3, which show longer-range correlations at room temperature.

The main conclusion to be drawn from this work is the occurence of anion disorder in UO_2 and ThO_2 at high temperatures. Diffraction measurements, which provide a direct probe of anion disorder, show unambiguously that a growing fraction of anions vacate their regular sites above 2000K in UO_2 and above 2200K in ThO_2. The results are supported by the observation of diffuse quasi-elastic scattering in UO_2 above 2000K which is in broad agreement with the diffraction data. Investigations of the lattice dynamics of UO_2 also indicate the onset of disorder in this temperature range, but do not give much

direct information concerning the nature of the disorder. No evidence has been seen of the electronic disorder predicted to occur in UO_2 above 1500K, but it should be noted that such behaviour can only be investigated indirectly through electron-phonon interactions using neutron scattering techniques. The results presented in this thesis should also facilitate the interpretation and prediction of the thermodynamic properties of UO_2 and ThO_2 at high temperatures, which are of great importance for the nuclear power industry.

REFERENCES

Ackermann R J 1955 Ph.D. Thesis (University of Kansas)

Ackermann R J, Gilles P W and Thorn R J 1956 J. Chem. Phys. 25, 1089

Albinati A, Cooper M J, Rouse K D, Thomas M W and Willis B T M 1980 Acta Cryst. A36, 265

Aldebert P and Traverse J P 1981 High Temperatures - High Pressures 13, 251

Allpress J G and Rossell H J 1975 J. Sol. State. Chem. 15, 68

Axe J D 1965 Phys. Rev. 139, A1215

Axe J D and Pettit G D 1966 Phys. Rev. 151, 676

Bacon G E 1975 Neutron Diffraction, 3rd ed. (Oxford:Clarendon)

Bates J L, Hinman C A and Kawada T 1967 J. Am. Ceram. Soc. 50, 652

Becker P J and Coppens P 1974 Acta Cryst. A30, 129 - 147 and 148 - 153

Boeuf A, Caciuffo R, Rebonato R, Rustichelli F, Fournier J M, Kischko U and Manes L 1982 Phys. Rev. Letters 49, 1086

Born M and Huang K 1954 Dynamical Theory of Crystal Lattices (Oxford: Clarendon)

Bredig M A 1972 Etude des Transformations Cristallines à Haute Temperature, Colloques Int. CNRS No. 205, p.183

Browning P, Hyland G J and Ralph J 1983 High Temperatures - High Pressures 15, 169

Burnett S J 1964 Properties of Refractory Materials AERE - R4567

Carr V M, Chadwick A V and Saghafian R 1978 J. Phys. C11, L637

Carter R E and Roth W L 1968 Electromotive Force Measurements in High Temperature Systems (ed. C. B. Alcock) p.125 (Elsevier:New York)

Catlow C R A 1977 Proc. Roy. Soc. A353, 533

Catlow C R A and Hayes W 1982 J. Phys. C15, L9

Chadwick A V 1983 Solid State Ionics 8, 209

Cheetham A K 1973 in Chemical Applications of Neutron Scattering (ed. B.T.M. Willis) p.225 (OUP)

Chudley C T and Elliott R J 1961 Proc. Phys. Soc. 77, 353

Clausen K, Hayes W, Hutchings M T, Kjems J K, Schnabel P and Smith C 1981 Solid State Ionics 5, 589

Clausen K, Hayes W, Macdonald J E, Schnabel P, Hutchings M T and Kjems J K 1983 High Temperatures - High Pressures 15, 383

Cochran W 1971 Crit. Rev. Solid State Science 2, 1

Cooper M J and Rouse K D 1970 Acta Cryst. A26, 214

Dawson B, Hurley A C and Maslen V W 1967 Proc. Roy. Soc. A298, 289

Dick B J and Overhauser A W 1958 Phys. Rev. 112, 90

Dickens M H and Hutchings M T 1978 J. Phys. C11, 461

Dickens M H, Hutchings M T, Kjems J K and Lechner R E 1978 J. Phys. C11, L583

Dickens M H, Hayes W, Smith C, Hutchings M T and Kjems J K 1979a in Fast Ion Transport in Solids (eds. P. Vashishta, J. N. Mundy and G. K. Shenoy) p.229-32 (Elsevier North Holland:Amsterdam)

Dickens M H, Hayes W, Hutchings M T and Klepmann W G 1979b J. Phys. C12, 17

Dickens M H, Hayes W, Hutchings M T and Smith C 1982 J. Phys. C15, 4043

Dolling G, Cowley R A and Woods A D B 1965 Canad. J. Phys. 43, 1397

Dorner B 1972 Acta Cryst. A28, 319

Dorner B 1982 Coherent Inelastic Neutron Scattering in Lattice Dynamics, Springer Tracts in Modern Physics vol.93 p.17 (Springer Verlag: Berlin)

Elcombe M M 1972 J. Phys. C5, 2702

Elcombe M M and Pryor A W 1970 J. Phys. C3, 492

Etsell T H and Flengas S N 1970 Chem. Rev. 70, 339

Faber J, Mueller M H and Cooper B R 1978 Phys. Rev. B17, 4884

Feinberg A and Perry C H 1981 ILL Report (experiment 7.03.154)

Fink J K 1982 Intl. J. of Thermodynamics 3, 165

Fink J K, Chasanov M G and Leibowitz L 1981 J. Nucl. Mater. 102, 17

Fischer D F, Fink J K and Leibowitz L 1981 J. Nucl. Mater. 102, 220

Frederickson D R and Chasanov M G 1970 J. Chem. Thermo. 2, 263

Fritz I J 1976 J. Appl. Phys. 47, 4353

Gillan M J and Dixon M 1981 Solid State Ionics 5, 593

Gillan M J and Richardson D D 1979 J. Phys. C12, L61

Hamilton W C 1965 Acta Cryst. 18, 502

Harding J H, Masri P and Stoneham A M 1980 J. Nucl. Mater. 92, 73

Hein R A, Sjodahl L A and Szwarc R 1968 J. Nucl. Mater. 25, 99

Hoch M and Momin A C 1969 High Temperatures - High Pressures 1, 401

Hutchings M T 1982 A.I.P. Conf. Proc. No. 89, 209

Hutchings M T, Clausen K, Dickens M H, Hayes W, Kjems J K, Schnabel P G and Smith C 1984 J. Phys. C17, 3903 and AERE - R11127

Hyland G J and Stoneham A M 1981 J. Nucl. Mater. 96, 1

Ishigame M and Kojima M 1976 J. Phys. Soc. Japan 41, 202

Jacucci G and Rahman A 1978 J. Chem. Phys. 69, 4117

Kellermann E W 1940 Phil. Trans. R. Soc. A238, 513

Kerrisk J F and Clifton D G 1972 Nucl. Technol. 16, 531

Killeen J C 1980 J. Nucl. Mater. 88, 185

Kittel C 1971 Introduction to Solid State Physics 4th ed. (Wiley)

Kjems J K, Andersen N H, Schoonman J and Clausen K 1983 Physica 120B, 357

Koester L and Rauch H 1981 Report on IAEA Contract 2517/RD

Koto K, Schulz H and Huggins R A 1980 Solid State Ionics 1, 355

Leibowitz L, Mishler L W and Chasanov M G 1969 J. Nucl. Mater. 29, 356

Lidiard A B 1974 in Crystals with the Fluorite Structure (ed. W. Hayes) p.101 (Oxford:Clarendon).

Macedo P M, Capps W and Wachtman J B 1964 J. Am. Ceram. Soc. 47, 651

MacInnes D A 1978 J. Nucl. Mater. 78, 225

MacInnes D A 1979 Proc. Intl. Symp. on Thermodynamics of Nuclear Materials (IAEA:Vienna) SM - 236/37, 129

Matzke Hj 1976 Plutonium and Other Actinides (eds. H. Blank and R. Lidner) p.801 (North Holland:Amsterdam)

Moore G E and Kelley K K 1947 J. Am. Chem. Soc. 69, 2105

Morinaga M, Cohen J B and Faber J 1979 Acta Cryst. A35, 789

Morinaga M, Cohen J B and Faber J 1980 Acta Cryst. A36, 520

Munir Z A 1981 Int. J. Thermophys. 2, 177

Ogard A E and Leary J A 1968 Thermodynamics of Nuclear Materials (IAEA:Vienna) p.651

Rand M H, Ackermann R J, Gronvold F, Oetting F L and Pattoret A 1978 Rev. Int. Hautes Tempér. Refract. Fr. 15, 355

Rouse K D and Cooper M J 1969 Acta Cryst. A25, 615

Rouse K D and Cooper M J 1980 AERE Report R9940

Rouse K D, Cooper M J, York E J and Chakera A 1970 Acta Cryst. A26, 682

Schnabel P G 1983 D. Phil. Thesis (Oxford University)

Schröter W and Nölting J 1980 J. Physique Colloque 41, C6 - 20

Schulz H and Zucker U H 1981 Solid State Ionics 5, 41

Shannon R D and Prewitt C T 1969 Acta Cryst. B25, 925

Slagle O D 1978 Deformation Behaviour of UO_2 at Temperatures above 2400°C, HEDL - TME - 78 - 31

Smith C 1980 D. Phil. Thesis (Oxford University)

Squires G L 1978 Introduction to the Theory of Thermal Neutron Scattering (CUP)

Steele D and Fender B E F 1974 J. Phys. C7, 1

Stubican V S, Hink R C and Ray S P 1978 J. Am. Ceram. Soc. 61, 17

Suzuki Y, Takahashi T and Nagae N 1981 Solid State Ionics 3/4, 483

Szwarc R 1969 J. Phys. Chem. Solids 30, 705

Van Hove L 1954 Phys. Rev. 95, 249

Viechnicki D and Stubican V S 1965 J. Am. Ceram. Soc. 48, 292

Vineyard G H 1958 Phys. Rev. 110, 999

Wachtman J B, Wheat M L, Anderson H J and Bates J L 1965 J. Nucl. Mater. 16, 39

Walker A B, Dixon M and Gillan M J 1981 Solid State Ionics 5, 601

Walker A B, Dixon M and Gillan M J 1982 J. Phys. C15, 4061

Willis B T M 1963 Proc. Roy. Soc. A274, 134

Willis B T M 1969 Acta Cryst. A25, 277

Willis B T M 1978 Acta Cryst. A34, 88

Willis B T M and Hazell R G 1980 Acta Cryst. A36, 582

Woods A D B, Cochran W and Brockhouse B N 1960 Phys. Rev. 119, 980

Zachariasen W H 1967 Acta Cryst. 23, 558

APPENDIX A.1

WELDING TECHNIQUES

In view of tungsten's brittleness and high melting point, considerable difficulty may be expected in sealing and welding 0.3mm thick sample tubes onto mounting rods or tubes. In order to achieve the localised, low-power heating required, the electron beam welding technique was chosen, in which a focussed electron beam impinges on the joint. Machined tungsten collars were made to join the sample tube onto a pyrometer sighting tube or onto mounting rods for operation with thermocouples. In order to avoid burning a hole through tungsten, the electron beam was focussed onto the thicker collars in such a way that the molten tungsten would flow onto the thinner metal of the sample tube. The techniques, which were developed in conjunction with K Habgood and M Paul who performed the welding, are illustrated in Fig. A.1.

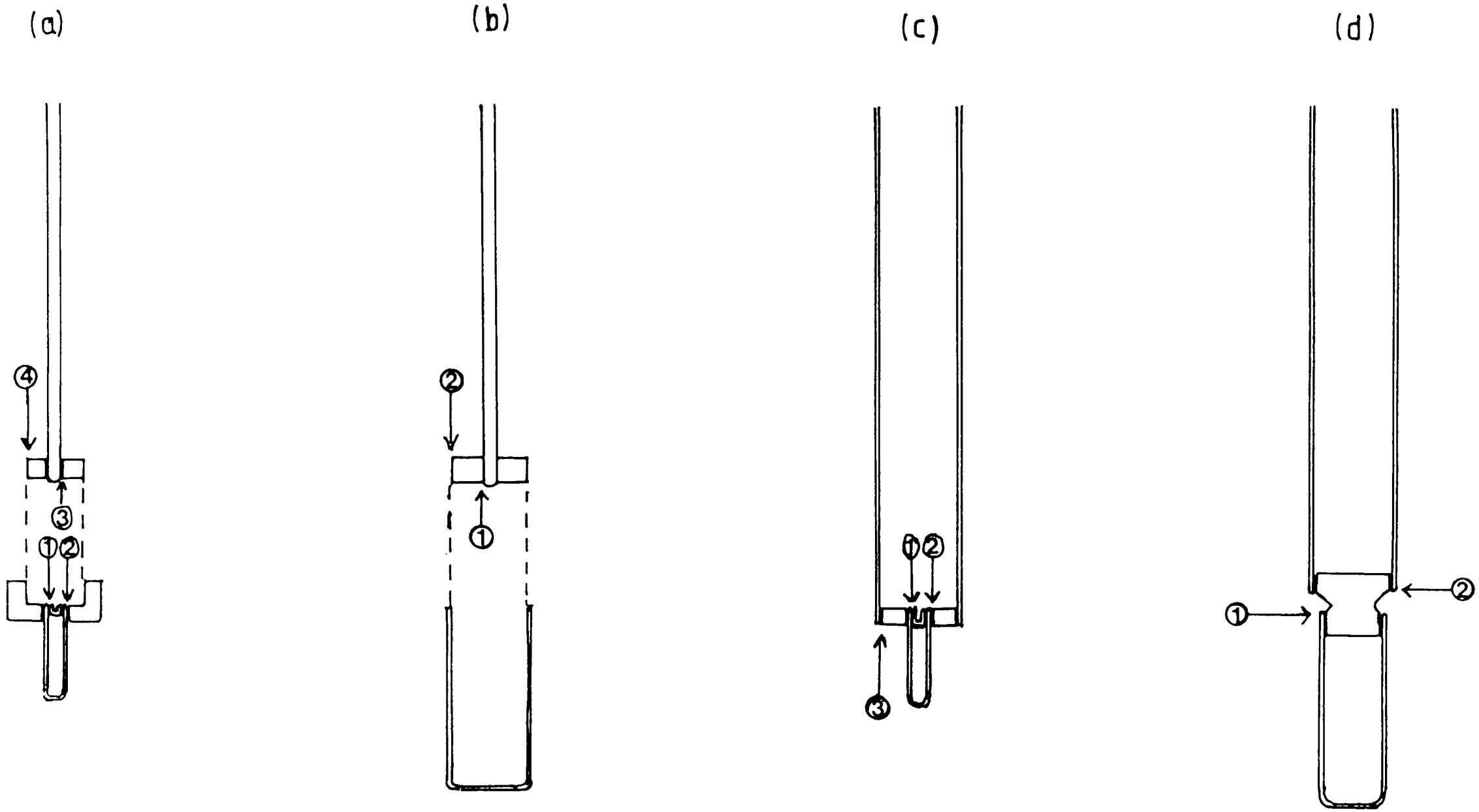

Fig. A.1.1 A schematic diagram of the welding procedures developed for sealing and mounting sample tubes onto tungsten rods (for use with thermocouples - (a) and (b)) and onto sighting tubes (for use with a pyrometer - (c) and (d)).

APPENDIX A.2

STRUCTURE FACTORS FOR THE MODELS USED IN THE DIFFRACTION ANALYSIS

The structure factor for a unit cell (fig. 1.1) may be expressed as a product of the structure factor for the four face-centred cubic lattice points and that for the basis of the metal ion and the oxygen ions.

$$F(hkl) = \left[1 + \cos\ (h + k) + \cos\ (k + l) + \cos\ (l + h)\right] . \times \left[b_M e^{-W_M} + b_o F_i^o \right]$$

where F_i^o is the contribution from the oxygen ions for model i.

$$F_{\underline{I}}^o = 2 \cos \tfrac{1}{2}\pi (h + k + l).\ e^{-W_o}$$

$$F_{\underline{IA}}^o = F_{\underline{I}}^o .\ C_{123}^o .\ hkl$$

$$F_{\underline{II}}^o = (1 - n_d) F_{\underline{IA}}^o$$

$$F_{\underline{III}}^o = F_{\underline{II}}^o + n_d e^{-W_o^I} F_R \quad \text{with } x = 0.5$$

$$F_{\underline{IV}}^o = F_{\underline{II}}^o + n_d e^{-W_o^I} F_I \quad \text{with } y = 0.0$$

$$F_{\underline{V}}^o = F_{\underline{II}}^o + n_d e^{-W_o^I} F_R$$

$$F_{\underline{VI}}^o = F_{\underline{II}}^o + n_d e^{-W_o^I} (2/3\ F_R + 1/3\ F_I)$$

$$F_{\underline{VII}}^o = F_{\underline{II}}^o + n_d e^{-W_o^I} (\tfrac{1}{2} F_R + \tfrac{1}{2} F_I)$$

$$F_{\underline{VIII}}^o = F_{\underline{II}}^o + n_d e^{-W_o^I} \left[(1 - d) F_R + d F_I \right]$$

$$F_{\underline{IX}}^o = F_{\underline{II}}^o + n_d e^{-W_o^I} \left\{ 2/3\ F_R + \frac{4}{9} \cos \tfrac{1}{2}\pi (h + k + l) \times \left[\frac{1}{h} \sin \tfrac{1}{2}\pi h + \frac{1}{k} \sin \tfrac{1}{2}\pi k + \frac{1}{l} \sin \tfrac{1}{2}\pi l \right] \right\}$$

where

$$F_R = \tfrac{1}{2}\left[\cos 2\pi x(h + k + l) + \cos 2\pi x\,(h + k - l) + \cos 2\pi x(h - k + l) + \cos 2\pi x(-h + k + l)\right]$$

$$F_I = {}^{1}/_{3}\cos \pi(h + k + l)\left[\cos w(h + k) + \cos w(h - k) + \cos w(k + l) + \cos w(k - l) + \cos w(l + h) + \cos w(l - h)\right]$$

with $w = \tfrac{1}{2}\pi(1 - 4y)$.

APPENDIX A.3

DIFFRACTION RESULTS AND LEAST SQUARES ANALYSIS

Observed and Calculated Intensities for best-fitting Models

ALPHA : α_{TDS} , Thermal diffuse scattering correction

FO : $(I_o \sin\gamma\cos\nu)^{\frac{1}{2}}$ where I_o = observed Bragg intensity

FC : Structure Factor for best-fitting model

UO_2

293K

H	K	L	ALPHA	FC	FO	SIGMA
2	2	8				
0	0	8	0.013	116.82	116.22	0.56
3	3	7	0.013	57.89	57.43	0.24
1	1	7	0.010	59.94	59.93	0.24
4	4	6	0.013	13.14	13.42	0.82
2	2	6	0.009	17.15	17.98	0.47
0	0	6	0.007	18.58	18.55	0.11
5	5	5				
3	3	5	0.009	60.85	60.99	0.17
1	1	5	0.005	62.50	62.54	0.25
4	4	4	0.010	122.55	123.44	0.77
2	4	4	0.004	126.58	127.59	0.76
0	0	4	0.003	125.38	125.30	0.16
5	5	3	0.012	58.96	59.15	0.30
3	3	3	0.005	62.50	62.40	0.48
1	1	3	0.002	63.41	62.85	0.51
6	6	2				
4	4	2	0.007	18.58	18.85	0.70
2	2	2	0.002	23.20	23.05	0.14
0	0	2	0.000	24.75	24.84	0.20
5	5	1	0.010	59.94	60.13	0.23
3	3	1	0.003	63.14	63.08	0.47
1	1	1	0.000	61.67	59.76	0.89
6	6	0				
4	4	0	0.006	126.06	126.19	0.18
2	2	0	0.001	119.68	120.60	1.55
0	2	8	0.013	13.14	12.73	0.40
1	3	7	0.012	58.96	59.05	0.38
2	4	6	0.011	119.97	119.59	0.71
0	2	6	0.008	124.61	123.62	1.00
1	3	5	0.007	61.72	61.75	0.38
0	2	4	0.003	21.62	21.84	0.41
1	5	7				
0	4	6	0.011	15.76	15.91	0.26

1873K

H	K	L	ALPHA	FC	FO	SIGMA
2	2	8	0.134	38.54	36.50	1.80
0	0	8	0.127	44.64	43.30	3.50
3	3	7	0.130	28.22	28.00	0.70
1	1	7	0.104	32.98	31.20	1.20
4	4	6	0.131	8.79	8.60	0.40
2	2	6	0.089	5.83	5.80	0.30
0	0	6	0.071	4.22	4.60	0.30
5	5	5				
3	3	5	0.087	32.83	31.80	1.00
1	1	5	0.050	44.88	42.10	1.80
4	4	4	0.100	60.09	61.70	0.70
2	2	4	0.043	88.91	88.80	2.40
0	0	4	0.025	97.54	93.00	4.00
5	5	3	0.119	32.89	31.20	1.90
3	3	3	0.050	49.50	50.10	1.90
1	1	3	0.015	56.39	54.70	1.30
6	6	2				
4	4	2	0.071	3.21	4.00	0.60
2	2	2	0.017	10.80	11.20	0.30
0	0	2	0.004	19.68	19.30	1.00
5	5	1				
3	3	1	0.032	48.79	48.50	3.30
1	1	1	0.002	57.72	57.30	3.50
6	6	0				
4	4	0				
2	2	0	0.010	101.76	103.10	3.00
0	2	8	0.131	8.84	9.20	2.00
1	3	7				
2	4	6	0.095	49.21	49.20	2.80
0	2	6				
1	3	5	0.069	42.43	38.90	3.00
0	2	4	0.034	4.12	4.20	0.40
1	5	7				
0	4	6				

2098K

H	K	L	ALPHA	FC	FO	SIGMA
2	2	8	0.365	3.38	3.42	0.20
0	0	8	0.313	4.04	4.10	0.34
3	3	7	0.328	2.96	2.75	0.56
1	1	7	0.221	3.39	3.23	0.14
4	4	6	0.333	1.24	1.41	0.15
2	2	6	0.187	1.13	1.83	0.54
0	0	6	0.136	0.92	1.10	0.54
5	5	5				
3	3	5	0.182	3.10	2.92	0.14
1	1	5	0.096	4.89	4.88	0.06
4	4	4	0.206	5.79	5.93	0.29
2	2	4	0.073	9.87	9.86	0.24
0	0	4	0.044	11.66	11.55	0.46
5	5	3	0.274	3.58	3.52	0.26
3	3	3	0.096	5.76	5.75	0.15
1	1	3	0.027	6.69	6.54	0.14
6	6	2				
4	4	2	0.147	0.87	0.97	0.20
2	2	2	0.030	0.84	1.45	0.50
0	0	2	0.005	2.19	2.12	0.20
5	5	1	0.221	3.01	3.22	0.15
3	3	1	0.055	5.41	5.32	0.21
1	1	1	0.004	7.17	7.23	0.15
6	6	0	0.365	3.40	3.78	0.40
4	4	0	0.118	8.35	8.70	0.25
2	2	0	0.017	13.11	13.11	0.20
0	2	8	0.333	1.25	1.15	0.50
1	3	7	0.274	2.70	2.60	0.25
2	4	6	0.259	4.83	4.94	0.21
0	2	6	0.155	6.89	6.80	0.25
1	3	5	0.132	4.67	4.54	0.15
0	2	4				
1	5	7	0.365	2.37	2.25	0.50
0	4	6	0.226	1.19	1.23	0.30

2218K

H	K	L	ALPHA	FC	FO	SIGMA
2	2	8	0.395	3.65	3.73	0.10
0	0	8	0.339	4.38	4.41	0.20
3	3	7	0.355	3.32	3.23	0.11
1	1	7	0.240	3.89	3.77	0.06
4	4	6	0.361	1.63	1.69	0.17
2	2	6	0.202	1.56	1.68	0.06
0	0	6	0.148	1.32	1.58	0.21
5	5	5	0.411	1.80	1.69	0.21
3	3	5	0.197	3.64	3.62	0.06
1	1	5	0.104	5.60	5.58	0.10
4	4	4	0.224	6.29	6.31	0.07
2	2	4	0.080	10.28	10.09	0.14
0	0	4	0.047	11.45	11.16	0.14
5	5	3	0.297	4.01	3.92	0.10
3	3	3	0.104	6.46	6.54	0.09
1	1	3	0.029	7.30	7.33	0.08
6	6	2	0.416	1.54	1.56	0.15
4	4	2	0.159	1.33	1.04	0.26
2	2	2	0.032	0.94	1.19	0.08
0	0	2	0.006	2.56	2.49	0.06
5	5	1	0.240	3.49	3.35	0.15
3	3	1	0.059	6.17	6.25	0.09
1	1	1	0.004	7.19	7.33	0.13
6	6	0	0.395	3.65	3.88	0.15
4	4	0	0.128	8.91	8.89	0.07
2	2	0	0.019	11.65	11.85	0.15
0	2	8				
1	3	7	0.297	3.10	3.13	0.07
2	4	6	0.281	5.25	5.32	0.07
0	2	6	0.168	7.50	7.41	0.15
1	3	5	0.143	5.33	5.36	0.09
0	2	4				
1	5	7				
0	4	6	0.245	1.66	1.53	0.18

2403K

H	K	L	ALPHA	FC	FO	SIGMA
2	2	8	0.453	2.55	2.68	0.10
0	0	8				
3	3	7	0.408	2.29	2.33	0.29
1	1	7	0.275	2.82	2.71	0.11
4	4	6				
2	2	6				
0	0	6	0.169	1.21	1.25	0.54
5	5	5				
3	3	5	0.226	2.71	2.40	0.30
1	1	5	0.119	4.44	4.45	0.10
4	4	4	0.257	4.73	4.57	0.13
2	2	4	0.091	8.69	8.43	0.10
0	0	4	0.054	10.63	10.43	0.05
5	5	3	0.341	2.87	2.88	0.20
3	3	3	0.119	5.36	5.40	0.15
1	1	3	0.033	6.53	6.47	0.10
6	6	2				
4	4	2	0.182	1.03	0.97	0.40
2	2	2				
0	0	2	0.007	1.58	1.81	0.05
5	5	1	0.275	2.54	2.46	0.15
3	3	1	0.068	4.94	4.83	0.17
1	1	1	0.004	7.04	7.11	0.02
6	6	0	0.453	2.58	3.07	0.30
4	4	0	0.147	7.32	7.49	0.04
2	2	0	0.022	12.49	12.31	0.10
0	2	8				
1	3	7	0.341	2.23	2.30	0.25
2	4	6	0.322	3.84	3.95	0.16
0	2	6	0.192	5.71	5.60	0.05
1	3	5	0.164	4.13	4.19	0.06
0	2	4	0.072	0.51	1.69	0.40
1	5	7	0.454	1.81	1.62	0.30
0	4	6				

2527K

H	K	L	ALPHA	FC	FO	SIGMA
2	2	8				
0	0	8	0.439	2.59	2.80	0.08
3	3	7				
1	1	7	0.310	2.78	2.70	0.08
4	4	6				
2	2	6	0.262	1.87	1.74	0.10
0	0	6	0.191	2.04	2.02	0.12
5	5	5				
3	3	5	0.255	2.81	2.72	0.30
1	1	5	0.134	4.81	4.73	0.17
4	4	4	0.289	4.35	4.35	0.11
2	2	4	0.103	8.43	8.31	0.30
0	0	4	0.061	10.06	9.50	0.12
5	5	3	0.385	2.65	2.56	0.28
3	3	3	0.134	5.86	5.78	0.07
1	1	3	0.037	7.11	6.99	0.11
6	6	2				
4	4	2	0.206	1.63	1.67	0.09
2	2	2	0.042	0.71	0.90	0.07
0	0	2	0.007	1.74	1.84	0.04
5	5	1	0.310	2.54	2.44	0.08
3	3	1	0.076	5.45	5.51	0.14
1	1	1	0.005	6.94	7.00	0.15
6	6	0				
4	4	0	0.166	7.12	7.08	0.06
2	2	0	0.024	10.65	10.83	0.08
0	2	8				
1	3	7	0.385	2.18	2.12	0.09
2	4	6	0.363	3.37	3.54	0.11
0	2	6	0.217	5.24	5.36	0.12
1	3	5	0.185	4.40	4.48	0.05
0	2	4	0.082	1.27	1.45	0.14
1	5	7				
0	4	6	0.317	1.46	1.22	0.15

2690K

H	K	L	ALPHA	FC	FO	SIGMA
2	2	8				
0	0	8	0.571	1.40	1.42	0.23
3	3	7	0.489	1.83	2.07	0.20
1	1	7	0.513	1.48	1.64	0.16
4	4	6	0.345	2.09	2.04	0.12
2	2	6				
0	0	6	0.291	1.53	1.32	0.26
5	5	5	0.212	1.70	1.72	0.15
3	3	5	0.594	0.80	0.60	0.30
1	1	5	0.283	2.10	1.93	0.10
4	4	4	0.149	3.85	3.75	0.08
2	2	4	0.322	3.12	3.02	0.12
0	0	4	0.114	6.61	6.34	0.20
5	5	3	0.068	8.07	7.70	0.34
3	3	3	0.428	1.98	2.09	0.10
1	1	3	0.149	4.80	4.87	0.09
6	6	2	0.041	5.99	5.96	0.11
4	4	2	0.601	0.81	1.06	0.30
2	2	2	0.229	1.50	1.50	0.10
0	0	2	0.047	1.12	1.03	0.12
5	5	1	0.008	1.01	1.00	0.04
3	3	1	0.345	1.89	1.95	0.06
1	1	1	0.085	4.37	4.51	0.06
6	6	0	0.005	5.81	5.94	0.17
4	4	0	0.571	1.42	1.97	0.25
2	2	0	0.184	5.45	5.59	0.12
0	2	8	0.027	8.75	8.67	0.23
1	3	7				
2	4	6	0.422	1.57	1.58	0.07
0	2	6	0.404	2.38	2.46	0.11
1	3	5	0.241	3.95	3.89	0.06
0	2	4	0.205	3.45	3.39	0.05
1	5	7				
0	4	6	0.353	1.24	1.08	0.30

2778K

H	K	L	ALPHA	FC	FO	SIGMA
2	2	8				
0	0	8	0.527	1.37	1.83	0.30
3	3	7	0.553	1.19	1.40	0.25
1	1	7	0.372	1.68	1.73	0.10
4	4	6				
2	2	6	0.314	1.25	1.07	0.26
0	0	6	0.229	1.49	1.54	0.10
5	5	5				
3	3	5	0.305	1.57	1.49	0.13
1	1	5	0.161	3.18	3.26	0.10
4	4	4	0.347	2.42	2.31	0.10
2	2	4	0.123	5.27	5.11	0.15
0	0	4				
5	5	3	0.462	1.65	1.56	0.12
3	3	3	0.161	4.07	4.06	0.09
1	1	3	0.045	4.89	4.83	0.12
6	6	2				
4	4	2	0.247	1.36	1.33	0.08
2	2	2	0.050	1.22	1.22	0.10
0	0	2	0.009	0.50	0.50	0.06
5	5	1	0.372	1.44	1.50	0.20
3	3	1	0.092	3.60	3.60	0.06
1	1	1	0.006	4.36	4.42	0.10
6	6	0				
4	4	0	0.199	4.28	4.27	0.10
2	2	0				
0	2	8				
1	3	7	0.462	1.18	1.32	0.31
2	4	6	0.436	1.83	1.78	0.17
0	2	6	0.260	3.17	3.27	0.10
1	3	5	0.221	2.92	2.95	0.08
0	2	4				
1	5	7				
0	4	6	0.380	1.05	0.66	0.32

2843K

H	K	L	ALPHA	FC	FO	SIGMA
2	2	8				
0	0	8	0.563	0.95	1.24	0.17
3	3	7				
1	1	7	0.397	1.29	1.15	0.15
4	4	6				
2	2	6				
0	0	6	0.244	1.45	1.58	0.08
5	5	5				
3	3	5	0.326	1.36	1.10	0.20
1	1	5	0.172	2.35	2.36	0.26
4	4	4	0.370	1.62	1.69	0.11
2	2	4	0.132	3.36	3.64	0.20
0	0	4	0.078	3.85	3.96	0.15
5	5	3				
3	3	3	0.172	2.80	2.74	0.09
1	1	3	0.048	3.15	3.27	0.26
6	6	2				
4	4	2	0.263	1.41	1.29	0.18
2	2	2	0.054	1.21	1.20	0.08
0	0	2	0.094	0.29	0.38	0.20
5	5	1	0.397	1.18	0.88	0.17
3	3	1	0.098	2.60	2.51	0.30
1	1	1	0.006	2.69	2.72	0.15
6	6	0				
4	4	0	0.212	2.76	2.99	0.12
2	2	0	0.031	4.06	3.82	0.15
0	2	8				
1	3	7	0.493	0.96	0.81	0.25
2	4	6	0.465	1.24	1.44	0.20
0	2	6	0.277	2.10	1.97	0.08
1	3	5	0.236	2.12	2.06	0.15
0	2	4	0.104	1.50	1.58	0.20
1	5	7				
0	4	6				

2905K

H	K	L	ALPHA	FC	FO	SIGMA
2	2	8				
0	0	8	0.604	0.77	1.11	0.20
3	3	7				
1	1	7	0.426	1.05	1.07	0.25
4	4	6				
2	2	6				
0	0	6	0.262	1.13	1.10	0.15
5	5	5				
3	3	5	0.350	1.15	1.15	0.14
1	1	5	0.184	2.18	2.32	0.30
4	4	4	0.398	1.47	1.47	0.08
2	2	4	0.141	3.16	3.09	0.16
0	0	4	0.084	3.62	3.55	0.25
5	5	3	0.530	0.91	0.85	0.16
3	3	3	0.184	2.57	2.56	0.17
1	1	3	0.051	2.89	3.02	0.16
6	6	2				
4	4	2	0.282	1.06	1.07	0.12
2	2	2	0.057	1.17	1.17	0.06
0	0	2	0.010	0.31	0.31	0.09
5	5	1	0.426	0.95	0.95	0.10
3	3	1	0.105	2.44	2.41	0.13
1	1	1				
6	6	0				
4	4	0	0.227	2.66	2.65	0.10
2	2	0				
0	2	8				
1	3	7				
2	4	6	0.500	1.06	0.99	0.30
0	2	6	0.298	1.96	1.92	0.20
1	3	5				
0	2	4				
1	5	7				
0	4	6				

ThO_2

293K

H	K	L	ALPHA	FC	FO	SIGMA
2	2	8	0.026	10.80	10.77	0.14
0	0	8	0.022	10.98	10.96	0.14
3	3	7	0.023	6.36	6.26	0.16
1	1	7	0.016	6.48	6.49	0.05
4	4	6				
?	2	6				
?	0	6	0.010	0.64	0.92	0.26
5	5	5	0.027	6.29	6.38	0.16
3	3	5	0.013	6.53	6.50	0.09
1	1	5	0.007	6.57	6.57	0.06
4	4	4	0.015	11.17	11.02	0.10
2	2	4	0.005	10.95	10.97	0.14
0	0	4	0.003	10.57	10.61	0.06
5	5	3	0.019	6.43	6.41	0.07
3	3	3	0.007	6.57	6.49	0.06
1	1	3	0.002	6.43	6.47	0.09
6	6	2				
4	4	2	0.010	0.64	0.55	0.12
2	2	2	0.002	1.09	1.22	0.12
0	0	2	0.000	1.25	1.20	0.09
5	5	1	0.016	6.48	6.42	0.10
3	3	1	0.004	6.54	6.51	0.08
1	1	1	0.000	5.88	5.92	0.06
6	6	0	0.026	10.80	10.82	0.07
4	4	0	0.008	11.13	11.06	0.07
2	2	0	0.001	9.73	10.00	0.21
0	2	8				
1	3	7	0.019	6.43	6.54	0.14
2	4	6	0.018	11.10	11.11	0.07
0	2	6	0.011	11.19	11.19	0.10
1	3	5	0.009	6.56	6.61	0.05
0	2	4	0.004	0.94	1.14	0.12
1	5	7	0.026	6.28	6.63	0.16
0	4	6	0.016	0.37	0.66	0.40

2291K

H	K	L	ALPHA	FC	FO	SIGMA
2	2	8	0.258	3.10	3.18	0.09
0	0	8	0.221	3.66	3.74	0.07
3	3	7	0.232	2.73	2.70	0.16
1	1	7	0.156	3.14	3.11	0.05
4	4	6	0.235	1.36	1.57	0.23
2	2	6	0.131	1.48	1.47	0.09
0	0	6	0.096	1.29	1.26	0.12
5	5	5	0.269	1.63	1.77	0.24
3	3	5	0.128	3.05	3.02	0.06
1	1	5	0.067	4.36	4.40	0.06
4	4	4	0.145	5.01	5.01	0.04
2	2	4	0.052	7.56	7.59	0.06
0	0	4	0.031	8.55	8.52	0.03
5	5	3	0.193	3.20	3.14	0.06
3	3	3	0.067	4.85	4.89	0.06
1	1	3	0.019	5.51	5.60	0.10
6	6	2				
4	4	2	0.103	1.29	1.17	0.08
2	2	2	0.021	0.68	0.80	0.06
0	0	2	0.004	0.46	0.83	0.08
5	5	1	0.156	2.89	2.85	0.08
3	3	1	0.038	4.79	4.78	0.05
1	1	1	0.002	5.51	5.58	0.04
6	6	0	0.258	3.10	3.27	0.16
4	4	0	0.083	6.78	6.70	0.05
2	2	0	0.012	8.62	8.94	0.24
0	2	8	0.235	1.36	1.45	0.09
1	3	7	0.193	2.60	2.55	0.16
2	4	6	0.183	4.24	4.35	0.08
0	2	6	0.109	5.74	5.72	0.06
1	3	5	0.093	4.13	4.13	0.06
0	2	4	0.041	0.78	0.84	0.14
1	5	7	0.260	2.26	2.52	0.14
0	4	6	0.159	1.42	1.25	0.18

2555K

H	K	L	ALPHA	FC	FO	SIGMA
2	2	8	0.303	2.61	2.26	0.12
0	0	8	0.259	3.13	3.34	0.08
3	3	7	0.272	2.41	2.53	0.10
1	1	7	0.183	2.94	2.89	0.06
4	4	6				
2	2	6	0.154	1.58	1.72	0.08
0	0	6	0.112	1.64	1.60	0.07
5	5	5	0.316	1.40	1.60	0.12
3	3	5	0.150	2.88	2.84	0.06
1	1	5	0.079	4.39	4.41	0.10
4	4	4	0.170	4.53	4.56	0.06
2	2	4	0.060	7.69	7.70	0.04
0	0	4	0.036	8.82	8.78	0.05
5	5	3	0.227	2.95	2.90	0.13
3	3	3	0.079	5.08	5.05	0.04
1	1	3	0.022	6.00	5.98	0.09
6	6	2				
4	4	2	0.121	1.51	1.53	0.12
2	2	2	0.025	0.76	0.98	0.09
0	0	2	0.004	0.34	0.55	0.08
5	5	1	0.183	2.68	2.55	0.08
3	3	1	0.045	4.86	4.83	0.06
1	1	1	0.003	6.03	6.03	0.02
6	6	0	0.303	2.63	2.92	0.09
4	4	0	0.097	6.60	6.54	0.04
2	2	0	0.014	9.45	9.49	0.05
0	2	8				
1	3	7				
2	4	6	0.214	3.78	3.88	0.11
0	2	6	0.127	5.41	5.38	0.08
1	3	5	0.109	4.12	4.17	0.08
0	2	4	0.048	1.17	1.03	0.14
1	5	7	0.305	1.96	2.25	0.18
0	4	6	0.187	1.50	1.37	0.09

2738K

H	K	L	ALPHA	FC	FO	SIGMA
2	2	8	0.345	2.02	1.74	0.16
0	0	8	0.295	2.49	2.73	0.16
3	3	7	0.309	2.01	2.04	0.12
1	1	7	0.207	2.51	2.46	0.08
4	4	6				
2	2	6	0.175	1.52	1.74	0.09
0	0	6	0.127	1.65	1.65	0.07
5	5	5	0.359	1.02	1.23	0.20
3	3	5	0.170	2.42	2.39	0.11
1	1	5	0.089	4.02	3.98	0.04
4	4	4	0.193	3.76	3.79	0.06
2	2	4	0.069	6.96	6.94	0.06
0	0	4	0.041	8.17	8.15	0.04
5	5	3	0.258	2.54	2.46	0.17
3	3	3	0.089	4.79	4.78	0.04
1	1	3	0.025	5.87	5.78	0.09
6	6	2				
4	4	2	0.137	1.53	1.45	0.08
2	2	2	0.028	1.24	1.21	0.06
0	0	2	0.005	0.16	0.29	0.12
5	5	1	0.207	2.23	2.17	0.15
3	3	1	0.051	4.47	4.47	0.04
1	1	1	0.003	5.90	5.87	0.06
6	6	0	0.345	2.03	2.31	0.12
4	4	0	0.110	5.84	5.83	0.05
2	2	0	0.016	9.07	9.22	0.10
0	2	8				
1	3	7				
2	4	6	0.243	3.07	3.14	0.15
0	2	6	0.145	4.63	4.62	0.05
1	3	5	0.123	3.72	3.79	0.09
0	2	4	0.054	1.43	1.22	0.22
1	5	7	0.347	1.57	1.75	0.13
0	4	6	0.212	1.38	1.37	0.10

2803K

H	K	L	ALPHA	FC	FO	SIGMA
2	2	8				
0	0	8	0.312	2.32	2.23	0.18
3	3	7				
1	1	7	0.220	2.22	2.20	0.14
4	4	6				
2	2	6				
0	0	6	0.135	1.75	1.36	0.32
5	5	5				
3	3	5	0.180	2.30	2.18	0.22
1	1	5	0.095	3.54	3.86	0.19
4	4	4	0.205	3.36	3.31	0.08
2	2	4	0.073	6.18	6.35	0.10
0	0	4	0.043	7.48	7.34	0.32
5	5	3	0.273	2.25	2.05	0.11
3	3	3	0.095	4.24	4.25	0.06
1	1	3	0.026	5.42	5.25	0.12
6	6	2				
4	4	2	0.145	1.31	1.43	0.13
2	2	2	0.029	1.75	1.83	0.07
0	0	2	0.005	0.49	0.43	0.09
5	5	1	0.220	1.96	1.83	0.08
3	3	1	0.054	3.88	3.91	0.09
1	1	1	0.003	5.53	5.27	0.11
6	6	0				
4	4	0	0.117	5.47	5.01	0.32
2	2	0	0.017	8.63	8.79	0.14
0	2	8				
1	3	7	0.273	1.82	1.86	0.21
2	4	6	0.258	2.79	3.01	0.16
0	2	6	0.153	4.03	4.13	0.18
1	3	5	0.131	3.33	3.38	0.06
0	2	4				
1	5	7				
0	4	6				

2909K

H	K	L	ALPHA	FC	FO	SIGMA
2	2	8	0.405	1.45	1.13	0.46
0	0	8	0.346	1.84	2.09	0.13
3	3	7	0.364	1.57	1.70	0.13
1	1	7	0.244	2.03	2.03	0.08
4	4	6				
2	2	6	0.205	1.38	1.56	0.08
0	0	6	0.150	1.62	1.67	0.08
5	5	5	0.423	0.68	1.09	0.26
3	3	5	0.200	1.92	1.90	0.07
1	1	5	0.105	3.55	3.56	0.05
4	4	4	0.227	2.93	2.97	0.12
2	2	4	0.080	6.15	6.11	0.11
0	0	4	0.048	7.36	7.29	0.08
5	5	3	0.303	2.10	1.98	0.16
3	3	3	0.105	4.30	4.31	0.08
1	1	3	0.029	5.63	5.49	0.09
6	6	2				
4	4	2	0.161	1.51	1.40	0.09
2	2	2	0.033	1.43	1.43	0.05
0	0	2	0.006	0.53	0.59	0.14
5	5	1	0.244	1.73	1.62	0.09
3	3	1	0.060	4.04	4.04	0.05
1	1	1	0.004	5.55	5.68	0.12
6	6	0	0.405	1.45	1.73	0.31
4	4	0	0.130	4.97	4.97	0.05
2	2	0	0.019	8.36	8.59	0.20
0	2	8				
1	3	7				
2	4	6	0.286	2.32	2.41	0.14
0	2	6	0.170	3.79	3.77	0.05
1	3	5	0.145	3.28	3.25	0.06
0	2	4	0.064	1.47	1.39	0.10
1	5	7	0.408	1.17	1.54	0.17
0	4	6	0.249	1.24	0.95	0.15

Details of Least Squares Fits to high temperature data

UO_2

T = 1873K

Model	S	$B_M(A^2)$	$B_0(A^2)$	$C^0_{123}x10^3$	$n_d(\%)$	$B^I_0(A^2)$	x	y	$ex10^3$	d	$R_w(\%)$
I	391(30)	1.79(11)	3.23(11)						4.4(14)		11.66
IA	406(25)	1.86(8)	3.30(8)	2.6(7)					4.7(12)		8.68
II	441(35)	1.95(9)	3.33(8)	2.7(6)	1.7(7)				6.0(16)		8.04
III	485(39)	2.06(10)	3.40(8)	2.9(6)	1.4(4)	4.0†			8.0(19)		7.06
IV	413(32)	1.88(9)	3.31(9)	2.6(7)	1.9(5)	4.0†		0.0†	5.0(14)	1.0	8.62
V	437(22)	1.94(6)	3.23(7)	2.4(5)	3.0(8)	4.0†	0.33†		6.0(11)	0.0	6.54
VI	438(30)	1.94(8)	3.30(8)	2.6(6)	1.6(8)	4.0†	0.33†	0.0†	6.0(14)	0.33	7.82
VII	430(31)	1.92(9)	3.32(8)	2.6(7)	1.0(7)	4.0†	0.33†	0.0†	5.7(14)	0.5	8.21
VIII											
IX	447(26)	1.94(6)	3.23(7)	2.4(6)	3.0(8)	4.0†	0.33†		6.4(13)	0.33	7.03

T = 2098K

Model	S	$B_M(A^2)$	$B_0(A^2)$	$C^0_{123}x10^3$	$n_d(\%)$	$B^I_0(A^2)$	x	y	$ex10^3$	d	$R_w(\%)$
I	6.24†	2.53(6)	4.39(15)						3.9(6)		12.2
IA	6.24†	2.49(2)	4.40(7)	6.0(6)					4.0(3)		4.88
II	6.24†	2.49(2)	4.36(9)	6.0(6)	1.1(17)				3.9(3)		4.81
III	6.24†	2.47(3)	4.40(6)	5.8(5)	0.3(2)	6.0(100)			4.0(3)		4.89
IV	6.24†	2.50(2)	4.40(7)	6.0(5)	0.8(4)	5.3(57)		0.0†	3.9(3)	1.0	4.84
V	6.24†	2.49(3)	4.32(11)	5.5(10)	2.1(2)	4.5†	0.33(6)		3.9(3)	0.0	4.77
VI	6.24†	2.49(6)	4.35(13)	5.8(10)	1.7(3)	4.5†	0.35(8)	0.0†	3.8(3)	0.33	4.76
VII	6.24†	2.49(2)	4.33(13)	5.5(13)	1.1(4)	4.5†	0.36(21)	0.0†	3.9(3)	0.5	4.88
VIII											
IX	6.24†	2.49(3)	4.36(12)	5.8(9)	1.4(3)	4.5†	0.36(58)		3.9(3)	0.33	4.87

† fixed value

T = 2218K

UO_2

Modei	S	$B_M(A^2)$	$B_0(A^2)$	$C^0_{123}x10^3$	$n_d(\%)$	$B^I_0(A^2)$	x	y	$ex10^3$	d	$R_w(\%)$
I	8.9(9)	2.53(13)	4.84(18)						13.1(34)		13.32
IA	8.9(4)	2.51(5)	4.84(7)	6.0(5)					13.2(14)		5.25
II	9.5(4)	2.60(5)	4.78(6)	5.9(4)	3.1(11)				15.1(14)		4.02
III	9.5(5)	2.61(6)	4.84(7)	6.0(5)	1.6(5)	14.5(68)			15.3(17)		4.20
IV	9.5(4)	2.61(5)	4.78(6)	5.9(4)	3.0(9)	'∞'		0.0†	15.1(15)	1.0	4.02
V	9.1(3)	2.56(5)	4.68(12)	4.7(3)	4.4(25)	3.0(16)	0.33(1)		13.6(12)	0.0	4.06
VI	9.0(4)	2.55(6)	4.74(8)	5.4(6)	2.4(13)	2.1(32)	0.33†	0.0†	13.6(14)	0.33	4.59
VII	9.6(4)	2.61(5)	4.86(9)	6.0(5)	0.6(3)	'∞'	0.33†	0.0†	15.4(12)	0.5	4.50
VIII											
IX											

T = 2403K

modei	S	$B_M(A^2)$	$B_0(A^2)$	$C^0_{123}x10^3$	$n_d(\%)$	$B^I_0(A^2)$	x	y	$ex10^3$	d	$R_w(\%)$
I	6.17†	2.74(9)	5.63(18)						4.6(4)		6.38
IA	6.17†	2.80(10)	5.57(17)	5.4(29)					4.4(4)		5.79
II	6.17†	2.93(11)	5.16(23)	6.4(25)	4.8(21)				4.2(4)		5.07
III	6.17†	2.81(10)	5.57(18)	5.4(29)	0.0(7)	7.0†			4.4(5)		5.79
IV	6.17†	2.83(10)	5.58(23)	5.8(27)	2.8(23)	7.9(36)		0.0†	4.3(4)	1.0	5.01
V	6.17†	2.91(7)	5.06(28)	3.0(24)	7.3(32)	1.3(13)	0.34(1)		3.6(3)	0.0	3.00
VI	6.17†	2.92(7)	5.24(24)	4.7(20)	6.9(27)	0.9(13)	0.35(1)	0.03(2)	3.6(3)	0.33	2.88
VII	6.17†	2.92(8)	5.11(21)	4.6(21)	9.3(26)	2.8(14)	0.33†	0.0†	3.9(3)	0.5	3.85
VIII	6.17†	2.96(6)	4.76(16)	2.2(16)	12.5(19)	2.6(8)	0.33†	0.0†	3.5(3)	0.15(7)	2.74
IX	6.17†	2.81(11)	5.55(23)	5.3(29)	0.0(48)	6.0†	0.33†		4.4(5)	0.33	5.79

† fixed value

UO_2

T = 2527K

Model	S	$B_M(A^2)$	$B_0(A^2)$	$C^0_{123}\times10^3$	$n_d(\%)$	$B^I_0(A^2)$	x	y	$ex10^3$	d	$R_w(\%)$
I	9.9(14)	3.45(23)	7.28(36)						19.8(57)		16.23
IA	8.4(10)	3.30(19)	6.96(29)	11.0(36)					14.7(36)		11.50
II	11.0(15)	3.72(22)	6.86(25)	8.6(25)	6.1(19)				23.8(63)		9.03
III	11.8(18)	3.83(23)	7.05(24)	9.7(25)	2.8(8)	4.8(28)			28.3(81)		9.12
IV	9.7(9)	3.59(14)	6.52(19)	9.9(18)	7.4(16)	7.2(32)		0.0†	18.9(34)	1.0	7.27
V	10.7(11)	3.73(17)	6.44(21)	5.2(23)	12.3(21)	6.7(21)	0.34†		22.1(44)	0.0	7.00
VI	10.0(8)	3.66(13)	6.17(28)	5.7(20)	14.2(38)	5.3(16)	0.32(1)	0.01(3)	19.7(31)	0.33	5.94
VII	9.8(8)	3.62(13)	6.39(24)	7.3(18)	10.1(23)	3.7(18)	0.34(2)	0.03(2)	18.9(31)	0.5	6.16
VIII	10.0(9)	3.66(13)	6.25(19)	5.7(22)	12.9(25)	4.8(17)	0.33†	0.01(4)	19.6(31)	0.33(15)	5.94
IX	8.6(8)	3.41(15)	6.24(25)	2.9(33)	13.3(31)	1.8(9)	0.33†		14.5(28)	0.33	8.84

T = 2690K

Model	S	$B_M(A^2)$	$B_0(A^2)$	$C^0_{123}\times10^3$	$n_d(\%)$	$B^I_0(A^2)$	x	y	$ex10^3$	d	$R_w(\%)$
I	5.7(9)	3.57(26)	8.45(52)						12(6)		23.81
IA	5.8(7)	3.59(39)	8.46(39)	15.5(35)					12(5)		17.80
II	7.4(6)	4.06(13)	7.48(20)	12.5(15)	10.5(13)				22(4)		7.87
III	8.2(8)	4.19(15)	7.90(20)	12.6(16)	4.4(5)	8.0†			26(6)		9.01
IV	7.2(5)	4.03(11)	7.15(18)	12.1(12)	13.4(11)	14.7(34)		0.0†	20(4)	1.0	6.83
V	7.6(5)	4.13(11)	5.94(69)	7.0(25)	38.3(125)	10.2(18)	0.31(1)		22(4)	0.0	6.29
VI	7.4(4)	4.08(10)	6.97(26)	9.0(15)	17.2(33)	7.6(17)	0.34(1)	0.0†	21(3)	0.33	6.01
VII	7.3(4)	4.05(10)	7.14(21)	10.7(14)	13.9(24)	7.0(17)	0.36(2)	0.0†	20(3)	0.5	6.06
VIII	7.4(4)	4.08(10)	6.96(16)	9.0(15)	17.7(15)	7.7(13)	0.34†	0.0†	21(3)	0.35(13)	6.02
IX	7.2(5)	4.05(11)	6.67(22)	9.2(18)	26.1(25)	9.7(18)	0.34†		19(4)	0.33	7.22

† fixed value

T = 2778K

UO_2

modèle	S	$B_M(A^2)$	$B_O(A^2)$	$C^O_{123}\times10^3$	n_d(%)	$B^I_O(A^2)$	x	y	$e\times10^3$	a	R_w(%)
I	3.8(10)	3.50(47)	8.89(74)						15(12)		31.37
IA	4.2(9)	3.71(38)	9.15(60)	20.1(60)					17(10)		26.57
II	6.5(8)	4.52(21)	8.09(25)	17.9(21)	18.6(38)				46(12)		8.55
III	7.1(10)	4.68(25)	8.53(25)	17.2(21)	6.9(7)	10.8(32)			49(14)		8.97
IV	6.0(5)	4.42(14)	7.57(19)	16.8(14)	18.6(11)	19.9(28)		0.0†	40(7)	1.0	6.15
V	6.7(5)	4.58(14)	7.39(18)	12.6(20)	25.3(16)	11.9(16)	0.34†		49(8)	0.0	5.70
VI	6.3(5)	4.51(15)	7.38(31)	13.6(18)	23.1(44)	10.7(18)	0.34(2)	0.04(3)	44(8)	0.33	5.23
VII	6.3(5)	4.49(14)	7.54(27)	14,9(16)	20.0(35)	10.3(22)	0.35(2)	0.05(2)	43(8)	0.5	5.41
VIII	6.4(5)	4.52(13)	7.40(17)	13.4(19)	22.9(19)	10.6(15)	0.34†	0.05†	44(7)	0.31(16)	5.22
IX	4.3(7)	3.80(30)	8.20(58)	8.1(73)	19.4(52)	4.1(18)	0.34†		19(9)	0.33	19.16

T = 2843K

modèle	S	$B_M(A^2)$	$B_O(A^2)$	$C^O_{123}\times10^3$	n_d(%)	$B^I_O(A^2)$	x	y	$e\times10^3$	d	R_w(%)
I	3.8(20)	4.44(63)	11.2(5)						84(116)		21.0
IA	3.5(13)	4.34(56)	11.1(4)	20.2(87)					84(64)		17.1
II	4.1(17)	4.59(60)	10.2(6)	17.4(70)	11.8(52)				110(91)		14.6
III	3.7(15)	4.46(58)	10.4(5)	19.3(69)		12.0†			95(81)		14.8
IV	3.2(16)	4.30(66)	9.6(7)	20.0(62)	11.8(39)	12.0†		0.05(3)	72(81)	1.0	13.6
V	3.7(12)	4.52(52)	9.3(8)	12.5(64)	20.3(64)	12.0†	0.34†		91(58)	0.0	13.8
VI	3.7(13)	4.50(61)	9.4(7)	15.5(63)	17.0(59)	12.0†	0.34†	0.06(8)	91(59)	0.33	13.5
VII	3.8(13)	4.53(60)	9.5(7)	16.6(62)	15.6(54)	12.0†	0.34†	0.06(6)	95(54)	0.5	13.4
VIII											
IX	3.5(13)	4.33(57)	11.1(4)	20.3(90)	17.8(27)	12.0†	0.34†		82(65)	0.33	16.8

† fixed value

T = 2905K

UO_2

Model	S	$B_M(A^2)$	$B_O(A^2)$	$C^O_{123} \times 10^3$	$n_d(\%)$	$B^I_O(A^2)$	x	y	$ex10^3$	d	$R_w(\%)$
I	2.9(9)	4.52(52)	11.8(5)						60(50)		26.2
IA	2.9(8)	4.50(46)	11.8(4)	26.6(130)					61(44)		23.4
II	4.71†	5.23(11)	10.5(4)	19.6(67)	13.2(25)				173(27)		14.0
III	4.71†	5.29(12)	10.6(3)	17.4(65)	5.4(10)				168(26)		13.7
IV	4.71†	5.31(8)	9.1(3)	14.1(35)	17.8(26)	15.2(111)		0.04(4)	190(19)	1.0	7.7
V											
VI	4.71†	5.35(7)	9.1(4)	11.1(36)	22.0(59)	11.3(31)	0.35(2)	0.02(6)	186(17)	0.33	6.4
VII	4.71†	5.33(7)	9.0(3)	12.5(35)	19.4(48)	10.9(37)	0.35(3)	0.04(3)	189(18)	0.5	6.7
VIII	4.71†	5.34(7)	9.0(3)	11.5(31)	20.8(16)	10.5(22)	0.35†	0.03†	187(16)	0.37(13)	6.5
IX	4.71†	5.36(7)	8.4(2)	10.2(31)	31.8(22)	11.9(24)	0.35†	0.03†	183(14)	0.33	7.1

† fixed value

ThO_2

T = 2291K

Model	S	$B_M(A^2)$	$B_0(A^2)$	$C^0_{123}\times10^3$	n_d(%)	$B^I_0(A^2)$	x	y	$ex10^3$	a	R_w(%)
I	3.36†	2.28(5)	4.48(12)						7.8(5)		7.58
IA	3.36†	2.30(3)	4.48(8)	5.0(8)					7.7(3)		4.08
II	3.36†	2.32(3)	4.23(11)	4.9(7)	5.9(3)				7.4(3)		3.70
III	3.36†	2.32(3)	4.41(10)	5.0(8)	1.6(8)	6.0†			7.7(3)		4.20
IV	3.36†	2.34(2)	4.17(6)	4.9(5)	6.1(9)	6.0†		0.0†	7.8(2)	1.0	2.85
V	3.36†	2.34(3)	4.07(11)	3.8(6)	8.9(21)	6.0†	0.33†		6.8(4)	0.0	3.61
VI	3.36†	2.34(2)	4.11(9)	4.3(6)	8.3(16)	5.7(24)	0.34†	0.0†	7.1(3)	0.33	3.06
VII	3.36†	2.34(2)	4.13(8)	4.5(5)	7.7(14)	5.0(20)	0.34†	0.0†	7.4(2)	0.5	2.87
VIII	3.36†	2.34(2)	4.17(9)	4.8(5)	6.6(15)	5.5(20)	0.34†	0.0†	7.7(3)	0.81(23)	2.80
IX											

T = 2555K

Model	S	$B_M(A^2)$	$B_0(A^2)$	$C^0_{123}\times10^3$	n_d(%)	$B^I_0(A^2)$	x	y	$ex10^3$	d	R_w(%)
I	4.05†	2.73(6)	5.35(16)						8.0(4)		8.05
IA	4.05†	2.77(3)	5.34(8)	6.9(8)					7.9(2)		3.70
II	4.05†	2.83(6)	5.31(8)	6.8(8)	1.8(14)				8.2(4)		3.63
III	4.05†	2.77(3)	5.32(8)	7.0(8)	1.0(6)	6.5†			7.7(2)		3.68
IV	4.05†	2.78(3)	5.11(10)	7.3(7)	5.0(16)	6.5†		0.04(2)	7.6(2)	1.0	3.30
V	4.05†	2.80(3)	4.93(12)	6.0(8)	8.6(21)	9.8(36)	0.34†		7.4(2)	0.0	2.99
VI	4.05†	2.81(3)	4.95(11)	5.9(7)	8.1(20)	6.4(27)	0.34†	0.02(5)	7.4(2)	0.33	2.89
VII	4.05†	2.80(3)	4.98(11)	6.2(7)	7.6(18)	5.8(28)	0.34†	0.03(2)	7.5(2)	0.5	2.93
VIII	4.05†	2.80(3)	4.95(12)	6.0(8)	8.1(20)	6.0(27)	0.34†	0.04†	7.4(2)	0.39(19)	2.89
IX	4.05†	2.78(3)	5.14(8)	6.1(7)	7.0(16)	6.5†	0.34†		7.5(2)	0.33	3.04

† fixed value

ThO_2

T = 2738K

Modèle	S	$B_M(A^2)$	$B_O(A^2)$	$C^O_{123}\times10^3$	$n_d(\%)$	$B^I_O(A^2)$	x	y	$ex10^3$	a	$R_w(\%)$
I	4.00†	3.15(8)	6.35(23)						9.0(10)		12.10
IA	4.00†	3.20(5)	6.35(13)	10.2(13)					8.8(6)		6.18
II	4.00†	3.41(10)	6.22(13)	10.1(12)	4.9(22)				9.8(7)		5.80
III	4.00†	3.21(4)	6.17(12)	10.2(11)	3.2(9)	7.0†			8.8(5)		5.38
IV	4.00†	3.25(3)	5.76(14)	10.3(10)	10.0(22)	12.4(49)		0.04(2)	8.5(5)	1.0	4.06
V	4.00†	3.26(3)	5.38(21)	4.7(14)	16.4(32)	7.0†	0.33(1)		7.3(4)	0.0	3.70
VI	4.00†	3.27(2)	5.47(12)	8.6(8)	15.8(19)	9.0(21)	0.35(2)	0.06(3)	7.2(3)	0.33	2.78
VII	4.00†	3.26(2)	5.51(13)	9.4(8)	15.1(20)	8.3(22)	0.35(2)	0.07(2)	7.3(4)	0.5	2.93
VIII	4.00†	3.27(2)	5.43(16)	8.3(10)	16.3(25)	8.9(21)	0.35(2)	0.57(3)	7.2(4)	0.32(15)	2.78
IX	4.00†	3.23(4)	6.12(11)	9.0(11)	8.5(18)	7.0†	0.35†		8.1(4)	0.33	4.90

T = 2803K

Modèle	S	$B_M(A^2)$	$B_O(A^2)$	$C^O_{123}\times10^3$	$n_d(\%)$	$B^I_O(A^2)$	x	y	$ex10^3$	d	$R_w(\%)$
I	2.99†	2.90(12)	7.63(52)						4.8(15)		22.17
IA	2.99†	3.03(12)	7.61(44)	11.7(41)					4.7(13)		17.11
II	2.99†	3.13(10)	5.84(47)	10.6(26)	24.6(56)				4.1(10)		13.32
III	2.99†	3.06(8)	6.66(34)	12.4(25)	7.9(14)	7.0†			4.5(9)		12.21
IV	2.99†	3.21(6)	5.31(29)	10.8(17)	21.1(27)	9.7(33)		0.04(1)	3.7(6)	1.0	7.74
V	2.99†	3.12(9)	5.90(45)	10.0	19.8(41)	7.0†	0.37(1)		3.7(10)	0.0	12.60
VI	2.99†	3.19(6)	4.80(38)	6.7(22)	29.0(49)	8.0(29)	0.34(2)	0.04(3)	3.5(6)	0.33	7.73
VII	2.99†	3.19(9)	5.06(27)	6.9(17)	24.6(28)	4.8(17)	0.35(1)	0.04(1)	3.5(6)	0.5	6.68
VIII	2.99†	3.19(6)	5.12(26)	7.4(19)	23.7(24)	4.7(17)	0.35†	0.04†	3.6(5)	0.53(8)	6.64
IX	2.99†	3.16(9)	5.50(49)	6.3(26)	28.3(47)	7.0†	0.35†		3.4(10)	0.33	12.54

† fixed value

T = 2909K

ThO_2

Model	S	$B_M(A^2)$	$B_O(A^2)$	$C^O_{123}x10^3$	$n_d(\%)$	$B^I_O(A^2)$	x	y	$ex10^3$	a	$R_w(\%)$
I	3.96†	3.80(10)	7.67(28)						10.6(23)		17.82
IA	3.96†	3.78(7)	7.68(19)	14.7(27)					10.3(15)		11.31
II	3.96†	3.86(4)	6.35(17)	12.8(13)	24.4(29)				9.4(8)		6.22
III	3.96†	3.81(5)	7.14(16)	12.8(18)	6.0(10)	7.5†			10.4(10)		8.79
IV	3.96†	3.84(4)	6.56(17)	13.6(14)	13.9(19)	7.5†		0.07(1)	10.1(9)	1.0	6.58
V	3.96†	3.88(4)	6.24(20)	11.0(14)	21.4(24)	13.2(17)	0.35(1)		8.2(7)	0.0	5.30
VI	3.96†	3.89(3)	6.41(18)	11.6(14)	18.1(23)	9.1(17)	0.36(1)	0.06(2)	8.6(7)	0.33	4.74
VII	3.96†	3.88(3)	6.45(18)	12.3(14)	17.2(21)	7.8(18)	0.37(2)	0.07(1)	8.8(7)	0.5	4.72
VIII	3.96†	3.88(3)	6.44(19)	12.1(15)	17.5(23)	8.1(20)	0.37(2)	0.07(2)	8.8(8)	0.44(14)	4.69
IX	3.96†	3.86(5)	7.43(18)	14.3(24)	8.5(25)	7.5†	0.38(3)		9.3(11)	0.33	8.33

model	S	$B_M(A^2)$	$B_O(A^2)$	$C^O_{123}x10^3$	$n_d(\%)$	$B^I_O(A^2)$	x	y	$ex10^3$	d	$R_w(\%)$

† fixed value

APPENDIX A.4

ThO_2 PHONON ENERGIES

Error in last digit(s) shown in parentheses

ζ(r.l.u.)	$\hbar\omega$(meV)
[000] zone-centre	
0.0	34.6(12)‡
0.0	33.9(15)
0.0	57.9(1)†
0.0	57.6(10)
0.0	70.3(12)‡
[ζ00] Δ_1 branches	
0.1	4.6(2)*
0.15	6.4(2)*
0.2	9.0(2)*
0.35	14.1(5)
0.4	16.1(4)
0.5	19.5(5)
0.6	22.7(5)
0.75	24.5(15)
[ζ00] Δ_5 branches	
0.2	4.6(1)
0.3	6.3(1)
0.4	8.2(1)
0.5	10.0(2)
0.6	11.4(1)
0.7	12.4(2)
0.8	13.5(5)
0.9	14.5(3)
1.0	15.4(5)
0.2	35.0(7)
0.5	34.2(8)
0.7	34.2(10)
0.9	34.8(10)
0.5	58.2(15)*
0.7	55.2(20)*
0.9	54.2(16)*
1.0	55.2(20)*
[ζ00] Δ_2' branches	
0.4	49.6(15)
0.5	45.8(8)
0.6	40.5(8)
0.7	35.0(8)
0.8	29.8(8)
[$\zeta\zeta$0] Σ_1 branches	
0.05	3.2(3)*
0.1	5.8(3)*

ζ (r.l.u.)	$\hbar\omega$ (meV)
0.25	13.9(7)
0.35	17.8(9)
0.5	20.2(5)
0.7	19.7(6)
0.8	17.2(6)
0.9	15.1(7)

[$\zeta\zeta$0] Σ_3 branches

0.15	4.6(1)
0.2	6.3(1)
0.3	9.2(1)
0.4	12.2(1)
0.5	15.2(2)
0.6	18.5(3)
0.7	21.1(4)
0.8	23.0(5)
0.2	33.8(10)
0.4	32.9(10)
0.55	30.0(6)
0.7	28.8(6)
0.8	26.4(6)
1.0	23.4(10)
0.2	57.4(12)
0.4	55.1(12)
0.6	43.8(23)*
0.7	40.7(23)*
0.75	36.1(10)

[$\zeta\zeta$0] Σ_4 branches

0.2	6.8(1)
0.3	9.7(2)
0.4	11.3(3)
0.5	11.9(4)
0.6	13.8(5)
0.7	14.5(7)
0.1	33.8(10)
0.2	36.6(6)
0.3	39.8(7)
0.4	43.1(5)
0.5	46.7(6)
0.6	49.6(6)
0.7	52.8(6)
0.8	55.4(8)
0.9	57.0(10)

[$\zeta\zeta\zeta$] Λ_1 branches

0.1	7.0(3)*
0.15	11.3(3)*
0.25	18.1(7)
0.4	21.6(7)
0.5	22.2(7)
0.2	55.6(10)
0.35	52.7(8)
0.5	50.6(10)

[$\zeta\zeta\zeta$] Λ_3 branches

0.2	7.9(2)
0.3	10.0(2)
0.4	11.7(7)
0.5	12.7(5)

ζ(r.l.u.)	$\hbar\omega$ (meV)	ζ(r.l.u.)	$\hbar\omega$ (meV)
0.2	36.0(8)	0.2	55.2(10)
0.3	39.0(7)	0.4	49.8(8)
0.5	46.4(7)	0.5	46.4(8)

* - Extrapolated from constant-energy scans

† - From first order Raman Scattering

‡ - From second order Raman Scattering

APPENDIX A.5

SUMMARY OF RESOLUTION-CORRECTED PHONON ENERGIES FOR ELASTIC CONSTANTS ANALYSIS

Error in last digit(s) shown in parentheses

	(ζ00)TA	E(meV)		(ζζ0)TA	E(meV)		(ζ00)LA	q(r.l.u.)		(ζζ0)LA	q(r.l.u.)
T(K)	0.1	0.15	0.2	0.1	0.15	0.2	5 meV	6 meV	7 meV	5 meV	7 meV
293	1.93(7)	2.77(7)	3.68(6)	3.71(10)	5.37(9)		.127(10)	.141(10)	.168(10)		.124(6)
293 †	1.89(6)	2.78(6)	3.64(6)	3.66(6)		6.76(6)	.125(8)	.142(8)	.169(8)	.092(6)	.126(6)
2081	1.63(6)	2.41(6)	3.15(6)	3.04(8)	4.45(7)	5.71(7)	.142(11)	.162(10)	.198(10)	.110(6)	
2271	1.63(5)	2.39(5)	3.13(6)	3.02(6)		5.53(6)	.147(10)	.171(10)	.201(10)	.111(5)	
2390 †	1.48(6)	2.24(6)	2.98(6)	2.69(7)	3.99(6)	5.08(6)	.151(11)	.176(12)	.214(12)	.119(6)	.161(7)
2478	1.51(5)	2.26(5)	2.96(5)	2.73(7)	3.76(6)	5.01(7)	.151(11)	.172(11)	.210(11)	.114(6)	.162(7)
2589	1.47(5)	2.19(5)	2.88(5)	2.58(6)	3.74(6)		.152(11)	.180(12)		.115(6)	.163(8)
2683	1.32(5)	2.04(5)	2.74(5)	2.36(5)	3.50(6)		.154(11)	.188(10)	.229(13)	.121(7)	.169(8)
2771	1.25(5)	1.95(6)	2.61(6)	2.17(5)	3.30(6)	4.12(6)	.162(10)	.197(14)	.234(13)	.123(8)	.175(7)
2929	1.17(15)	1.81(10)	2.35(15)	1.98(10)	2.95(15)	3.63(20)	.166(32)	.222(36)	.248(29)	.122(11)	.205(15)
	Resolution Corrections at three temperatures (incorporated in the above results)										
293	0.03	0.01	0.00	-0.17	-0.12	-0.10	-.021	-.013	-.012	-.009	-.006
2081	0.05	0.03	0.01	-0.11	-0.09	-0.06	-.017	-.009	-.010	-.008	-.006
2683	0.07	0.04	0.03	-0.02	-0.02	-0.02	-.011	-.005	-.006	-.003	-.002

† measured after 2683K data

APPENDIX A.6

DETERMINATION OF $X^D(\underset{\sim}{Q})$ ON AN ABSOLUTE SCALE

In this appendix we describe the relations used in the determination of the diffuse QES intensity on an absolute scale. As noted in §7.4.3, this involves the normalisation of the diffuse intensity to the intensity of scattering from acoustic phonons in order to eliminate the unknown spectrometer constants.

The scattering cross-section for QES varies slowly with $\underset{\sim}{Q}$ and therefore the simplified expressions for the resolution function, (equations 3.41 - 3.43), may be used in the evaluation of the observed intensity $\mathcal{I}(\underset{\sim}{Q}_o, \omega_o)$. On integrating over an energy scan at constant $\underset{\sim}{Q}$ of the diffuse scattering, we obtain the following expression for the integrated diffuse intensity $\mathcal{J}^D(\underset{\sim}{Q}_o)$, evaluated experimentally in equation (7.3).

$$\mathcal{J}^D(\underset{\sim}{Q}_o) = \hbar \int \mathcal{I}(\underset{\sim}{Q}_o, \omega_o) d\omega_o = \frac{\sigma_{coh}}{4\pi} N_a V_I V_F \, e^{-2W_a(\underset{\sim}{Q}_o)} \, \mathcal{X}^D(\underset{\sim}{Q}_o) \qquad (A.6.1)$$

Here N_a is the number of anions in the crystal, V_I and V_F are the resolution volumes of the monochromator and analyser systems ($\propto k^3 \cot\theta$) and $\mathcal{X}^D(\underset{\sim}{Q})$ is the diffuse scattering per anion (equation 7.4).

We consider the detected neutron count relative to a fixed count, C_M, of the neutron monitor installed in the incedent beam before the sample. This measures the incedent neutron flux with an efficiency which is proportional to k_i^{-1}. Since the flux is proportional to $k_i V_I$, we can write $C_M = cV_I$ where c is a constant. The integrated intensity per monitor count is then

$$\frac{\mathcal{J}^D(\underset{\sim}{Q}_o)}{C_M} = \frac{AV_F}{c} \quad \frac{\sigma_{coh}}{4\pi} \quad N_a \, e^{-2W_a(\underset{\sim}{Q}_o)} \quad \mathcal{X}^D(\underset{\sim}{Q}_o) \qquad (A.6.2)$$

The corresponding expression for the integrated intensity $\mathcal{I}^{ph}(\underset{\sim}{Q}_o)$ of an energy scan of a low wavevector acoustic phonon, of energy $\hbar\omega_{ph}$, is

$$\frac{\mathcal{I}^{ph}(\underset{\sim}{Q}_o)}{C_M} = \frac{AV_F}{c} N_1 \frac{\hbar^2}{\hbar\omega_{ph}} \frac{k_B T}{\hbar\omega_{ph}} \frac{|\underset{\sim}{Q}.\underset{\sim}{\xi}_{ph}|^2}{M_1} |F(\underset{\sim}{Q})|^2 \qquad (A.6.3)$$

$N_1 = \frac{1}{2}N_a$ and M_1 are the number and mass of the fluorite primitive unit cell and $\underset{\sim}{\xi}_{ph}$ is the polarisation vector for the observed mode. Since all ions move in phase by the same amount for low $\underset{\sim}{q}$ acoustic phonons, the scalar product has been taken out of the expression for the inelastic structure factor $G(\underset{\sim}{Q})$ (equation 3.24), leaving the Bragg structure factor $F(\underset{\sim}{Q})$ for the neighbouring Bragg peak (equation 3.18). Another consequence of the low acoustic phonon energy is that $k_B T \gg \hbar\omega_{ph}$, and hence the phonon population factor has been replaced by $k_B T / \hbar\omega_{ph}$.

The final step in the normalisation process is to account for the energy dependence of $V_F \propto k_f^3 \cot \theta_A$, which may be normalised to its value for elastic scattering. We may write

$$\frac{AV_F}{c} = C_s \frac{k_f^3 \cot \theta_A}{k_i^3 \cot \theta_A^o} \qquad (A.6.4)$$

where θ_A^o is the analyser angle for elastic scattering and C_s is a constant which absorbs all spectrometer constants. On inserting equation (A.6.4) into (A.6.2) and (A.6.3), the value of $C_s N_a$ may be deduced from (A.6.3) and used in (A.6.2) to obtain $X^D(\underset{\sim}{Q})$ on an absolute scale.

The values of the integrated intensities of the QES and the (0.15, 0.15, 0)TA phonon peak and the values of $C_s N_a$ at each temperature are given in Table A.6.1. The resulting values of $X^D(\underset{\sim}{Q})$

at the three $\underset{\sim}{Q}$ values investigated are listed in Table A.6.2. However it should be noted that the deduced values of $C_s N_a$ decrease with increasing temperature up to 2683K. The decrease in $C_s N_a$ above 2400K may be partly attributed to sample evaporation, but no evidence of evaporation was observed below 2400K. This discrepancy is probably due to the breakdown of the harmonic approximation, on which the quoted phonon scattering cross-section is based. The data has subsequently been re-analysed by M. A. Hackett and R. Osborn in conjunction with new data covering a more extensive range of $\underset{\sim}{Q}$ values and temperatures. They concluded that the thermal vibration parameter B_u assigned to the incoherent scattering in equation (7.3) is too small, and re-calculated $X^D(\underset{\sim}{Q})$ for the current data using revised values of $C_s N_a$ and the thermal parameters. Their results for $X^D(\underset{\sim}{Q})$, also listed in Table A.6.2, are in reasonable agreement with the original results, which have consequently been used in the body of the thesis.

TABLE A.6.1

INTEGRATED INTENSITIES OF (0.15, 0.15, 0)TA PHONON AND DIFFUSE SCATTERING SCANS

Error in last digit(s) shown in parentheses

T(K)	$\mathcal{I}^{ph}(Q)\left\{\frac{k_f^3 \cot \theta_A}{k_i^3 \cot \theta_A^o}\right\}^{-1}$	$C_s N_a \times 10^3$	$\mathcal{I}^D(\zeta, 0, 0)$ for $\zeta =$		
			1.85	2.15	2.4
293	147.4(20)	17.5(10)	-	-11(8)	-
2081	269.7(18)	14.4(9)	0	0	0
2271	299.1(30)	14.9(15)	31(9)	27(9)	-21(8)
2478	255.8(17)	10.9(9)	39(9)	70(9)	-1(9)
2589	253.4(17)	9.7(9)	47(10)	76(10)	10(9)
2683	277.6(12)	9.7(6)	13(9)	60(11)	2(9)
293	96.3(19)	11.5(10)	-1(9)	-	-
2390	218.7(15)	9.1(8)	-	13(9)	24(9)
2778	217.2(14)	7.2(7)	-	50(10)	11(9)

Note: The experimental runs have been listed in chronological order

TABLE A.6.2

$X^D(Q)$ ON AN ABSOLUTE SCALE FOR THIS WORK AND FOR M. A. HACKETT'S REVISED ANALYSIS

Error in last digit(s) shown in parentheses

	This analysis			M. A. Hackett's Analysis			
T(K)	$X^D(\zeta, 0, 0)$ for ζ =			C_sN_a	$X^D(\zeta, 0, 0)$ for ζ =		
	1.85	2.15	2.4		1.85	2.15	2.4
293	-	-0.02(2)	-	17.5	-	0.00(2)	-
2081	0.0	0.0	0.0	17.5	0.00(3)	0.04(2)	0.00(3)
2271	0.10(3)	0.10(3)	-0.08(3)	17.5	0.09(3)	0.12(2)	-0.07(3)
2478	0.18(5)	0.36(6)	-0.00(4)	17.0	0.17(3)	0.28(3)	0.01(3)
2589	0.25(6)	0.46(7)	0.07(6)	15.5	0.24(4)	0.35(4)	0.06(4)
2683	0.07(5)	0.37(7)	0.01(6)	13.5	0.18(4)	0.34(5)	0.03(4)
293	-0.00(3)	-	-	11.5	-	-	-
2390	-	0.08(5)	0.16(6)	10.9	-	0.14(4)	0.14(5)
2778	-	0.44(10)	0.11(9)	9.5	-	0.44(7)	0.12(6)